Advanced Applications of Raman Spectroscopy for Environmental Analyses

Rebecca Halvorson Lahr

Dissertation submitted to the faculty of the Virginia Polytechnic Institute and State
University in partial fulfillment of the requirements for the degree of

Doctor of Philosophy in Civil Engineering

Peter J. Vikesland
Amy J. Pruden
Andrea M. Dietrich
Maren Roman

November 8, 2013
Blacksburg, VA

Keywords: Surface-enhanced Raman spectroscopy (SERS), drop coating deposition Raman (DCDR), cyanotoxin, microcystin-LR, cellular imaging, gold nanoparticles, intracellular biosynthesis, *Pseudokirchneriella subcapitata*, algae, cellulose, wax-printed microfluidic paper based analytical devices (µPADs)

Advanced Applications of Raman Spectroscopy for Environmental Analyses

Rebecca Halvorson Lahr

ABSTRACT

Due to an ever-increasing global population and limited resource availability, there is a constant need for detection of both natural and anthropogenic hazards in water, air, food, and material goods. Traditionally a different instrument would be used to detect each class of contaminant, often after a concentration or separation protocol to extract the analyte from its matrix. Raman spectroscopy is unique in its ability to detect organic or inorganic, airborne or waterborne, and embedded or adsorbed analytes within environmental systems. This ability comes from the inherent abilities of the Raman spectrometer combined with concentration, separation, and signal enhancement provided by drop coating deposition Raman (DCDR) and surface-enhanced Raman spectroscopy (SERS).

Herein the capacity of DCDR to differentiate between cyanotoxin variants in aqueous solutions was demonstrated using principal component analysis (PCA) to statistically demonstrate spectral differentiation. A set of rules was outlined based on Raman peak ratios to allow an inexperienced user to determine the toxin variant identity from its Raman spectrum. DCDR was also employed for microcystin-LR (MC-LR) detection in environmental waters at environmentally relevant concentrations, after pre-concentration with solid-phase extraction (SPE). In a cellulose matrix, SERS and normal Raman spectral imaging revealed nanoparticle transport and deposition patterns, illustrating that nanoparticle surface coating dictated the observed transport properties. Both SERS spectral imaging and insight into analyte transport in wax-printed paper microfluidic channels will ultimately be useful for microfluidic paper-based analytical device (μPAD) development. Within algal cells, SERS produced 3D cellular images in the presence of intracellularly biosynthesized gold nanoparticles (AuNP), documenting in detail the molecular vibrations of biomolecules at the AuNP surfaces. Molecules involved in nanoparticle biosynthesis were identified at AuNP surfaces within algal cells, thus aiding in mechanism elucidation.

The capabilities of Raman spectroscopy are endless, especially in light of SERS tag design, coordinating detection of analytes that do not inherently produce strong Raman vibrations. The increase in portable Raman spectrometer availability will only facilitate cheaper, more frequent application of Raman spectrometry both in the field and the lab. The tremendous detection power of the Raman spectrometer cannot be ignored.

Table of Contents

Table of Figures

Table of Tables

1

Introduction

The applications of Raman spectroscopy are ubiquitous and remarkable. It's not often that a single instrument can be employed to analyze samples across multiple analyte classes (i.e., inorganic and organic, gaseous and aqueous, chemical and microbial), yet Raman spectroscopy is capable of just that. With the help of surface-enhancements facilitated by noble-metal nanomaterials and the sample concentration capacity of drop-coating deposition Raman (DCDR) spectroscopy, the Raman spectrometer can be used for analysis of rock composition, identification of drugs of abuse within human fingerprints, detection of airborne bacteria, identification of single molecules in aqueous systems, and diagnosis of osteoarthritis by analysis of synovial fluid.[1-8] Despite its capabilities, Raman spectroscopy is rarely utilized in environmental engineering.

The widespread utility of the Raman spectrometer and its application to detection of environmentally relevant contaminants is explored in this dissertation. Detection capabilities are demonstrated for organic molecules and inorganic metal nanoparticles in diverse matrixes such as nanopure water, environmental waters, cellulose networks, and inside of algal cells. **Chapter two** establishes the ability of DCDR to detect and differentiate between eight microcystin variants in nanopure water solutions. This chapter was published in *Analytical Chemistry* in 2011.[9] **Chapter three** shows that DCDR is applicable for microcystin detection at environmentally relevant concentrations in environmental waters. This section is part of the peer-reviewed manuscript "Drop coating deposition Raman (DCDR) for microcystin-LR identification and quantitation" published in *Environmental Science and Technology* in 2011.[2] **Chapter four** employs the surface-enhancement effects of noble metal nanomaterials to track their presence in cellulose networks with a Raman spectrometer, thus facilitating characterization of nanomaterial transport in wax-printed paper microfluidic devices as a function of particle surface coating. **Chapter five** documents the utility of three-dimensional surface-enhanced Raman spectroscopy (SERS) cellular imaging for surface analysis of intracellular gold nanoparticles. **Chapter six** summarizes the engineering significance of the documented research efforts. The chapters included herein collectively demonstrate the tremendous detection power of the Raman spectrometer.

2

Differentiation of Microcystin, Nodularin, and their Component Amino Acids by Drop-Coating Deposition Raman Spectroscopy

*Rebecca A. Halvorson, Weinan Leng, and Peter J. Vikesland**

Department of Civil and Environmental Engineering and Institute of Critical Technology and
Applied Science (ICTAS), Virginia Tech, 418 Durham Hall, Blacksburg, VA 24060-0246
* pvikes@vt.edu, tel. 540-231-3568

Reproduced with permission from
Analytical Chemistry **2011**, *83* (24): 9273-9280.

ABSTRACT

Raman spectra of microcystin-LR (MC-LR), MC-RR, MC-LA, MC-LF, MC-LY, MC-LW, MC-YR, and nodularin collected by drop coating deposition Raman (DCDR) spectroscopy are sufficiently unique for variant identification. Amino acid spectra of L-phenylalanine, L-leucine, L-alanine, D-alanine, L-glutamic acid, L-arginine, L-tryptophan, L-tyrosine, and N-methyl-D-aspartic acid were collected in crystalline, DCDR, and aqueous forms to aid in cyanotoxin Raman peak assignments. Both peak ratio analysis and principal components analysis (PCA) properly classified 72 DCDR spectra belonging to the eight toxins. Loading plots for the first three principal components (PCs) most heavily weighted the peaks highlighted in the peak ratio analysis, specifically the 760 cm^{-1} tryptophan peak, 853 cm^{-1} tyrosine peak, and 1006 cm^{-1} phenylalanine peak. Peak ratio analyses may be preferred under some circumstances because of the ease and speed with which the ratios can be computed, even by untrained lab technicians. A set of rules was created to mathematically classify toxins using the peak ratios. DCDR methods hold great potential for future application in routine monitoring because portable and handheld Raman spectrometers are commercially available, DCDR spectra can be collected in seconds for biomolecule mixtures as well as samples containing impurities, and the method requires far fewer consumables than conventional cyanotoxin detection methods.

INTRODUCTION

The microcystins (MCs), a class of cyclic heptapeptide cyanotoxins produced by cyanobacteria, are ubiquitous contaminants of surface waters worldwide.[10] A recent survey of U.S. lakes and water supply reservoirs indicated that 80% of the tested water bodies were positive for microcystin, which was not always fully removed from the water by the drinking water treatment plant.[10] Furthermore, the MCs and other cyanotoxins are associated with fatalities of wild and domestic animals as well as humans at low doses.[11] MCs primarily damage the liver of an organism by inhibiting protein phosphatases 1 and 2A, but they are also suspected carcinogens.[11] Hence, the World Health Organization has established a guideline for MC-LR, one of the most commonly detected MCs, recommending that drinking water contain less than 1 μg/L (≈1 nM).

More than 89 MC toxins have been identified, all composed of a seven membered cyclic heptapeptide with 3-amino-9-methoxy-2,6,8-trimethyl-10-phenyl-4,6-decadienoic acid (Adda) in amino acid position five (**Figure 2.1**). Adda must be intact for the toxin to exhibit protein phosphatase inhibition.[11-13] Although variations have been identified across all seven amino acids within the heptapeptide, one of the most common differences between variants is the identity of the amino acids in positions two and four.[11,14] Toxicity is greatly affected by small differences in the toxin structure (**Figure 2.1**).

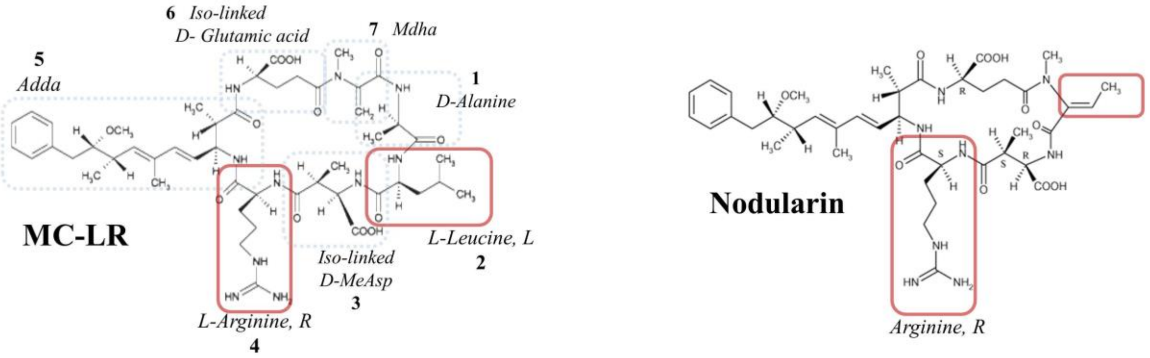

Toxin	LD$_{50}$*	1	2	3	4	5	6	7
MC-LR	50	D-Ala	L-Leu	D-MeAsp	L-Arg	Adda	D-Glu	Mdha
MC-RR	600	D-Ala	L-Arg	D-MeAsp	L-Arg	Adda	D-Glu	Mdha
MC-LA	50	D-Ala	L-Leu	D-MeAsp	L-Ala	Adda	D-Glu	Mdha
MC-LF		D-Ala	L-Leu	D-MeAsp	L-Phe	Adda	D-Glu	Mdha
MC-LY	90	D-Ala	L-Leu	D-MeAsp	L-Tyr	Adda	D-Glu	Mdha
MC-LW		D-Ala	L-Leu	D-MeAsp	L-Trp	Adda	D-Glu	Mdha
MC-YR	70	D-Ala	L-Tyr	D-MeAsp	L-Arg	Adda	D-Glu	Mdha
Nodularin	50	--	--	D-MeAsp	L-Arg	Adda	D-Glu	Mdhb
Others	50-1200	D-Ser, D-Leu	L-Ala, L-Glu, L-Val, L-Glu(OMe), L-Phe, L-Met(O), L-Hphe, L-Htyr, L-Trp, L-Harg, L-HIle, L-H$_4$Y	D-Asp	Aba, L-Leu, L-Glu, L-Glu(OMe), L-Harg, L-Met(O)	DMAdda, (6Z)Adda, ADMAdda	D-Glu(OMe)	Dha, L-Ser, L-MeSer, Dhb, MeLan

*LD$_{50}$ values (µg/kg) correspond to mouse toxicity for intraperitoneal injections.

Lesser known abbreviations are given in alphabetical order. (6Z)Adda: Adda with a *cis* configuration at the 6th carbon of Adda; Aba: amino-isobutyric acid; Adda: 3-amino-9-methoxy-2-6,8-trimethyl-10-phenyl-4,6-decadienoic acid; ADMAdda: *O*-acetyl-Adda; Dha: dehydroalanine; Dhb: dehydrobutyric acid; DMAdda: desmethyl-Adda; Glu(OMe): glutamate methyl ester; H$_4$Y: 1,2,3,4-tetrahydrotyrosine; Harg: homoarginine; HIle: homoisoleucine; Hphe: homophenylalanine; Htyr: homotyrosine; Mdha: N-methyl-dehydroalanine; MeLan, *N*-methyllanthionin; Met(O): methionine-*S*-oxide.

Figure 2.1. Microcystin variant LD$_{50}$ values are affected by minor structural differences.[11,14-15]

Unfortunately, current detection protocols utilizing HPLC with a UV-Vis detector, enzyme-linked immunosorbent assays (ELISA), or protein phosphatase inhibition assays (PPIA) often report total toxicity or equivalents of MC-LR rather than toxin identity and concentration. This limitation exists because the UV-Vis profiles of many of the MCs overlap, ELISA methods generally use monoclonal or polyclonal antibodies that target either the 4-arginine in MC-LR, MC-RR, MC-YR and other MCs or the ADDA group common to all microcystins, protein phosphatase inhibition assays monitor the combined toxicity of the sample, and quality MC standards for lesser known variants are costly if even available commercially.[16-18] LC-MS-MS, MALDI-MS, and SELDI-TOF-MS can distinguish between toxin variants; however, instrument costs are high, MALDI-MS and SELDI-MS are subject to interference problems, and LC-MS-MS methods are instrument specific and require expensive toxin standards for each analysis.[16-18]

A method to detect cyanotoxin variants reliably, rapidly, and economically has yet to be established to accommodate routine cyanotoxin monitoring programs.[16]

Raman spectroscopy is a powerful analytical technique that provides a unique spectral fingerprint for any polarizable molecule.[4] Spectra can be collected thru glass, plastic, or transparent substances such as water that are generally less polarizable than analytes of interest. Raman spectroscopy has even been used to distinguish between molecules with similar structures, including structural differences as minute as chirality.[4,19] A drop coating deposition Raman (DCDR) method has recently demonstrated success in distinguishing between similarly structured biomolecules (i.e., human, bovine, and porcine insulin), identifying components in protein mixtures, producing Raman spectra of analytes in samples containing buffers and fluorescing components, and even quantifying MC-LR.[2,20-24] Neither DCDR nor other Raman methods have been applied for nodularin or microcystin variants. Results included herein establish that DCDR can be used to distinguish between microcystin variants based on the presence and absence of certain peaks, the ratios of specific peak heights, or principal component analysis (PCA).

EXPERIMENTAL

Chemicals. MC-LR, MC-RR, MC-LA, and nodularin were purchased from Enzo Life Sciences. MC-LF, MC-LY, MC-LW, and MC-YR were provided by Dr. Armah A. de la Cruz, U.S. EPA, Office of Research and Development, National Exposure Research Laboratory, Cincinnati, OH. L-phenylalanine (Phe), L-leucine (Leu), L-alanine (L-Ala), D-alanine (D-Ala), and L-glutamic acid (Glu) were purchased from Alpha Aesar; L-arginine (Arg) from Enzo Life Sciences; and L-tryptophan (Trp), L-tyrosine (Tyr), and N-methyl-D-aspartic acid (MeAsp) from Sigma Aldrich. Solid toxins were dissolved to 1 g/L in methanol and stored at -20 °C. Aqueous toxin standards were prepared by evaporating methanol from 10 µL of stock solution, diluting with 100 µL of nanopure water, and refrigerating at 4 °C until analysis.

Raman analyses. Raman spectra were obtained with a WITec Alpha500R Raman spectrometer (utilizing a 785 nm laser, 300 grooves/mm and 1200 grooves/mm gratings, a UHTS300 spectrometer, a DU 401 BR-DD CCD camera, 10 and 100× microscope objectives, and 20-50 mW of laser power). Nine distinct 2 µL DCDR spots of each of the eight aqueous toxin samples at 100 mg/L concentrations were dried on a quartz substrate for Raman analysis.[2]

Amino acid DCDR spectra were collected after drying 10 µL of a 100 mg/L solution on quartz. Aqueous phase Raman spectra of 1.5 g/L MC-LR and the amino acids at concentrations near their respective solubilities (150 g/L L-arginine, 29 g/L L-phenylalanine, 24 g/L L-leucine, 8.6 g/L L-glutamic acid, 160 g/L L-alanine, 160 g/L D-alanine, 7.7 g/L N-methyl-D-aspartic acid, 0.45 g/L L-tyrosine, and 11 g/L L-tryptophan) were collected from samples in aluminum foil pans that produced negligible Raman signal while holding ample volume for 300 second acquisitions despite some solvent evaporation. Spectra of the amino acid crystalline solids were obtained after placing a small amount of sample on a microscope slide and focusing on the sample with the confocal microscope. Both Raman gratings were used for the crystalline solids to determine what level of resolution was required to identify peaks within the cyanotoxin spectra. Details of all spectral acquisition parameters, background subtraction, and spectral normalizations are included in the supporting information.

Raman spectra of the amino acids were compared to cyanotoxin spectra and literature spectra to identify specific peaks that correspond to variant amino acids (leucine, arginine, alanine, etc.) in each cyanotoxin Raman spectrum. Following spectral processing, Raman intensities for key peaks in the toxin spectra were compiled, ratios of relevant peaks computed, and peak ratios plotted against one another. PCA was conducted using MATLAB 7.10 (R2010a) and the Statistics Toolbox 7.3 (R2010a).

RESULTS & DISCUSSION

DCDR. When an aqueous drop containing an analyte of interest dries on a glass substrate the residue remaining after solvent evaporation exhibits spatial variability. Many analytes (e.g., lysozyme, insulin, lactoferrin, albumin) deposit on the outer ridge of the drop as the sample dries – conveniently concentrated for Raman analysis.[20,24-26] A similar drying pattern was observed for the cyanotoxins (**Figure SI. 2.1**).[2] DCDR spectra were collected for deposits of MC-LR, MC-RR, MC-LA, MC-LF, MC-LY, MC-LW, MC-YR, and nodularin as well as the amino acids L-phenylalanine, D-alanine, L-leucine, L-glutamic acid, L-arginine, L-tryptophan, L-tyrosine, and N-methyl-D-aspartic acid (**Figure 2.2**).

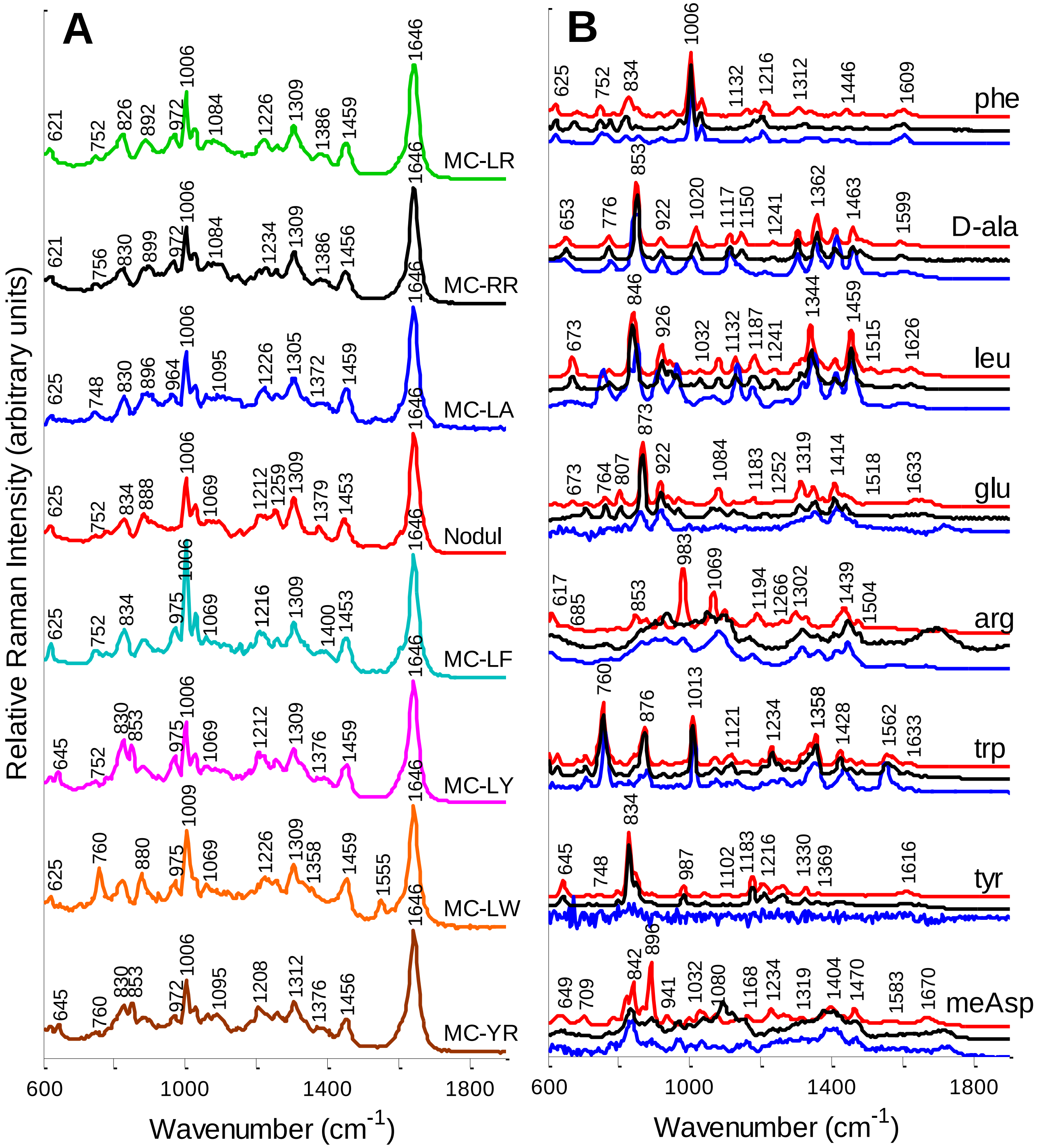

Figure 2.2. Raman spectra of the cyanotoxins and amino acids. A) Raman spectra of seven microcystin variants and nodularin. B) Amino acids collected in three sample states: solid amino acids (red, top spectrum in each set), DCDR samples (black, middle spectrum in each set), and aqueous samples with concentrations near the corresponding maximum solubility (blue, bottom spectrum in each set). The quartz background spectrum was subtracted from the sample spectra. All spectra are re-scaled and offset for ease of viewing.

Amino acid components of the cyanotoxins. Although Raman spectra for the amino acids have been reported in the literature, comparisons between crystalline, aqueous, and DCDR spectra for the amino acids relevant to cyanotoxin structure have not yet been compiled in a single source. Therefore, spectra for the amino acids were collected using the same Raman acquisition parameters as the cyanotoxins and the peaks compared to each other and the literature prior to assigning molecular vibrations to each cyanotoxin peak.

DCDR samples often remain hydrated over time, potentially due to the formation of a protective skin of dried material on the outer surface of the DCDR sample ridge that shelters the inner sample.[20,26] Therefore, DCDR spectra most frequently resemble aqueous phase spectra for molecules of interest (e.g., lysozyme, insulin, glucose), but they can also resemble the crystalline phase (e.g., fructose).[20,23] Significant differences were observed between the aqueous and crystalline phases for arginine and N-methyl-D-aspartic acid, though most of the amino acid Raman spectra displayed only minor differences between samples with varying physical states (**Figure 2.2B** and **Table SI. 2.1**; SI contains further discussion). This distinction is not definitive for amino acids with low water solubilities; at the maximum solubility of amino acids such as tyrosine, the Raman spectrum of the aqueous phase sample was too weak to distinguish many peaks from the baseline.[27] DCDR spectra of phenylalanine, alanine, leucine, glutamic acid, tryptophan, and tyrosine at 100 mg/L more closely resembled the crystalline phase, while that of arginine and N-methyl-D-aspartic acid resembled the aqueous phase. It is impossible to speculate whether the DCDR spectrum of MC-LR is more closely related to the solid or aqueous state; a sufficient Raman signal was not observed from an aqueous sample of MC-LR at 1.5 g/L (near maximum solubility).[28] Peak positions and strengths were recorded for all the amino acids in the three physical states and peak assignments based on those in the literature were made (**Table SI. 2.1**).

Common features of toxin spectra. The general cyanotoxin spectrum contains peaks describing the peptide bonds (very strong amide I at 1646 cm^{-1} and moderately strong amide III at 1200-1300 cm^{-1}), the phenyl ring in the Adda residue (620, 828, 1006, and 1031 cm^{-1}), and various CH, CH_2, CH_3, and C-C functional groups (752, 828, 880-900, 970, 1030, 1057, 1086, 1307, and 1453 cm^{-1}; **Table 2.1**).[27,29-31] Phenyl groups and other non-polar moieties generally have a tendency to produce strong Raman vibrations,[4,32] and this trend was observed for MC-LR, as shown by a comparison of the MC-LR spectrum with that of phenylalanine (**Figure 2.3**). A composite spectrum resembling that of MC-LR can be produced by adding the aqueous phase spectra of D-alanine, L-leucine, N-methyl-D-aspartic acid, L-arginine, L-phenylalanine, D-glutamic acid, and another D-alanine (each spectrum was normalized by dividing by the molarity of its amino acid sample). As expected, the most prevalent differences occur between 1200-1300 cm^{-1} and near 1646 cm^{-1}, regions that describe amide bond vibrations in proteins (**Figure 2.3**).[29] A number of the peaks in the composite spectrum of the amino acid components are red-shifted by approximately 25 cm^{-1} relative to the MC-LR peaks. Such shifts are not unexpected; changes in Raman frequency are often associated with stress or strain in a molecule as may occur when the amino acids are forced into the seven-membered ring formation.[4]

Table 2.1. Cyanotoxin Raman peak assignments.[a]

Peak (cm^{-1})[b]	**Toxin**	**Molecular vibration (from literature)[c]**
619-625	All	Phenyl ring C-H in-plane bending,[31,33] phenyl ring deformation,[32,34] phenyl ring C-C twisting,[31-32] Glu and MeAsp COO$^-$ wagging[31]
645	-LY, -YR	Tyr C-C twisting[29]
748-756	All[d]	Phenyl ring C-H out-of plane bending,[27,33] Glu COO$^-$ bending,[35] Glu CH$_2$ rocking,[32] Tyr CH$_2$ twisting[32]
760	-LW	Trp ring symmetric breathing,[27,31-32,36] Glu CH$_2$ rocking and COO$^-$ bending[32]
828	All	Adda C-C stretch[34] and CH$_2$ rocking,[31,33] MeAsp C-C stretch,[29] Tyr ring C-C symmetric stretch,[32] Tyr Fermi resonance doublet,[31,36] arg side chain C-N torsion,[27] Arg side chain C-C stretch,[32] Arg C-skeletal rocking vibration,[37] Trp CH$_2$ rocking[32]
853	-LY, -YR	Tyr CH$_2$ rocking,[32] Tyr symmetric ring stretch,[36] Tyr ring breathing,[27], Tyr Fermi resonance doublet[31,36]
880-900	All[d]	Arg CH$_2$ rock,[32] C–N stretch, and N–H stretch;[37] Glu COO$^-$ bend,[27] C-COO$^-$ stretch,[34] CH$_2$ rock,[32] and C-C stretch;[31-32,34] MeAsp C-C and C-COO$^-$ stretch;[34] Trp indole ring H-scissoring,[27] indole NH displacement,[31] and indole ring vibration with NH bending;[36] Tyr C-C vibrations[29]
964-975	All but Nod	Leu and Ala C-C stretch,[31,38] Leu and Ala CH$_3$ rocking,[32] Trp aromatic ring H-twisting[27]
1006*	All	Phenyl ring in-plane bending,[27] phenyl ring symmetric breathing,[33-34,39] phenyl ring C-C symmetric stretch,[31-32,36] Trp indole ring breathing,[27,31-32,36,39] Glu C-C and C-O stretching,[29] Leu C-C stretch[38]
1030	All	Phenyl in-plane CH bending,[27,31-34,36] MeAsp C-C and C-N stretch,[35] Arg C$_\gamma$-C$_\delta$,[27] Leu CH$_2$ twist,[32] Leu C-N stretch[38]
1057	-LW	Trp C-C stretching,[29] Arg CH$_2$ twisting,[32] Arg N–H and C–C vibrations,[37] MeAsp C-C and C-N stretch[35]
1086	All[d]	Arg C-N-H asymmetric bend,[27] Arg NH$_2$ vibrations,[37] Glu C-C and C-N stretching,[35] Leu C-N stretch,[38] MeAsp C-C and C-O stretching,[34] MeAsp CH$_2$ twisting[32]
1200-1300	All[d]	Amide III,[29] Adda C-H out-of plane bending, phenyl ring deformation,[27] phenyl ring breathing,[31] phenyl ring C-C stretching,[33] phenyl-C stretch,[34,36] Trp C-ring stretching,[29] Trp indole ring vibration,[32] Trp aromatic H-rocking,[27] Glu CH$_2$ twist and rock,[34] MeAsp CH$_2$ wagging,[29] MeAsp CH$_2$ twisting, rocking, and deformation,[34] Leu CH$_2$ torsion,[27,38] Arg C$_\delta$ twisting, C$_\gamma$ wagging, C$_\beta$ twist,[27] Arg NH$_3^+$ rocking,[32] Tyr ring-O stretching,[27,36] Tyr symmetric ring deformation[36]
1307	All	Ala H-C$_\alpha$-C$_{\text{terminal}}$ vibrations; Ala and Arg C$_\beta$-C$_\alpha$-H vibrations;[27] Ala and Glu CH$_2$ twisting, rocking, and deformation;[34] Glu CH$_2$ wagging;[31] Glu, Arg, and Leu C$_\alpha$-H bending;[32] Arg N–H rocking and C=O stretching;[37] Arg C$_\beta$ twist and C$_\gamma$ rock vibrations;[27] phenyl ring stretching;[27,34] Adda C-H bending;[32,34] Adda CH$_2$ wagging;[31] phenyl ring C-H in-plane bending[33-34]
1453	All	Glu CH$_2$ bending,[35] Leu CH$_2$ bending,[32] Leu CH$_2$ scissoring,[31] Leu CH$_3$ asymmetric bending,[38] Arg CH$_2$ bending,[32] Arg N-C-N asymmetric stretch, Arg C-N-H side chain vibrations,[27] Arg C–H vibrations[37,39]
1555	-LW	Trp indole ring stretching[27,36]
1646*	All	Amide I, water in aqueous peptide sample[29-31]

[a] An extended table is included in the Supporting Information (Table S-2). [b] Experimental intensity specified by **most intense peak***, **strong peaks**, **moderate peaks**, and weak peaks. Designations should be considered alongside spectra shown in **Figure 2.2**. [c] Three-letter amino acid codes: phenylalanine (Phe), alanine (Ala), leucine (Leu), glutamic acid (Glu), arginine (Arg), tryptophan (Trp), tyrosine (Tyr), and N-methyl-D-aspartic acid (MeAsp). [d] Peaks have differing shape and intensity, but they are consistently present.

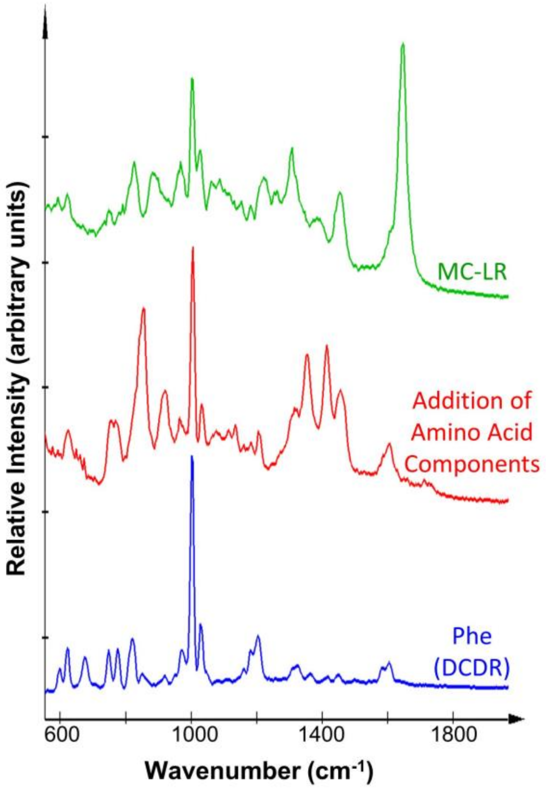

Figure 2.3. Microcystin-LR compared to phenylalanine and the addition of the aqueous phase amino acid component spectra, computed after normalizing each amino acid spectrum to a concentration of 1 M.

Variant identification via Raman spectral analysis. The 300 grooves/mm Raman grating produced sufficient spectral resolution to distinguish between four of the most similar toxins and all of the amino acids (**Figure SI. 2.2** and **SI. 3.3**); additional grooves per millimeter increase the spectral resolution at the cost of signal intensity and a slower measurement.[40] The most notable differences between cyanotoxin spectra include the disappearance of the 970 cm^{-1} peak in nodularin (C-C and CH_3 vibrations of D-alanine and leucine are not present in nodularin), the appearance of peaks at 645 cm^{-1} and 853 cm^{-1} in toxins containing tyrosine (tyrosine C-C twisting, CH_2 rocking, symmetric ring stretching, and ring breathing modes), the increase in intensity of the 1006 cm^{-1} symmetric ring breathing peak for toxins containing phenylalanine as a variant amino acid (MC-LF), the appearance of a peak at 760 cm^{-1} due to tryptophan ring breathing modes in species containing tryptophan (MC-LW), and the shifting of amide III peak positioning and intensity for all toxins (**Table 2.1** and **Figure 2.2**).

Plots of ratios of selected peak intensities are useful for sample identification in that they demonstrate mathematical differences between the toxin spectra shown in **Figure 2.2**.[41-42] For example a peak at 853 cm^{-1} is observed only in toxins containing tyrosine. If we compute the ratio of the intensity of the 853 cm^{-1} tyrosine peak divided by the intensity at a relatively constant peak amongst the toxins (i.e., 828 cm^{-1}), then only toxins containing tyrosine will have 853 cm^{-1} / 828 cm^{-1} ratios over 0.7. Such calculations can also be conducted to demonstrate the disappearance of the 970 cm^{-1} peak for nodularin, the increase in intensity of the 1006 cm^{-1} symmetric ring breathing peak when phenylalanine is a variant amino acid, and the increase in intensity of the 760 cm^{-1} tryptophan ring breathing peak for toxins with tryptophan as a variant amino acid (**Figure 2.4 a-c**). The toxins MC-LR, MC-RR, and MC-LA display the least molecular differences, and therefore these congeners are more difficult to distinguish from one another. However, peaks in the amide III region and C-C or CH_3 vibrations displayed at 970 cm^{-1} with respect to symmetric ring breathing modes at 1006 cm^{-1} allow clear differentiation of MC-LR, MC-RR, and MC-LA. The first three peak ratio plots shown in **Figure 2.4 a-c** demonstrate differentiation of the eight toxins examined, but numerous other peak ratio plots can also aid in the classification process (**Figure SI. 2.4**).

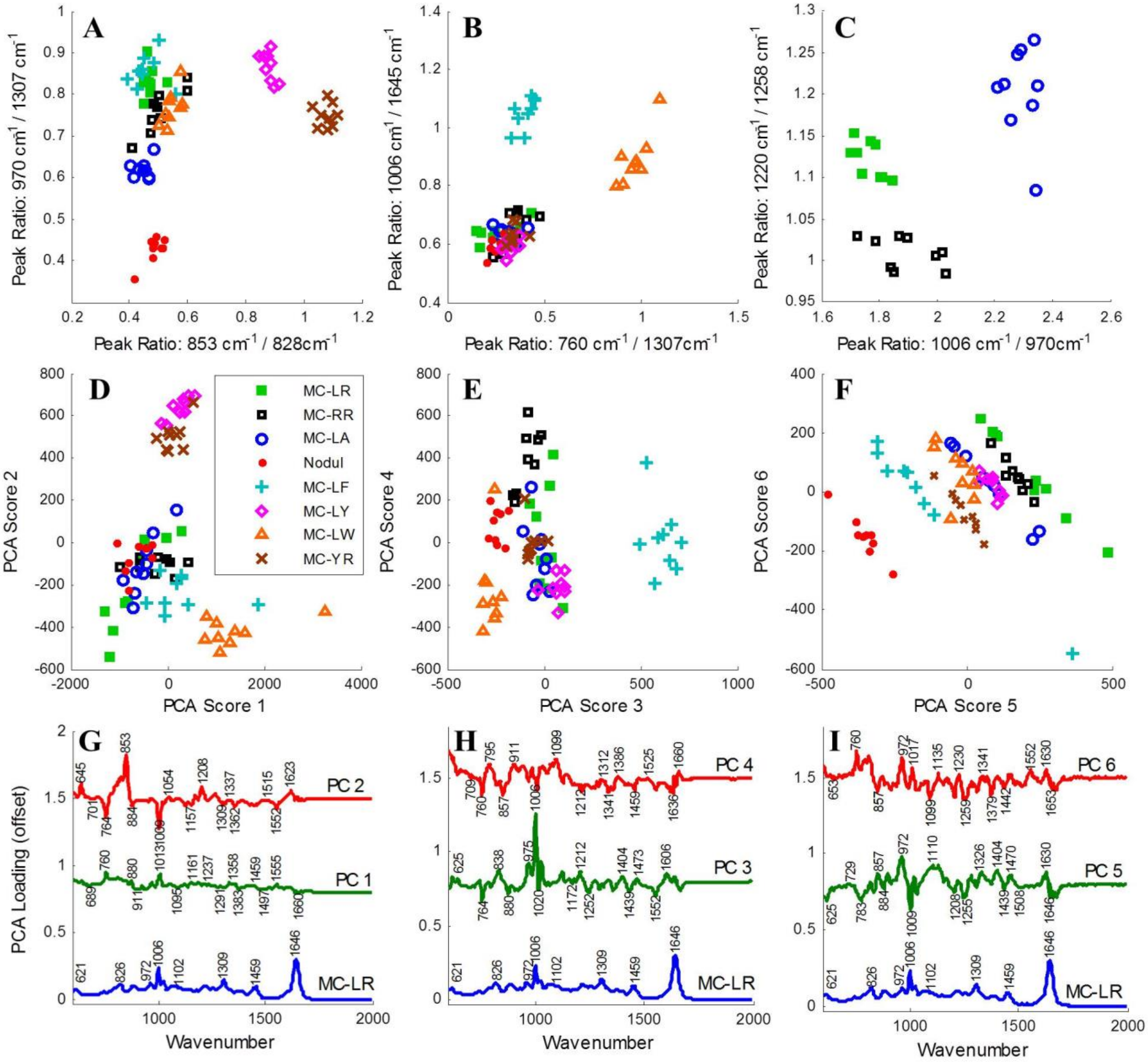

Figure 2.4. Identification of cyanotoxin variants using peak height ratios or PCA. Each point on plots A-F represents the results from a different Raman spectrum. Peak height ratio analyses require minimal computation while still allowing the eight toxins to be properly classified for all 72 DCDR samples (A-C). PCA score plots also differentiate between the different toxin identities, but the PCA model takes into account the whole spectrum (D-F). PC loadings spectra demonstrate the features within the Raman spectra of the eight cyanotoxins that are responsible for the most variation in the data set (G-I).

Principal component analyses. Twelve PCs were chosen for the final analysis after a 10-fold cross validation (**Figure SI. 2.5**, SI contains further discussion). A multilinear regression was developed by arbitrarily assigning a number to each toxin and developing a multilinear regression between toxin number and the first twelve PCs. This regression can be used to assign a toxin identity to an unknown sample using its DCDR spectrum. The regression of the PCA results properly classified all 72 DCDR spectra from the eight toxins (**Figure 2.5**). The PCA scores for each toxin also grouped the spectra in a similar manner as the peak ratio plots, with tryptophan, tyrosine, and phenylalanine containing toxins most easily separated from the rest by PCs 1-3. PC1 most heavily weighted peaks that correspond to the tryptophan variant amino acid, and MC-LW spectra were separated from the rest of the toxin spectra by the score for the first component (**Figure 2.4d** and **g)**. PC2 most heavily weighted the 853 cm^{-1} peak, corresponding to the tyrosine ring symmetric stretching and breathing vibrations observed only in tyrosine containing toxins (**Figure 2.4d** and **g**). PC3 most heavily weighted phenylalanine symmetric ring breathing modes at 1006 cm^{-1}, allowing MC-LF to be distinguished from the rest of the toxins (**Figure 2.4e** and **h**). Separation of the remaining toxin variants required consideration of multiple components at once, and for these classifications the PCA models are most valuable.

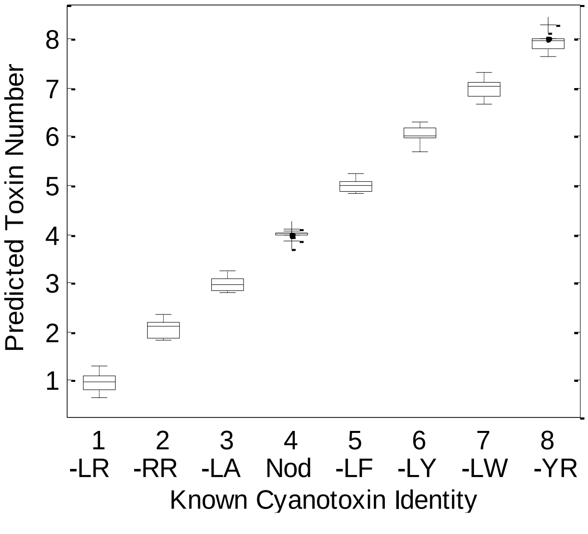

Figure 2.5. A multilinear regression was applied between arbitrarily assigned toxin numbers and the first twelve PCs for the 72 DCDR spectra. The principal component regression model with twelve PCs correctly classified all 72 DCDR samples of the eight toxins.

Rules for cyanotoxin variant identification. The eight cyanotoxins studied in this experiment can be distinguished from one another using PCA scores or by computing peak ratios and applying a set of classification rules (**Table 2.2**). Peak ratio computations may be preferred because the analysis is quite straightforward and could be applied by inexperienced technicians more rapidly than PCA.[41-42] Plots of peak ratios calculated for all nine spectra of each variant toxin allow visualization of the identification rules (**Figure 2.4 a-c**). The rules below are not the only set that would allow proper classification of the cyanotoxins, but simply one that were successful for this data set. For example, tryptophan presence is successfully documented using either the 760 cm^{-1} / 1307 cm^{-1} or the 1555 cm^{-1} /1307 cm^{-1} peak ratio. Additional rules will be necessary to characterize additional toxins, but these six provide a promising start since they succinctly differentiate a few of the most common forms of microcystin.

Table 2.2. Rules for toxin identification via Raman spectral analysis.

Rule	Description	Peak Ratio	Value	MCs Identified	Distinguished from	Fig
Rule 1	Only nodularin lacks a peak at 970 cm^{-1}.	970/1307	<0.5	Nod	-LR, -RR, -LA, -LF, -LY, -LW, -YR	4a
Rule 2a	Only tyrosine containing toxins have a peak at 853 cm^{-1}. The 853/828 ratio is affected by the local environment of the tyrosine side chain and it correlates to the protonation state of the residue.[30,43-46]	853/828	>0.8	-LY, -YR	-LR, -RR, -LA, -LF, -LW, nod	4a
Rule 2b		853/828	>1.0	-YR	-LY	4a
Rule 3	Only tryptophan containing toxins have a strong peak at 760 cm^{-1}.	760/1307	>0.7	-LW	-LR, -RR, -LA, -LF, -LY, -YR, nod	4b
Rule 4	Phenyl rings such as that in Adda and the phenylalanine variant amino acid cause a strong peak at 1006 cm^{-1}.	1006/1648	Double intensity	-LF	-LR, -RR, -LA, -LY, -YR, nod	4b
Rule 5a	The ratio of different C-C, CH_3, CH_2, CH, and C-N vibrations plotted against each other can identify subtle differences between toxins.	1006/970	>2.1	-LA	-LR and -RR	4c
Rule 5b		1100/1307	>0.71	-RR	-LR	S-4f
Rule 6	Amide III peak positioning and intensity is toxin specific.	1220/1258	<1.05	-RR	-LR and -LA	4c

FUTURE OUTLOOK

DCDR is capable of producing spectra that allow differentiation of cyanotoxin variants, quantifying MC-LR with 2-200 ng of sample residue, detecting 5 μg/L MC-LR after solid-phase extraction (SPE) and subsequent DCDR analysis, identifying MC-LR through a dissolved organic matter matrix, and determining protein concentrations from mixtures of lysozyme, lactoferrin, and albumin.[2,24] Further testing of cyanotoxin mixtures and samples containing impurities will be necessary before the DCDR method will provide precise and accurate qualitative and quantitative results for environmental samples. Evaluation of portable Raman spectrometers and handheld Raman instruments will also be valuable to determine the feasibility of field analysis of the cyanotoxins. Even without significant development the method could provide cheap, but valuable information regarding toxin identity on purified samples before or after ELISA analyses are conducted. Many cyanobacterial blooms are dominated by one or two toxins that greatly affect the overall toxicity of the bloom, most frequently MC-LR or MC-RR in the Midwestern United States.[47] Considering the drastic difference in toxicity between MC-LR and MC-RR as well as that of other variants, a rapid toxin identity test alongside ELISA or another quantitation method would be insightful. Application of DCDR for cyanotoxin identification has potential to be the cheap, reliable, rapid, and accurate method that is highly sought after for cyanotoxin monitoring programs to ensure public health.

ACKNOWLEDGEMENTS

This work was supported by an EPA STAR graduate research fellowship to R.A.H. (F08B20329) and research grants from the Water Research Foundation (#4212) and the Virginia Tech Institute for Critical Technology and Applied Science (ICTAS).

SUPPORTING INFORMATION

This SI contains Raman analysis parameters, optical images of DCDR drop drying patterns, discussion of the amino acid Raman peaks, extended peak assignment tables for both the amino acids and the cyanotoxins, description of the benefits and drawbacks of the Raman instrument grating chosen for the analysis, discussion of principal component analysis, and additional data to support conclusions made within the manuscript text.

Experimental.

Safety considerations. All toxin samples and labware were disinfected with >0.5% NaOCl for at least 30 minutes following use.[48] Extreme caution was taken to keep all toxin samples contained. Bleach solutions containing toxins were disposed of by Virginia Tech Environmental Health and Safety.

DCDR spectra of cyanotoxins. Two spectra were obtained for each DCDR sample spot: a single spectrum consisting of the average of ten, five second acquisitions collected from the toxin and a similar spectrum of the quartz background at the same focal depth as the toxin spectrum. All DCDR spectra were collected with the 785 nm laser and 100× microscope objective. The background quartz signals, thoroughly documented in a previous publication,[2] were subtracted from the sample spectra and the resulting 72 toxin spectra from the eight toxins were analyzed to identify differences amongst the spectra and to distinguish between toxin variants. Prior to data analysis the spectral baselines were corrected (the average intensity of the spectrum at 1775-2000 cm^{-1} was subtracted from the intensity at every point in the spectrum) and the intensities were normalized (the spectrum was multiplied by a factor to set the 1646 cm^{-1} peak height to an intensity of 1000 a.u.).

DCDR spectra of amino acids. The average of ten, five second acquisitions were collected with the 785 nm laser and 100× microscope objective for each amino acid residue dried from 10 μL of a 100 mg/L solution. Samples with weak DCDR signals at 100 mg/L (arginine and methyl aspartic acid) were further examined at higher concentrations to verify Raman spectra.

Aqueous phase Raman spectra of 1.5 g/L MC-LR. Five spectra of three hundred second acquisition were collected and averaged by the WITec Raman spectrometer (10× microscope objective, 300 grooves/mm grating, and 785 nm laser). Background spectra of nanopure water in the aluminum foil pan were subtracted from the sample spectra.

Aqueous phase Raman spectra of the amino acids. The average of one to five spectra of three hundred second acquisition (samples with low water solubilities displayed weak Raman signals that were only observed when many spectra were averaged) were acquired with the 785 nm laser, 10× microscope objective, 300 grooves/mm grating. Background spectra of nanopure water in the aluminum foil pan were subtracted from the sample spectra.

Crystalline phase Raman spectra of the amino acids. Spectra of the crystalline solids were obtained using the WITec Raman spectrometer, 785 nm laser, 100× microscope objective, and the average of five spectra of thirty second acquisitions with the 1200 grooves/mm grating or ten spectra of five second acquisitions with the 300 grooves/mm grating. Spectra were collected with both Raman gratings to determine what level of resolution was required to identify peaks within the cyanotoxin spectra.

Results & Discussion.

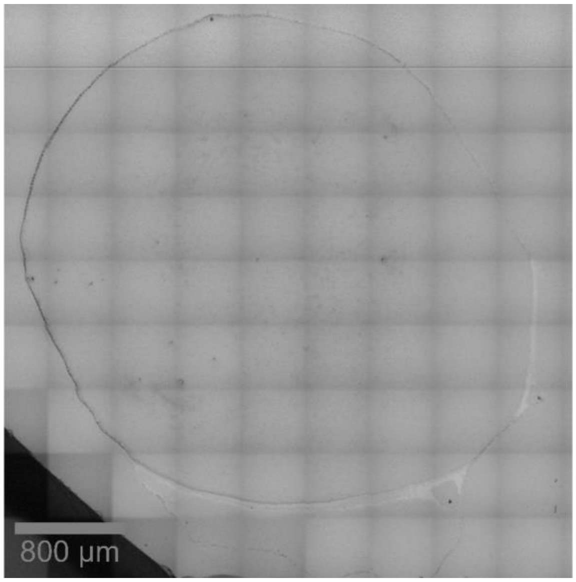

Figure SI. 2.1. An optical image of a typical microcystin DCDR drop on a quartz substrate.

Amino acid Raman spectra. A majority of the amino acids displayed very similar Raman spectra both in the solid form and when aqueous solutions were dried on quartz, but minor peak shifts and intensity variations were observed for phenylalanine (Phe) and glutamic acid (Glu) samples and major differences were observed for arginine (Arg) and N-methyl-D-aspartic acid (MeAsp; **Figure 2.2b, Table SI. 2.1**). Raman vibrations are sensitive to molecular packing, hydrogen bonding, and hydration state.[4,19-20] It is therefore not unexpected to observe differences between spectra of the same amino acid in different states. These changes were documented to create a comprehensive list of peaks that may be observed in the cyanotoxin spectra.

Studies have demonstrated that evaporation of water from a phenylalanine sample causes an increase in the intensity of aromatic ring vibrations, and the presence of water within "dried" samples can cause migration of low wavenumber peaks to positions up to 14 cm^{-1} away.[33] Although the increasing intensity trend and 14 cm^{-1} peak migrations were not observed consistently for all aromatic ring vibrations and low wavenumber peaks in the experimental phenylalanine spectra shown in **Figure 2.2**, the literature confirms changes in the spectra do occur as the sample state changes. The more hydrated phenylalanine samples (aqueous samples >

DCDR samples > crystalline samples) demonstrated more intense COO^-, C-N, ring C-H, and symmetric ring breathing vibrations (1410 and 778 cm^{-1}) and less intense C-C, CH, and CH_2 vibrations (825, 1184, 1311, and 1449 cm^{-1}). The more hydrated phenylalanine samples also displayed an upward shift in the position of the 471-485 cm^{-1} peak, but a downward shift in the 789-768 cm^{-1} symmetric ring breathing peak. A downward shift in the 1215-1208 cm^{-1} phenyl ring deformation, breathing, and stretching peak was also observed for the more hydrated phenylalanine samples. The more hydrated glutamic acid samples also displayed more intense COO^- vibrations at 708 and 1416 cm^{-1} as well as weaker COOH deformation, C-C stretching, and CH_2 rocking at 869 cm^{-1}, both similar to the trend in the phenylalanine samples. The trend for glutamic acid C-C, CCN, and C-COO^- stretching (944 and 970 cm^{-1}) was more intense for the more hydrated samples, opposite of what was observed for phenylalanine.

Both arginine and N-methyl-D-aspartic acid display broader features for the dried samples, with peaks in the 700-1500 cm^{-1} region that overlap. Arginine peaks corresponding to C-C skeletal, CH, CH_2, CH_3, COO^-, CN, C=N, NH_2, and NH vibrations displayed the greatest differences between the two sample states (**Figure 2.2b, Table SI. 2.1)**. Often amino acid solutions arrange into dimers in which NH_2 and NH_3^+ groups or COO^- and COOH groups hydrogen bond with one another, especially for solutions with elevated concentrations (such as the elevated concentrations that occur in the later stages of sample evaporation).[33,49] This behavior is displayed in the Raman spectrum by a C=O band that appears near 1700 cm^{-1}, a broad signal produced by out of plane OH-O vibrations in the 875-960 cm^{-1} region, and C-O stretching bands from carboxylic acids at 1220-1320 cm^{-1}.[29,33] These traits are visible in the DCDR arginine and N-methyl-D-aspartic acid Raman spectra, suggesting that dimers form before the sample dries on the quartz substrate.

Table SI. 2.1. Amino acid Raman peak assignments for solid (300 and 1200 grooves/mm), DCDR, and aqueous samples of L-phenylalanine (Phe), D-alanine (Ala), L-leucine (Leu), L-glutamic acid (Glu), L-arginine (Arg), L-tryptophan (Trp), L-tyrosine (Tyr), and N-methyl-D-aspartic acid (MeAsp). Experimental intensity specified by: **most intense peak*,** **strong peaks,** **moderate peaks,** and weak peaks.

Phenylalanine Raman peaks (cm^{-1})

Solid 300 gr	Solid 1200 gr	DCDR	Aqueous	Molecular vibration from literature
532	525	524	528	COO$^-$ in-plane bending, ring in-plane bending,[27] ring C-H in-plane bending[33]
601	604	601	577	COO$^-$ in-plane bending,[27] ring C-H in-plane bending[33]
625	**620**	**625**	**629**	Ring C-H in-plane bending,[31,33] ring deformation,[32,34] ring C-C twisting,[31-32] COO$^-$ wagging[31]
685	682	**681**		COO$^-$ symmetric in-plane bending[33]
752	**747**	**752**	**756**	COO$^-$ bending,[32] ring C-H out-of plane bending[27,33]
791	785	**780**	**772**	Ring C-H out-of-plane bending,[33] symmetric ring breathing[36]
834	**833**	**822**	826	C-C skeletal stretch,[34] CH$_2$ rocking[31,33]
	853	853		C-C skeletal stretch, C-CH$_2$ stretching,[34] ring C-H out-of-plane bending[33]
861			**861**	C–CO$^-$ stretching[33]
918	913			C-C stretch,[27,34] C-COO$^-$ stretching,[31,34] CH$_2$ rocking[33]
		922	930	Ring C-H out-of-plane bending[33]
956	950	953		C-C stretching,[27], ring C-H out-of-plane bending[33]
		975	975	Ring C-H out-of-plane bending[33]
1006*	**1004***	**1006***	**1009***	In-plane bending of ring,[27] symmetric ring breathing,[33-34,39] symmetric ring C-C stretch[31-32,36]
1039	**1032**	**1032**	**1035**	In-plane CH bending[27,31-34,36]
			1073	C-N stretch, amino terminal group, NH$_3$ twist,[34] ring C-H in-plane bending[33]
	1154			CH$_2$ rocking,[32] ring C-H in-plane bending[33]
1165	1163	1165	1165	Ring C-H in-plane bending[27,33]
1187	1184	1182		C-O stretching,[27] CH$_2$ twisting and rocking, NH$_3$ rocking, CH-NH$_2$ vibrations,[34] C-H in-plane bending[27,36]
	1188		1190	In plane ring C-H bending[33]
1216		**1208**	**1212**	C-H out-of plane bending, ring deformation,[27] NH$_3^+$ rocking,[32] ring breathing,[31] ring C-C stretching,[33] phenyl-C stretch[34,36]
	1291		1273	Ring C-H in-plane bending[33]
	1306			Ring stretching,[27,34] C-H bending,[32,34] CH$_2$ wagging,[31] ring C-H in-plane bending[33-34]
1312	1319			Ring C-C stretching[33]
	1334	1326		CH$_2$ symmetric out-of-plane bending[33]
1344	1340		1341	Ring stretching,[34] CH$_2$ symmetric out-of-plane bending[33]
		1369	1362	CH$_2$ symmetric out-of-plane bending[33]
1414	1410	1421	1411	C-H deformation,[27,34] C-N stretch,[34] COO$^-$ symmetric stretch[31-34]
	1436			CH$_2$ scissoring[31]
1446	1445	1453	1449	CH deformation,[34] symmetric in-plane CH$_2$ bending,[32-33] ring C-C stretching[33]
1497	1493			Ring C-C stretching[33]

		1504	1508	NH_3^+ symmetric in-plane bending[33]
1593	1585	1584	1586	Ring C-C stretch,[31,33-34,36] asymmetric COO^- stretching[33]
	1602			COO^- asymmetric stretch,[32] ring C-C stretch[31,33,36]
1609	1610	1609	**1609**	C=O stretch,[27] ring C-C stretch[32-34]

Alanine Raman peaks (cm^{-1})

D-Ala Solid 300 gr	**L-Ala Solid 1200 gr**	**D-Ala Solid 1200 gr**	**D-Ala DCDR**	**D-Ala Aqueous**	**Molecular vibration from literature**
540	530	531	536	536	Deformation of O=C-O and C-C-O [34]
	553				
653	652	652	657	653	COO^- wagging[34]
776	771	771	**776**	783	W…O-$C_{terminal}$, W5…W1, N-C_α-$C_{terminal}$,[27] CO_2^- bend[32]
853*	**850***	**850***	**857***	**861***	N-C, CO_2^-, C_α-$C_{terminal}$-O symmetric bending,[27] C-CH_3 stretching,[34] C-C stretch[27,31-32,34]
922	919	921	926	926	W…O-$C_{terminal}$, W-W,[27] C-C stretch,[27,32,34] C_α-N stretch,[27,32] C-COO^- stretch[31,34]
	1011	1011			C-C stretch, C-N stretch, C-NH_2 stretch[34]
1020	**1020**	**1019**	**1020**	**1009**	CH_3 rocking[32]
	1111	1112			C_α-N stretch,[32,34] C-C stretch, NH_3^+ rocking[32]
1117	1117		1117	**1121**	C_α-C_β, N-C, and C_β-C_α-$C_{terminal}$ vibrations[27]
1150	1146	1146	1150		Asymmetric CH_3 rocking,[32] C-C stretch, NH_2 twist, NH_3^+ wag,[34] NH_3^+ deformation[31]
				1216	
1241	1238	1238			NH_3^+ rocking[32]
1309	**1304**	**1304**	**1309**	**1309**	H-C_α-$C_{terminal}$, COO^- symmetric stretch, C_β-C_α-H,[27] CH_2 twisting, rocking, and deformation[34]
	1310				CH_3 twisting, bending, wagging[29]
1362	**1357**	**1357**	**1362**	**1358**	CH deformation,[34] symmetric COO^- stretching,[27,34] symmetric CH_3 bending[31-32]
	1370	1377			C_β symmetric rocking and bending[27]
1414	**1406**	**1406**	1414	**1418**	C_β asymmetric rocking,[27] COO^- symmetric stretch,[31-32,34] C_α-H deformation, C-N stretch[34]
1463	**1461**	**1461**	**1463**	**1466**	C_β asymmetric rocking,[27] CH and CH_3 deformation,[34,39] asymmetric CH_3 bending[31-32]
	1480	1482	1484		NH_3^+ vibrations[29]
1501	1498	1498			Symmetric NH_3^+ bending[32]
	1506				
1599	1596	1595	1596	1603	Asymmetric COO^- stretch,[27,32,34] NH_2 scissoring,[34] W(H-O-H)[27]

Leucine Raman peaks (cm^{-1})

Solid 300 gr	Solid 1200 gr	DCDR	Aqueous	Molecular vibration from literature
540	**533**	540	544	COO^- rocking[38]
673	**668**	673	673	COO^- wagging[38]
780	774	780	760	COO^- bending[27,32,38]
	835*		**834**	COO^- out-of-plane vibration[27,38]
846*	**846***	**842***	**857***	CH_2 rocking,[27,38] C-C stretch,[31-32] CH_3 rocking[32]
926	**924**	**926**	915	C-COO^- stretch,[31] C-C stretch[38]
953	946	**953**		C-C stretch[31] [38]
965	963	964	**968**	CH_3 rocking,[32] C-C stretch[31,38]
1009	1003	1006	1002	C-C stretch[38]
1032	1030	1032	1020-1087	CH_2 twist,[32] C-N stretch[38]
1084	1082	1084	1073	NH_3^+ rocking,[27] C-N stretch[38]
1132	1129	1132	**1139**	NH_3^+ rocking,[32,38] NH_3^+ deformation[31]
	1174			NH_3^+ rocking[27,38]
1187	1186	1183	1183	NH_3^+ rocking[27,38]
1241	1238	1241	1255	CH_2 torsion,[27,38] NH_3^+ rocking[32]
1302	1295	1298	1277	CH_2 twisting and bending, CH bending[29]
	1313			C_α-H bending[32]
1319		**1319**	1323	CH_2 wagging[32]
1344	**1339**	**1348**	**1355**	C-H bending,[32,38] CH_3 symmetric deformation[31]
	1360			CH_3 symmetric stretch[29]
1369	1370			CH_3 symmetric bending[32]
	1384			CH_3 symmetric bending[38]
1414	1407	1411	1418	COO^- symmetric stretch,[31-32] CH_3 symmetric bending[38]
1459	**1454***	**1459**	**1456**	CH_2 bending,[32] CH_2 scissoring,[31] CH_3 asymmetric bending[38]
	1470			CH_3 asymmetric bending[32,38]
1515	1513	1515		NH_3^+ symmetric bending[32]
	1555			COO^- stretch[38]
1583	1581	1583	1603	COO^- asymmetric stretch[32,38]
1626	1622	1630		NH_3^+ asymmetric bending,[32] COO^- stretch[38]

Glutamic Acid Raman peaks (cm^{-1})

Solid 300 gr	Solid 1200 gr	DCDR	Aqueous	Molecular vibration from literature
544	**537**	544		COOH bending[35]
		581		COO$^-$ bending[35]
625	621			COO$^-$ wagging[31]
673	667	681		COO$^-$ bending[35]
713	708	**713**		COO- deformation[31]
	748			COO$^-$ bending[35]
764	761	**768**		CH_2 rocking, skeletal COO$^-$ bending[32]
807	**802**	**811**		CC skeletal stretch, C-CH_3 stretching[34]
873*	**871***	**873***	**861**	COOH deformation,[27] C-COO$^-$ stretching,[34] CH_2 rocking,[32] C-C stretch[31-32,34]
922	**916**	**922**	**922**	C-C-N stretching,[27] C-COOH stretching,[34] C-C stretch[31,34]
942	942	**941**		CCN stretch, COO$^-$ stretch,[34] C-COO$^-$ stretch[31]
975	969	**972**		C-C stretch[31]
	986			C-C stretch[29]
	1006			C-C and C-O stretching[29]
	1040			C-C stretch,[50] C-NH_2 stretch, C-N stretching[34]
	1065	1065		
1084	**1079**	**1091**		C-C and C-N stretching[35]
1132	1126	1132		NH_3^+ rocking,[32,35] NH_3^+ deformation[31]
	1147			
	1163	1154		NH_3^+ rocking[35]
1183	1179			C-CN asymmetric stretching[34]
	1213	1212		CH_2 twist and rock[34]
1319	**1316**	**1312**		CH_2 twisting, rocking, and bending;[34] C_α-H bending;[32] CH_2 wagging[31]
1355	**1349**	**1358**	**1362**	CH_3 deformation, COOH stretch, C-NH_3 stretch,[34] CH_2 scissoring[31]
	1374			CO stretching and OH bending[35]
1414	**1406**	**1411**	**1418***	COO$^-$ symmetric stretching[27,31-32,39]
1442	1436	1442		CH_2 bending,[32] CH_2 scissoring[31]
	1450			CH_2 bending[35]
	1458			CH_2 bending[35]
1633	1632			Asymmetric skeletal NH_3^+ bending,[32,34] asymmetric COO- stretching[35]
	1658	1666		Side chain C=O stretching[32]
1676	1677			
			1723	COO$^-$ stretch[29,35]

Arginine Raman peaks (cm^{-1})

Solid 300 gr	Solid 1200 gr	DCDR	Aqueous	Molecular vibration from literature
552	**550**	544	532	
581	576			COO^- rocking, NH_2 torsion[51]
617	**612**	**617**	613	COO^- in-plane bending[51]
		768		COO^- bending[51]
			783	NH_2 bending[51]
	848			C-C stretch, CH_2 rocking[32]
853		820-1140		Side chain C-N torsion,[27] side chain C-C stretch,[32] C-skeleton rocking vibration[37]
880	881		**873**	CH_2 rocking,[32] C–N and N–H stretching[37]
		907	**911**	Dimer out-of-plane OH-O vibrations,[29,33] C-C stretch[51]
922	922	**938**	**938**	Side chain N-C-N symmetric stretch,[27] side chain C-C stretch[27,32]
983*	**982***		**987**	C_α-C_β, $N_{terminal}$-C_α vibrations,[27] N–H stretching[37]
1035	1036			C_γ-C_δ vibrations[27]
1069	**1066**	**1054***		CH_2 twisting,[32] N–H and C–C vibrations[37]
1102	**1100**	**1095**	**1087***	C-N-H asymmetric bend,[27] COO^- and NH_2 vibrations[37]
1132	1122			Skeletal NH_3^+ rocking[32]
1194	1190	1176	1179	C-N-H asymmetric bend, side chain C-N vibrations[27]
	1197			C–N rocking[37]
1266	1262			C_δ twisting, C_γ wagging, C_β twist,[27] skeletal NH_3^+ rocking[32]
	1296			
1302	1306	**1323**	**1323**	Dimer C-O stretching,[29,33] C_α-H bending,[32] N–H rocking and C=O stretching,[37] C_β twist, COO^- symmetric stretch, C_γ rock, C_β-C_α-H_α[27]
1330	1330			CH_2 wagging[32]
	1350			CH_2 deformation,[51] CH_2 torsion[51]
	1375	1362	1365	
	1421	1411	1418	C_β rocking, C_γ wag, COO^- symmetric stretch, $N_{terminal}$-C_α-H_α,[27] asymmetric CH_2 vibrations[37]
1439	**1434**	**1449**	**1449**	N-C-N asymmetric stretch, C-N-H side chain vibrations[27] C–H vibrations[37,39]
	1449			CH_2 bending[32]
1477	1475	1478		C_δ and C_γ bending,[27] skeletal NH_3^+ symmetric bending,[32] C–H and N–H rocking[37]
	1547		1596	C–H and C–N stretching[37]
	1616			Skeletal NH_3^+ asymmetric bending,[32] NH_2 vibrations[29]
		1693	1676	Dimer C=O vibrations,[29,33] asymmetric C=N stretching,[37,51] asymmetric COO^- stretching,[51] asymmetric NH_3^+ bending[51]
	1713			

Tryptophan Raman peaks (cm^{-1})

Solid 300 gr	Solid 1200 gr	DCDR	Aqueous	Molecular vibration from literature
516	526			
536	533	532	548	
	546			
577	573	577	585	
	580			
601	**595**	**601**		
629	625	633	617	$\mathrm{COO^-}$ wagging[31]
	658			C-C twisting[29]
689	684	689		
713	705	709	713	$\mathrm{COO^-}$ deformation[31]
	740			
	744			$\mathrm{COO^-}$ bending,[32] symmetric ring breathing[29]
760*	**754***	**760***	**764***	Indole ring symmetric breathing[27,31-32,36]
	764			Ring breathing[29]
	777			Ring breathing[29]
807	803	807	811	Ring breathing, C-C stretching[29]
	839		834	$\mathrm{CH_2}$ rocking[32]
848	848	846		Pyrrole ring H-bending[27]
	865		862	Indole ring vibration[32]
876	**874**	**876**	**884**	Indole ring H-scissoring,[27] indole NH displacement,[31] indole ring vibration with NH bending[36]
930	928	930		C-$\mathrm{COO^-}$ stretching[31]
968	962	964	968	Aromatic ring H-twisting[27]
	988		979	C-C stretching[29]
1013	**1008**	**1013**	**1017**	Indole ring breathing[27,31-32,36,39]
	1067			C-C stretching[29]
1076	1076	1076	1080	Pyrrole H-scissoring,[27] C-C stretching[29]
	1103			C-C and C-N stretching[29]
1121	1118	1121	1113	Benzene H-scissoring,[27] indole ring vibration[32]
	1131		1139	$\mathrm{NH_3^+}$ rocking[32]
	1149			$\mathrm{CH_2}$ rocking[32]
1165	1160	1161		C-C and C-N stretching[29]
1212	1205	1213	1208	C-ring stretching[29]
1234	**1231**	**1237**	1237	$\mathrm{NH_3^+}$ rocking,[32] ring vibrations[31]
	1246			Indole ring vibration[32]
1253	1255	1252	1266	Aromatic H-rocking[27]
1284	1277	1284		$\mathrm{CH_2}$ wagging[29]
1314	1313	1319	1305	C-N asymmetric stretching, $\mathrm{CH_2}$ twisting, wagging, or bending, C-H deformation[29]

	1326			CH_2 twisting, wagging, deformation[29]
1341	**1337**	1344		C-H bending,[27,31] indole ring vibration[32]
1358	**1358**	**1358**	**1355**	Indole ring vibration[31-32,36,39]
1428	1422	**1428**	**1442**	Indole ring stretching,[27,39] COO^- symmetric stretch[32]
	1449			CH_2 bending[32]
1456	1457	1453	1457	CH_2 scissor,[27,31] indole ring vibration[32]
1491	1485	1494		Indole ring stretching,[27,32] NH_3^+ symmetric bending[32]
1562	1557	1559	**1559**	Indole ring stretching,[27,36] COO^- asymmetric stretch[32]
1576	1576	1579	1579	Indole ring vibration[32,36]
1623	1616	1620	1623	NH_3^+ asymmetric bending, indole ring vibrations[31-32,36]

Tyrosine Raman peaks (cm^{-1})

Solid 300 gr	**Solid 1200 gr**	**DCDR**	**Aqueous**	**Molecular vibration from literature**
532	526	532		
577	573	577		OH out of plane bending[29]
645	**640**	**645**		C-C twisting[29]
	646			C-C twisting[29]
721	713	721		COO^- deformation[31]
748	741	744		CH_2 twisting, COO^- bending[32]
803	797	803		Ring breathing mode[29]
834*	**829**	**834**	**834**	Ring C-C symmetric stretch,[32] Fermi resonance doublet: out-of-plane ring bending overtone[31,36]
846	**845**			Ring breathing,[27], Fermi resonance doublet: ring breathing[31,36]
		849		CH_2 rocking,[32] symmetric ring stretch[36]
	879			C-C stretching, ring bending, CH_2 rocking[29]
899	897	888		C-C vibrations[29]
987	**983**	987		C-C stretching[29]
1043	1042	1043		C-O, C-N, and C-C stretching
1183	**1178**	**1183**		Ring C-H in-plane bending,[31,36] phenyl-C stretch[36]
	1199			Ring symmetric stretching,[27] phenyl-C stretch[31]
1216	**1212**	**1216**		
1250	1246	1251		NH_3^+ rocking[32]
1266	1263	**1266**		Ring-O stretching vibration,[27] C-O stretching, symmetric ring deformation[36]
	1282			CH_2 wagging[29]
1330	1326	1330		C_α-H bending[31-32]
1369	1364	1369		
1432	1433	1428		CH_2 bending[32]
1616	1614	1616		NH_3^+ asymmetric bending[32]
		1650		

N-Methyl-D-aspartic acid Raman peaks (cm^{-1})

Solid 300 gr	**Solid 1200 gr**	**DCDR**	**Aqueous**	**Molecular vibration from literature**
569	**563**	577		COO$^-$ bending[35]
625	625	625		COO$^-$ wagging[31]
649	643	649		C-C twisting[29]
709	704			COO$^-$ deformation[31]
791	784	780	783	COO$^-$ out-of-plane vibration,[27] CH_2 and CH_3 rocking, C-C stretching,[34] skeletal COO$^-$ bending[32]
826	**822**		834	C-C stretch[29]
842	**841***	**838**	**846***	CH_2 rocking[35]
870	865	873		C-C stretch,[27,31-32,34] C-COO stretch,[34] CH_2 rocking[32]
896*	**891**	**896**	896	C-C stretch, C-COOH stretch[34]
		907		C-N and C-C stretching[35]
941	936			C-C-N stretch,[34] COO$^-$ stretch,[27,34] C-C stretch,[32,34] C-COO$^-$ stretch[31]
		975	**968**	Dimer out-of-plane OH-O vibrations,[29,33] C-C stretch[31]
1002	1000	1002	1009	
1032	1028	**1043**	**1035**	C-C and C-N stretch[35]
	1043			
	1064	1059		C-C and C-N stretch[35]
1080	1075	1074		C-C and C-O stretching,[34] CH_2 twisting[32]
		1099*		NH_3^+ wagging[27]
1139	1133	**1124**		NH_3^+ wagging,[27,34] NH_3^+ deformation,[31] NH_3^+ rocking,[32,35] C-C stretching, NH_2 twist[34]
	1159			C-C and C-N stretching[29]
1168	**1167**	**1167**	**1165**	NH_3^+ rocking[35]
1234	1227	1227		CH_2 wagging[29]
		1241		CH_2 twisting, rocking, and deformation[34]
1269	1278			CH_2 wagging[32]
1319	1312	1319		CH bending,[27,34] COO$^-$ stretching,[34]
	1360			CH_2 scissoring,[31] CH bending[35]
	1394	**1379**	**1390**	CO stretching, OH bending[35]
1404	**1401**	**1411**	**1411**	COO$^-$ symmetric stretching,[31-32,34] C_α-H deformation, C-N stretch[34]
1432	1432	1418		symmetric COO$^-$ stretching[27,35]
1470	**1463**	1463	**1473**	CH_2 bending[32]
1670	1666			NH_2 shear vibration,[27] C=O stretching[32]
		1719	1729	Dimer C=O vibrations,[29,33] COO$^-$ stretching[29,35]

Table SI. 2.2. Detailed peak identifications for microcystins and nodularin.

Peak (cm^{-1})[a]	Toxin	Amino Acid[b]	Molecular vibration (from literature)
619-625	All	R, E, MeD, F, W	Phenyl ring C-H in-plane bending,[31,33] phenyl ring deformation,[32,34] phenyl ring C-C twisting,[31-32] Glu and MeAsp COO$^-$ wagging[31]
645	-LY, -YR	MeD, Y	Tyr C-C twisting[29]
748-756	All[c]	E, F, Y	Phenyl ring C-H out-of plane bending,[27,33] Glu COO$^-$ bending,[35] Glu CH$_2$ rocking,[32] Tyr CH$_2$ twisting[32]
760	-LW	W, E	Trp indole ring symmetric breathing,[27,31-32,36] Glu CH$_2$ rocking and COO$^-$ bending[32]
783	All[c]	A, R, L, MeD, F	Phenyl ring C-H out-of-plane bending,[33] phenyl symmetric ring breathing,[36] Ala N-C$_\alpha$-C$_{\text{terminal}}$,[27] Arg NH$_2$ bending,[51] MeAsp COO$^-$ out-of-plane vibration,[27] MeAsp CH$_2$ and CH$_3$ rocking, MeAsp C-C stretching[34]
828	All	R, L, MeD, F, W, Y	Adda C-C skeletal stretch,[34] adda CH$_2$ rocking,[31,33] Tyr ring C-C symmetric stretch,[32] Fermi resonance doublet between ring breathing and out-of-plane ring bending overtone,[31,36] Arg side chain C-N torsion,[27] Arg side chain C-C stretch,[32] Arg C-skeleton rocking vibration,[37] MeAsp C-C stretch,[29] Trp CH$_2$ rocking[32]
853	-LY, -YR	Y, R, A, L, MeD, F	Tyr CH$_2$ rocking,[32] Tyr symmetric ring stretch,[36] Tyr ring breathing,[27] Tyr Fermi resonance doublet between ring breathing and out-of-plane ring bending overtone[31,36]
880-900	All[c]	R, E, MeD, W, Y	Arg CH$_2$ rocking,[32] Arg C–N and N–H stretching,[37] Glu COO$^-$ deformation,[27] Glu C-COO$^-$ stretching,[34] Glu CH$_2$ rocking,[32] Glu C-C stretch,[31-32,34] MeAsp C-C stretch, MeAsp C-COO$^-$ stretch,[34] Trp indole ring H-scissoring,[27] Trp indole NH displacement,[31] Trp indole ring vibration with NH bending,[36] Tyr C-C vibrations[29]
930-939	All	R, E, L, MeD, F, W	Arg side chain N-C-N symmetric stretch,[27] Arg side chain C-C stretch,[27,32] Glu and MeAsp C-C-N and COO$^-$ stretch,[34] Glu and MeAsp C-COO$^-$ stretch,[31] MeAsp C-C stretch,[32,34] Leu C-C stretch,[38] phenyl ring C-H out-of-plane bending,[33] Trp C-CO stretching[31]
964-975	All but Nod	E, L, MeD, W	Leu and Ala C-C stretch,[31,38] Leu and Ala CH$_3$ rocking,[32] Trp aromatic ring H-twisting[27]
1006*	All	E, L, F, W	Phenyl ring in-plane bending,[27] phenyl ring symmetric breathing,[33-34,39] phenyl ring C-C symmetric stretch,[31-32,36] Trp indole ring breathing,[27,31-32,36,39] Glu C-C and C-O stretching,[29] Leu C-C stretch[38]
1030	All	R, L, MeD, F	Phenyl in-plane CH bending,[27,31-34,36] MeAsp C-C and C-N stretch,[35] Arg C$_\gamma$-C$_\delta$,[27] Leu CH$_2$ twist,[32] Leu C-N stretch[38]
1057	-LW	R, MeD, W	Trp C-C stretching,[29] Arg CH$_2$ twisting,[32] Arg N–H and C–C vibrations,[37] MeAsp C-C and C-N stretch[35]
1069	All[c]	R, F, W	Arg CH$_2$ twisting,[32] Arg N–H and C–C vibrations,[37] phenyl ring C-H in-plane bending,[33] Trp C-C stretching[29]
1086	All[c]	R, E, L, MeD	Arg C-N-H asymmetric bend,[27] Arg NH$_2$ vibrations,[37] Glu C-C and C-N stretching,[35] Leu C-N stretch,[38] MeAsp C-C and C-O stretching,[34] MeAsp CH$_2$ twisting[32]
1098	All[c]	R, MeD	Arg C-N-H asymmetric bend,[27] Arg NH$_2$ vibrations,[37] MeAsp NH$_3^+$ wagging[27]
1100	All[c]	R	Arg C-N-H asymmetric bend,[27] Arg NH$_2$ vibrations[37]
1103	All[c]	W	Trp C-C and C-N stretching[29]
1111	All[c]	A	Ala C$_\alpha$-N stretch,[32,34] Ala C-C stretch,[32]
1117	All[c]	A, W	Ala C$_\alpha$-C$_\beta$, N-C, and C$_\beta$-C$_\alpha$-C$_{\text{terminal}}$ vibrations,[27] Trp indole ring vibrations[27,32]
1131	All[c]	R, E, L, MeD, W	MeAsp C-C stretching,[34] Arg NH$_3^+$ rocking[32]

Peak (cm^{-1})[a]	**Toxin**	**Amino Acid[b]**	**Molecular vibration (from literature)**
1153	All[c]	A, F	Ala asymmetric CH_3 rocking,[32] Ala C-C stretch,[34] Adda CH_2 rocking,[32] phenyl ring C-H in-plane bending[33]
1156	All[c]	MeD	MeAsp C-C and C-N stretching[29]
1167	-LW	E, MeD, F, W	Trp C-C and C-N stretching,[29] phenyl ring C-H in-plane bending[27,33]
1174	-LW	L	
1177	-LY, -YR	R, E, Y	Tyr ring C-H in-plane bending,[31,36] Tyr phenyl-C stretch,[36] Arg C-N-H asymmetric bend, Arg side chain C-N vibrations,[27] Glu C-CN asymmetric stretching[34]
1200-1300	All[c]		Amide III[29]
1210	All[c]	F, W	Adda C-H out-of plane bending, phenyl ring deformation,[27] phenyl ring breathing,[31] phenyl ring C-C stretching,[33] phenyl-C stretch,[34,36] Trp C-ring stretching[29]
1212	All[c]	E	Glu CH_2 twist and rock[34]
1220	All[c]	MeD	MeAsp CH_2 wagging[29]
1240	All[c]	A, L, MeD, W	Leu CH_2 torsion,[27,38] MeAsp CH_2 twisting, rocking, and deformation,[34] Trp indole ring vibration[32]
1256	All[c]	W	Trp aromatic H-rocking[27]
1258	All[c]	R, Y	Arg C_δ twisting, C_γ wagging, C_β twist,[27] Arg NH_3^+ rocking,[32] Tyr ring-O stretching,[27,36] Tyr symmetric ring deformation[36]
1307	All	R, A, E, L, F	Ala H-C_α-$C_{terminal}$ vibrations; Ala and Arg C_β-C_α-H vibrations;[27] Ala and Glu CH_2 twisting, rocking, and deformation;[34] Glu CH_2 wagging;[31] Glu, Arg, and Leu C_α-H bending;[32] Arg N–H rocking and C=O stretching;[37] Arg C_β twist and C_γ rock vibrations;[27] phenyl ring stretching;[27,34] adda C-H bending;[32,34] adda CH_2 wagging;[31] phenyl ring C-H in-plane bending[33-34]
1347	All[c]	R, L, F, W	Leu C-H bending,[32,38] Leu CH_3 symmetric deformation,[31] Arg CH_2 deformation and torsion,[51] phenyl ring stretching,[34] adda CH_2 symmetric out-of-plane bending,[33] Trp C-H bending,[27,31] Trp indole ring vibration[32]
1379	All[c]	A, R, E, MeD, F	Ala C_β symmetric rocking and bending,[27] Glu and MeAsp CO stretching and OH bending,[35] adda CH_2 symmetric out-of-plane bending[33]
1384	All[c]	L	Leu CH_3 symmetric bending[38]
1392	All[c]	MeD	MeAsp CO stretching and OH bending[35]
1442	All[c]	E, W	Glu CH_2 bending,[32] Glu CH_2 scissoring,[31] Trp indole ring stretching[27,39]
1450	All[c]	E, F, W	Glu CH_2 bending,[35] adda CH deformation,[34] adda symmetric in-plane CH_2 bending,[32-33] phenyl ring C-C stretching,[33] Trp CH_2 bending[32]
1453	All	R, E, L	Leu CH_2 bending,[32] Leu CH_2 scissoring,[31] Leu CH_3 asymmetric bending,[38] Arg CH_2 bending,[32] Arg N-C-N asymmetric stretch, Arg C-N-H side chain vibrations,[27] Arg C–H vibrations,[37,39] Glu CH_2 bending,[35]
1459	All[c]	A, MeD	Ala C_β asymmetric rocking,[27] Ala CH and CH_3 deformation,[31-32,34,39] MeAsp CH_2 bending[32]
1480-1575			*Amide II (very weak Raman signal, often negligible)*[29]
1555	-LW	W	Trp indole ring stretching[27,36]
1586	-LW	R, F, W	Trp indole ring vibration[32,36]
1600-1700*	All		Amide I, water in aqueous peptide sample[29-31]
1602		F	Phenyl ring C-C stretch[31,33,36]
1609		F	Phenyl ring C-C stretch[32-34]
1616		R, Y	Arg NH_3^+ asymmetric bending,[32] Arg NH_2 vibrations,[29]
1620		W	Trp indole ring vibrations[31-32,36]
1632		E	Glu asymmetric COO^- stretching[35]
1660		E	Glu side chain C=O stretching[32]
1670		MeD	MeAsp C=O stretching[32]
1676		R, E	Arg asymmetric C=N stretching,[37,51] Arg asymmetric NH_3^+ bending[51]

Peak (cm^{-1})[a]	**Toxin**	**Amino Acid[b]**	**Molecular vibration (from literature)**
1693		R	Arg asymmetric C=N stretching,[37,51] Arg asymmetric NH_3^+ bending[51]

[a] Experimental intensity specified by: **most intense peaks*,** **strong peaks,** **moderate peaks,** weak peaks, and *peaks not found in the toxin spectra*. Designations should be considered alongside spectra shown in **Figure 2.2**.

[b] Amino acids listed displayed the indicated peaks for at least one of the physical states. One letter and three letter amino acid codes: Phenylalanine (F/Phe), alanine (A/Ala), leucine (L/Leu), glutamic acid (E/Glu), arginine (R/Arg), tryptophan (W/Trp), tyrosine (Y/Tyr), N-methyl-D-aspartic acid (MeD/MeAsp).

[c] Peaks have differing shape and intensity, but they are consistently present.

Raman grating selection. Raman spectra of MC-LR, MC-RR, MC-LA, nodularin, and the amino acids were collected with both the 1200 grooves/mm and 300 grooves/mm gratings (**Figure SI. 2.2**, **Figure SI. 2.3**). The increase in resolution achieved by the 1200 grooves/mm grating did not uncover any additional peaks in the cyanotoxins that would facilitate clearer differentiation between toxins. Instead, improving the resolution increased the amount of time required to take each spectrum from 50 s to 360 s and decreased the signal to noise ratio. The amino acid peaks displayed sharper, more distinct peaks with the 1200 grooves/mm grating that more clearly demonstrates differences between L-alanine and D-alanine. However, the cyanotoxin spectra suggest that the 300 grooves/mm grating provided sufficient peak resolution to facilitate microcystin variant determination in less time; therefore, subsequent experiments were conducted using the 300 grooves/mm grating. Future experiments that require improved peak resolution may require the use of the 1200 grooves/mm grating.

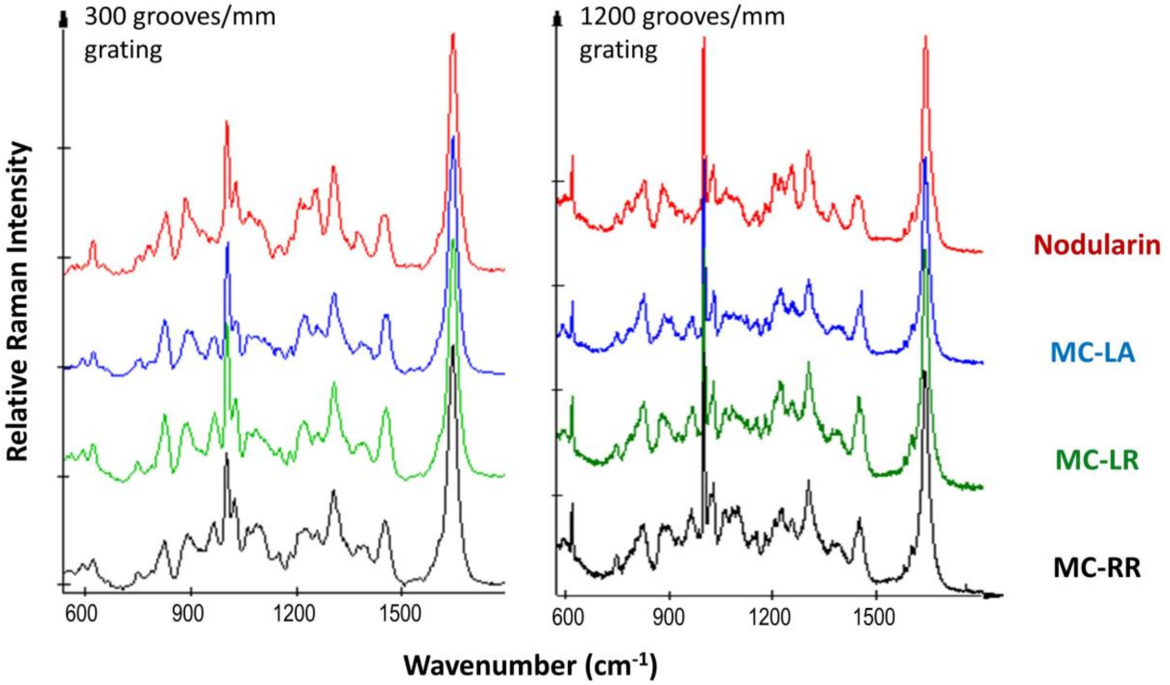

Figure SI. 2.2. Nodularin (red), MC-LA (blue), MC-LR (green), and MC-RR (black) spectra. A 785 nm laser, 100× objective, and 300 grooves/mm grating (left) or 1200 grooves/mm grating (right) were used to collect spectra. The 1200 grooves/mm spectra display improved peak resolution at the cost of a decrease in signal to noise and an increase in acquisition time (five spectra of 10 s acquisitions with the 300 grooves/mm grating or three spectra of 120 s acquisitions with the 1200 grooves/mm grating). There are sufficient differences between the 300 grooves/mm spectra of each toxin to distinguish between microcystin variants. Relative scaling and vertical offsets are arbitrary.

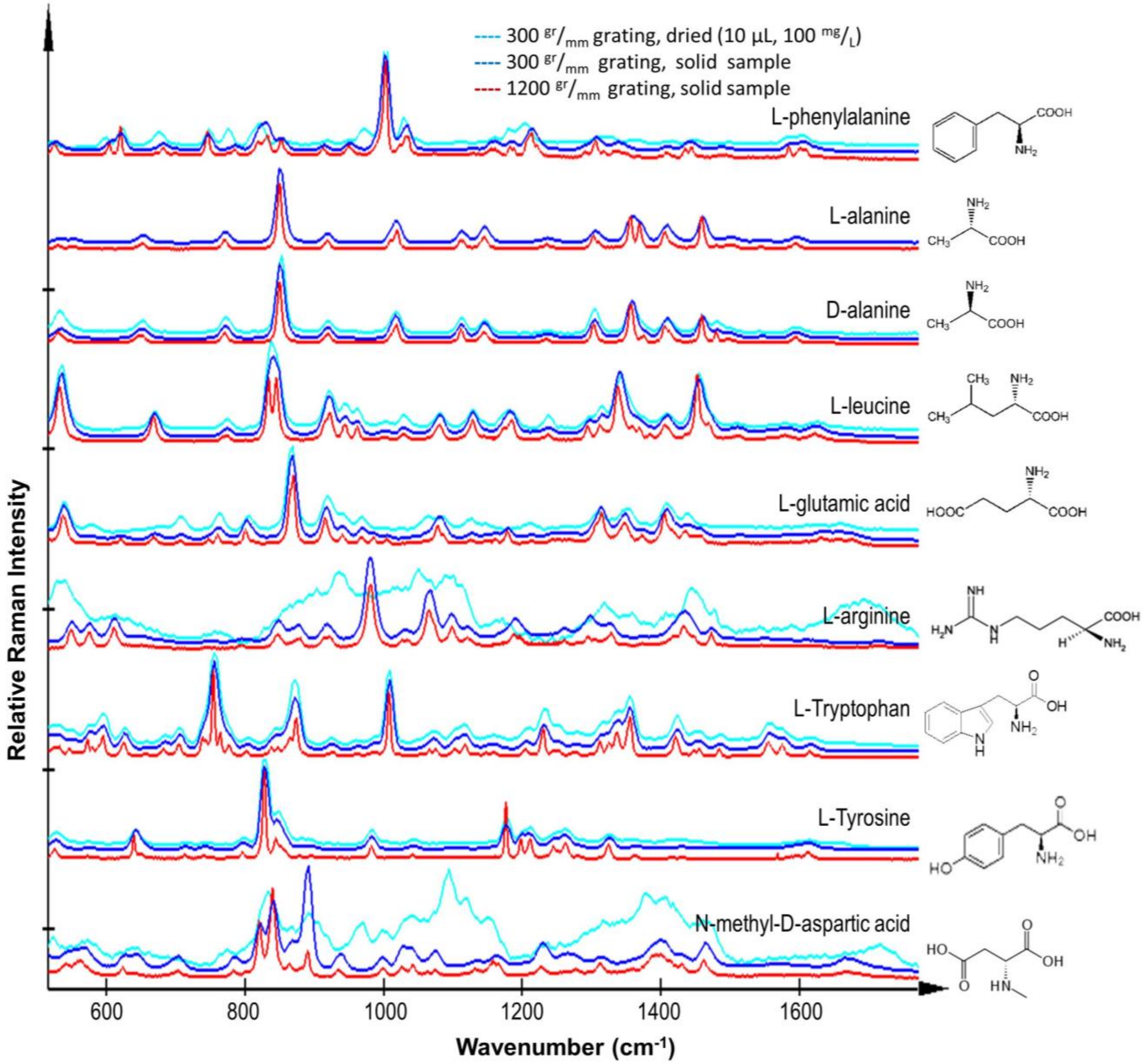

Figure SI. 2.3. Raman spectra of amino acids relevant to the cyanotoxin structure at two instrument resolutions. Solid amino acids were analyzed using the 785 nm laser, 100× objective, and both the 300 grooves/mm grating (dark blue) and 1200 grooves/mm grating (red). DCDR spectra collected with a 300 grooves/mm are also shown for comparison to demonstrate broadening of Raman features in the more hydrated samples (light blue). Relative scaling and vertical offsets are arbitrary.

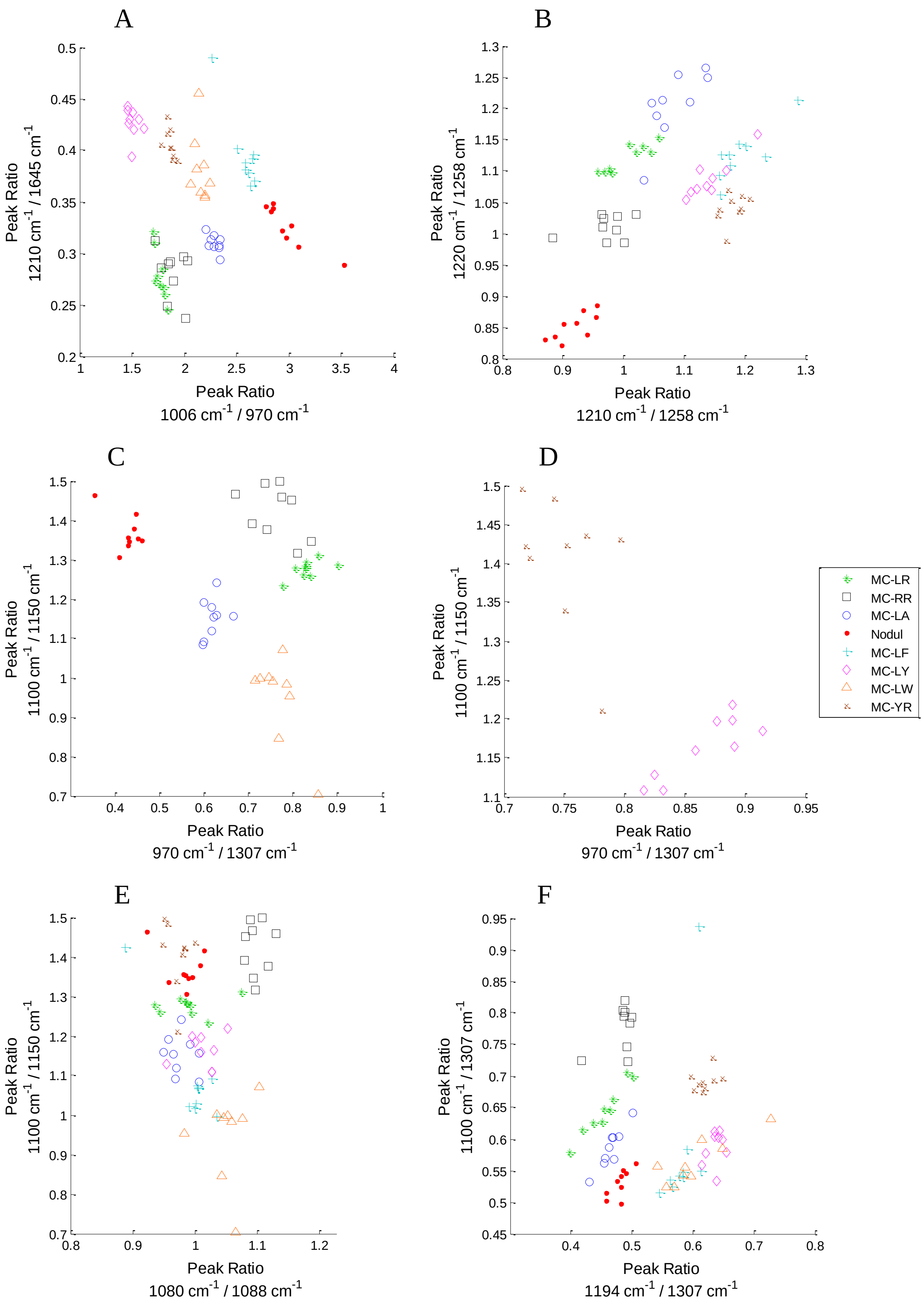

Figure SI. 2.4. Additional peak height ratio plots to aid in cyanotoxin variant identification. Variants can be distinguished from one another by noting the presence or lack of certain peaks, but in some cases plots of peak height ratios are more effective. Each point on the plots represents a different Raman spectrum.

Principal component analysis. To determine the proper number of principal components to be used in PCA, the estimated mean squared prediction error was computed with a 10-fold cross validation. This measure and the percent variance experienced in the data set were plotted against the number of PCs used in the model (**Figure SI. 2.5**). Twelve PCs were chosen for the final model, a reasonable number for PCA application to Raman spectra considering the success of fifteen PCs in describing 90% of the variance in a study of bacterial mixtures; twelve PCs in identifying endospores, chemical agent simulants, and toxin simulants using a partial lease squares-discriminate analysis; and seven PCs in classifying 98.7% of the variance among spectra of nine strains of *Bacillus*.[52-54]

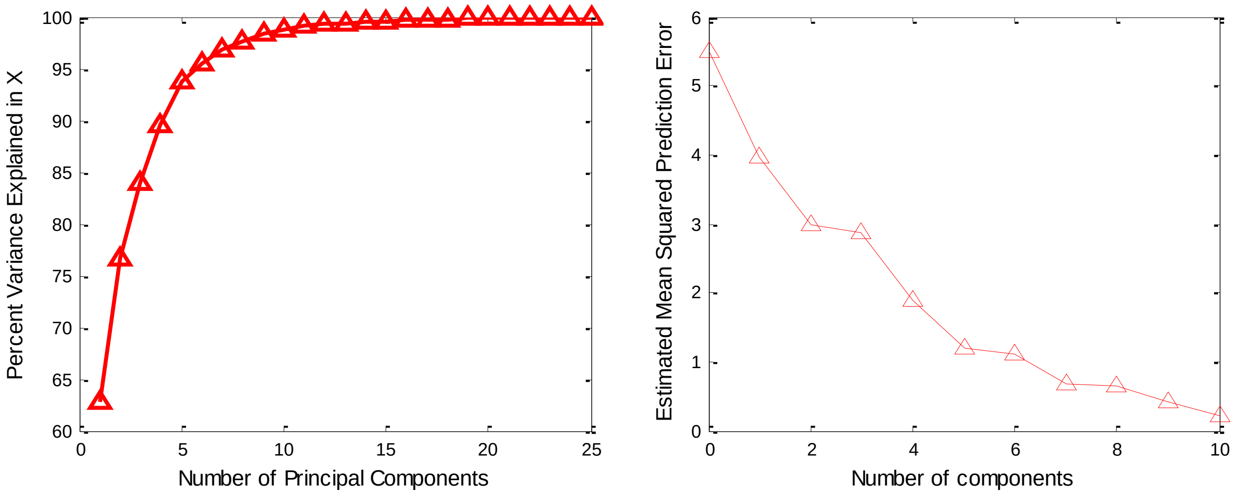

Figure SI. 2.5. The number of principal components that are chosen for the PCA model determines the final fit of the data to the model. Although only eight toxins were examined, additional PCs were included to account for background signals and the fluorescence of sample impurities. The percent of variance explained in x by each component and a ten-fold cross validation of the PCA model were considered before choosing the number of components required to properly classify the toxins without over describing this specific data set.

3

Microcystin-LR Detection in Environmental Waters at Environmentally Relevant Concentrations

*Rebecca A. Halvorson and Peter J. Vikesland**

Department of Civil and Environmental Engineering and Institute of Critical Technology and
Applied Science (ICTAS), Virginia Tech, 418 Durham Hall, Blacksburg, VA 24060-0246
* pvikes@vt.edu, tel. 540-231-3568

Reproduced in part with permission from
Environmental Science and Technology **2011**, 45 (13): 5644-5651.

This chapter includes the environmentally relevant analyses from the 2011 *Environmental Science and Technology* article “Drop coating deposition Raman (DCDR) for microcystin-LR identification and quantitation” by Halvorson and Vikesland that were not included in the M.S. thesis of R.H. Lahr.[2,55] This data proves the utility of DCDR for detection of environmentally relevant concentrations of microcystin-LR in environmental waters. The full article may be found in Appendix A.

ABSTRACT

A drop coating deposition Raman (DCDR) method was developed for the analysis of 2-200 ng samples of microcystin-LR (MC-LR), a ubiquitous and deadly hepatotoxin secreted by cyanobacteria. Solid phase extraction (SPE) of the toxin from a water sample enabled identification of MC-LR at 5 μg/L to 100 mg/L concentrations and the collected results suggest lower detection limits can be readily attained following DCDR substrate modification. Application of DCDR to environmental samples requires sample purification such as SPE before analysis, including critical cartridge wash and toxin rinsing steps. Raman based methods may one day facilitate simpler and faster sample throughput than traditional MC-LR detection methods.

INTRODUCTION

Despite the capabilities of drop coating deposition Raman (DCDR), a sample purification and pre-concentration step will be required for DCDR to be successful for the analysis of microcystin-LR (MC-LR) at environmentally relevant concentrations. Solid phase extraction (SPE) using octadecyl silanised (C18) cartridges is routinely employed as a pre-concentration and purification step for analysis of plant, animal, or complex water samples containing MC-LR.[17] An ISO standard (ISO 20179:2005) exists for reverse-phase SPE and HPLC of microcystins-LR, -RR, and –YR.[56] The current study provides evidence that the DCDR method can be applied for rapid analysis and quantitation of samples containing MC-LR at quantities as low as 2 ng, even if this mass of material must be obtained after a solid phase extraction (SPE) step.

EXPERIMENTAL

Samples of 2-500 mL containing 5 mg/L, 10 μg/L, and 5 μg/L MC-LR from Enzo Life Sciences (ALX-350-012) were extracted with 6 mL Empore^{TM} C18 and 3 mL Oasis® Waters SPE cartridges. The cartridge washing protocol included sequential 6 mL washes of methanol, nanopure water, methanol, and water again before application of the toxin to the cartridge; however, additional washing protocols were considered. Two to five hundred milliliters of aqueous MC-LR solutions were applied to cartridges at slow drip rates (<5 mL/min) before the toxin was eluted by 11 mL of methanol. The methanol was evaporated from the SPE elutant by heating to 45° C under nitrogen. Sample vials were rinsed with 1.5 mL of methanol and the samples transferred to smaller amber vials, from which the methanol was completely evaporated again as above. The toxin residue was finally dissolved in 100 μL of nanopure water, thoroughly vortexed and shaken, and briefly centrifuged for a few seconds to produce the solution analyzed by DCDR.

Water from the New River at McCoy Falls, Virginia was collected on 3/4/2011 and filtered through a series of filters to a final pore size of 0.45 μm. New River water samples were spiked to 10 μg/L MC-LR prior to SPE and DCDR.

DCDR involved drying 2 µL of sample on a quartz substrate and examination with a WiTec Alpha500R AFM Raman spectrometer with a UHTS300 spectrometer, DU 401 BR-DD CCD camera, 100× microscope objective, 300 gr/mm grating, and a TOPTICA XTRA diode 785 nm laser. Raman spectral maps 6 µm wide by 50-100 µm long were collected perpendicularly to the sample residue ridge with 30 or 300 s per spectrum, 2 spectra per µm perpendicular to the drop edge, and 1 spectra per 2 µm parallel to the drop edge.[2] The point of most intense Raman signal in each Raman spectral map was probed to obtain a single Raman spectrum based upon the average of 10 spectra collected over 5 s each.

RESULTS & DISCUSSION

Environmentally Relevant Concentrations. Before DCDR will be applicable to environmental samples containing MC-LR at concentrations of concern (i.e., 1 µg/L WHO drinking water limit or 6-20 µg/L U.S. recreational water guidelines),[10,16] it must be combined with purification and concentration steps, an example of which is provided in the schematic in **Figure 3.1** (SPE followed by DCDR). DCDR spectra of an array of samples with differing concentrations and volumes extracted by SPE resembled the pre-SPE MC-LR spectrum, but a decrease in the intensity and sharpness of the 1648 cm^{-1} peak, an increase in the intensity of the 1457 cm^{-1} peak, and additional differences in the overall intensity of the toxin signal were consistently observed (**Figure 3.2 and 4.3**). SPE was determined to be the step in the sample concentration procedure that caused the greatest changes to the MC-LR spectrum. This conclusion was reached after comparison of DCDR spectra collected from each step of the SPE process, including the MC-LR stock solutions, organic solvent spiked samples, heated and rehydrated samples, various SPE “blanks” after limited and extensive cartridge rinsing, and SPE elutants from MC-LR extractions (**Figure 3.4**). Only after the SPE process were peak shifts and intensity changes in the MC-LR Raman spectrum observed. Thorough rinsing of the cartridge greatly decreased the amount of background material detected by DCDR.

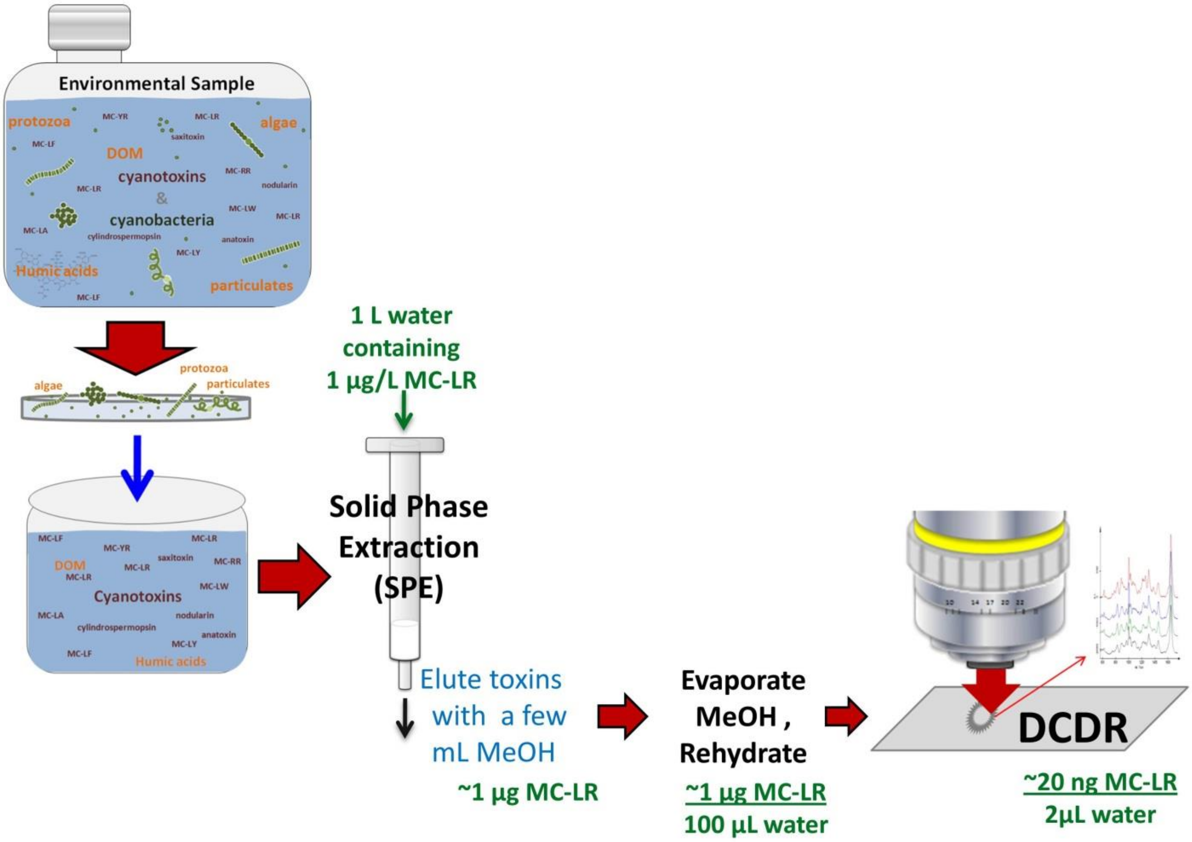

Figure 3.1. SPE may be applied for sample purification and concentration before DCDR. Estimated toxin outputs assume high recoveries of toxin following SPE, which are not impossible to achieve as documented in the literature.[57]

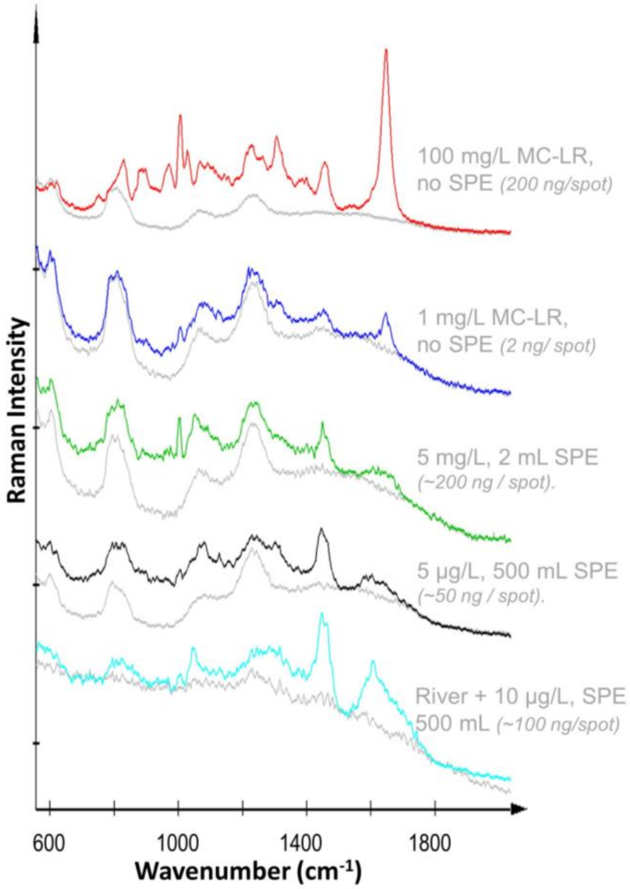

Figure 3.2. MC-LR DCDR spectra are affected by the SPE process, but features including the 1006 cm^{-1}, 1307 cm^{-1}, 1457 cm^{-1}, and 1648 cm^{-1} peaks remain. The quartz background for each sample is indicated in grey.

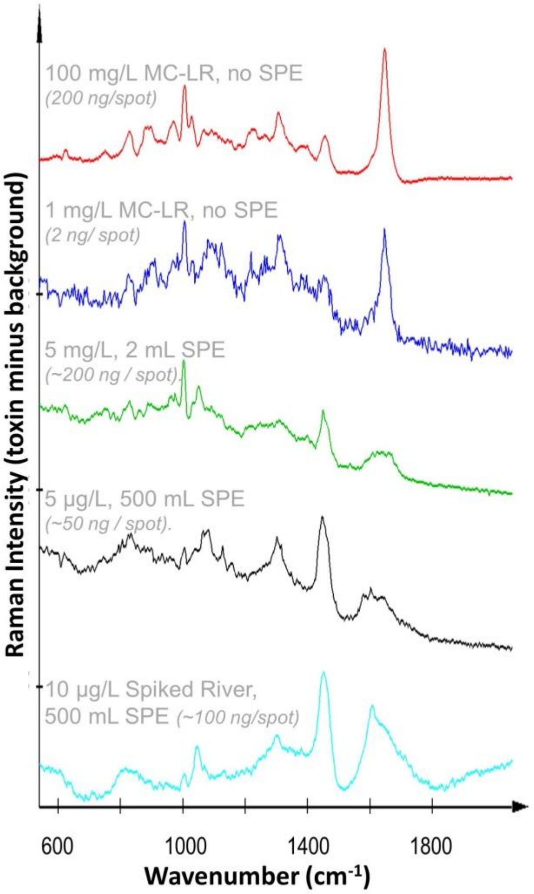

Figure 3.3. Background subtracted MC-LR DCDR spectra. Although the quartz background signal is useful for documenting perspective of the overall intensity of the toxin signals relative to the background, background subtracted spectra were used for more thorough analysis of peak differences.

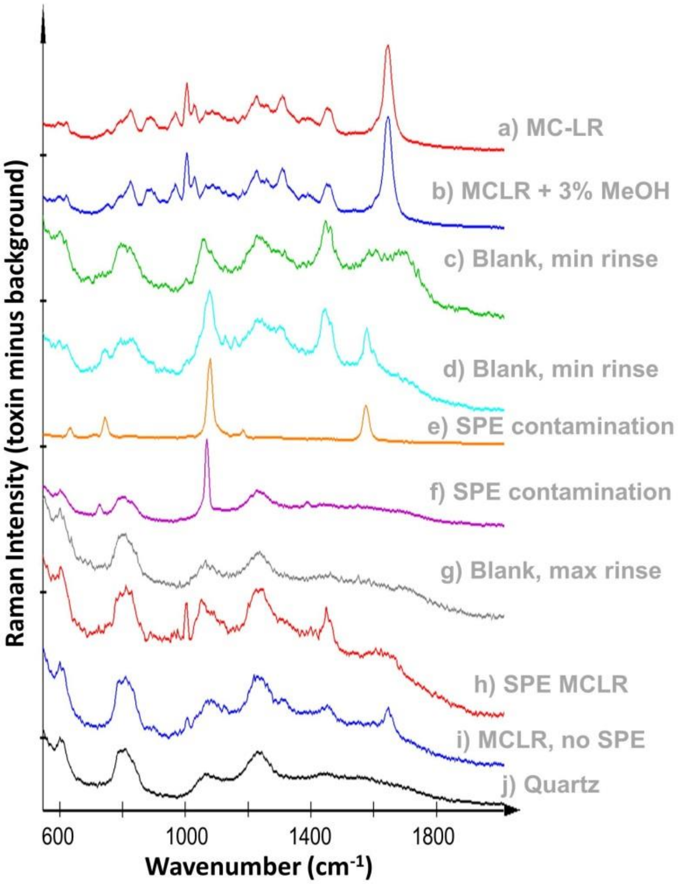

Figure 3.4. DCDR spectra tracking both toxin and impurity signals throughout the SPE process. Thorough rinsing of the SPE cartridge before extraction is necessary to obtain the clearest toxin spectra. Two microliters of each of the following samples were applied for DCDR analysis: (a) a freshly prepared 50 mg/L MC-LR aqueous solution; (b) a 50 mg/L MCLR aqueous solution with 3% v/v methanol; (c) a “blank” sample of anything that eluted from the SPE cartridge in methanol after limited cartridge rinsing (6 mL each of methanol, water, methanol, and more water); (d) a “blank” sample with limited cartridge rinsing; (e & f) any sample after SPE commonly contained crystals in the inner portions of the drop with the spectra indicated here; (g) a “blank” sample of the elutant from a SPE cartridge in methanol after extensive cartridge rinsing (the same steps as c, with additional methanol, water, acetone, water, methanol, and water rinses, (h) the SPE elutant resulting from extraction of 2 mL of a 5 mg/L MC-LR solution, made from the same stocks as samples a and b above and rehydrated in 100 μL water; (i) a 1 mg/L MC-LR solution that did not undergo SPE; and (j) the quartz background observed beneath all samples. The spectrum of MC-LR after heating with methanol to evaporate solvent followed by rehydration in water, without SPE is identical to a & b.

Following SPE, the intensity of the toxin spectra decreased more than ten-fold compared to that expected if SPE recoveries were high. The intensity drop was correlated to an increase in both drop area and drop edge width as measured from optical images of post-SPE samples (**Table 3.1** and **Figure 3.5**). Contamination of the DCDR sample drop by organic solvent, SPE media components, or other impurities likely decrease the surface tension of the sample droplet, creating a larger drop area despite application of a constant sample volume. Modified substrates such as AnchorChip targets designed for matrix-assisted laser desorption/ionization (MALDI) applications use a polymeric, hydrophobic outer ring of specified dimensions on a hydrophilic substrate to contain sample drops within a designated area, and such a substrate may produce the drop size containment necessary to lower the detection limits of the DCDR method for cyanotoxin detection.

Table 3.1. Computed sample ridge thickness for optimal Raman signal.

MC-LR Sample ID	**Mass (ng)**	**Measured drop edge width (μm)**	**Measured drop area (μm^2)**	**Measured drop perimeter (μm)**	**Calculated thickness at ridge (μm)**
100 mg/L, no SPE	200	16	3.0×10^6	6300	2.43
50 mg/L, no SPE	100	12	5.1×10^6	8100	1.30
25 mg/L, no SPE	50	10	2.8×10^6	6000	1.02
10 mg/L, no SPE	20	5	2.7×10^6	6000	0.79
5 mg/L, no SPE	10	7	4.9×10^6	8200	0.22
1 mg/L, no SPE	2	2	3.0×10^6	6500	0.16
SPE of 2 mL, 5 mg/L	200	36.0	1.3×10^7	13000	0.5
SPE of 500 mL, 5 μg/L	50	33.6	8.7×10^6	10600	0.2
SPE of 500 mL, River Water with 10 μg/L MCLR spike	100	79.9	1.6×10^7	14400	0.11

* Assumes MC-LR volume of 2 nm^3, a uniform drop edge, and 100% recovery of MC-LR thru the SPE process. High recoveries of MC-LR during SPE are reasonable.[57]

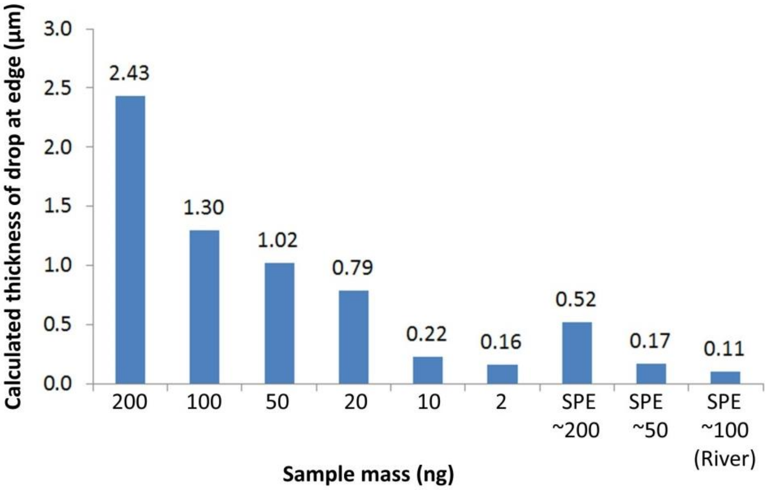

Figure 3.5. Comparisons between the calculated DCDR drop edge thickness for samples of different masses pre- and post- SPE.

Environmental Waters. SPE was applied to a 500 mL sample of New River water spiked with 10 µg/L of MC-LR, and the resulting DCDR drop exhibited a great deal of impurities compared to a sample prepared in nanopure water (**Figure 3.6**). The calculated drop edge thickness is expected to contain significant error considering impurities that co-deposit with the toxin in the drop edge. Despite the error, the increases in drop area and drop edge width still account for the weak intensity of the toxin Raman signal (**Figure 3.2** and **Table 3.1**). Techniques have been developed to deal with impurities that are soluble in methanol during SPE, including sample rinse steps that increase the methanol percentage in water several times before the final toxin elution.[58-59] Such rinse steps were not incorporated in the current study. Additionally, photobleaching a DCDR sample with the Raman laser prior to Raman acquisition can eliminate some of the background fluorescence produced by impurities in the sample; extensive MC-LR degradation by the 785 nm laser in this case is not expected considering the stability of DCDR spectra collected for a 10 µL sample containing 100 mg/L MC-LR over time under the 785 nm Raman laser. At least 11 minutes of photobleaching were required to produce the spectrum shown for the New River sample (**Figure 3.2** and **Figure 3.7**). Furthermore, Zhang et al. documented success in coupling HPLC and DCDR for human insulin; this coupling applied to MC-LR may provide ample purification, while also producing more descriptive information of the eluted compounds than UV-Vis, PDA, or MS detectors in relation to the microcystins.[20,60-61]

The development of surface-enhanced Raman (SERS) tags that specifically bind to MC-LR may also enable enhancement of the toxin spectrum despite the presence of impurities.[1,62-63]

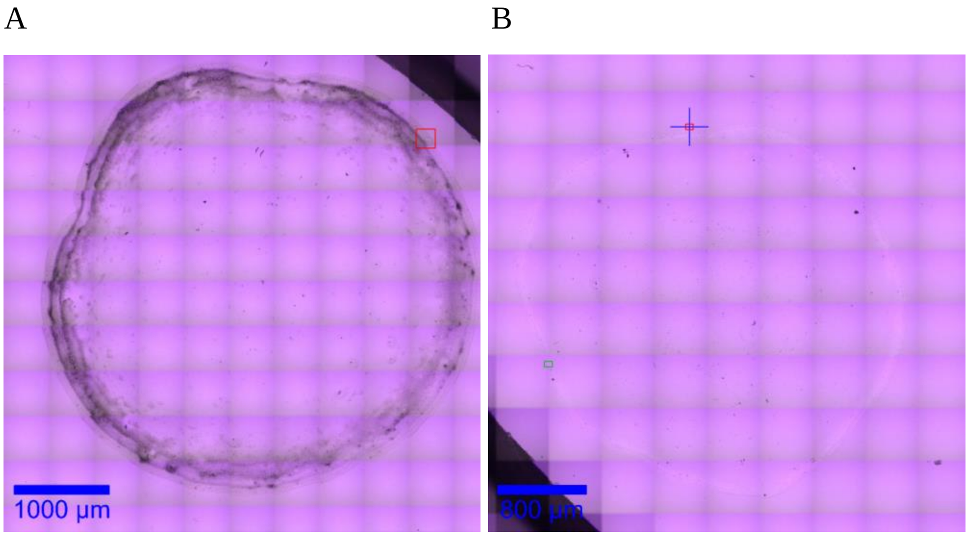

Figure 3.6. Optical images of a DCDR drop after SPE of 500 mL of samples containing (A) New River water spiked with 10 µg/L MC-LR and (B) nanopure water containing 5 µg/L MC-LR.

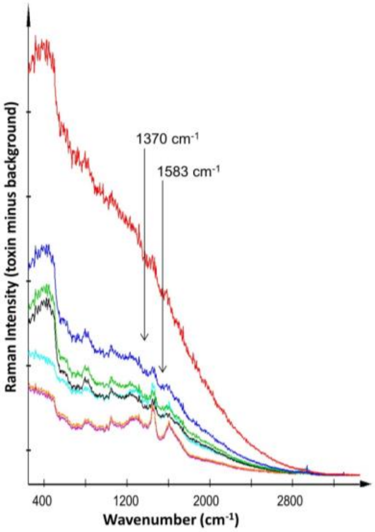

Figure 3.7. Photobleaching decreased background fluorescence, and allowed signals from the sample to shine thru the background. Spectra were collected in a single location at the following time intervals (top down): 0 min, 1.3 min, 2.5 min, 3.5 min, 6.6 min, 11.2 min, 12.6 min, and 14.6 min. Graphite peaks due to the decomposition of organic matter upon laser contact observed by peaks at 1370 and 1583 cm^{-1} do not grow in these spectra as the samples are exposed to the laser.[64]

FUTURE OUTLOOK

The strength of the correlation between concentration and Raman intensity in the pre-SPE samples, the previous success of DCDR for predictions of sample concentration for a number of different biomolecules in sample mixtures, and the concentration levels that DCDR was capable of identifying despite dramatic increases in the DCDR drop area following SPE suggest the DCDR method could be applied for identification and quantitation of MC-LR at environmentally relevant concentrations.[24,65] Development of a substrate to contain DCDR droplets, determination of specific washing protocols for SPE cartridges, and identification of a proper purification protocol utilizing SPE rinses, HPLC purification, or SERS tags that preferentially bind MC-LR will be necessary before DCDR will be practical for analysis of environmental samples at sub µg/L concentrations.

ACKNOWLEDGEMENTS

This work was supported by an EPA STAR graduate research fellowship to R.A.H. (F08B20329) and research grants from the Water Research Foundation (#4212) and the Virginia Tech Institute for Critical Technology and Applied Science (ICTAS). We thank Dr. Weinan Leng for his insights and assistance with the WITec Alpha 500R.

4

Raman-Based Characterization of Microfluidic Paper-Based Analytical Devices (μPADs)

R. Halvorson Lahr, G. Wallace, P.J. Vikesland

Department of Civil and Environmental Engineering and Institute of Critical Technology and
Applied Science (ICTAS), Virginia Tech, 418 Durham Hall, Blacksburg, VA 24060-0246

ABSTRACT

There is great interest in the use of microfluidic paper-based analytical devices (μPADs) for low-cost diagnostics. Transport of nanoparticles in cellulose matrices influences preparation and use of μPADs for nanoparticle (NP) detection strategies and surface-enhanced Raman spectroscopy (SERS) conducted in the presence of paper scaffolding. Citrate (cit), BSA, PEG, PVP, and DNA stabilized AuNP and AgNP transport in wax-printed μPADs was primarily affected by nanoparticle surface functionalization rather than particle size. Sample pH influenced the transport of 15 nm BSA-cit-AuNP, but not 15 nm cit-AuNP because of the effects of solution pH on the charge and conformation of BSA. Normal Raman and SERS spectral maps imaged cellulose fibers and deposition patterns of algal cells, amaranth, and nanoparticles in wax-printed μPADs. The substrate underlying the μPAD (i.e., PTFE, polystyrene, air, cellulose) during analyte application influences cit-AuNP deposition patterns in the cellulose, with more AuNP observed on the upper cellulose fibers when PTFE underlies the μPAD. Water soluble amaranth dye and PVP-AgNP are attracted to the wax boundary layer, but travel efficiently with the water mobile phase. At low pH, cit-AuNP and BSA-cit-AuNP deposit onto the cellulose fibers at the center of the channel with minimal transport, maintaining minimum interaction with the wax. Negative DLVO interaction energies and positive electrophoretic mobilities correlate with nanoparticle deposition in the negatively charged cellulose matrix and minimal particle transport. Samples with low positive DLVO interaction energy barriers generally did not travel in cellulose, though DLVO does not fully explain particles for which steric hindrance or Lewis acid-base interactions between particles and the cellulose are significant. Nanoparticle flow in

µPADs can be engineered by printing wax-boundaries on paper, pre-wetting cellulose, modifying particle surface coatings, regulating solution pH, or changing the underlying substrate identity.

INTRODUCTION

Microfluidic analytical devices (µPADs) have been developed for the detection of glucose, proteins, cholesterol, metals, and microorganisms via colorimetric, electrochemical, chemiluminescence, surface-enhanced Raman spectroscopy (SERS), and extraction based detection schemes; however, development of these diagnostics is far from optimized.[66-69] Many of these devices require nanoparticles to be embedded in the paper to facilitate SERS or colorimetric detection. These embedded nanoparticles can be produced by direct assembly (i.e., addition of pre-synthesized nanoparticles to paper) or by in situ synthesis.[67] Direct assembly often produces papers with highly heterogeneous nanoparticle deposition due to capillary transport of nanoparticles during the drying process and the “coffee ring” effect.[67,70] Nanoparticle transport studies have been conducted in porous media, but existing nanoparticle transport studies in cellulose are largely limited to the deposition of TiO_2 based dyes within paper pulp.[71] This manuscript represents, to our knowledge, the first attempt to track noble-metal nanoparticle deposition patterns in µPADs with SERS as a function of nanoparticle surface coating.

Normal Raman and surface-enhanced Raman spectroscopy (SERS) spectral mapping. Normal Raman spectroscopy can be used to identify polarizable molecules based on their ability to inelastically scatter light.[1,4] The technique is especially useful for samples of high concentrations and little fluorescence. Gold or silver nanomaterials can be tracked to some degree by their visibly pink or green colors that arise due to surface plasmon resonance (SPR) absorbance near 520 and 400 nm respectively.[3,72-74] Alternatively, SERS can record images of noble-metal nanoparticle deposition quickly and efficiently at low concentrations in transparent or translucent media, as long as the laser wavelength used to produce the Raman spectra overlaps with the SPR absorbance of the nanoparticles, thus producing a Raman signal enhancement.[1,3] The resolution of the sampling region per Raman spectrum is dictated by the Raman laser wavelength, the numerical aperture of the microscope objective, and the refractive index of the media through which the laser light travels.[75-76] For a 785 nm Raman laser and 10× microscope objective with a numerical aperture of 0.3 positioned over a dry sample (laser light travels through air), the region sampled by the laser per spectrum is ≈1.6 µm in the lateral direction and ≈17.4 µm in the axial direction. Improvements in resolution can be made by using a higher power objective, an oil immersion objective, or a lower laser wavelength.

Although nanomaterials are frequently incorporated into μPADs, their transport properties and deposition patterns in μPADs remain unexplained. Herein, wax-printed μPADs were characterized with Raman spectroscopy, and the transport of nanoparticles with various surface coatings was examined. These results are relevant to nanomaterial transport studies, the production of nanoparticle impregnated μPADs, and SERS. Nanoparticle transport is discussed in terms of electrostatic, van der Waals, Lewis acid-base, and steric forces between nanoparticles and cellulose.

MATERIALS & METHODS

$HAuCl_4$ was purchased from MP Biomedical; 5 kDa HS-PEG-OCH_3 and 3.4 kDa HS-PEG-COOH from NANOCS; rhodamine B isothiocyanate (RBITC), malachite green isothiocycante (MGITC), and oligonucleotide (5’-NH2-TCGGC ACGTT CTCAG TAGCG CTCGC TGGTC ATCCC ACAGC TACGT-3’) from Invitrogen; *N*-hydroxysulfosuccinimide (sulfo-NHS) and bovine serum albumin (BSA) from Sigma-Aldrich; 1-ethyl-3-[3-dimethylaminopropyl]carbodiimide hydrochloride (EDC) from Fluka; and *Pseudokirchneriella subcapitata* cultures from Marinco Bioassay Laboratory Aquaculture. Dissolved organic matter (DOM) from the Great Dismal Swamp in North Carolina was filtered to remove all constituents greater than 0.45 µm, freeze dried, and rehydrated prior to use.[2]

Substrate preparation and characterization. Wax-printed microzone papers of 2 mm spot sizes and wax-printed channels of 1.2 mm channel width, 0.3 mm wax wall thickness, and 3 mm sampling spot diameters (dimensions of designs before heating; **Figure SI. 4.1**) were designed in Adobe Photoshop CS and printed on Whatman Grade 1 chromatography paper using a Xerox ColorQube 8570 printer.[77-78] After printing, the paper was heated wax-side up on a digital hot plate at 150 °C for 60 seconds, wax side down for 30 seconds, and wax side up for another 30 seconds. Wax printed papers were characterized using a LEO (Zeiss) 1550 field emission scanning electron microscope (FESEM), a FTA125 goniometer, and a Sony Cyber-shot DSC-

S750 digital camera. Prepared wax-printed channels were placed in Petri dishes with the printed side up for testing with nanoparticle solutions.

Sample description and characterization. Nanoparticle synthesis methods published elsewhere were carried out as described in the supporting information (**Table SI. 4.1**). Nanoparticle core sizes were determined using ImageJ (NIH, Ver. 1.46) to size electron micrographs obtained with either a Zeiss 10CA transmission electron microscope (TEM) with an AMT Advantage GR/HR-B CCD Camera System or a JEOL JEM 1400 TEM with a Gatan Orius CCD camera controller (**Table 4.1**). A Varian Cary 5000 UV-Vis-NIR spectrophotometer documented the surface plasmon resonance band locations and the stability of the nanoparticle solutions prior to use (**Figure SI. 4.2**). An Accumet AB15 Plus pH Meter (Fisher Scientific) evaluated pH as controlled by dropwise addition of 1 M HCl, 1 M NaOH, or 10 M NaOH. A Malvern Zetasizer Nano ZS instrument and autotitrator measured the hydrodynamic diameter (z-average), electrophoretic mobility, and conductivity of the nanoparticle solutions (**Table 4.1**). The autotitrator monitored pH with an accuracy of 0.2 pH units, collected measurements every 0.5 pH units, and titrated with 0.1 M NaOH and 0.1 M HNO_3. The transport behavior of citrate reduced 15 nm AuNP (15 nm cit-AuNP),[79-81] citrate reduced 46 nm AuNP (46 nm cit-AuNP),[80-82] bovine serum albumin coated – citrate reduced AuNP of 15, 46, and 64 nm (BSA-cit-AuNP),[80-81,83] PEG coated – citrate reduced 46 nm AuNP (46 nm MixPEG-cit-AuNP, 46 nm OCH_3-PEG-cit-AuNP, and 46 nm COOH-PEG-cit-AuNP),[84] mixed PEG and dye-tagged – citrate reduced 46 nm AuNPs (46 nm PEG-MGITC-cit-AuNP and 46 nm PEG-RBITC-cit-AuNP),[84] oligonucleotide and mixed PEG coated – citrate reduced 46 nm AuNP with dye-tags (46 nm DNA-PEG-MGITC-cit-AuNP),[84] Au nanorods (AuNR),[85] and PVP AgNP (8 nm PVP10K-AgNP, 8 nm PVP55K-AgNP, and 40 nm PVP55K-AgNP)[86-88] was contrasted with that of soluble amaranth dye, 50 g/L $HAuCl_4$, and Great Dismal Swamp DOM.

Table 4.1. Characteristics of the nanoparticles applied to wax-printed papers.

Sample	**TEM size (nm)**	**Hydrodynamic diameter (nm)**	**PDI**	**Zeta Potential (mV)**	**pH**	**Electrophoretic Mobility (µm·cm/Vs)**	**Conductivity (mS/cm)**	**Refs.**
15 nm cit-AuNP	15±7	18±0.1	0.32	-58.9±9.7	6.4	-3.1±0.5	0.4	[79-81]
46 nm cit-AuNP	46±5	36±0.2	0.25	-31±17	3.5	-2.4±1.3	0.3	[80-82]
15 nm BSA-cit-AuNP	15±7	26±0.2	0.19	-31.4±16.0	8.1	-1.6±0.8	2.1	[80,83]
46 nm BSA-cit-AuNP	46±5	58±1.2	0.25	16.7±9.8	4.4	1.3±0.8	0.2	[80-81,83]
64 nm BSA-cit-AuNP	64	58±0.1	0.43	18.6±13	4.2	1.5±1.0	0.2	[80,83]
46 nm OCH$_3$-PEG-cit-AuNP	47±5	126±2	0.47	-51.3±9.2	6.1	-2.7±0.5	0.002	[84]
46 nm COOH-PEG-cit-AuNP	47±5	78±1.5	0.4	-36.9±8.5	5.8	-1.9±0.4	0.002	[84]
46 nm OCH$_3$/COOH-PEG-cit-AuNP	47±5	91±1.4	0.42	-48.7±10.3	6.3	-2.5±0.5	0.002	[84]
46 nm MixPEG-MGITC-cit-AuNP	47±5	84±1.2	0.25	-50.6±10.7	5.8	-2.6±0.6	0.02	[84]
46 nm MixPEG-RBITC-cit-AuNP	47±5	88±2.3	0.25	-55.9±14.9	5.7	-2.9±0.8	0.004	[84]
46 nm DNA-MixPEG-MGITC-cit-AuNP	47±5	91±2.5	0.34	-55.2±8.2	6.5	-2.9±0.4	0.009	[84]
40 nm PVP10K-AgNP	41	65±1.3	0.28	-18.9±12.8	6.6	-1.0±0.67		[80,89]
40 nm PVP55K-AgNP	42±10	78±0.6	0.18	-41.2±17.4	8.3	-2.2±0.9		[86-87]
8 nm PVP55K-AgNP	8±5	79±1.5	0.41	-32±16.7	9.5	-1.7±0.9		[86-87]
8 nm PVP10K-AgNP	7±3	56±2.2	0.44	-33.9±16.8	9.2	-1.8±0.9		[86,88-89]
AuNR	65×20	58±25.4	0.2	-28.7±14.3		-2.3±1.1	0.0144	[85]

Nanoparticle transport within wax-printed cellulose. Aliquots of 2 µL of each nanoparticle solution or the three soluble species (amaranth, HAuCl$_4$, and DOM) were pipetted into µPAD sampling spots printed-side up in a Petri dish open to the air. The pH was adjusted with concentrated NaOH or HCl to obtain samples of amaranth, DOM, 15 nm cit-AuNP, and 15 nm BSA-AuNP at each whole number pH value from 3-10 before application onto the µPADs. After drying for at least 10 minutes at room temperature, digital photographs of each channel were taken with a Sony Cyber-shot DSC-S750. Channels were then rinsed three times with 4 µL of nanopure water (Barnstead Nanopure water purification system), dried for at least 10 minutes at room temperature, and photographed again. A ruler was included in all photographs to facilitate travel distance measurements with the ImageJ software. Analyte deposition patterns both in wax-printed channels and microzone papers were imaged by Raman spectroscopy with a WITec

Alpha500R Raman UHTS300 spectrometer, DU 401 BR-DD CCD camera, 785 nm laser, 300 grooves/mm, 10× microscope objective, and 0.05-115 mW of laser power. A Raman peak specific to each analyte on a cellulose surface, was chosen using **Figure 4.1**, and the intensity of that peak was used to generate Raman spectral images from thousands of Raman spectra collected across a wax-printed paper channel or well-plate.

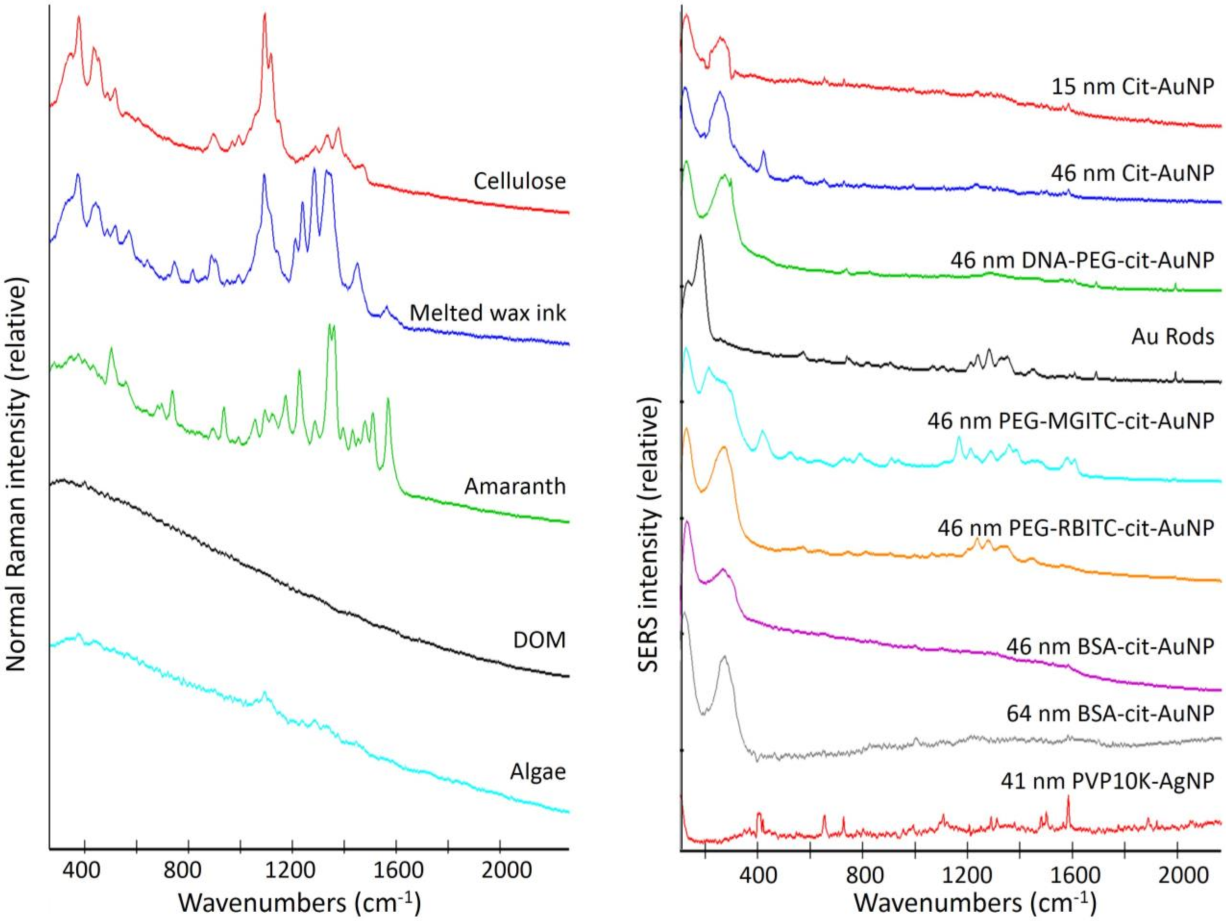

Figure 4.1. Raman and SERS spectra of each analyte captured within wax-printed cellulose were characterized such that analyte deposition patterns could be tracked within the cellulose. Instrument parameters are included in **Table SI. 4.2.**

RESULTS & DISCUSSION

Wax-printed paper characterization. Whatman Grade 1 chromatography paper is an ideal substrate for µPAD compatibility with SERS because it is widely available, cheap, well characterized, compatible with any commercially available wax printer, and it produces a clear Raman spectrum with few peaks and little fluorescence due to its purity and lack of additives (**Figure 4.1**).[78,90] The paper is composed of a 3D mat of intertwined cellulose fibers with a tendency to sorb water and a negative zeta potential at all pH values examined (**Figure SI. 4.3**).[91-96]

A Xerox ColorQube printer, a newer model succeeding the Xerox Phaser that was used for the pioneering µPAD developments, is compatible with a wax-based ink that melts below 120ºC.[78,97-98] This more energy efficient Xerox ink requires a lower re-flow temperature than the original Xerox ink and is likely composed of carbon black pigment and hydrophobic polymer or hydrocarbon mixture (**Table SI. 4.3**).[99-101] The wax re-flow process caused wax spreading within the paper from an initial printed dimension of 0.3 mm wax to a heated dimension of approximately 0.8 mm to 1.1 mm for the back of the paper and the original printed side respectively (**Figure SI. 4.1**).[78] FE-SEM shows smooth regions on the cellulose fibers after wax re-flow that are not observed on the cellulose fibers without wax (**Figure SI. 4.3**). Photographs, FE-SEM images, and SERS spectral maps indicate that the melted wax successfully contained nanoparticles and aqueous solutions of <12 µL within the channels (**Figure SI. 4.1 & Figure SI. 4.4**). Channel dimensions were chosen to produce the most consistent fluid transport and the strongest, most concentrated SERS signals (**Figure 4.2**).

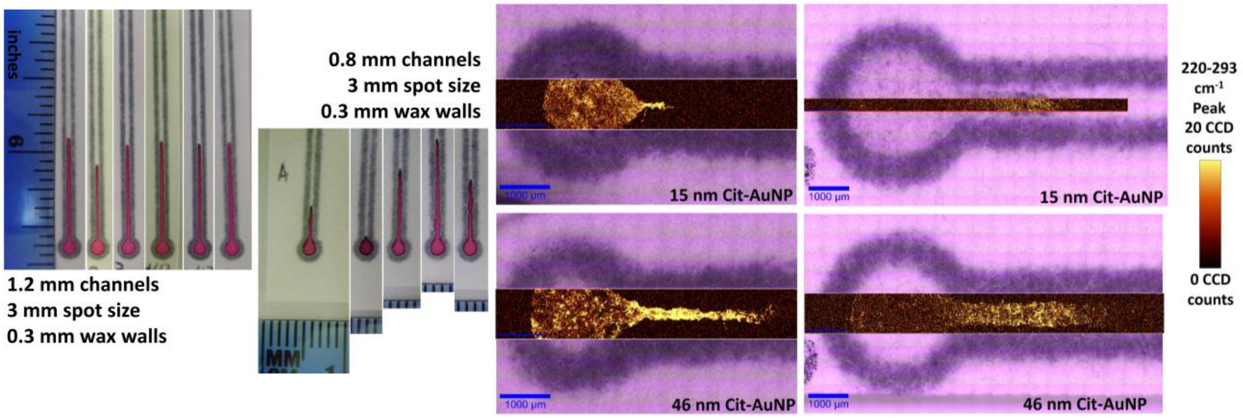

Figure 4.2. Channel dimensions were chosen to produce the most consistent fluid flow and strong SERS signals. Narrow channels concentrated samples to facilitate strong SERS signals, but the spread of the wax caused channels narrower than 1.2 mm to periodically constrict flow as observed in the photographs on the left. Optical images collected using a 10× microscope objective (purple) and overlaid SERS spectral maps demonstrate nanoparticle deposition patterns within the wax-printed cellulose channels. Nanoparticles are still observed within channels over 1.2 mm wide, though longer acquisition times, SERS tags bound to nanoparticles, or higher laser powers are often required. Spectra were collected with a 785 nm laser, 300 gr/mm grating, 10× microscope objective, 0.05 seconds per spectrum, and 5 to 10 spectra per µm.

Contact angle measurements were collected for water droplets on the wax ink block, heated and unheated wax printed on chromatography paper, and water-soaked printed papers. As suggested by Noh and Phillips, wax-printed paper absorbs water droplets if given sufficient time after deposition; hence, water droplets were analyzed immediately after placement on the sample.[102] After heating for wax re-flow, the original wax-printed side of the paper (front) had a higher contact angle than the back of the paper when both samples were not pre-wetted, proving that the original printed side retains most of the wax, making it more hydrophobic (**Table SI. 4.4**). The hydrophobicity and the clear difference in the amount of wax spreading between the two sides of the paper suggest that solution flow may be dependent upon the orientation of the paper (original printed side up or down). Contact angles were also consistently lower for papers that were pre-wetted before measurements were collected. The water adsorption properties of cellulose are well documented, and although high purity cotton cellulose such as that in Whatman grade 1 chromatography paper sorbs less water than other types of cellulose,[91] the dry or pre-wetted state remains an important variable to hold constant or engineer to improve functionality of wax-printed paper devices. For consistency, the nanoparticle transport experiments reported here were conducted with dry papers as purchased and stored on a lab bench.

Fluid transport within wax-printed channels. Upon pipetting an aqueous solution onto the sampling spot of a wax-printed paper channel, a large liquid droplet forms, contained by surface tension and hydrophobic interactions between wax and water, that feeds solution into the water-sorbing cellulose channel. Water is carried along the cellulose channel by capillary action, the phenomenon observed upon balance between adhesion of water molecules to cellulose fibers and cohesion between water molecules.[98,103-105] As the paper "wet-out process" occurs, fluid transport can be modeled using the Washburn equation, with the surface tension force encompassing adhesion and cohesion as measured by the water contact angles (SI contains equations).[103,106] Once the paper has been wetted, fluid transport is typically modeled by Darcy's law in terms of volumetric flow, with the pressure differential caused by the fluid droplet in the sampling spot acting like a water tower that supplies pressure head to a thirsty town downhill.[103-105]

Solutes within the water (i.e., amaranth dye, DOM, nanomaterials) can be drawn down the channel with the water phase, deposited onto the cellulose fibers, or drawn into the wax boundary layer by hydrophobic interactions. The travel distances of water soluble amaranth, $HAuCl_4$, and DOM applied to cellulose within 2 µL sample droplets were limited only by the fluid travel distance. This result, also observed elsewhere for soluble dyes,[78,102-103,107] indicates these species remain in the aqueous phase throughout transport, despite other forces that are present. These soluble species moved and accumulated at the end of the channels as samples were rinsed with 4 µL aliquots of nanopure water (**Figure SI. 4.5**). Additional 4 µL rinse steps did not fully remove the color of amaranth from the cellulose, indicating that although the amaranth dye has an affinity towards the aqueous phase, some dye also deposits within the cellulose.

The measured range of travel distances for amaranth over the course of a year varied from 1.7 to 3.3 cm with a mean of 2.3 cm and standard deviation of 0.5 cm. As these experiments were carried out on a lab bench, such variation was expected due to humidity, temperature, airflow, imperfections in the wax-printed paper, direction of cellulose fibers, inconsistent contact with the underlying substrate, and human error.[78,91] To account for day to day fluctuations in capillary flow, the measured nanoparticle travel distances were normalized to the measured travel of the amaranth dye. In essence, retention factors were calculated as traditionally used in paper chromatography, with amaranth dye acting as a tracer to record the distance of fluid travel.[108] Prior to such normalization, standard deviations were low for sets of the same sample conducted on the same day and high for sets conducted on different days. Once the normalization scheme was employed, average travel distances for each nanoparticle were comparable throughout the year.

Nanoparticle deposition patterns. As nanoparticles in aqueous solutions travel through wax-printed paper channels, they are influenced by the mobile phase (water), the stationary phase (cellulose), the channel boundaries (wax), the underlying substrate, and the overlying air (temperature, humidity, air flow). SERS spectral maps and 10× microscope images recorded more highly detailed images of the deposition patterns of the nanoparticles than could be obtained by camera or the naked eye, such that the underlying substrate on which the wax-printed channels lie was clearly shown to influence nanoparticle deposition in cellulose. Two microliters of 46 nm cit-AuNP were applied to wax-printed paper well-plates secured with tape to a given substrate (PTFE, polystyrene Petri dish, air, a second wax-printed paper, or fresh chromatography paper). Lack of tape to secure samples in place caused paper curling during solution drying, causing both contact with the underlying surface and cellulose fiber orientation to be inconsistent. Raman spectral maps were collected and the intensity of the 188-332 cm^{-1} peak (which results from Au(0)-Cl vibrational modes[109-111]) was tracked across the papers. Pixels were counted in Raman spectral maps for which white pixels occurred when the SERS intensity was greater than 50 CCD counts, and the results indicate that more nanoparticles were deposited on the upper layers of cellulose fibers in the sample secured on the PTFE surface than that on a Petri dish or suspended in air (**Figure 4.3**). The ability of PTFE to influence the flow pattern can be used to engineer substrates when one wishes to deposit nanoparticles in a desired location. Further nanoparticle transport experiments were conducted for wax-printed papers placed in polystyrene Petri dishes.

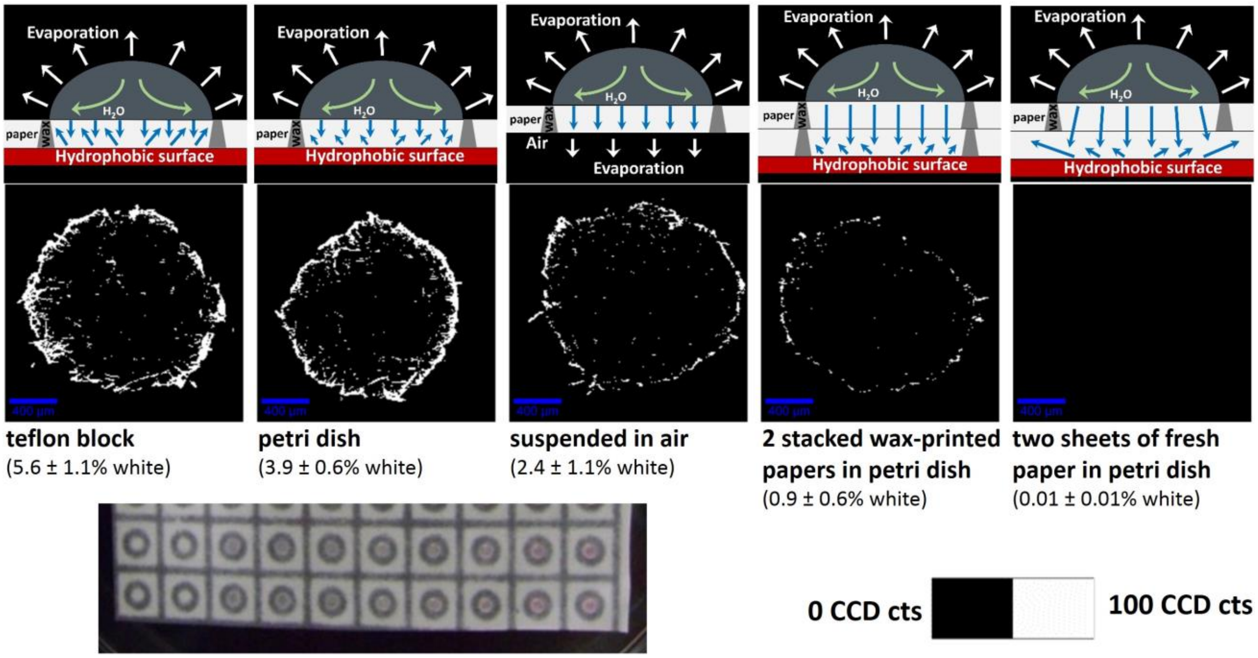

teflon block (5.6 ± 1.1% white)

petri dish (3.9 ± 0.6% white)

suspended in air (2.4 ± 1.1% white)

2 stacked wax-printed papers in petri dish (0.9 ± 0.6% white)

two sheets of fresh paper in petri dish (0.01 ± 0.01% white)

Figure 4.3. The location of 46 nm cit-AuNP deposition in wax-printed paper well-plates is influenced by the substrate on which paper is placed during AuNP application. A photograph of the wax-printed well-plate demonstrates the solutions are contained within the wax-printed circles (bottom left). White areas in the SERS spectral maps indicate 188-332 cm^{-1} SERS signals ≥ 50 CCD counts. The spatial scale bars represent 400 µm. White pixels in each Raman spectral map were counted for n=3 images with ImageJ software to demonstrate statistical differences in nanoparticle deposition for the differing underling substrates. Cartoons demonstrating hypothesized fluid flow within the drying droplet and cellulose are for each sample.

Raman spectral images were collected of the deposition patterns of an array of analytes to observe potential “coffee ring” artifacts of drying (**Figure 4.4**).[70] Two microliters of each sample were pipetted onto wax-printed microzone plates and allowed to dry for at least 10 minutes prior to imaging. These images are valuable references indicating the tendency of each analyte to a) associate with the wax phase, b) interact with cellulose fibers, or c) be influenced by the coffee ring effect as the water droplet dries. Cit-AuNP, amaranth, and DOM tend to deposit near the wax boundaries, a property that indicates affinity for the nonpolar wax phase or the influence of the “coffee ring” effect. Interestingly, the cetyltrimethylammonium bromide (CTAB) coated AuNR were able to transport to some degree into the wax boundary layer, but not completely through it. These particles also interacted closely with the cellulose fibers. The surfactant properties of CTAB would facilitate such affinity for both the wax and cellulose phases. Excess

CTAB in the AuNR solution formed a visible precipitate during the sample drying process that was recorded in microscope images. PEG coated AuNP coated cellulose fibers, and only appeared to be minimally influenced by the coffee ring effect. The hydrophobicity of the nanoparticle surface coating appears to play a significant role in tendency of the particles to transport into the wax, deposit on the cellulose, or be carried by water flow patterns within the droplet generated by drop drying.[70]

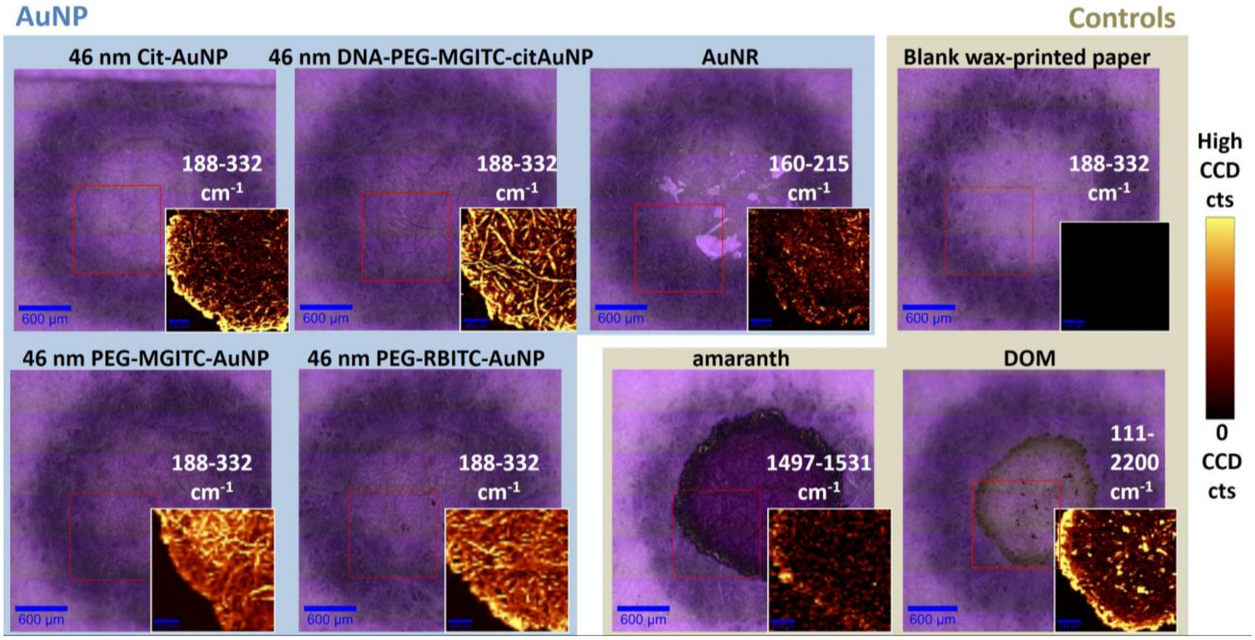

Figure 4.4. Analyte deposition patterns in wax-printed microzone papers were recorded with a Raman spectrometer. Example Raman spectra are indicated in **Figure 4.1**, with instrument parameters in **Table SI. 4.2**. The scale bar is not consistent for each analyte due to variations in peaks for which images were created, laser power variability, and differing aggregation states influencing SERS enhancement abilities of the nanomaterials. Analytes in the first row were imaged with a Raman intensity scale bar of 0-100 CCD counts, the first three samples in the second row with 0-500 CCD counts, and the fluorescence of DOM with 0-10000 CCD counts.

Additional microscope images, normal Raman spectral maps, and SERS spectral maps capture detailed information concerning the cellulose fibers and transport of solutes applied to the channels in aqueous solutions (**Figure 4.5** & **Figure 4.6**). Optical images clearly delineate the channels due to the black pigment within the wax-based ink. Normal Raman spectral images are capable of depicting the topography of the cellulose fibers by documenting the 1052-1171 cm^{-1} peak that occurs due to CC and CO stretching modes of cellulose.[112] Fluorescence is characteristically stronger and produces broader transitions than Raman vibrations and is known to completely overshadow Raman spectra and hinder typical analyses. This traditionally undesirable fluorescent signal can be seen clearly enough within a Raman spectral map to track deposition locations of algal cells, demonstrating their deposition just barely within the wax-printed paper channel inlet (Figure 4.5). Furthermore, the Raman spectrometer, with a 785 nm laser, is sensitive enough to record the normal Raman signals of the cellulose fibers beneath the fluorescence of the algal cells in the channels. Such capabilities will ultimately be useful for documenting the transport and deposition of fluorescent or Raman active species within µPADs.

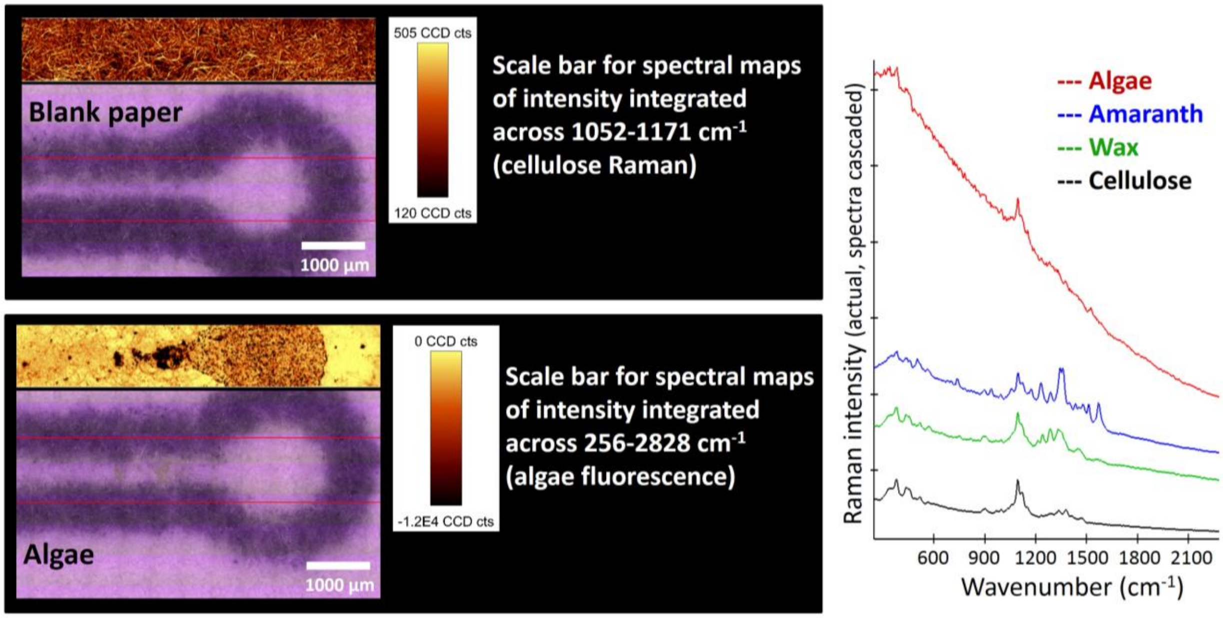

Figure 4.5. Normal Raman spectral maps image the topography of the cellulose fibers and deposition patterns of fluorescent species such as algal cells, even within the same wax-printed paper channel. Raman spectral images were collected with a 785 nm laser, 10× microscope objective, 300 groves/mm grating, approximately 40 mW of laser power, and 0.05 seconds per spectrum.

Deposition patterns of the nanomaterials were recorded with SERS, at a much lower laser power than required for normal Raman, demonstrating that amaranth dye and 41 nm PVP10K-AgNP partition towards the boundary layer, but farther along the length of the channels than the cit-AuNP or BSA-cit-AuNP (**Figure 4.6**). Hence, the amaranth and 41 nm PVP10K-AgNP have a higher affinity for both wax and water than cellulose fibers. The cit-AuNP and BSA-cit-AuNP remain in the center of the channels as they travel, maintaining minimum interaction with the wax boundary layer, as demonstrated by SERS spectral maps (**Figure 4.6**). Both the PVP and amaranth dye have nonpolar moieties within their molecular structures that interact with the wax. The carboxylic acid groups on citrate give it the ability to hydrogen bond with cellulose, and the BSA protein generally folds such that sufficient hydrophilic groups are exposed to the solution to make the molecule stable in water.[113-114] These hydrophilic functional groups would have a greater affinity for cellulose than the nonpolar wax boundary layer.

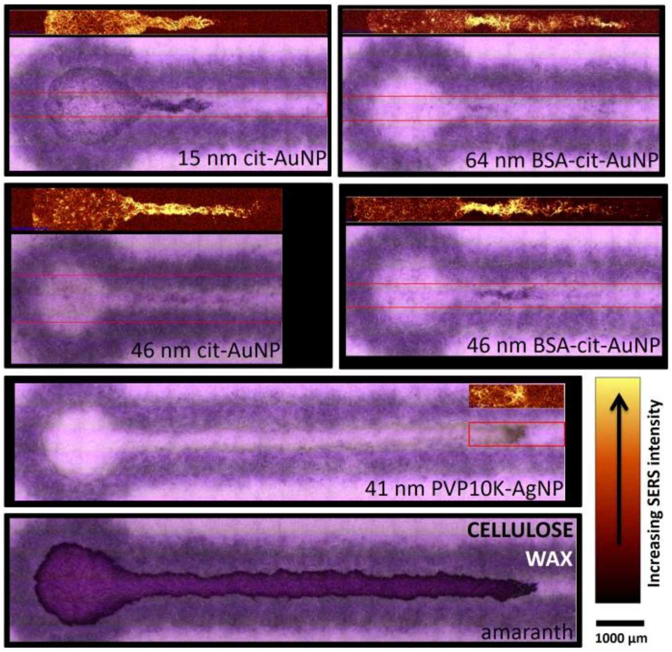

Figure 4.6. Microscope images (purple) and SERS spectral maps record nanoparticle drying patterns within narrow wax-printed channels of 0.8 mm channel widths. Optical images were collected with a 10× microscope objective. Raman spectral maps were collected with a 785 nm laser, < 1 mW of laser power, a 10× microscope objective, 300 grooves per mm grating, 0.05 seconds per spectrum, and a resolution of 5 µm per spectra in the lengthwise channel direction by 10 µm per spectra wide. Both PVP-AgNP and amaranth dye partition towards the wax layer as well as traveling far in the cellulose, demonstrated by wax-channel outlines of PVP-AgNP and amaranth captured in microscope images and Raman spectral maps.

Nanoparticle transport within wax-printed channels. Nanoparticle travel distances were a function of the nanoparticle surface coating, with cit-AuNP depositing in or near the sampling spot and PVP or PEG coated particles traveling further along the channel, but rarely as far as the amaranth dye (**Figure 4.7**). After the initial sample was added to the channel and allowed to dry (approximately 10-30 minutes), three rinses of 4 µL of nanopure water had no influence on the transport distance of any of the nanoparticles at any pH except the 8 nm PVP10K-AgNP particles that traveled similarly to amaranth after rinsing (**Figure SI. 4.6**).

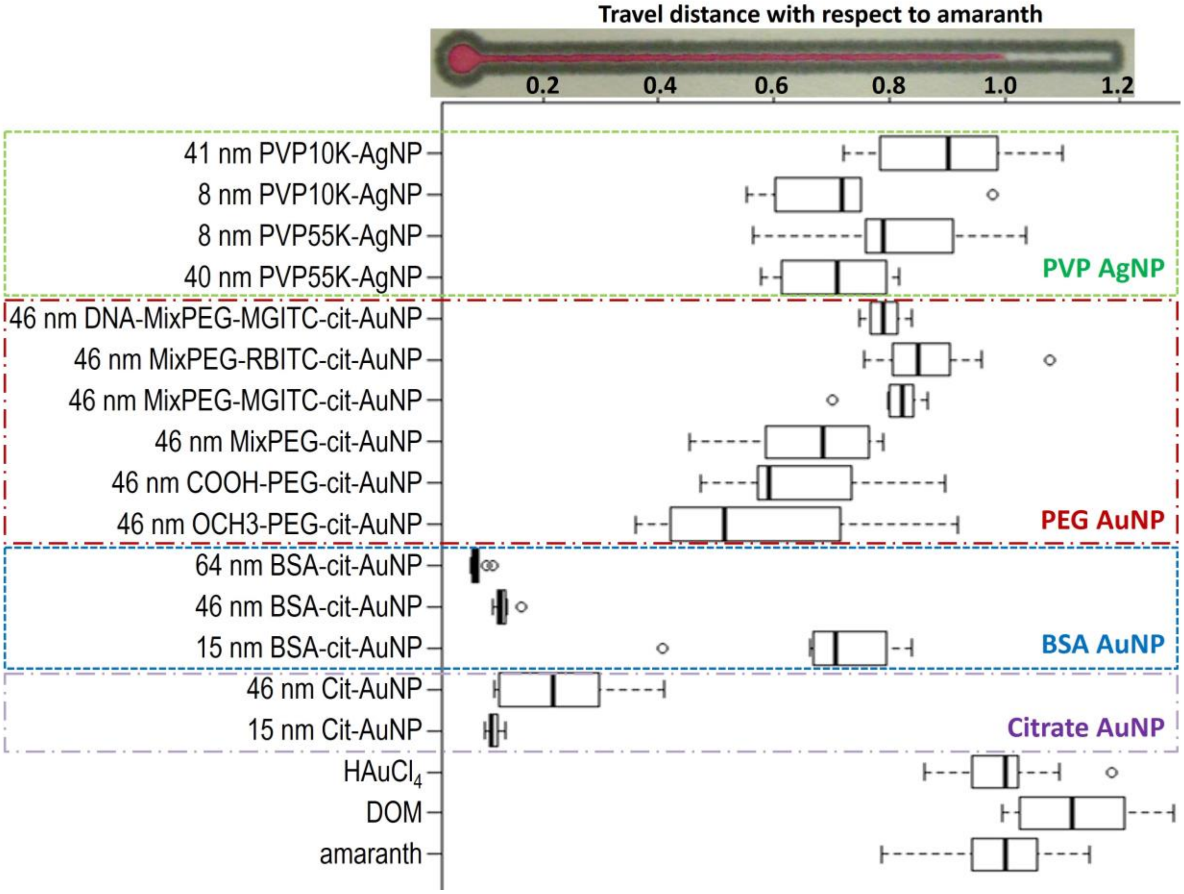

Figure 4.7. Nanoparticle transport distances without rinse steps in wax-printed channels on chromatography paper. The boxes represent the first and third quartile, with a bold line at the median. The smallest or largest sample measurement within 1.5 times the box size are represented by the whiskers.[115]

pH influence on nanoparticle transport. Amaranth, DOM, 15 nm cit-AuNP, and 15 nm BSA-cit-AuNP were tested at pH values of 3-10. Only the transport of 15 nm BSA-cit-AuNP was influenced by pH, depositing in or near the sampling spot at pH 3 and traveling half the length of the channel at pH 6-10 (**Figure 4.8**). BSA undergoes a structural conformation and zeta potential transition from positive at pH <4 to negative at pH >5.[113] Negatively charged particles repel negatively charged cellulose fibers,[94-95,116] but because opposite charges attract, the positively charged BSA particles (low pH) are instead deposited in the cellulose stationary phase. Nanoparticle travel depends upon pH only when the charge, conformation, or aggregation state of either interacting surface is a function of pH.[117] Although pH had no effect on the movement of 15 nm cit-AuNP, these particles aggregated at basic pH after five minutes of drying time as identified by a color change from bright red to purple within the paper.[74] Such aggregation may be desired for SERS applications of the 15 nm cit-AuNP within µPADs conducted with laser wavelengths above 600 nm.

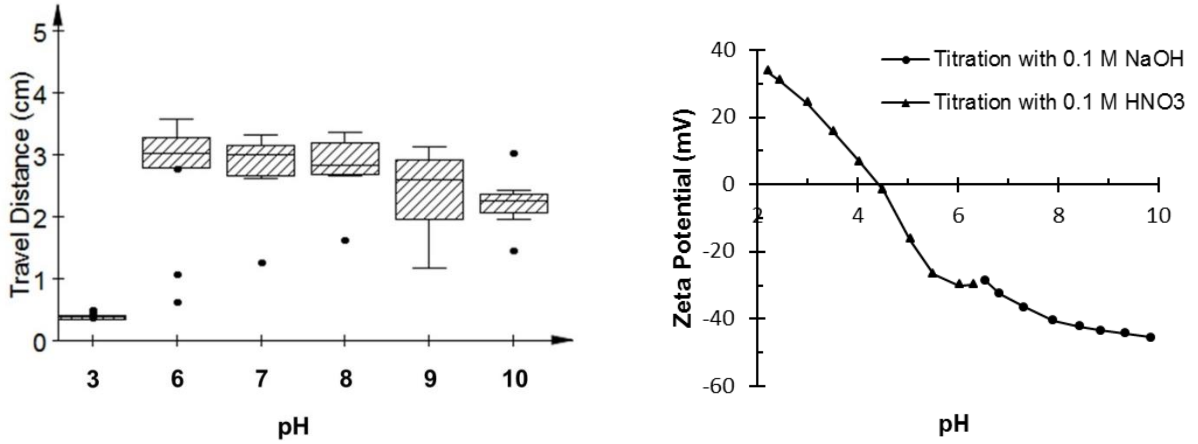

Figure 4.8. Travel distance (n=9) and zeta potential of 15 nm BSA-cit-AuNP as a function of pH. BSA-cit-AuNP were colloidally unstable at pH 4 and 5; therefore, they were not examined in the channels.

Forces influencing particle transport. Nanoparticle transport in cellulose is influenced by van der Waals, electrostatic, Lewis acid-base, and steric forces, as described by Derjaguin, Landau, Verwey, and Overbeek theory (DLVO) and extended DLVO (xDLVO).[118-121] DLVO provides a way to quantify interactions between colloids and surfaces as a function of distance, with insight into Lifshitz-van der Waals and electrostatic colloidal interactions when perspective is maintained on the potentially faulty assumptions that surfaces are smooth and the particles are spherical, the pitfalls of calculating surface potential from zeta potential, and subjective estimates of the Hamaker constant.[87,94,119-120,122-125] xDLVO extends the analysis to include terms for Lewis acid-base and steric interactions, at the cost of simplicity and established experimental techniques to parameterize models for nanoparticles with thick surface coatings. DLVO calculations have been valuable in colloid science for modeling coagulation and flocculation, membrane fouling, immobilization of proteins, deposition of TiO_2 dyes in paper pulp, and transport of colloids in nanofluidic devices, and thus provide insight into Lifshitz-van der Waals and electrostatic forces between noble-metal nanomaterials and µPADs.[71,126-128]

Electrostatic and van der Waals forces. Estimates of Lifshitz-van der Waals and electrostatic colloidal interactions were computed using measured zeta potential and particle sizes (TEM core size and DLS hydrodynamic diameter) alongside estimated Hamaker constants and ionic strength (SI contains details). Correlations between core size, coating thickness, hydrodynamic diameter, zeta potential, ionic strength, or conductivity and nanoparticle transport distance did not exist. However, as expected, particles that traveled minimally in the cellulose channels had low primary maximum DLVO interaction energy barriers between the nanoparticle and cellulose (**Figure 4.9**). Particles with high primary maximum values were expected to resist interaction with cellulose and instead travel far with the mobile aqueous phase. Despite imprecise and widely varying ionic strength estimates, extrapolation of surface potential from zeta potential, and lack of precise Hamaker constant approximations, only the PVP-AgNPs dramatically depart from this trend. Furthermore, DLVO suggests that once a particle overcomes the primary maximum, deposition is irreversible.[94,119] Irreversible deposition was observed in that the nanoparticles (excluding 8 nm PVP10K-AgNP) could not be rinsed down the channel like the amaranth dye after the initial drying period.

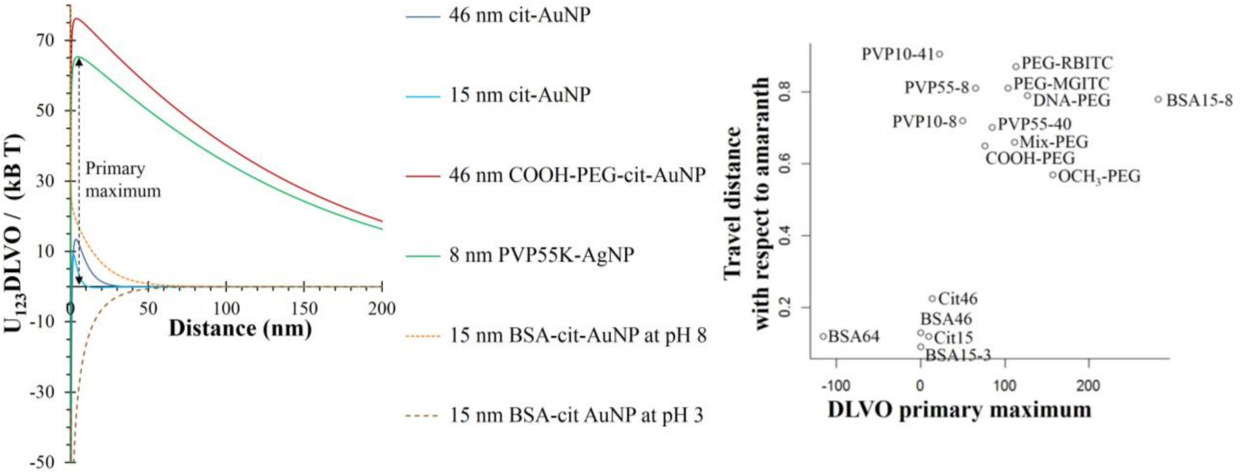

Figure 4.9. DLVO interaction energies for a nanoparticle approaching a cellulose surface were compared to travel distance. Nanoparticles that do not travel in wax-printed cellulose have low DLVO interaction energy barriers. Low ionic strength in nanoparticle solutions that include centrifugation steps and re-suspension in water causes broadening and an increase of the primary maximum due to extension of the electrical double layer about the particle.[94] For particle coatings considered thicker than the range of van der Waals forces (estimated from TEM images, hydrodynamic diameter measurements, and coating molecular weights), Hamaker constants of the coating were employed rather than the metal core (all particles except cit-AuNP).[119] Additional DLVO plots and discussion of Hamaker constants are included in the SI.

Lewis acid-base interactions. Forces that influence transport but are not included in traditional DLVO theory include Lewis acid-base forces and steric hindrances.[118-119,129] Lewis acid-base affects arise from polar interactions and encompass the terms “hydrophobic interaction” and “hydration pressure” often used to explain forces that cause particles to contradict DLVO.[118] Although Lewis acid-base interactions decay exponentially in aqueous solutions at a decay length of 0.1 nm, they can be stronger than electrostatic and van der Waals forces by two orders of magnitude.[118] As described by van Oss, the distinction between dipole-dipole interactions (Lifshitz-van der Waals component of DLVO) and electron-donor-electron-acceptor (Lewis acid-base component of xDLVO) interactions is oftentimes blurry.[118] PEG has been characterized to have strong dipole interactions, strong dispersion forces, and only moderate hydrogen bonding when considered as a stationary phase for chromatography.[130] Thus, the contribution of xDLVO forces for PEG are not expected to be as strong as for nanoparticle coatings that exhibit strong hydrogen bonding. PVP tends to form hydrogen bonds when mixed with polymers such as polystyrene sulfonic acid with available –OH groups, and has also been proven to hydrogen bond with cellulose through the carbonyl group.[131-134] However, the PVP-AgNP does not deposit in the cellulose, but instead travels with the aqueous phase. Thus other forces are at play, such as the predicted electrostatic repulsion, the observed affinity of PVP-AgNP for the wax phase, and the observed affinity of PVP-AgNP for the water phase (**Figure 4.6**).

Steric forces. Steric repulsion is defined by Prime and Whitesides in terms of 1) compression of a polymer coating upon contact with a second particle or surface and 2) solvent expulsion from a polymer layer upon compression.[135-136] Steric repulsion is frequently cited as an important stabilizing force for polymer coated nanoparticles, especially for PEG and PVP coatings.[87,123,136-138] xDLVO has improved estimates of attachment efficiency for a variety of polymer coated nanoparticles by adding a term encompassing electrosteric repulsion and the decrease of friction force obtained using Oshima’s soft particle analysis, and these improvements were observed despite the use of particle core Hamaker constants to describe particles with 0.7-70 nm coatings, thicknesses beyond the typical range of van der Waals attraction.[87,119,122,139] Considering the definition of steric repulsion given by Jeon and Prime, the comparative compressibility of PVP and PEG likely causes the observed difference in DLVO fit.[135-136] The pyrrole ring in PVP makes it a much more rigid molecule than PEG, such that compression of PVP is a more energy intensive process for PVP than PEG.[138,140] This idea is discussed in terms of polyethylene oxide by Jeon et al.; much like a rubber ball, surface compression of a polyethylene oxide coating on a nanomaterial surface acts to spring proteins away upon approach.[135] Furthermore, PVP polymers blended with PEG also generally transmit water vapor and have higher swellability,[141] suggesting that PVP coatings are less accessible to any constituents of the water phase and that more energy would be required to expel upon compression any water that did make it into the PVP coating. Therefore, a steric term is expected to increase the primary maximum for PVP to a larger extent than any of the other coatings.

FUTURE OUTLOOK

µPADs offer rapid detection of a wide array of analytes in a portable, cheap, and effective manner, often employing nanomaterial based signal output. Imaging and understanding nanomaterial transport characteristics within µPADs will facilitate production of nanoparticle based µPADs. Raman spectroscopy and SERS provide an ideal tool for tracking analytes, reagents, and noble-metal nanoparticles in paper, polymer, or surface coatings, and it will continue to be useful as nanomaterials are incorporated into products that reach all aspects of our lives. The most reproducible results for µPAD field deployable diagnostics will be conducted in well contained devices, in which user error and sample deposition inconsistencies are minimized. Although the core identity remains important for a toxicity endpoint because, for example, silver ions are known to leach from AgNP, it is clear that nanoparticle surface coatings heavily influence particle deposition in a cellulose matrix. For particles with thick coatings that make up the bulk of the nanoparticle, especially when thicker than the range of van der Waals forces, DLVO theory best explains expected van der Waals and electrostatic forces when nanoparticles are modeled as if they were composed of their surface coatings rather than their metal cores. Better estimates of model inputs (such as Hamaker constant) that are difficult to measure must be developed to improve the accuracy of transport models, and thus to aid in development of µPADs employing nanomaterials for detection or separation.

ACKNOWLEDGEMENTS

This work was supported by an AWWA Abel Wolman graduate research fellowship to R.H.L. and research grants from the Bill and Melinda Gates Foundation and the Virginia Tech Institute for Critical Technology and Applied Science (ICTAS). We thank Dr. Weinan Leng, Dr. Matt Hull, and Jason Jones for particle synthesis and characterization and Matt Chan for DLVO insight and spreadsheets.

SUPPORTING INFORMATION

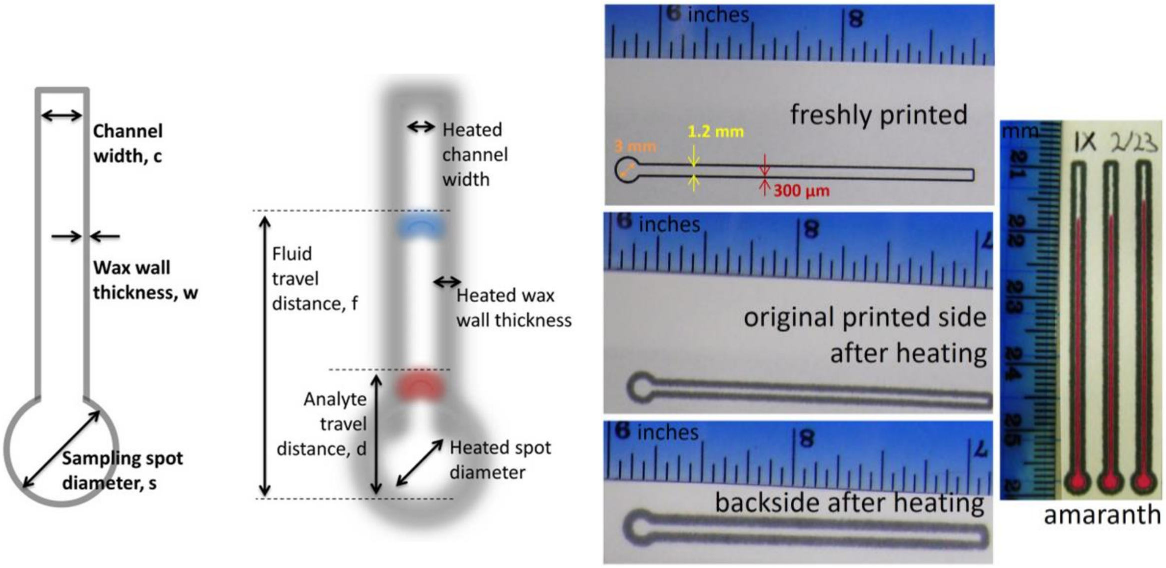

Figure SI. 4.1. The µPAD dimensions describe measurements designed in Adobe Photoshop software (left). Heating the papers to re-flow the wax caused lateral as well as axial wax spreading, creating narrower channels in the tested µPADs than the original printed dimensions. Photographs of printed, heated µPADs containing amaranth dye demonstrate the ability of wax to contain aqueous solutions (right).

Table SI. 4.1. Nanoparticle synthesis procedures.

Particle	**Synthesis Method**	**Synthesized by**	**Refs.**
15 nm Cit-AuNP	Spiked 10 mL of 38.8 mM sodium citrate into 100 mL of hot 1 mM $HAuCl_4$ and reflux until particles form.	M. Hull at Virginia Tech	79-81
46 nm Cit-AuNP	Spiked 1.6 mL of absorbance 3.0 15 nm Cit-AuNP seeds and 0.44 mL of 38.8 mM sodium citrate into 100 mL of hot 0.254 mM $HAuCl_4$. Reflux until particles form (1 hr).	M. Hull at Virginia Tech	80-82
15, 46, 64 nm BSA-cit-AuNP	Spike 0.1 mg BSA per mL of the appropriate size of Cit-AuNP.	M. Hull at Virginia Tech	80-81,83
46 nm MixPEG-cit-AuNP	Added dropwise 1 µM HS-PEG-COOH to 46 nm Cit-AuNP to achieve 3000 COOH-PEG molecules per AuNP. Particles were then mixed for 15 minutes before adding excess 10 µM HS-PEG-OCH_3 to achieve 16000 OCH_3-PEG molecules per AuNP. After mixing for an additional 15 minutes, AuNP were centrifuged and washed several times to remove excess PEG. The OCH_3-PEG coated 46 nm AuNP (46 nm OCH_3-PEG-cit-AuNP) and COOH-PEG coated 46 nm AuNP (46 nm COOH-PEG-cit-AuNP) were prepared similarly as 46 nm MixPEG-cit-AuNP except that a single type of PEG was used at a concentration of 19000 PEG molecules per AuNP.	W. Leng and R. Lahr at Virginia Tech	Leng unpublished results, 84
46 nm PEG-MGITC-cit-AuNP and 46 nm PEG-RBITC-cit-AuNP	Added 300 dye molecules per AuNP via syringe to a vortexing tube of 46 nm Cit-AuNP, incubation overnight at 4°C, and pegylation as described previously.	W. Leng at Virginia Tech	84
46 nm DNA-PEG-MGITC-cit-AuNP	Added 50 µL of 4 mg/mL EDC in PBS and 55 µL of 10 mg/mL sulfo-NHS in PBS to 1 mL of 10^{10} 46 nm PEG-MGITC-AuNP in PBS buffer. Twelve nmol of oligonucleotide were then added in 200 µL to the AuNP solution before shaking overnight at room temperature, protected from light. Excess reagents were removed by centrifugation (5 rounds at 10000 × g for 10 minutes each). All PEG coated AuNP were stored in the dark at 4°C in 50% (v/v) ethanol-water solutions and re-suspended in nanopure water before use.	W. Leng at Virginia Tech	84
46 nm PEG-Peptide-cit-AuNP	A 0.1 mL spike of 380 µM peptide was added to 50 mL of 46 nm Cit-AuNP to achieve 10000 peptides per AuNP. After stirring for 2 hours at room temperature, 100 µM OCH3-PEG-HS was added to a molar ratio of 9000 PEG molecules per AuNP. The solution was incubated at room temperature overnight.	W. Leng at Virginia Tech	84
36 nm EDTA-AgNP	Vigorously shook a mixture containing 100 mL of 0.16 mM EDTA and 4 mL of 0.1 M NaOH spiked with 1 mL of 26 mM $AgNO_3$.	M. Hull at Virginia Tech	80,89
8 nm PVP10K-AgNP and 8 nm PVP55K-AgNP	PVP (1.5 g of 10 kDa or 55 kDa) was dissolved in 280 mL water, mixed with 9 mL of 0.1 M $AgNO_3$, stirred 5 min, spiked with 11 mL of 0.08 M ice-cold sodium borohydride, and centrifuged to remove excess reagent.	Purchased from Liu Lab at Duke	86-87
41 nm PVP10K-AgNP and 40 nm PVP55K-AgNP	PVP was dissolved in ethylene glycol (1.5 g of 10 kDa in 75 mL or 20 g of 55 kDa in 50 mL), mixed with $AgNO_3$ (0.05 g or 1.5 g), heated under stirring (120°C for 1 hr or 140°C for 24 hr), and dialyzed or centrifuged to remove unbound species.	Lui lab at Duke, Luna Innovations (Blacksburg, VA)	80,86,88-89
AuNR	$HAuCl_4$ was mixed with CTAB and reduced with sodium borohydride to produce 1.5 nm spherical AuNP. AuNP were further grown in the presence of CTAB, $AgNO_3$, $HAuCl_4$, and ascorbic acid overnight at 33 ºC. Centrifugation removed excess CTAB.	J. Jones and M. Hull at Virginia Tech	85

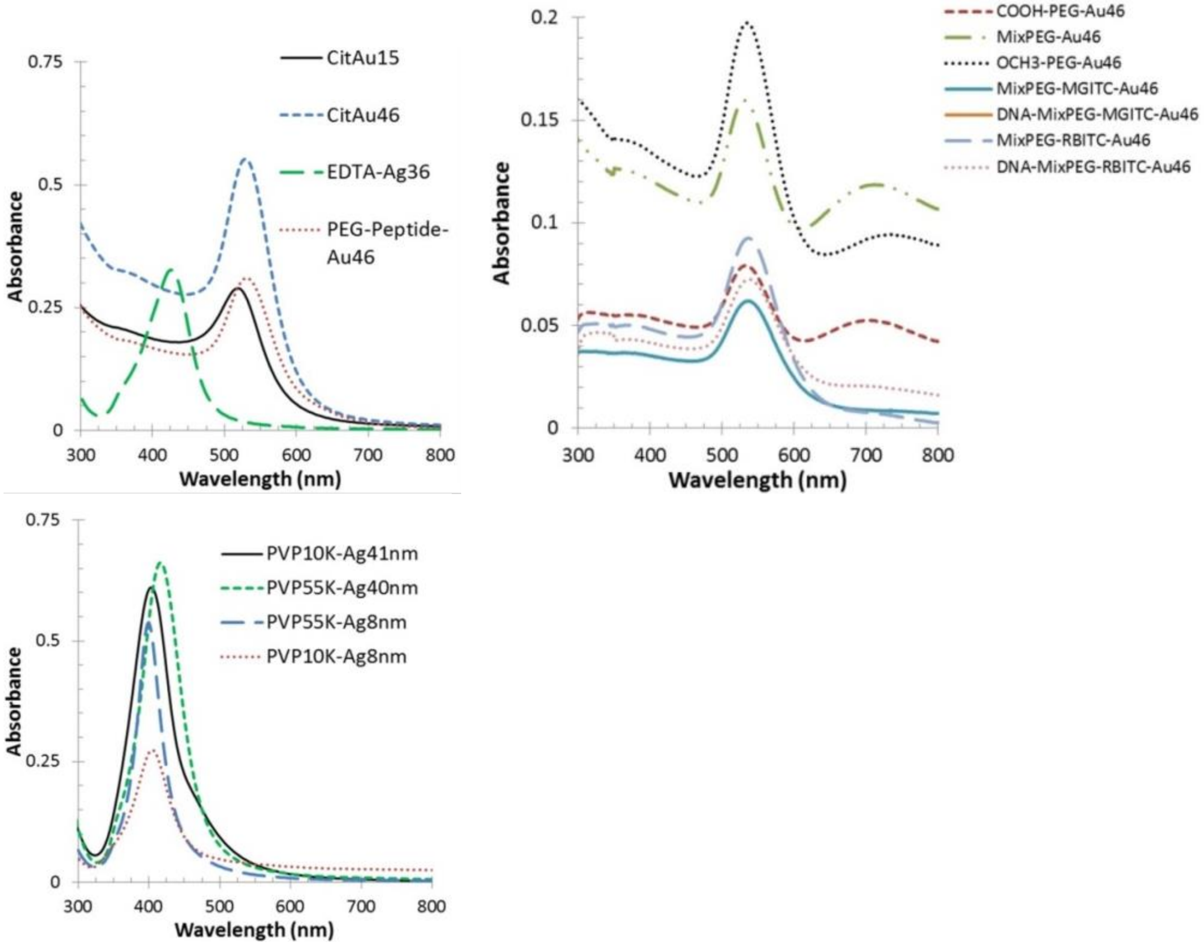

Figure SI. 4.2. UV-Vis spectra of aqueous nanoparticle solutions.

Table SI. 4.2. Specific instrument parameters used to collect Raman and SERS spectra of each analyte are indicated. All spectra were collected in paper with a 785 nm laser, 300 grooves per mm grating, and 10× microscope objective.

Sample	**Acquisition time (seconds)**	**Number of averaged spectra**	**Approximate laser power (mW)**
Cellulose	1	10	>100
Wax melted on paper	1	10	>100
Amaranth	1	10	> 100
15 nm Cit-AuNP	0.05	120000 spectra over a 6000 µm × 1000 µm Raman spectral map	< 0.3
46 nm Cit-AuNP	0.01	145000 spectra over a 7000 µm × 1000 µm Raman spectral map	< 0.3
DNA-PEG-MGITC-cit-AuNP	0.01	40000 spectra over a 2000 µm × 2000 µm Raman spectral map	< 5
AuNR	0.01	40000 spectra over a 2000 µm × 2000 µm Raman spectral map	< 5
46 nm PEG-MGITC-cit-AuNP	0.01	2500 spectra over a 1000 µm × 1000 µm Raman spectral map	< 25
46 nm PEG-RBITC-cit-AuNP	0.01	2500 spectra over a 1000 µm × 1000 µm Raman spectral map	< 25
46 nm BSA-cit-AuNP	0.05	80000 spectra over a 8000 µm × 500 µm Raman spectral map	< 0.6
64 nm BSA-cit-AuNP	0.05	80000 spectra over a 8000 µm × 500 µm Raman spectral map	< 0.6
41 nm PVP10K-AgNP	0.05	20000 spectra over a 2000 µm × 500 µm Raman spectral map	< 0.6

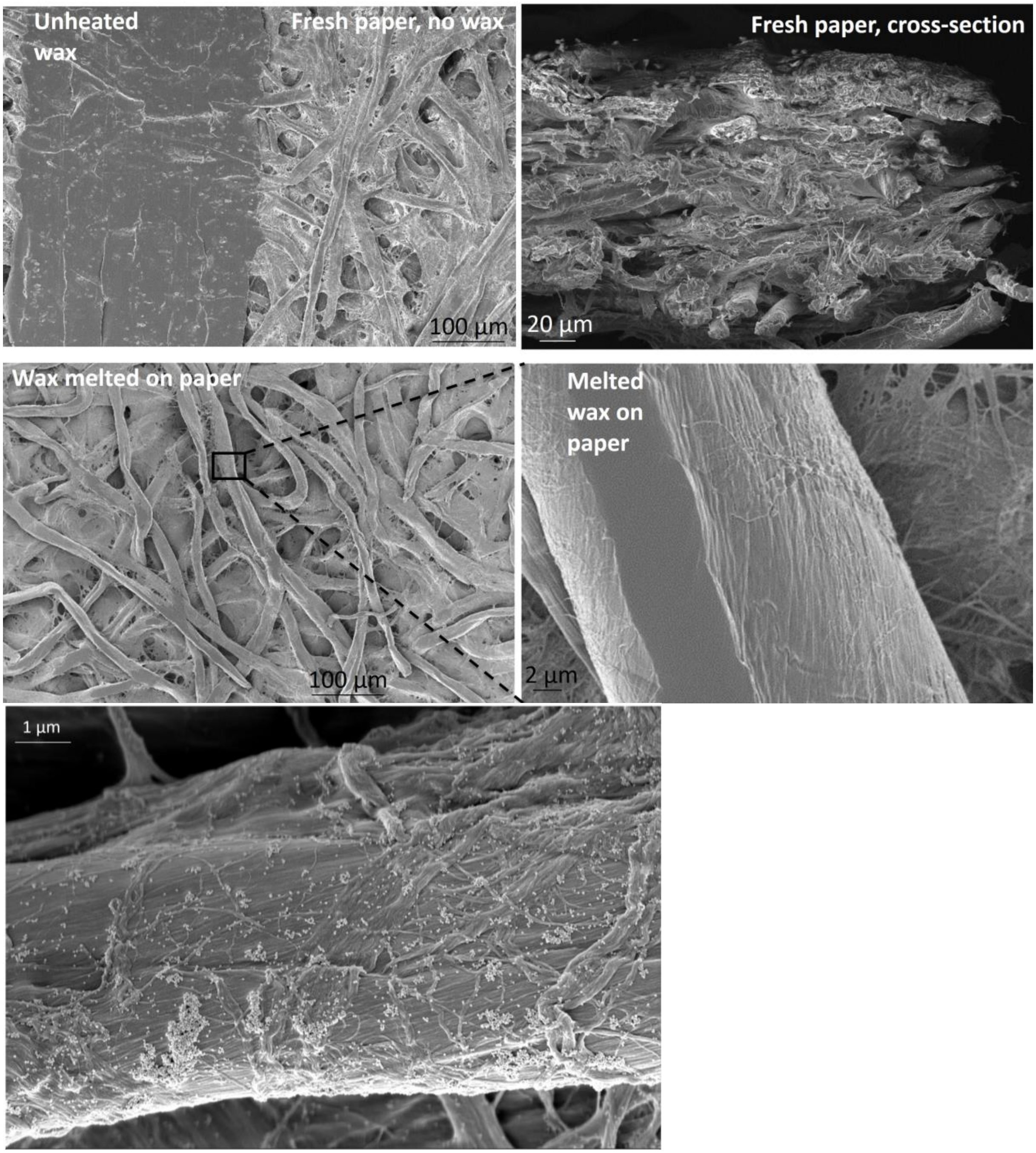

Figure SI. 4.3. FE-SEM images of Whatman grade 1 chromatography paper before and after heating including a) an un-heated wax-printed paper, b) a cross-section of chromatography paper without wax (sample frozen in liquid nitrogen, cut with a cold scalpel blade while still frozen, mounted onto an SEM stub, and sputter coated with Au for analysis), c) melted wax on paper, d) a close-up image of a wax-coated cellulose fiber, and e) a cellulose fiber on which 40 nm cit-AuNP were deposited. The relative scale of the nanomaterials with respect to the "sinusoidal corrugated" cellulose fiber surface, assumed to be smooth and flat by the DLVO model, is demonstrated.[94]

Table SI. 4.3. Possible peak assignments for Raman peaks displayed by melted wax ink. The phase changing ink likely contains carbon black pigment and a hydrophobic hydrocarbon mixture or polymer.[78,99-101]

Peak (cm^{-1})	**Molecular Vibration**	**Reference**
569	Ring vibrations, NO_2, nitric acid esters, aromatics	[29,142]
746	Ring breathing mode, CH deformation, CC, earth wax	[29,143]
818	C-C stretching, cyclohexane, ring vibration	[29,142]
889	Methylene rocking, cyclopentane, ring vibration, CH_2, COC, unsaturated and saturated waxes	[29,142-143]
904	C-O-C, ring vibrations	[29,142]
1213	Aromatic stretching, C-N stretching, methyl rocking, COC, C=C-O-C	[29,142]
1241	C=C-O-C, COC, phosphate, NO_2,	[29,142]
1287	Aromatics, nitric acid esters, pyrimidine bases, phosphodiesters	[29,142]
1333-1351	Carbon black, branched hydrocarbon chains, phenyl, CH_3, CH_2, CH, NO_2	[29,144-145]
1454	CH_3 and CH_2 modes, phospholipids, cyclopentane derivatives, unsaturated and saturated waxes	[29,142-143,146]
1564	COO-, purine bases, ring breathing modes, N-NO_2	[29,142]
1580	Carbon black	[144-145]

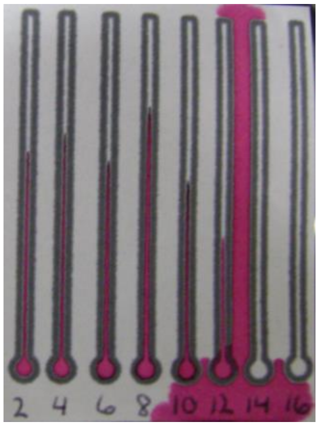

Figure SI. 4.4. Wax-printed paper channels (1.2 mm channel width, 0.3 mm wax walls, and 3 mm sampling spots, original printed side up in a Petri dish) typically contained amaranth solutions up to a volume of 12 µL.

Table SI. 4.4. Contact angle (degrees) measurements for wax on cellulose.

	Advancing Contact Angle (°)		Receeding Contact Angle (°)	
	dry sample	pre-wetted sample	dry sample	pre-wetted sample
Black Wax	113±6		94±7	
Unheated wax-printed paper	113±2	110±2	99±2	92±4
Heated wax-printed paper, original printed side	142±3	106±24	115±22	92±7
Heated wax-printed paper, back of paper	138±1	117±5	107±1	96±2
Paper (no wax)	0	0	0	0

Modeling fluid flow in uPADs.

Washburn equation
(for modeling the wet-out process)[103,106]

$$L^2 = \frac{\gamma D t}{4\mu}$$

L = distance fluid front has moved
γ = surface tension
D = average pore diameter
t = time of travel
µ = viscosity

Darcy's Law
(for modeling wetted paper)[103-105]

$$Q = \frac{\kappa W H}{\mu L} \Delta P$$

Q = volumetric flow
K = paper permeability to the fluid
WH = channel area perpendicular to flow
ΔP = pressure differential over length, L
µ = viscosity

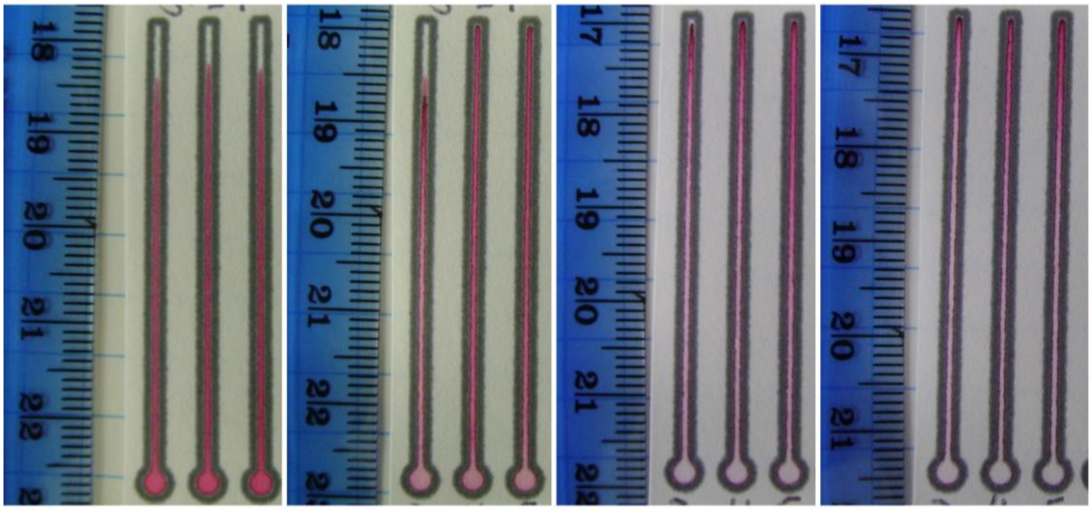

before rinse 4 µL rinse 2 x 4 µL rinse 3 x 4 µL rinse

Figure SI. 4.5. Amaranth dye deposited within the sampling spot (2 µL) travels with the aqueous phase through the paper. After at least 10 minutes of drying time and a 4 µL water rinse placed in the sampling spot, the amaranth is rinsed further along the channel. Additional rinse steps further concentrate the amaranth dye at the end of the channel.

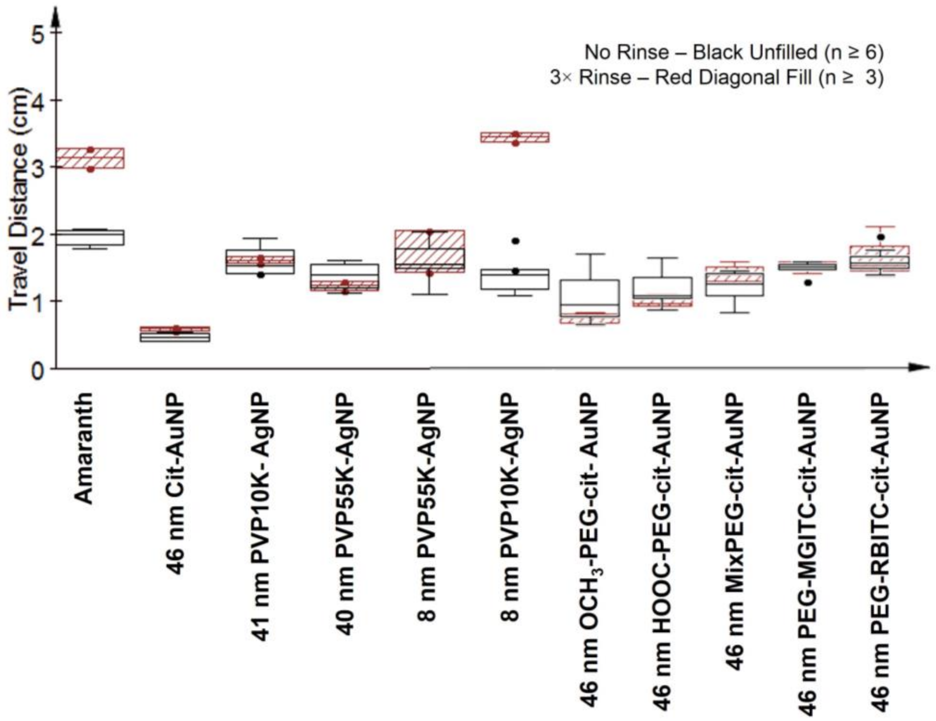

Figure SI. 4.6. Rinsing three times with 4 µL of nanopure water (12 µL total) had no influence on nanoparticle travel distances except for 8 nm PVP10K-AgNP.

DLVO calculations

DLVO calculations were conducted to examine the attractive and repulsive forces between each nanoparticle and the cellulose surface using zeta potential, hydrodynamic diameter, Hamaker constants estimated from literature values, and ionic strength estimated from conductivity and reagent concentrations employed during synthesis (**Table 4.1**, **Table SI. 4.5**, **Table SI. 4.6**, & Table SI. 4.7).[119,147]

Eqn 1 Lifshitz-van der Waals interaction:

$$U_{123}^{LW} = -\frac{A_{123}a_1}{6h}\left(1+\frac{14h}{\lambda}\right)^{-1}$$

Eqn 2 Electrostatic interaction:

$$U_{123}^{EL} = \pi\epsilon_r\epsilon_0 a_1\left[2\zeta_1\zeta_3\ln\left(\frac{1+e^{-\kappa h}}{1-e^{-\kappa h}}\right)+(\zeta_1^2+\zeta_3^2)\ln(1-e^{-2\kappa h})\right]$$

Eqn 3 Inverse Debye length:

$$\kappa = \sqrt{\frac{2N_A e^2\sum c_i z_i^2}{\epsilon_r\epsilon_0 k_B T}}$$

Table SI. 4.5. DLVO model parameters.

Eqn	**Description**	**Symbol**	**Value**	**Units**
U_{123}^{LW}	Hamaker constant between particle surface 1 and flat plate surface 3 separated by aqueous medium 2	A_{123}	estimated	N m
	Radius of particle (surface) 1	a_1	Measured hydrodynamic diameter (z-average)	m
	Distance between surface 1 and surface 1	h	variable	m
	Characteristic wavelength of the dielectric	λ	0.0000001	m
U_{123}^{EL}	Pi	π	3.141592654	
	Permittivity of the vacuum	ε_0	8.85×10^{-12}	F m
	Relative dielectric constant for water @ T (298 K)	ε_r	78.5	
	Surface (zeta) potential of particle surface 1	ζ_1	measured	N m/C
	Surface (zeta) potential of flat plate surface 3 (cellulose, lit value)[94-95]	ζ_3	-0.0377	N m/C
K	Avogadro's Number	N_A	6.022×10^{23}	mol -1
	Elementary charge	e	1.602×10^{-19}	C
	Ionic strength estimated from conductivity[148]	$\Sigma c_i z_i^2$	measured	mol/m^3
	Boltzmann's Constant	k_B	1.381×10^{-23}	J/K
	Temperature	T	298	K
	Inverse Debye length	κ	calculated	m^{-1}

Ionic strength

Nanoparticles are typically incorporated into µPADs immediately after synthesis, such that ionic strength is not directly controlled. However, ionic strength in nanoparticle solutions varies drastically depending upon the synthesis procedure employed. For instance, the reaction flask in which 15 nm cit-AuNP are produced contains 4 mM Cl^-, 3.9 mM Na^+, and 3.9 mM citrate in addition to Au, while PVP-AgNP involve centrifugation steps to remove excess reagents. Hence, ionic strength values were inferred from reagents used and synthesis protocols as well as conductivity measurements converted to ionic strength with a pre-factor of 1.27×10^{-6}.[148] The two values were compared to determine reasonable DLVO inputs (**Table SI. 4.6**).

Table SI. 4.6. Ionic strength was estimated from conductivity measurements, synthesis protocols, and reagent concentrations.

Sample	**Conductivity (mS/cm)**	**Ionic strength from pre-factor (mM)**	**Ionic strength from synthesis procedure (mM)**	**Ionic strength used for DLVO (mM)**
15 nm cit-AuNP	0.4	0.5	<13	0.5
46 nm cit-AuNP	0.3	0.4	<2	0.3
15 nm BSA-cit-AuNP			<13	0.5
46 nm BSA-cit-AuNP	0.2	0.2	<2	0.3
64 nm BSA-cit-AuNP	0.2	0.2	<2	0.3
46 nm OCH_3-PEG-cit-AuNP	0.002	0.002	0	0.007
46 nm COOH-PEG-cit-AuNP	0.002	0.003	0	0.007
46 nm OCH_3/COOH-PEG-cit-AuNP	0.002	0.003	0	0.007
46 nm MixPEG-MGITC-cit-AuNP	0.02	0.02	0	0.007
46 nm MixPEG-RBITC-cit-AuNP	0.004	0.005	0	0.007
46 nm DNA-MixPEG-MGITC-cit-AuNP	0.009	0.01	0	0.007
40 nm PVP10K-AgNP			0	0.007
40 nm PVP55K-AgNP			0	0.007
8 nm PVP55K-AgNP			0	0.007
8 nm PVP10K-AgNP			0	0.007

Hamaker constants

Hamaker constants were calculated with a combining relations equation,

$$A_{132} = (A_{11}^{0.5} - A_{33}^{0.5})(A_{22}^{0.5} - A_{33}^{0.5})$$

and literature values (**Table SI. 4.7**).[119] It is understood that the combining relations equations breaks down in aqueous systems for which non-dispersive forces dominate, but alternatives require parameters that are not widely available.[119,124]

Table SI. 4.7. Hamaker constant DLVO inputs. A_{11} represents the Hamaker constant of medium 1 interacting with itself across a vacuum. A_{132} was computed with the equation $A_{132} = (A_{11}^{0.5} - A_{33}^{0.5})(A_{22}^{0.5} - A_{33}^{0.5})$ and represents the Hamaker constant of medium 1 interacting with medium 2 across medium 3.[119,124]

Medium	**Hamaker constant A_{11} or A_{132} (J)**	**Used to create Figure 4.9 for the indicated nanoparticles**	**Reference**
Water	3.7×10^{-20}		119
Cellulose	8.4×10^{-20}		90,149-150
Au bulk	4.5×10^{-19}		151-153
Ag bulk	4.0×10^{-19}		151-152
10 nm AgNP	2.1×10^{-19}		154
50 nm AgNP	1.6×10^{-19}		154
Polymer (general estimate)	6×10^{-20}		155-156
BSA	2×10^{-20}		157-159
DNA	6.8×10^{-20}		160-161
$A_{\text{cellulose-water-AuNP}}$	4.69×10^{-20}	Cit-AuNP	calculated
$A_{\text{cellulose-water-AgNP40nm}}$	1.97×10^{-20}		calculated
$A_{\text{cellulose-water-AgNP8nm}}$	2.58×10^{-20}		calculated
$A_{\text{cellulose-water-polymer}}$	5.1×10^{-21}	PVP-AgNP, PEG-cit-AuNP	calculated
$A_{\text{cellulose-water-BSA}}$	-5.0×10^{-21}	BSA-cit-AuNP	calculated
$A_{\text{cellulose-water-DNA}}$	6.7×10^{-21}	DNA-PEG-cit-AuNP	calculated

We note that when Hamaker constants for bulk materials were applied rather than Hamaker constants of the surface coatings, several particles contradicted DLVO predictions, placing them in the upper left corner of **Figure 4.9**, including 15 nm BSA-cit-AuNP at pH >6 and PVP-AgNP. At pH >6 BSA-cit-AuNP have a positive surface charge, such that electrostatic forces between the particles and cellulose are attractive; therefore, travel of the nanoparticles is prevented in the negatively charged cellulose (**Figure 4.9**).[94-95,116] However, at pH >6, the zeta potential of BSA-cit-AuNP is negative, and the particles travel with the aqueous mobile phase rather than immediately depositing in the cellulose. The DLVO model does not predict the dramatic difference in transport distance for pH 3 vs. pH 6 BSA-cit-AuNP, suggesting that non-DLVO forces such as Lewis acid-base interactions or steric interactions are significant.

Although it is typical to apply the Hamaker constant of the bulk metal core material rather than the nanoparticle itself or the surface coating when computing van der Waals interaction energies, DLVO calculations were evaluated using both the metal core Hamaker constants as well as that of the surface coating material for three reasons. First, in colloidal systems for which DLVO was developed, it was typically safe to assume that the bulk material was that of the particle core;[119] however, for nanomaterials on the order of 15-64 nm with surface coatings nearly doubling the hydrodynamic diameter, the metal core comprises much less than 50% of the particle volume, and cannot be considered the "bulk". Second, Hamaker constant estimates require knowledge of the wavelength dependent dielectric value for each media.[90,119] AuNP and AgNP do not have the same dielectric properties as their bulk counterparts; therefore, Hamaker constant values are expected to be different. The Hamaker constants as a function of nanoparticle size estimated by Pinchuk were used for AgNP, but these values have not been previously computed for AuNP.[154] Third, Hamaker constants model van der Waals forces that work across short distances, and although it is generally assumed that the van der Waals forces due to the stabilizing coating are negligible at large distances, at a separation distance equal to the coating thickness the properties of the coating dominate.[119] The particle coatings analyzed herein are not trivial in size, as demonstrated by their molecular weights and the final hydrodynamic diameters (**Table 4.1**).

A negative Hamaker constant for the interaction of a particle with a cellulose surface through water (A_{132}) is computed for 15 nm BSA-cit-AuNP at pH 8 when the Hamaker constant for BSA interacting with itself in a vacuum ($A_{11}=2\times10^{-20}$ J) is applied rather than that of bulk Au (Table SI. 4.7).[157-159] A negative A_{132} is produced when A_{11} for the particle is below that of water (3.7×10^{-20}), as is the typical A_{11} of a protein ($1\text{-}1.5\times10^{-20}$ J).[119,162] The van der Waals attractive force never overcomes the electrostatic repulsion when the BSA Hamaker constant is applied to the DLVO model rather than that of Au bulk for the 15 nm BSA-cit-AuNP at pH 8 (**Figure SI. 4.7**A), and the DLVO model predicts the experimental data despite the lack of inclusion of steric stabilization or Lewis acid-base forces in the model. Using the BSA Hamaker constant does not significantly influence the DLVO model output for pH 3 BSA-cit-AuNP of any size until a separation distance less than 0.1 nm (shorter than a carbon-carbon bond length) because the zeta potential of the nanoparticles is positive (**Figure SI. 4.7**B-C). The BSA surface coating properties appear to be important in this case because the coating is thick in comparison to the particle size and the range of van der Waals forces and the BSA dictates charge as a function of pH.[119]

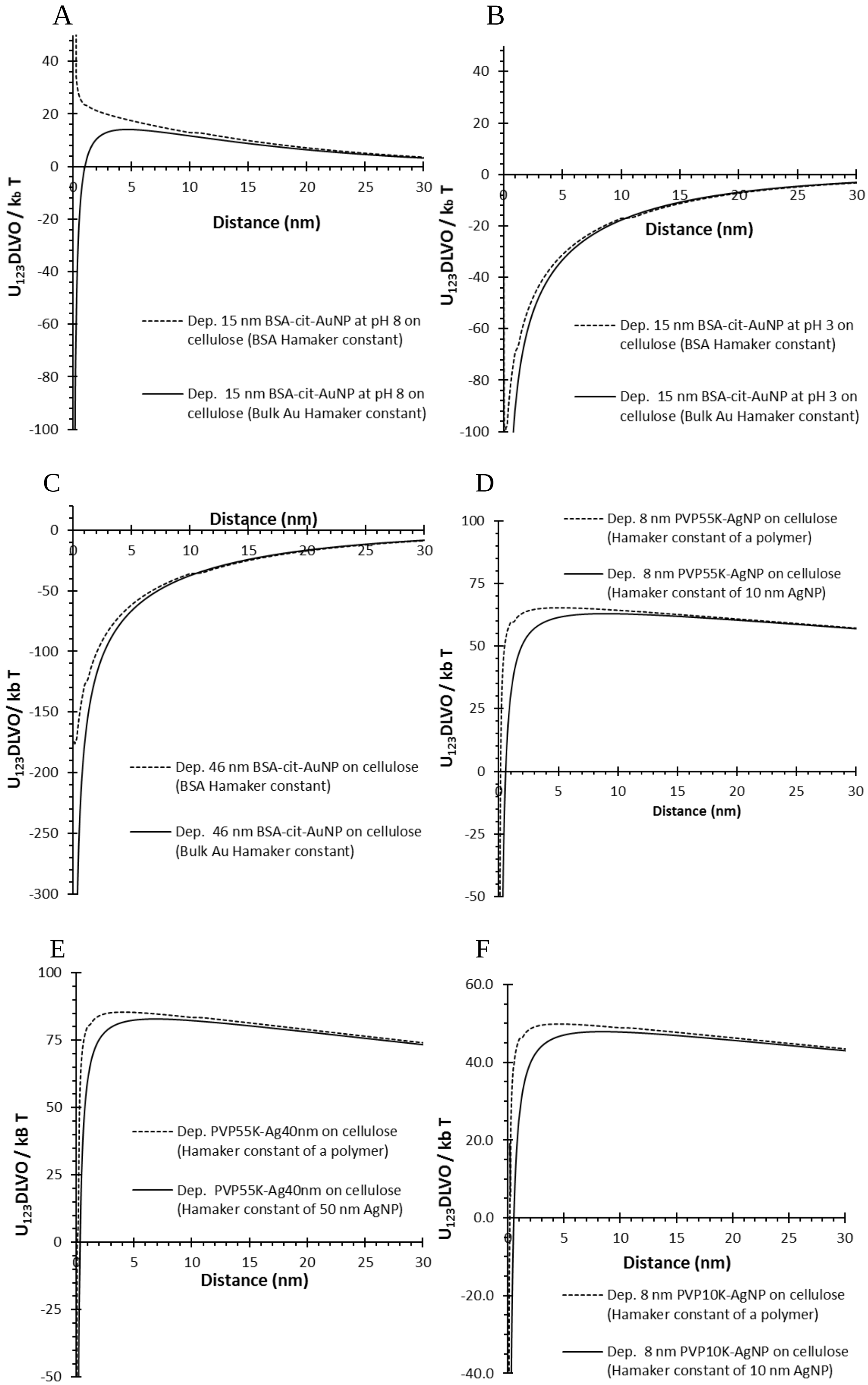

Figure SI. 4.7. DLVO interaction energies computed using Hamaker constant values for the metal core (solid line) and for the surface coating (dotted line).

For the interaction of PVP-AgNP with cellulose, replacing the Hamaker constant (A_{11}) of AgNP used to model the PVP-AgNP with a value an order of magnitude smaller (a reasonable value for a polymer)[155-156] reduces A_{132} by an order of magnitude and increases the DLVO interaction energy barrier very slightly. A more significant effect of applying a polymer Hamaker constant is that the van der Waals attractive force does not overcome the electrostatic repulsive force until the particle is closer to the surface (1-3 nm as opposed to 3-5 nm), and the interaction between the PVP-AgNP and cellulose does not become attractive until a distance just over 0.1 nm (**Figure SI. 4.7D-F**). DLVO suggests that electrostatic repulsion forces dominate until the PVP-AgNP approach within a typical bond length. Sterically, it is not likely that the particle would approach within this distance. Therefore, as observed, it is logical that the particles are not deposited in the cellulose.

5

Surface-enhanced Raman spectroscopy (SERS) cellular imaging of intracellularly biosynthesized gold nanoparticles

Rebecca H. Lahr and Peter J. Vikesland

Department of Civil and Environmental Engineering and Institute of Critical Technology and Applied Science (ICTAS), Virginia Tech, 418 Durham Hall, Blacksburg, Virginia 24061, USA.

ABSTRACT

To date, few surface-enhanced Raman spectroscopy (SERS) spectra and even fewer SERS cellular images have been collected of intracellularly grown gold nanoparticles (AuNPs). In this effort, SERS cellular imaging was used to detect intracellular and extracellular gold nanoparticles (AuNP) biosynthesized by *Pseudokirchneriella subcapitata* and to identify surface-associated biomolecules. Three-dimensional SERS spectral maps imaged AuNP biosynthesized in the presence of 0.005-0.5 mM $HAuCl_4$ over a variety of pH conditions. Algal growth and AuNP biosynthesis were monitored over a 72 hour exposure period using UV-Vis spectroscopy, electron microscopy, and elemental analysis. Principle component analysis (PCA) and cluster analysis of SERS data demonstrate reproducible trends in the SERS spectral maps. SERS cellular images contain peaks consistent with chlorophyll *a*, β-carotene, phytochelatin, hydroxyquinoline, NAD, and proteins such as the nitrate reductase enzyme. Each is a biomolecule previously suggested to be involved in intracellular AuNP biosynthesis. SERS hotspots indicate the association of RNA with AuNP, but RNA was not the predominant nanoparticle-associated biomolecule. Continued development of SERS spectral imaging will facilitate noble metal nanoparticle surface analyses to elucidate biosynthesis mechanisms, to monitor nanomaterial function and stability in polymer matrices, and to image AuNP employed for drug delivery applications.

INTRODUCTION

Surface-enhanced Raman spectroscopy (SERS) is a vibrational spectroscopic method that provides information about molecules positioned in the vicinity of noble metal nanostructures.[1,3,163] SERS enables generation of cellular images created by acquisition of hundreds to thousands of Raman spectra across a cell decorated with intracellular or extracellular noble metal nanoparticles. Raman vibrational peaks that correspond to specific biomolecules can be tracked across a single cell, thus documenting the location of biomolecules that associate with the noble metal nanostructures.[164] Such information aids in identification of nanoparticle locations and the delineation of cellular processes.[165] Recently, SERS cellular images collected for a variety of cells have shown the capacity of the method to measure pH in the immediate vicinity of a SERS tag, to mark certain molecular features within a cell, or to define those biomolecules in the immediate vicinity of a noble metal nanostructure.[164,166-168]_ENREF_14 To date, however, few SERS spectra and even fewer SERS cellular images have been collected of intracellularly grown gold nanoparticles (AuNPs).[164,169-172] Thus, SERS cellular imaging is an untapped resource. The work described herein enhances our understanding of intracellular AuNP biosynthesis mechanisms by extending SERS spectral imaging of biosynthesized AuNP to algal cells.

Algae, bacteria, and fungi have the capacity to biosynthesize gold and silver nanoparticles (AgNP) following dissolved metal uptake.[165,173-176] There is growing interest in the optimization of these biosynthesis processes for gold recovery from aqueous solutions and for “greener” nanoparticle syntheses.[177-178] During biosynthesis, dissolved gold ions (Au^{3+}) are reduced to Au^0 intracellularly or extracellularly without the use of acidic or caustic reagents or the input of significant amounts of energy as required for conventional syntheses.[165,173-174] AuNP bioproduction is attractive because particles of a wide variety of shapes and sizes can be produced by a single microbial species through growth condition modification (i.e., pH, initial Au concentration, temperature).[179-180] Furthermore, alterations in synthesis rates can be achieved by organism selection – after exposure to Au^{3+}, nanoparticles were observed within minutes for *Plectonema boryanum* and *Anabaena flos-aquae*, but *Calothrix pulvinata* required hours to produce particles.[173,179]

The mechanisms of AuNP and AgNP biosynthesis have been studied for bacteria, fungi, and plants using FT-IR spectroscopy, X-ray photoelectron spectroscopy, zeta potential measurements, enzymatic activity assays, and transmission electron microscopy-electron spectroscopic imaging; however, due to organism specific biochemistries and the tremendous variety of biomolecules that are capable of reducing Au^{3+} to Au^0, the exact mechanisms for intracellular biosynthesis of AuNP by most microorganisms remain unresolved.[181-183] One theory suggests the negatively charged cell wall electrostatically attracts Au^{3+}, that peptidoglycan or enzymes at the cell wall reduce Au^{3+} to Au^0, and following nucleation that nanoparticles are transported through the cell wall.[181-182] Alternate pathways suggested for Au^{3+} bioreduction by bacteria and fungi involve thylakoid membranes, reductase enzymes and cytochromes.[165,177,181,183]

Algal studies documenting intracellular AuNP biosynthesis typically focus solely on metal uptake for recovery from waste streams or omit discussion of the AuNP reduction mechanism.[177,181,184] Cyanobacteria lack internal organelles such that the mechanism suggested for blue-green algae may not be entirely applicable to green algae.[165] Incomplete understanding of the mechanisms responsible for uptake of Au^{3+} into algae and its conversion to AuNP limits optimization of these promising processes. We utilized SERS to systematically probe AuNP biosynthesis in an effort to close this data gap and develop SERS spectral imaging techniques for intracellular analyses. We note that the protocols developed herein for algal imaging are applicable to a variety of cellular environments.

RESULTS & DISCUSSION

Based upon cell counts, visual observations, and absorbance measurements at 682 nm, exposure to 0.005-0.04 mM $HAuCl_4$ had little effect on *P. subcapitata* growth rates, but growth halted in 0.08-0.5 mM $HAuCl_4$ (**Figure SI. 5.1**). After a 72 hour incubation, algal cells in control samples and incubations with less than 0.08 mM $HAuCl_4$ reached stationary phase. The decrease in pH due to $HAuCl_4$ addition was not the cause of cell death for initial $HAuCl_4$ concentrations greater than 0.08 mM; cell growth was also inhibited in 0.15 and 0.5 mM $HAuCl_4$ samples fixed at pH 8.

AuNP growth. AuNPs exhibit characteristic absorption bands (localized surface plasmon resonances, LSPR) whose location and magnitude are defined by the size of the nanoparticle and its local chemical environment. In water, the LSPR wavelength for discrete 15 nm gold spheres occurs at 520 nm, but as the diameter increases to 99 nm, the wavelength red-shifts to 575 nm.[74] Only two LSPR bands were observed by UV-Vis spectroscopy in any of the incubation flasks.

An LSPR band at 524 nm was exhibited by samples spiked with pre-synthesized 40 nm citrate AuNP, and another LSPR band at 567 nm was identified in incubations containing 0.15 mM $HAuCl_4$ at pH 3 (**Figure SI. 5.2**).

Environmental scanning electron microscopy (ESEM) images, collected for samples removed directly from incubation flasks every 24 hours and of 72 hour samples that were filtered and fixed in glutaraldehyde, demonstrate AuNP biosynthesis, but cannot differentiate intracellular AuNP from AuNP associated with the algal surface (**Figure 5.1**). AuNP are visible within 24 hours of incubation in the 0.5 mM $HAuCl_4$ sample, but longer incubation periods were required for lower initial gold concentrations. Transmission electron microscopy (TEM) cross-sectional images, obtained after 72 hours, confirm intracellular AuNP production and facilitate particle sizing (**Figure 5.1**). Energy-dispersive X-ray spectroscopy (EDX) further affirms that the nanoparticles are AuNP (**Figure SI. 5.3**). Extracellular AuNP production was sufficient to generate a UV-Vis peak only in the 0.15 mM $HAuCl_4$ condition at pH 3. At the initial algal concentration of 2×10^5 cells/mL, absorbance of chlorophyll *a*, carotenoid, and intracellular AuNP were not visible by UV-Vis spectroscopy (**Figure SI. 5.1** & **Figure SI. 5.2**). LSPR absorbances of intracellularly biosynthesized AuNP have been observed by Focsan et al. and others at higher cell counts.[165,185] Low cell counts and the intracellular nature of the AuNP result in few UV-Vis detectable AuNP.

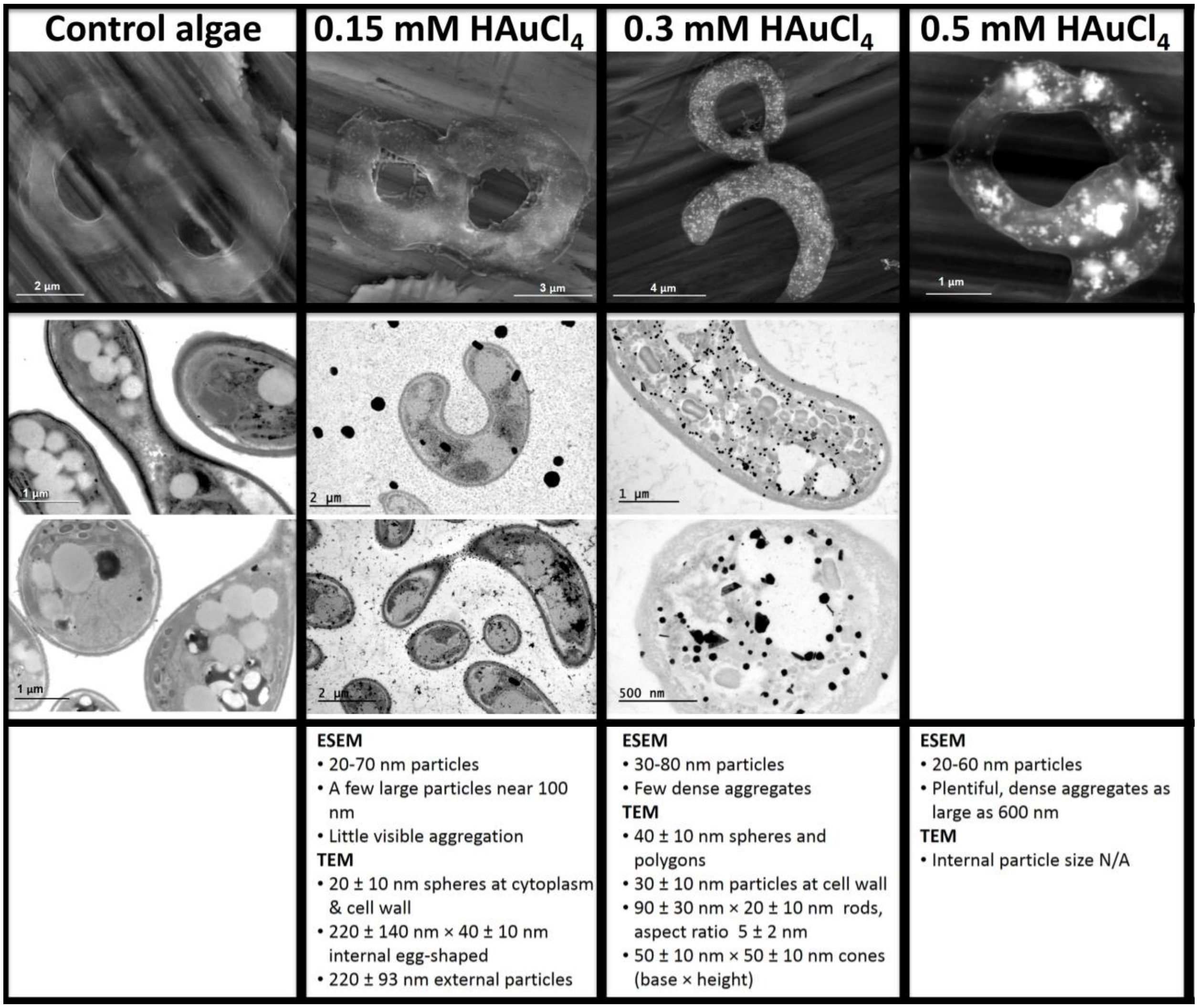

0.15 mM $HAuCl_4$

ESEM
- 20-70 nm particles
- A few large particles near 100 nm
- Little visible aggregation

TEM
- 20 ± 10 nm spheres at cytoplasm & cell wall
- 220 ± 140 nm × 40 ± 10 nm internal egg-shaped
- 220 ± 93 nm external particles

0.3 mM $HAuCl_4$

ESEM
- 30-80 nm particles
- Few dense aggregates

TEM
- 40 ± 10 nm spheres and polygons
- 30 ± 10 nm particles at cell wall
- 90 ± 30 nm × 20 ± 10 nm rods, aspect ratio 5 ± 2 nm
- 50 ± 10 nm × 50 ± 10 nm cones (base × height)

0.5 mM $HAuCl_4$

ESEM
- 20-60 nm particles
- Plentiful, dense aggregates as large as 600 nm

TEM
- Internal particle size N/A

Figure 5.1. ESEM whole cell (first row) and TEM cross-sectional images (second row) were collected of *P. subcapitata* incubated with 0-0.5 mM $HAuCl_4$ for 72 hours, filtered through a 0.2 µm filter, and fixed with 2.5% glutaraldehyde. Electron dense gold is displayed as white in ESEM images and black in TEM images. Staining with osmium tetroxide before cross-sectioning for TEM analysis identifies unsaturated lipids (i.e., cell and organelle membranes).[186] The third row summarizes the characteristics of the AuNPs for each condition. (Note: No TEM images for the 0.5 mM $HAuCl_4$ incubation were obtained.)

Raman and SERS characterization of algal cells. The growth and aggregation of biosynthesized AuNP results in enhanced Raman spectral intensity. In the presence of AuNP, SERS spectra are observed using 1% of the laser power and 10% of the acquisition time required for normal Raman cellular imaging (**Figure 5.2**). Control cells grown without $HAuCl_4$ display low intensity fluorescence signals without defined Raman spectral peaks when probed at low laser powers and short acquisition times. AuNP have the ability to quench fluorescence, and this property combined with the enhancement effect allowed SERS signals to be visible for cells incubated with $HAuCl_4$.[3] Furthermore, the SERS signal intensity increased with the initial gold concentration (**Figure 5.2**). A SERS spectrum is only obtained when the LSPR band of the noble metal nanostructure overlaps with the Raman laser wavelength.[1,3] For experiments conducted with a 785 nm Raman laser, AuNP must either be large (>40-50 nm) or have many particle junctions (overlapping AuNP electromagnetic fields) to produce a SERS effect.[1] Based upon the observed size of AuNP in the collected TEM and SEM images it would appear that the latter mechanism is primarily at play in this system. Importantly, the 785 nm laser selectively probes those biomolecules associated with larger particles or aggregates. Had a 514 nm laser been applied to the same samples, smaller particles or aggregates would have enhanced the Raman spectra thus resulting in identification of biomolecules associated with those smaller nanoparticles. SEM and TEM images suggest a lower wavelength laser is more practical for analysis of algal cells incubated with ≤0.15 mM $HAuCl_4$, while the 785 nm laser produces information relevant for cells incubated with 0.3 mM or 0.5 mM $HAuCl_4$.

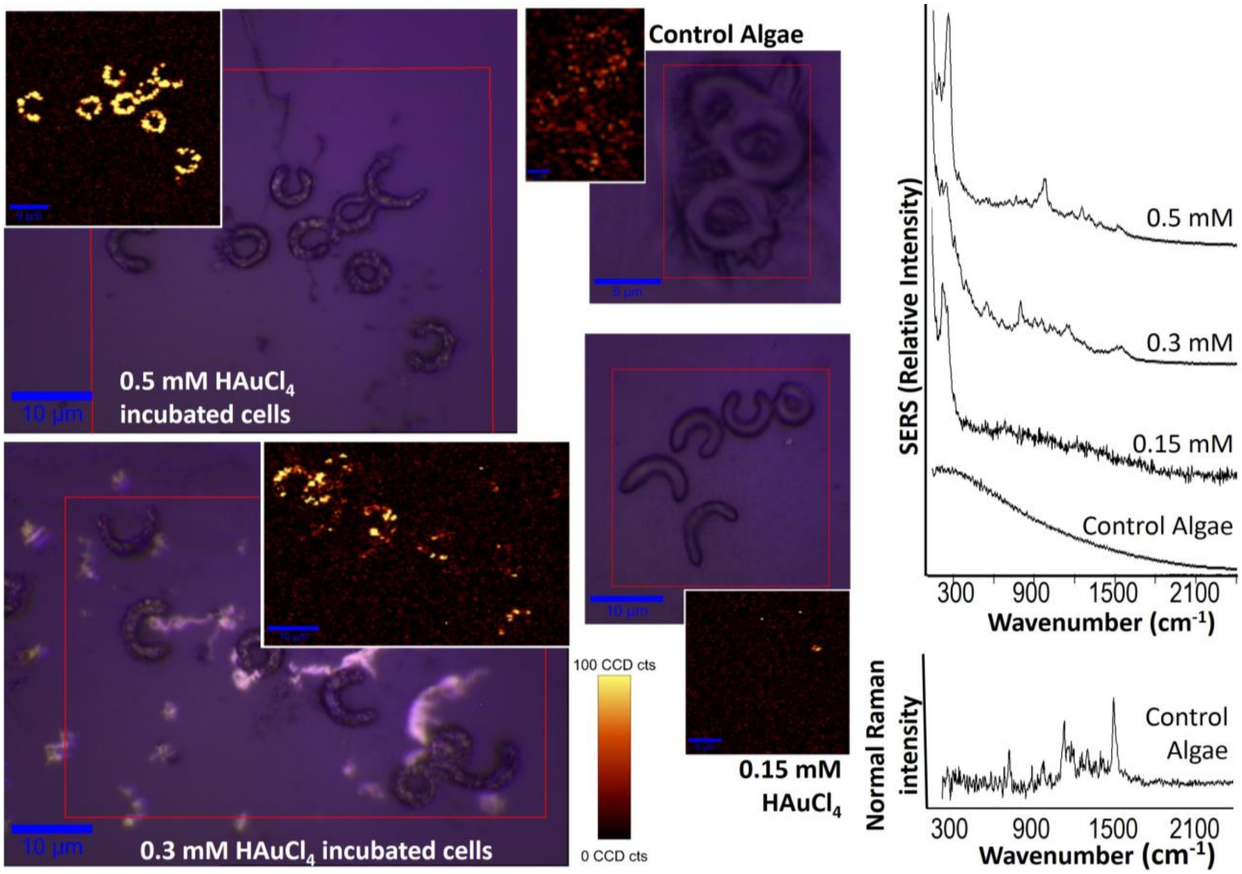

Figure 5.2. Optical images (purple) and the corresponding XY SERS spectral maps of control *P. subcapitata* sample (no gold added) as well as samples incubated with 0.15-0.5 mM $HAuCl_4$. The XY SERS maps were produced by mapping the intensity of the 260 cm^{-1} Raman band that corresponds to AuNP.[164] SERS spectra for the cells in each spectral map were averaged and are shown before baseline correction on arbitrary scales for viewing ease. The normal Raman spectrum was collected with a higher sample concentration, laser power, and acquisition time for comparison with SERS spectra. (**Table SI. 5.1** contains specific Raman spectrometer parameters for each condition.)

Three-dimensional Raman scans demonstrate that the majority of the SERS signal originates from within the algal cells rather than simply from their surface (**Figure 5.3**, video available online). The spectra observed within the cells exhibit spatial variability caused by the transient nature of SERS, the association of AuNP with a variety of biomolecules in the cell, and SERS hot spots produced at the junctions and corners of particles where electromagnetic fields produced by the surface plasmon bands of the nanostructures overlap.[1,3] SERS hot spots are operationally defined herein as a location that produces a spectrum containing unique peaks that are at least 10× more intense than the typical spectrum for that cell. Principal component analysis

(PCA) and cluster analysis were applied to find statistically relevant patterns within the SERS spectral maps.

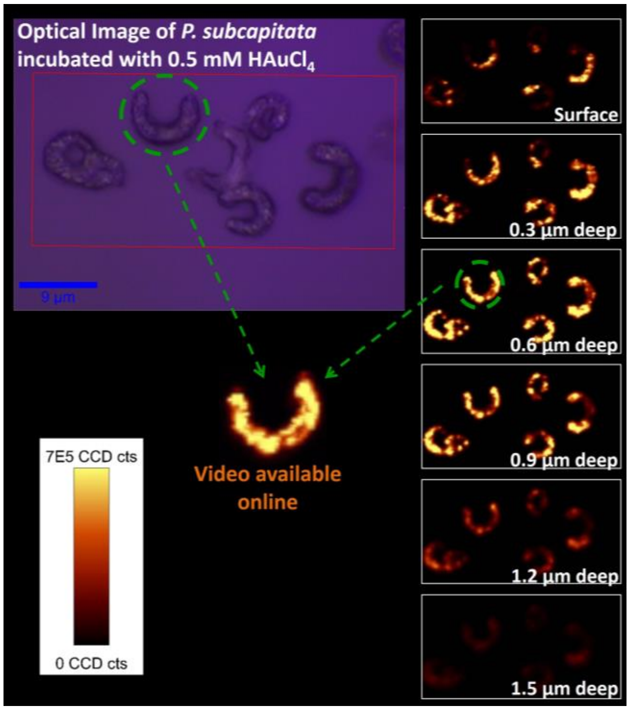

Figure 5.3. SERS signal originates from within the algal cell rather than at the surface, as demonstrated by stacked x,y,z SERS spectral maps. Three spectra per µm were collected, and the overall spectral intensity of each spectrum was used to convert 7560 spectra into a single image for each depth. High numbers of CCD counts (yellow) are observed by the instrument detector only inside of the cells. A video demonstrating the particle locations in 3D space within the indicated cell is available electronically.

Data reduction. PCA is a statistical method often used to emphasize variations in large datasets, rather than the variables that remain constant.[53] A new combination of the original variables, known as principal components (PCs), is created to order and highlight the aspects of the data set that are unique. The percentage of variability in the data described by each PC is computed, and the PCs are ordered by the amount of variability explained by each PC, with the first PC being the most significant. For a single algal cell incubated with 0.5 mM $HAuCl_4$ at pH 3, one PC explained 80-95% of the variability amongst spectra. The loadings for the first PC highlighted similar peaks for each cell, with cells incubated under similar conditions sharing more similarities than those of cells incubated under different conditions; however, some cell-to-cell variability was apparent (**Figure SI. 5.4**).

Cluster analysis partitions spectra within a SERS spectral image into a predefined number of groups of similar spectra.[53] In cluster analysis with two clusters defined (chosen based on the PCA results), the crescent shaped algal cell can be differentiated from the background. If the *P. subcapitata* cell SERS spectra are divided into additional clusters, a single spectrum of varying intensity is observed across the majority of each cell with periodic SERS hot spots (**Figure 5.4**). The most intense cluster of each cell typically matched the peaks highlighted by the loadings of the first PC (**Figure SI. 5.4** & **Figure SI. 5.5)**, demonstrating an agreement between PCA and cluster analysis, the reproducible nature of spectra across an algal cell, and the significance of the SERS peaks displayed by the algae. The most common SERS vibrations highlighted by cluster analysis and PCA were further studied to identify their origins.

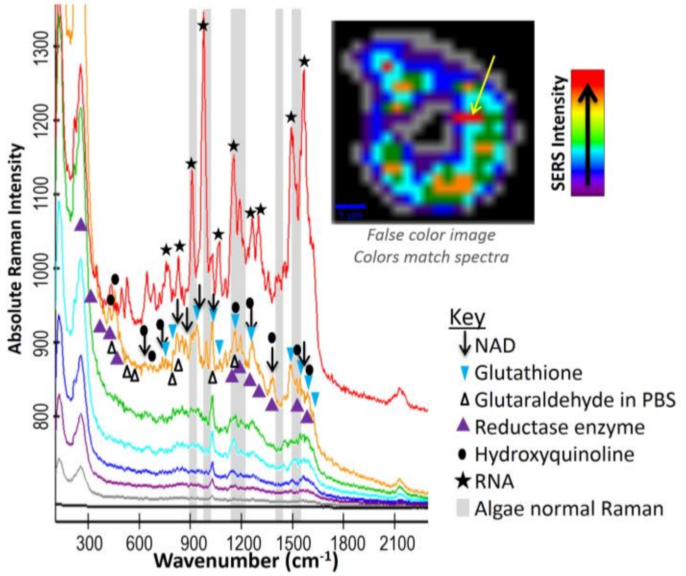

Figure 5.4. Cluster analysis of a cell incubated with an initial concentration of 0.5 mM $HAuCl_4$ at pH 3 in growth media demonstrates the intracellular nature of the biosynthesized AuNP. Each spectrum corresponds to the location indicated by the corresponding color in the Raman spectral map. A SERS hotspot, reflecting more intense and different peaks from those observed throughout the rest of the cell, is indicated by the yellow arrow. Absolute SERS intensities demonstrate the strength of each spectrum and the extent of the signal enhancement. The baseline of the most intense spectrum was shifted up by 100 CCD counts for reading ease (red spectrum). Biomolecule spectra are referenced in **Table SI. 5.2**.[9,29,39,187-203]

AuNP surface-associated biomolecules. Zeiri and Sengupta determined that silver nanoparticles extracellularly synthesized by *E. coli* reproducibly display a spectrum similar to that of flavin adenine dinucleotide (FAD) due to the high affinity of this molecule for the nanoparticle surface.[204-205] *P. subcapitata* biosynthesized AuNP do not follow such a simple trend, but PCA and cluster analyses provide evidence of patterns. Algal SERS spectra were compared to spectra of basic biomolecules as well as biomolecules thought to take part in the reduction or stabilization of biosynthesized AuNP (i.e., carotenoids, chlorophyll, polysaccharides, hexosamines, tannins, amino acids, quinones).[9,29,39,177-178,181,187-203,206-207] Normal Raman spectra are generally strongest for nonpolar functional groups, but the chemical enhancement mechanism for SERS distorts this trend. The SERS spectrum of a molecule in contact with an AuNP will be enhanced by 10-100× in addition to the enhancement expected from the biomolecule's position within the electromagnetic field generated about the AuNP due to laser irradiation.[1] Therefore, the strongest peaks are hypothesized to be generated by biomolecules associated with the AuNP surface. Biomolecules with the greatest number of peaks that matched the algal SERS spectra are indicated in **Figure 5.4**.

Mechanistic interpretation of SERS spectra. SERS spectra at all conditions contain elements associated with the metal binding peptide phytochelatin, hydroxyquinoline, nicotinamide adenine dinucleotide (NAD), and a protein such as a reductase enzyme. Therefore it is hypothesized that AuNP biosynthesis by *P. subcapitata* follows a similar mechanism as observed in fungi in which the metal binding peptide binds gold intracellularly, hydroxyquinoline and NADH transfer electrons to facilitate function of a reductase enzyme, and phytochelatin stabilizes AuNP after production.[206,208-209] The number of peaks that correspond with the biomolecules involved in this proposed mechanism for AuNP biosynthesis, rather than other common biomolecules, cannot be a coincidence. SERS vibrations associated with several of these biomolecules overlap, and the tendency for SERS to distort respective peak ratios due to orientation of the molecule about the AuNP surface hinders precise differentiation of all peaks. However, the ability of SERS to narrow down the list of biomolecules that are positioned within 4 nm of the AuNP surface is significant. Clearly, SERS spectral imaging is a powerful tool to compliment FT-IR, X-ray spectroscopies, assays of cell function, and in vitro syntheses for the determination of mechanisms responsible for AuNP biosynthesis.

Glutaraldehyde. The presence of the fixing agent glutaraldehyde has been shown to increase the capacity of the polysaccharide chitosan for gold.[177] Therefore, Raman peaks associated with the fixing agent glutaraldehyde were also highlighted in **Figure 5.4**. The low intensity of glutaraldehyde peaks suggests that it is not the most prevalent biomolecule at the AuNP surface.

RNA. Peaks associated with RNA were observed in SERS hotspots, but not in the typical algal SERS spectrum (**Figure 5.4**). RNA specific vibrations at 979 and 912 cm^{-1}, nucleobase vibrations at 1568, 1493, 1264, and 1304 cm^{-1}, and phosphate vibrations at 1192 cm^{-1} were observed at a stronger intensity than DNA specific peaks (i.e., 678, 785, 337, 1373, 1485, 1510, and 1575 cm^{-1}).[29,190] Considering the location of RNA within the cell and that DNA/RNA typically interacts with AuNP only when single stranded, it is logical to observe RNA rather than DNA.[210] Biosynthesized AuNP were observed by Shamsaie et al. in the nucleus of MCF10 epithelial cells and by Huang et al. in nasopharyngeal carcinoma cells upon incubation with $HAuCl_4$,[170-171] but there is significant evidence for fungi, bacteria, and plants that points toward biosynthesis via a reductase enzyme instead of RNA/DNA.[181] The rare occurrence of RNA SERS spectra, only in SERS hotspots, suggests that RNA is not the primary reducing or stabilizing agent within the *P. subcapitata* cells.

Chlorophyll a and carotenoids. Algal SERS spectra for all conditions maintain a set of peaks similar to those in the normal Raman spectrum of the algae (primary peaks highlighted in grey in **Figure 5.4**). This observation is interesting because SERS spectra are collected with a much lower laser power (<0.05 mW SERS versus >40 mW normal Raman), and no Raman or SERS signals were obtained for algae without AuNP at <0.05 mW of laser power. This finding suggests that the same biomolecules that are responsible for producing the algal normal Raman spectrum are interacting within 4 nm of the AuNP.[3] The peaks in the normal Raman algal spectrum are identified as chlorophyll *a* and β-carotene, identical to that observed by Wood et al. (**Figure SI. 5.6**). Therefore, chlorophyll *a* and β-carotene interact with the biosynthesized AuNP. Such a finding is not surprising; AuNP biosynthesized by cyanobacteria are found to associate with thylakoids where photosynthetic electrons are employed for Au^{3+} reduction,[165] AuNP have been produced by chloroplasts extracted from *Trifolium* leaf,[211] and Barazzouk et al. successfully employed AuNP to photoprotect chlorophyll because of its affinity to form a self-assembled monolayer on AuNP.[212] SERS spectra consistently display a peak at 2137 cm^{-1} that reflects C-N vibrations at a gold surface.[110-111] The detector on the Raman spectrometer employed for this analysis is less sensitive to high wavenumber peaks such as 2137 cm^{-1} with the 785 nm laser setup (indicated by instrument specifications and experimental verification). Although the peak at 2137 cm^{-1} is weak in some of the algae samples, its intensity in relation to the minimal sulfur SERS peaks at 630-670 cm^{-1} and 700-745 cm^{-1} suggest that a nitrogen atom rather than a sulfur atom most frequently coordinates with the AuNP, a finding supported by Mukhejee et al.[19,29,110,182]

Glutathione and phytochelatin. Glutathione is both a precursor of phytochelatin and a metal binding compound thought to help transport metals to polyphosphate granules, the cytoplasmic membrane, or vacuoles.[209] Phytochelatin is an oligomer of glutathione produced intracellularly by *P. subcapitata* and other algae in the presence of Cd, Zn, Cu, Ag, Hg, and Pb to bind metals for detoxification; this molecule has been employed experimentally to stabilize particles formed by a reductase enzyme.[206,208-209] SERS data suggests glutathione or phytochelatin is also produced by *P. subcapitata* in the presence of $HAuCl_4$. Ma et al. determined that surface area rather than concentration dictates the overall toxicity of a prefabricated metal NP to an organism.[213] Phytochelatin levels have been observed at an order of magnitude lower than that of the heavy metal;[209] this is expected for a molecule used as a surface coating for small nanoparticles rather than an agent used to bind each metal ion separately.

Reductase enzymes. Many microorganisms are thought to bio-reduce AuNP and AgNP by way of a NADH dependent reductase, especially nitrate reductase in the presence of NADH, hydroxyquinoline, and phytochelatin.[181-182,208,214] The enzyme acts with electron transfer by NADH and hydroxyquinoline, and the metal binding peptide phytochelatin stabilizes particles after formation.[208,214] Such a mechanism was proposed for AgNP synthesis by Duran and coworkers and proved valid in vitro for AgNP by Kumar et al.[181,208,214-215] The presence of all four molecules together (phytochelatin, nitrate reductase, NADH, and hydroxyquinoline) was required to produce AgNP particles in vitro.[214] Our SERS data suggest a similar mechanism is feasible for AuNP biosynthesis by algae.

Impact of initial conditions on AuNP biosynthesis. The most intense cluster spectrum and the loadings of the first PC for three distinct cells at each condition were compared to demonstrate the reproducibility of SERS results for a single incubation condition as opposed to varied incubation conditions (**Figure SI. 5.5**). Although cell-to-cell variability exists for a single incubation, greater differences are apparent between spectra for different incubation conditions. Algal cells respond uniquely to each incubation condition, as verified by TEM, SEM, UV-Vis, and SERS spectral imaging data showing dissimilar particles for each condition. SERS spectral maps of the 0.15 mM $HAuCl_4$ samples at pH 3 displayed large islands of SERS signal that did not directly correlate with the cells shown in the simultaneously collected optical images (**Figure 5.5**). This result, along with the observed UV-Vis LSPR absorbance, supports the hypothesis that the SERS active AuNPs in the 0.15 mM $HAuCl_4$ samples at pH 3 were predominantly extracellular. At pH 8 for the same initial concentration, the SERS signal also does not spatially correlate with the algal cells, indicating external particles; however, the dimensions of the SERS signal spots are inconsistently shaped and sized, a finding contrary to all other incubation conditions examined. The polydispersity of external AuNP for the 0.15 mM $HAuCl_4$ sample at pH 8 may explain the lack of a UV-Vis LSPR absorbance peak (i.e., an insufficient concentration of any single particle size to produce a detectable LSPR band). At the higher $HAuCl_4$ concentration (0.5 mM), the SERS spectral images closely match the optical images because the SERS active AuNP are intracellular (**Figure 5.5**). The intracellular AuNP at 0.5 mM $HAuCl_4$ grew large enough during the 72 hour incubation for the LSPR bands to occur near the 785 nm Raman laser wavelength, thus producing the observed SERS signals.

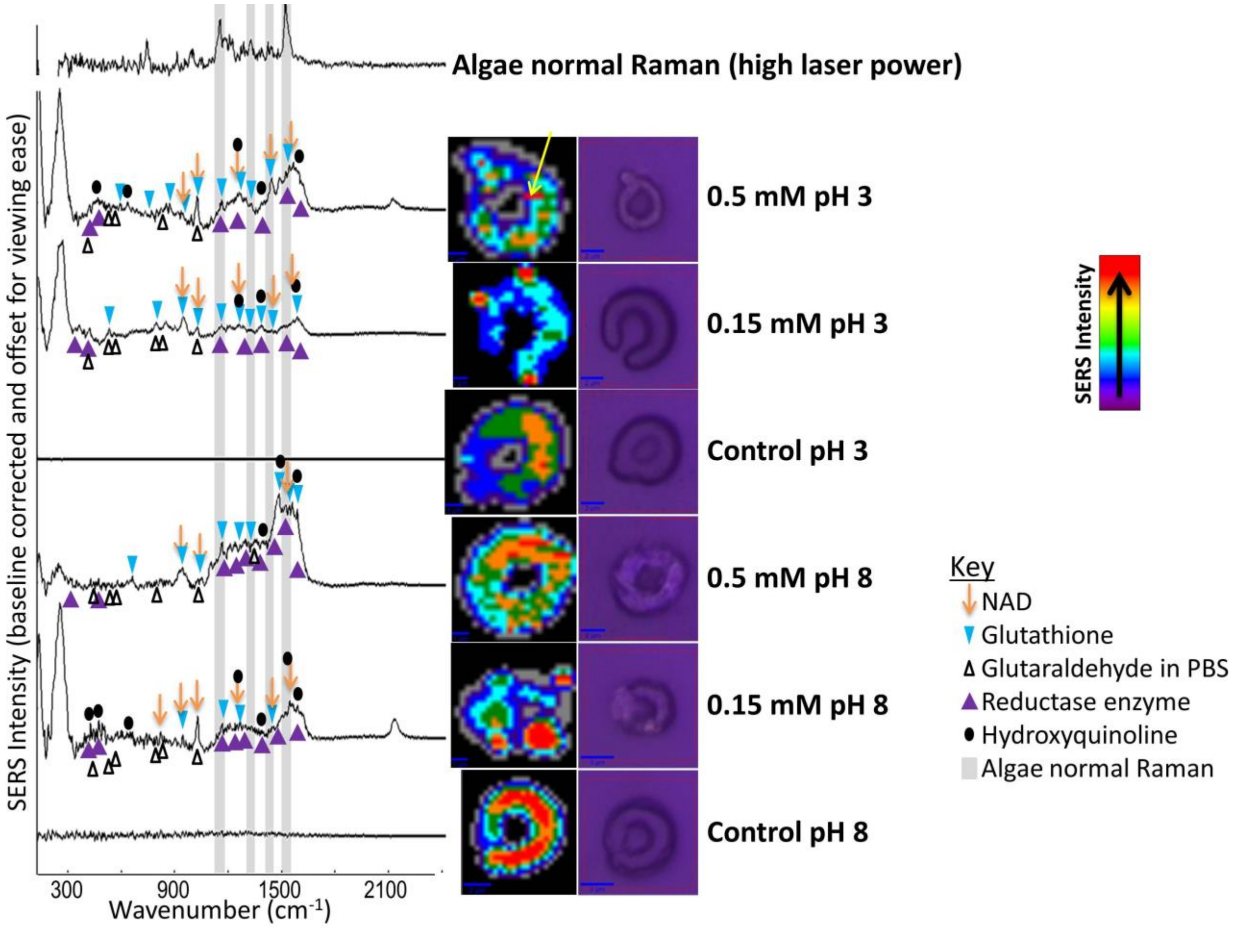

Figure 5.5. Cluster analysis of pH controlled algae incubations. Optical images (purple) and SERS spectral maps (false color images) are shown alongside an average spectrum taken of the most intense cluster for three distinct cells at the indicated condition. SERS hotspots (yellow arrow, 0.5 mM pH 3) were considered as a separate entity and the next most intense cluster was used for averaging. Variability was not observed in the control cell SERS spectral images, so data from a single cell are shown. To improve signal from that displayed in **Figure 5.2**, the laser power was reduced to <0.05 mW and acquisition time increased (**Table SI. 5.1**). Biomolecule spectra are referenced in **Table SI. 5.2**.[9,29,39,187-203]

Peak identifications for the pH controlled incubations at 0.5 mM and 0.15 mM $HAuCl_4$ are shown for the most intense clusters averaged for three cells, excluding SERS hotspots (**Figure 5.5**). Similar peaks were typically observed for all conditions, with intensity variability. The 0.15 mM $HAuCl_4$ cells at pH 3 do not have as high of a contribution of peaks from chlorophyll *a* or β-carotene as the other incubations. This finding is logical considering the extracellular nature of the particles. Cell lysis would be required before extracellular particles would be formed by or come into contact with chloroplasts. The intracellular nature of the AuNPs formed at 0.5 mM

$HAuCl_4$ also explains the higher intensity of peaks at 1200-1300 cm^{-1} and 1500-1600 cm^{-1}, attributed to amide vibrations of proteins, glutathione, or phytochelatin for the 0.5 mM $HAuCl_4$ samples.[29] The intracellular environment typically has a higher concentration of proteins, and phytochelatin is produced intracellularly.

The strength of the 2137 cm^{-1} SERS peak in comparison to the weaker peaks that periodically appear at 630-670 cm^{-1} and 700-745 cm^{-1} indicates more significant Au^0-N than Au^0-S vibrations.[19,29,110-111,216] A small 660 cm^{-1} peak is apparent in several 0.5 mM pH 8 and 0.15 mM pH 3 samples, but at a weaker intensity than the 2137 cm^{-1} Au^0-N vibration that is especially apparent in the 0.5 mM pH 3 and 0.15 mM pH 8 samples. Mukherjee et al. also observed linkages of AgNP with nitrogen atoms rather than sulfur in a single Raman spectrum of AgNP produced using cell-free aqueous filtrate from *Trichoderma asperellum*.[19] AuNP biosynthesized by chloroplasts and examined by FTIR by Zhang et al. were determined to be capped by glutathione bound via free amine groups.[211] Reduced glutathione has both thiol and amide groups available for coordination with Au^0. The oxidation of glutathione results in a disulfide bridge between the thiols of two glutathiones,[195] leaving the sulfur atoms more sterically hindered than the nitrogen atoms. Therefore, if glutathione were indirectly involved in the reduction of Au^{3+} to Au^0, linkage of glutathione to AuNP through nitrogen atoms would not be unexpected. The greater intensity of amide II and amide III vibrations in the algal cells further emphasizes that it is the C-N and N-H rather than the C=O that interacts most closely with the AuNP for *P. subcapitata*.[195]

FUTURE OUTLOOK

SERS spectral imaging provides valuable information regarding the location, size, and local molecular environment of noble metal nanostructures within transparent or translucent matrixes. The technique is especially useful for surface-analyses of gold or silver nanoparticles contained within cells, with applications in the study of nanoparticle biosynthesis mechanisms, transport behavior of nanomaterials within cells, or cell processes at nanomaterial surfaces. Raman lasers may be chosen to target analysis to specific nanoparticle sizes. Three-dimensional SERS cellular imaging produces large quantities of data within minutes, such that PCA or cluster analysis are necessary to quickly infer the most important aspects of the large datasets. Understanding the interactions between noble metal nanomaterials and their local environment will improve overall understanding of these systems such that they may be engineered to best fit the needs of society. SERS cellular imaging has yet to be explored to its full potential.

MATERIALS & METHODS

ACS reagent grade chemicals were purchased from Fisher Scientific, MP Biomedical, Acros, RICCA chemical company, and Electron Microscopy Sciences. $HAuCl_4$ was from MP Biomedical, phosphate buffered saline packets (0.01 M PBS; 0.138 M NaCl, 0.0027 M KCl at pH 7.4, 25°C) from Sigma (P-3813), and *P. subcapitata* cultures from Marinco Bioassay Laboratory Aquaculture.

Instrumentation. Absorbance measurements were obtained with a Varian Cary 5000 UV-Vis NIR spectrometer and a Biotek μQuant plate reader. An Accumet Basic AB15 Plus electrode from Fisher Scientific was used to monitor pH. TEM micrographs of samples processed and cross-sectioned with a LEICA Ultracut UCT Ultramicrotome were collected using a Zeiss 10CA TEM (60 kV) with an AMT Advantage GR/HR-B CCD Camera System and a JEOL JEM 1400 TEM (80 kV) with a Gatan Orius CCD Camera controller. ESEM images were recorded with a FEI Quanta 600 FEG operated in ESEM mode with a peltier stage control kit and a 500 μm gaseous SED detector. The ESEM probe current was continuously adjustable up to 100 nA, and resolution in extended vacuum mode was ≈1.5 nm. One droplet of aqueous phase sample was placed on the sample holder of the peltier stage and the instrument was set at 100% humidity, 6.7 bar pressure, 5º C, and 20 kV. The sample chamber humidity was then lowered to 80-90% humidity, the highest level at which intact cells were observed. EDX was conducted in parallel to ESEM.

Aqueous phase samples were pipetted onto glass slides and cells were allowed to settle onto the glass surface before SERS measurements were collected. Cells were examined both fixed and unfixed as well as wet and after drying using a WITec Alpha500R Raman UHTS300 spectrometer, DU 401 BR-DD CCD camera, 785 nm laser, 300 grooves/mm, 100× microscope objectives, and 0.05-50 mW of laser power. Principal component and cluster analyses (Manhattan distance and K-means clustering) were conducted with WITec Project Plus 2.10.3.3

before and after cosmic ray removal, baseline correction, and selection of the 400-2100 cm^{-1} spectral region.

Experimental. Algal cultures were grown and handled in accordance with OECD/OCED procedures.[217] Stock cultures were prepared by mixing 50 mL OECD/OCED media with 1 mL *P. subcapitata* culture (**Table SI. 5.3**). Stock cultures were grown for 3-6 days until the cell count was $>10^7$ cells/mL as determined with a microscope and hemocytometer or by UV-Vis absorbance readings at 440 or 682 nm (corresponding to chlorophyll *a* and carotenoid pigments within algal cells).[217]

Autoclaved 250 mL Erlenmeyer flasks were filled with 50 mL filtered OECD/OCDE media, 1 mL of *P. subcapitata* cells from the stock culture, and 1 mL of an aqueous solution containing the necessary amount of $HAuCl_4$ to make final concentrations of 0.005 – 0.5 mM $HAuCl_4$. Each concentration was run in triplicate. In parallel, a set of samples containing media and cells was spiked with 1 mL of previously prepared 40 nm citrate stabilized AuNP.[79] Prepared flasks were capped with autoclaved cotton balls and incubated at 23°C on a shaker table under fluorescent lighting for the duration of the incubation. Samples were removed from each flask for analysis at approximately 12 hour increments. The volume of solution in each flask did not fall below 40 mL during the 72 hour incubation. Visual descriptions with and without microscope and plate reader measurements at 300, 440, 520, 633, 682, and 785 nm were collected every 12 hours. Raman scans, optical images, and ESEM images were recorded every 24 hours. In addition, TEM images and 250-800 nm UV-Vis scans were collected at 72 hours. After 72 hours the flask contents were filtered through a 0.2 μm polycarbonate Millipore membrane filter and placed in a 2 mL centrifuge tube containing 2.5% glutaraldehyde in 0.01 M PBS buffer for analyses that could not be conducted immediately.

pH control. A set of pH regulated samples were setup, incubated, and monitored as previously described, however, pH was adjusted using 0.1 N NaOH or HCl before the algae was added to the flask containing media and $HAuCl_4$ solution.[174] pH was measured initially and every twelve hours throughout the incubation. Samples for which pH was regulated include: controls of algae in growth media, media controls containing 0.5 mM $HAuCl_4$ without algae, and algae in growth media containing 0.5 or 0.15 mM $HAuCl_4$, all of which were examined at both pH 3 and pH 8.

TEM cross-sectioning. After filtration and fixation as described previously, cells were washed in PBS, stained with 1% OsO_4, pelleted in agar, and suspended in Spurr's resin (SI contains additional details).[218-220] Cross-sections were cut, placed on grids, and examined by TEM. ImageJ (NIH, Ver. 1.46) was used to measure AuNP sizes from images. Averages and standard deviations were computed from at least 50 AuNP or all the AuNP of the specified size and location across at least five typical cells.

ACKNOWLEDGEMENTS

We thank Dr. Weinan Leng for his insights and assistance with the WITec Alpha 500R, Kathy Lowe for sample prep and TEM expertise, and Steve McCartney for ESEM advice and training. This work was supported by an Abel Wolman graduate research fellowship to R.H.L. from the American Water Works Association (AWWA) and research grants from the Center for the Environmental Implications of Nanotechnology (CEINT) and the Virginia Tech Institute for Critical Technology and Applied Science (ICTAS).

SUPPORTING INFORMATION

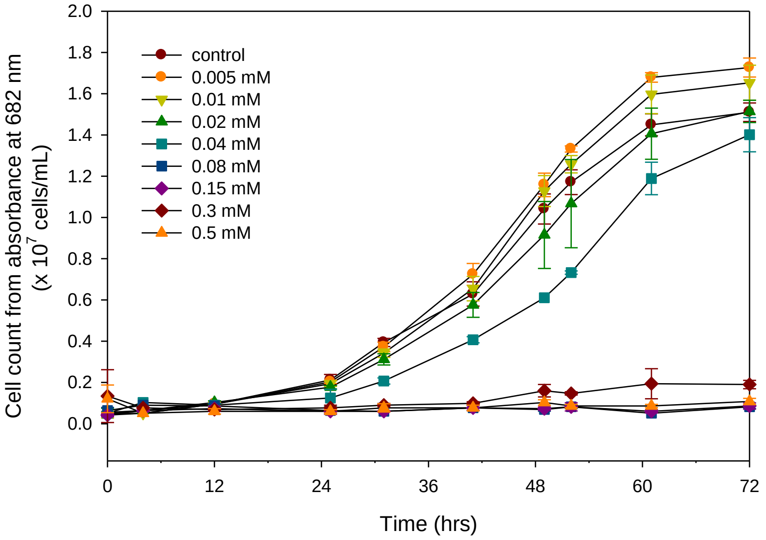

Figure SI. 5.1. Algae growth was observed in media containing 0-0.04 mM $HAuCl_4$ through a 72 hour period. Algae growth halted in media containing 0.08-0.5 mM $HAuCl_4$ throughout this time. A single spike of $HAuCl_4$ was added to produce the indicated concentration within the flask at time zero without pH control.

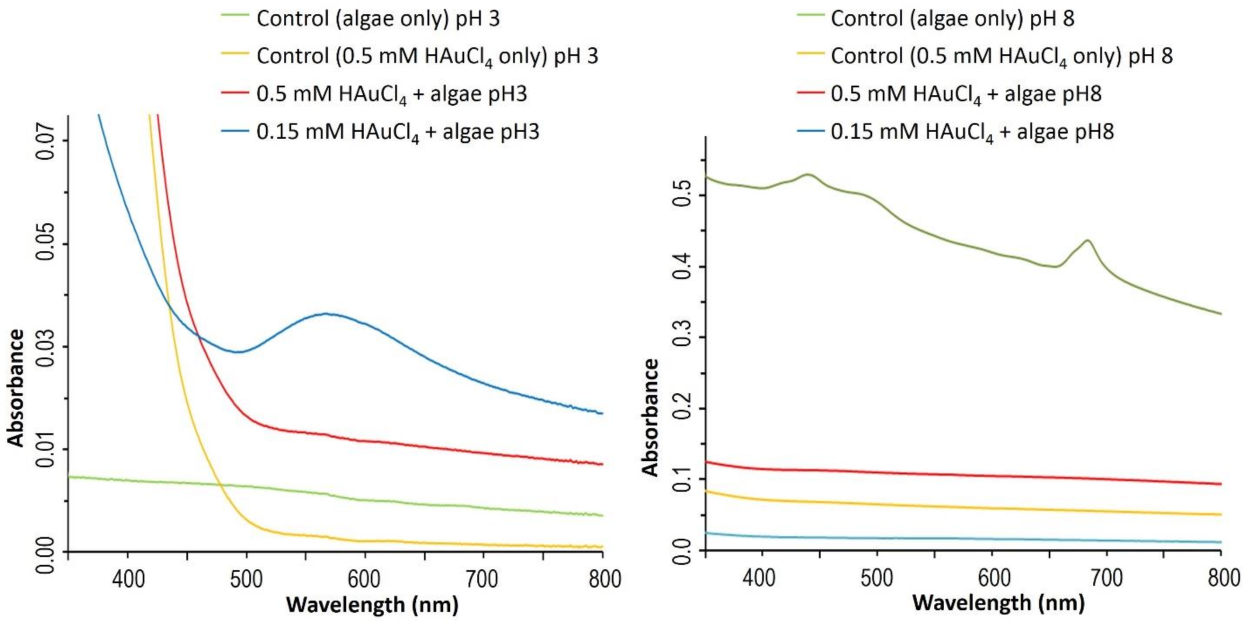

Figure SI. 5.2. UV-Vis spectra 86 hours after initial setup of pH controlled incubations. Only the 0.15 mM pH 3 sample developed external AuNP at a concentration detected by UV-Vis spectroscopy.

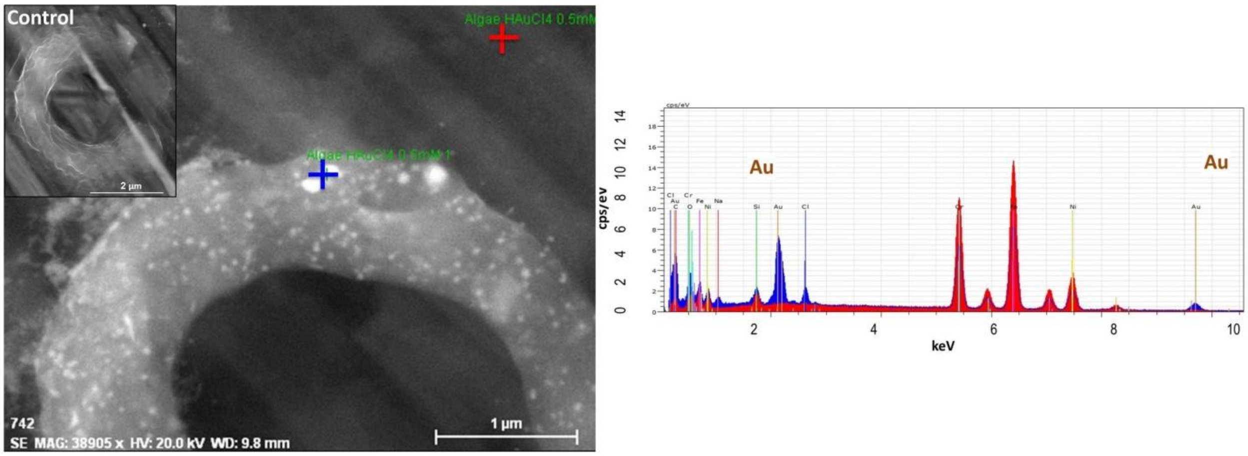

Figure SI. 5.3. EDX spectra of nanoparticles observed in association with algae after incubation with 0.5 mM $HAuCl_4$ corresponded to Au.

Table SI. 5.1. Raman spectrometer parameters for spectra shown. A 785 nm laser, 300 grooves/mm grating, and 100× microscope objective were used for all samples. Samples were placed on glass microscope slides for analysis.

Sample	**Normal Raman or SERS**	**Laser power (mW)**	**Acquisition time per spectrum (seconds)**	**Number of spectra averaged**
Algae stock culture	Normal Raman	>40	1	1 (replicates collected to ensure reproducibility)
0.5 mM $HAuCl_4$ + algae	SERS	<0.3	0.1	SERS spectral map average (3 spectra per µm collected, signal averaged across cells only)
0.3 mM $HAuCl_4$ + algae				
0.15 mM $HAuCl_4$ + algae				
Control algae				
pH controlled incubations (0.5 and 0.15 mM $HAuCl_4$ + algae)	SERS	<0.05	0.5	SERS spectral map average (3 spectra per um collected, signal averaged across areas specified by cluster analysis)

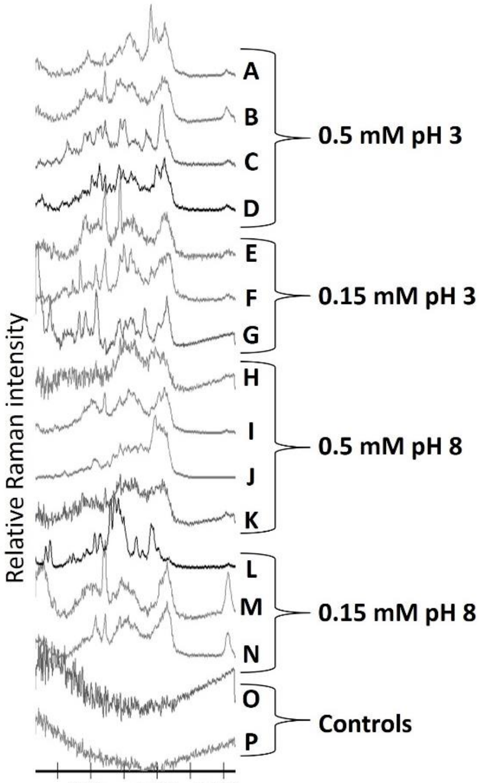

Figure SI. 5.4. Loadings of the first PC from PCA conducted across 16 cells. Each spectrum represents the first PC for a unique cell. The influence of SERS hotspots is especially apparent in spectra C and L.

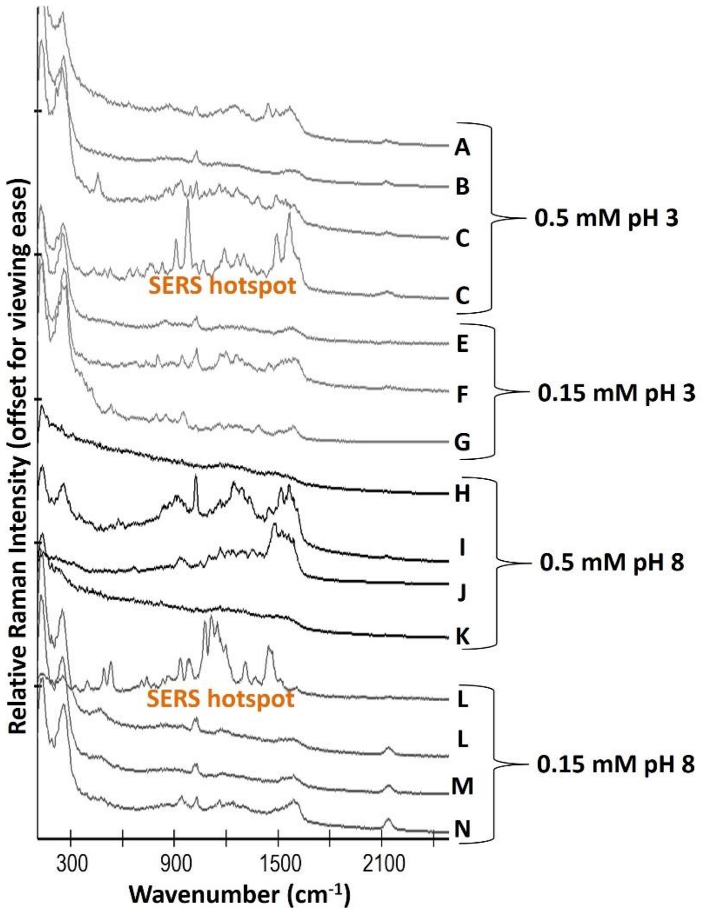

Figure SI. 5.5. Cluster analysis replicates. Each spectrum, not including SERS hotspots, represents the most intense cluster a unique cell. The second most intense cluster spectrum is also included for cells with SERS hotspots.

Table SI. 5.2. References to Raman spectra used for comparison with algal cells.

Molecule	References
Algae normal Raman	Experimentally obtained, peak ID from refs [202-203]
Fixing agent (2.5% glutaraldehyde in 0.01 M PBS)	Experimentally obtained
NAD	[197-201]
Glutathione	[195-196]
Reductase enzyme	[191-193]
Hydroxyquinoline	[194]
RNA and DNA	[29,39,189-190]
Additional references	[9,29,39,177,187-188,215]

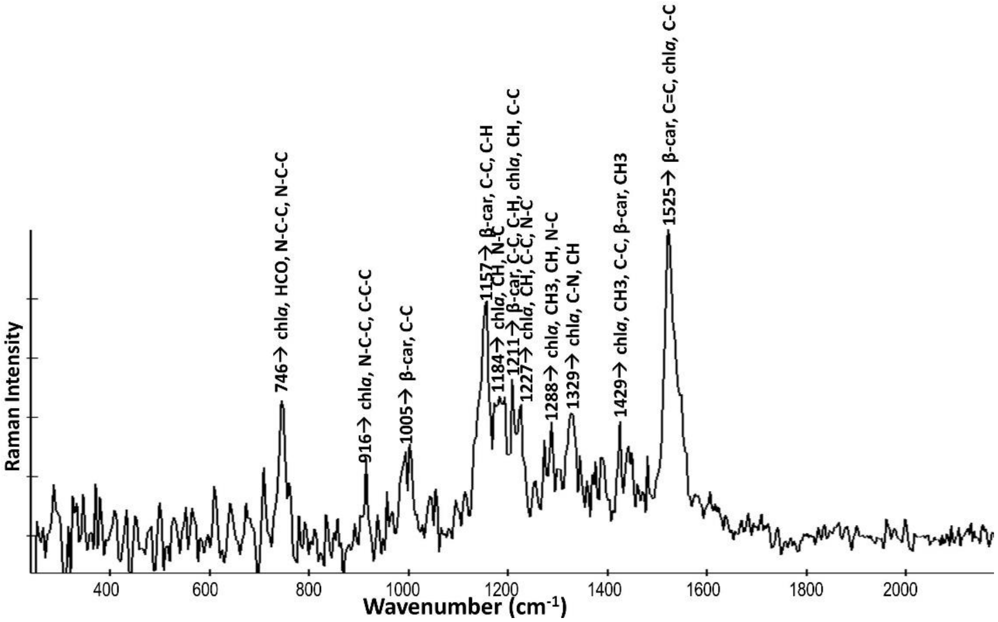

Figure SI. 5.6. Algae Normal Raman with peak identifications from Wood et al. 2005.[203]

Experimental. OECD/OCED media was prepared upon use by mixing the four stock solutions as described in **Table SI. 5.3**. All materials were autoclaved or filtered through a 0.2 μm filter to sterilize.

Table SI. 5.3. OECD/OCED Algal growth media ingredients.

Solution	*Ingredients*
Stock solution #1: Macronutrients	1.5 g/L NH_4Cl 1.2 g/L $MgCl_2 \cdot 6H_2O$ 1.8 g/L $CaCl_2 \cdot 2H_2O$ 1.5 g/L $MgSO_4 \cdot 7H_2O$ 0.16 g/L KH_2PO_4
Stock solution #2: Iron	64 mg/L $FeCl_3 \cdot 6H_2O$ 100 mg/L $Na_2EDTA \cdot 2H_2O$
Stock solution #3: Trace elements	185 mg/L H_3BO_3 415 mg/L $MnCl_2 \cdot 4H_2O$ 3 mg/L $ZnCl_2$ 1.5 mg/L $CoCl_2 \cdot 6H_2O$ 0.01 mg/L $CuCl_2 \cdot 2H_2O$ 7 mg/L $Na_2MoO_4 \cdot 2H_2O$
Stock solution #4: Bicarbonate	50 g/L $NaHCO_3$, $Na_2SiO_3 \cdot 9H_20$
Final media mix	10 mL stock solution #1 1 mL stock solution #2 1 mL stock solution #3 1 mL stock solution #4 Fill to 1 L

TEM cross-sectioning.

Established protocols were followed to process cells for TEM cross sectioning.[218-220] After filtration and fixation as described previously, samples were vortexed to free cells from filters and filters were removed. Samples were centrifuged for 5 min, re-suspended in 1 mL PBS buffer, and rinsed twice with 5 min centrifugation steps between each. Supernatant was discarded, and 1% OsO_4 in 0.1 M PBS buffer was added as an electron dense stain for 1 hr. Excess osmium stain was removed by two PBS washes with 10 minute centrifugation steps between each.

Sample tubes were placed in a warm water bath (≈55°C) alongside agar. Approximately 200 μL of agar (as little as possible) was added to sample tubes before vortexing for 2 seconds and centrifuging again for 3 minutes, creating a pellet of cells in agar. Agar partially solidified, and approximately 200 μL of 70% ethyl alcohol was added (a squirt) to facilitate removal of the sample block from the tube in a later step. Tubes were allowed to set in the fridge for 1 hr.

The agar block was scraped from the tube, excess agar removed, and cells were dehydrated with 15 minute incubations in ethanol of increasing concentrations (70%, 95%, and two incubations of 100% ethanol). After pipetting away ethanol, samples were incubated for 6-24 hours at room temperature in a 50:50 solution of 100% ethanol and Spurr's resin followed by 6-24 hours in 100% Spurr's resin. Additional 24-hour, 100% Spurr's resin infiltration steps were conducted until the agar block sank in the pure Spurr's solution. Sample blocks were then placed in a silicon sample mold (EMS 70900) with a sample label and new Spurr's resin was poured on top of the sample to fill mold. Sample blocks were cured by baking in an oven at 70°C for 16-24 hours. Cross-sections were cut with a diamond knife and ultramicrotome and placed on TEM grids.

6

Engineering Significance

THE NEED TO DETECT

There is an ever-increasing need for detection of contaminants in drinking water, air, food, and commercial products that are part of our everyday lives. With the population of the earth exceeding seven billion, we must ensure that wastes, byproducts, degradation products, and natural hazards do not contaminate valuable resources, and when they do, that early warning systems must exist to address these issues before they threaten anthropogenic and ecologic systems. The following three examples stress the need for detection method development.

- Silver nanomaterials are incorporated in clothing, personal care products, appliances, and other items we use every day as antimicrobial agents.[221-222] The leaching of nanomaterials from these products is known to occur, the extent to which can be severe, depending on the product.[223-224] Post-use degradation, transport, and long term influence on natural resources remain unclear, such that methods are needed to track low concentrations of these materials through the environment.

- The EPA maintains a Contaminant Candidate List (CCL) that highlights research needs for over 100 chemicals, chemical groups, and microbiological contaminants. For each of these, existing detection methods must be improved or developed, occurrence data must be collected, or toxicity at relevant concentrations must be studied.[225] The third list (CCL3) was published in 2009, and nominations for CCL4 were due in 2012.

- *Spirulina* is a common dietary supplement taken in the form of powder or capsules due to its high protein and ideal nutrient content.[226] This cyanobacteria often grows in the presence of other cyanobacteria that produce toxins such as the microcystins. Due to the lack of economically feasible or accessible detection methods and quality control measures, microcystin has been observed in commercially available *Spirulina* supplements at concentrations above the World Health Organization suggested limit of

1 µg/L. Unfortunately, this contamination was discovered well after products reached the market.[226]

RESPONSE- DETECTION METHOD DEVELOPMENT

Our ever increasing need to detect miniscule concentrations of organic, inorganic, and microbial species in water, air, cells, and material goods is largely being met by linking traditional instruments with detectors in new configurations, by modifying and improving immunoassays, by utilizing nanotechnology for new techniques, or by improving separation and purification techniques employed before analysis. For example, high pressure liquid chromatography-tandem mass spectrometry (HPLC-MS-MS) is one of the best options for detecting and quantifying cyanotoxin variants, an improvement on traditional high pressure liquid chromatography-mass spectrometry (HPLC-MS) methods. Microcystin-LR can also be quantified using one of many recently developed and commercially available enzyme-linked immunosorbant assays (ELISA) that have reduced analysis times and false positive rates in comparison with the first generations of microcystin ELISA kits.

Developments in Raman spectroscopy follow a similar trend. Historically Raman spectroscopy produced very low signals and required pure or high concentrations of samples.[1,3] As laser availability increased and cost decreased, the technique became more feasible to implement, but recent advancements in nanotechnology have facilitated the current boom in Raman spectroscopy use.[3] Simple separations facilitated by the coffee ring effect or Raman signal enhancements made possible by the surface plasmon resonance (SPR) of gold and silver nanomaterials allow detection of environmentally relevant concentrations of analytes without extensive pre-concentration steps.[112,121] Furthermore, the selective capacity of antibodies are often employed to tag or capture analytes in a similar fashion to ELISA methods before detection.[62] Hence, like other new detection protocols, Raman spectroscopy is an old technique matched with new protocols involving separation, nanotechnology, or the scientific principles employed by immunoassays.[1,70] Raman spectroscopy is distinguished from other techniques in its ability to detect species across multiple contaminant classes in a variety of transparent or translucent media.

A PRACTICAL PERSPECTIVE OF THE FUTURE FOR RAMAN SPECTROSCOPY

Normal Raman spectroscopy, drop coating deposition Raman spectroscopy (DCDR), and surface-enhanced Raman spectroscopy (SERS) each occupy distinct niches in terms of detection capabilities. Normal Raman spectroscopy, the simplest technique, is especially good at identifying pure compounds at high concentrations when the sample does not fluoresce.[4] DCDR extends the simplicity of normal Raman spectroscopy to solutions with analyte concentrations down to µM, even in the presence of impurities, mixtures, or small amounts of fluorescent species that co-deposit with the analyte.[20-21,227] SERS further extends the detection limits to levels as low as fM, in translucent matrixes, even in the presence of large amounts of fluorescence.[1,3] Strengths, limitations, and the near future expectations for each of these methods indicate Raman spectroscopy will continue to be valuable for analyte detection well into the future (**Table 6.1**). Not only are the reaches of Raman spectrometer applications growing, but instruments are becoming more widely available, cheaper, and more readily field deployable. Portable Raman spectrometers can now be purchased for as low as $15,000 for handheld instruments or $30,000 for portable bench top instruments. Each of the techniques used herein can be conducted to some degree with portable instruments and have the potential to be automated after establishment of a Raman based detection protocol. Therefore, we can only expect growth in Raman spectrometer use both in the laboratory and in the field.

IMPLICATIONS

Detection of any species of concern accurately, precisely, quickly, cheaply, and with less operator expertise has implications for public health, medical technology developments, resource discovery, resource preservation, and quality of life. Cheaper and simpler detection protocols that maintain reliability and accuracy will be preferentially implemented, even by those who are able to pay large premiums for detection systems. Additionally, such techniques will influence the lives of impoverished communities where the need for pollutant detection is often greatest. Indicator organisms of fecal contamination, assumptions that cyanotoxins occur most frequently where odorous compounds are also produced, and predictions of disinfection byproduct occurrence from source water quality are tremendously valuable for the protection of public health. However, if detection could be achieved of any species of concern cheaply, rapidly, reliably, accurately, and simply enough for the average high school student to conduct the analyses, we would then be a tremendous step closer to reducing exposure of the population to unwanted species, ultimately creating a healthier seven billion. The capacity of Raman spectroscopy to aid in achieving such a reality cannot be ignored.

Table 6.1. Strengths, limitations, and a practical outlook of normal Raman spectroscopy, DCDR, and SERS for future analyses.

Technique	Example analytes	Strengths	Limitations	Practical future outlook	Refs
Normal Raman spectroscopy	Concentrated or pure samples that do not fluoresce Rocks, minerals, inorganics Organic powders Concentrated liquids Polymers Art pigments Powders within human fingerprints	Complimentary nature of the results to infrared spectroscopy Detection in the presence of water Minimal expertise required Minimal sample preparation Adequacy of handheld instruments for most applications	Fluorescence overshadows Raman signals Pure or very high concentrations required Long acquisition times Tendency of samples to burn under the intense laser power required for analysis	Will continue to be useful for specific applications such as determining mineral composition or identifying unknown white powders DCDR and SERS will facilitate application of the Raman spectrometer for analysis of low analyte concentrations in environmental matrices	[1,3-6,228]
Drop coating deposition Raman (DCDR)	Solutes within liquids (i.e., salts, metals, organics, microbes) Mixtures Body fluids and proteins Cyanotoxins in environmental waters	Minimal sample preparation Short analysis times even for low concentrations (≈µM) Quantitation capabilities Remarkable separation with minimal user effort Successful mixture analysis Long term stability of DCDR sample spots	Species of similar molecular properties only partially separate Hindrance of fluorescent compounds that co-deposit with analyte Disruption of drying patterns by dust or substrate roughness	Improvements in substrate engineering, combination of DCDR with SERS, and additional research will no doubt enhance the capabilities of DCDR	[2,20,70,229]
Surface-enhanced Raman spectroscopy (SERS)	Low concentrations of any analyte that closely interacts with a noble metal nanomaterial or nanotag Organics, metals, microorganisms Air, water, solid surfaces Noble metal nanomaterials in complex matrices	Ability to detect anything that a) interacts directly with a noble-metal nanostructure or b) interacts with a SERS tag Single molecule detection Noble-metal nanostructures quench fluorescence Minimal sample preparation once an application is established Detects target analytes in the presence of similar species Noble-metal nanomaterials can be imaged in 3D in any translucent matrix Minimal gold or silver requirements (< $0.01 per analysis)[*]	Time of experienced scientists required to develop each application Development of a new tag is required for every analyte that does not associate with a noble-metal nanostructure Hindrance of background contamination that out-competes analytes for binding with the tag or noble-metal nanostructure Potential for nanomaterial surface burning when high laser powers are employed	Well-designed SERS tags can eliminate background issues, improve reproducibility, and reduce the need for specific lasers (i.e., a tag can be developed to be compatible with each available laser) Environmental samples often difficult to analyze due to competition for binding with tags Research developments are overcoming many obstacles There is no doubt that SERS will be a big player in future analyte detection protocols	[1,3]

[*] Very conservatively assuming $150 to make 5 L of 2 mM citrate-reduced AuNP (13 nm) and 100 uL per sample

Literature Cited

1. Halvorson, R. A.; Vikesland, P. J. Surface-enhanced Raman spectroscopy (SERS) for environmental analyses. *Environ. Sci. Technol.* **2010,** *44* (20), 7749-7755.
2. Halvorson, R. A.; Vikesland, P. J. Drop coating deposition Raman (DCDR) for microcystin-LR identification and quantitation. *Environ. Sci. Technol.* **2011,** *45* (13), 5644-5651.
3. Haynes, C. L.; McFarland, A. D.; Van Duyne, R. P. Surface-enhanced Raman spectroscopy. *Anal. Chem.* **2005,** *77* (17), 338A-246A.
4. Pelletier, M. J., Ed.*Analytical applications of Raman spectroscopy,* Blackwell Science: Malden, MA, 1999.
5. Haskin, L. A.; Wang, A.; Rockow, K. M.; Jolliff, B. L.; Korotev, R. L.; Viskupic, K. M. Raman spectroscopy for mineral identification and quantification for in situ planetary surface analysis: A point count method. *Journal of Geophysical Research: Planets* **1997,** *102* (E8), 19293-19306.
6. Day, J. S.; Edwards, H. G. M.; Dobrowski, S. A.; Voice, A. M. The detection of drugs of abuse in fingerprints using Raman spectroscopy I: Latent fingerprints. *Spectrochim. Acta, Part A* **2004,** *60* (3), 563-568.
7. Sengupta, A.; Laucks, M. L.; Davis, E. J. Surface-enhanced Raman spectroscopy of bacteria and pollen. *Appl. Spectrosc.* **2005,** *59* (8), 1016-1023.
8. Esmonde-White, K. A.; Mandair, G. S.; Raaii, F.; Jacobson, J. A.; Miller, B. S.; Urquhart, A. G.; Roessler, B. J.; Morris, M. D. Raman spectroscopy of synovial fluid as a tool for diagnosing osteoarthritis. *J. Biomed. Opt.* **2009,** *14* (3).
9. Halvorson, R. A.; Leng, W.; Vikesland, P. J. Differentiation of microcystin, nodularin, and their component amino acids by drop-coating deposition Raman spectroscopy. *Anal. Chem.* **2011,** *83* (24), 9273-9280.
10. Carmichael, W. W. *Assessment of blue-green algal toxins in raw and finished drinking water,* AWWA Research Foundation: Denver, CO, 2001.
11. Pearson, L.; Mihali, T.; Moffitt, M.; Kellmann, R.; Neilan, B. On the chemistry, toxicology and genetics of the cyanobacterial toxins, microcystin, nodularin, saxitoxin and cylindrospermopsin. *Mar. Drugs* **2010,** *8*, 1650-1680.
12. Van de Waal, D. B.; Verspagen, J. M. H.; Lurling, M.; Van Donk, E.; Visser, P. M.; Huisman, J. The ecological stoichiometry of toxins produced by harmful cyanobacteria: An experimental test of the carbon-nutrient balance hypothesis. *Ecol. Lett.* **2009,** *12* (12), 1326-1335.
13. Harada, K.-i.; Imanishi, S.; Kato, H.; Mizuno, M.; Ito, E.; Tsuji, K. Isolation of Adda from microcystin-LR by microbial degradation. *Toxicon* **2004,** *44*, 107-109.
14. Sivonen, K.; Jones, G. Cyanobacteria toxins. In *Toxic cyanobacteria in water: A guide to their public health consequences, monitoring and management,* Chorus, I.; Bartram, J., Eds.; E & FN Spon: London 1999; pp 55-124.
15. Christiansen, G.; Fastner, J.; Erhard, M.; Borner, T.; Dittmann, E. Microcystin biosynthesis in *Planktothrix*: Genes, evolution, and manipulation. *J. Bacteriol.* **2003,** *185* (2), 564-572.
16. Graham, J. L.; Loftin, K. A.; Kamman, N. Monitoring recreational freshwaters. *LakeLine* **2009,** *29*, 18-24.

17. McElhiney, J.; Lawton, L. Detection of the cyanobacterial hepatotoxins microcystins. *Toxicol. Appl. Pharmacol.* **2005,** *203*, 219-230.
18. Lawton, L. A., C. Edwards. Chapter 23: Conventional laboratory methods for cyanotoxins. In *Cyanobacterial harmful algal blooms: State of the science research needs*, Hudnell, H., Ed. Springer: New York 2007; pp 513-538.
19. Mukhejee, M.; Mukhopadhyay, A.; Charkraborty, T. Raman optical activity: A novel version of chiroptical spectroscopy. *Indian J. Phys.* **2008,** *82* (8), 987-1001.
20. Zhang, D.; Xie, Y.; Mrozek, M. F.; Ortiz, C.; Davisson, V. J.; Ben-Amotz, D. Raman detection of proteomic analytes. *Anal. Chem.* **2003,** *75* (21), 5703-5709.
21. Zhang, D.; Mrozek, M. F.; Xie, Y.; Ben-Amotz, D. Chemical segregation and reduction of Raman background interference using drop coating deposition. *Appl. Spectrosc.* **2004,** *58* (8), 929-933.
22. Ortiz, C.; Zhang, D.; Xie, Y.; Davisson, V. J.; Ben-Amotz, D. Identification of insulin variants using Raman spectroscopy. *Anal. Biochem.* **2004,** *332* (2), 245-252.
23. Ortiz, C.; Zhang, D.; Xie, Y.; Ribbe, A. E.; Ben-Amotz, D. Validation of the drop coating deposition Raman method for protein analysis. *Anal. Biochem.* **2006,** *353* (2), 157-166.
24. Filik, J.; Stone, N. Drop coating deposition Raman spectroscopy of protein mixtures. *Analyst* **2007,** *132* (6), 544-550.
25. Deegan, R. D.; Bakajin, O.; Dupont, T. F.; Huber, G.; Nagel, S. R.; Witten, T. A. Capillary flow as the cause of ring stains from dried liquid drops. *Nature* **1997,** *389*, 827.
26. Kopecký Jr, V.; Baumruk, V. Structure of the ring in drop coating deposited proteins and its implication for Raman spectroscopy of biomolecules. *Vib. Spectrosc* **2006,** *42* (2), 184-187.
27. Zhu, G.; Zhu, X.; Fan, Q.; Wan, X. Raman spectra of amino acids and their aqueous solutions. *Spectrochim. Acta, Part A* **2011,** *78* (3), 1187-1195.
28. Rivasseau, C.; Martins, S.; Hennion, M.-C. Determination of some physicochemical parameters of microcystins (cyanobacterial toxins) and trace level analysis in environmental samples using liquid chromatography. *J. Chromatogr. A* **1998,** *799* (1-2), 155-169.
29. Movasaghi, Z.; Rehman, S.; Rehman, I. U. Raman spectroscopy of biological tissues. *Appl. Spectrosc. Rev.* **2007,** *42* (5), 493 - 541.
30. Chinsky, L.; Jolles, B.; Laigle, A.; Turpin, P. Y. Resonance Raman spectra of poly(L-lysine), aromatic amino acids, L-histidine and native and thermally unfolded ribonuclease A. *J. Raman Spectrosc.* **1985,** *16*, 235-241.
31. Stewart, S.; Fredericks, P. M. Surface-enhanced Raman spectroscopy of amino acids adsorbed on an electrochemically prepared silver surface. *Spectrochim. Acta, Part A* **1999,** *55* (7-8), 1641-1660.
32. Simons, L.; Bergstrom, G.; Bomfelt, G.; Forss, S.; Stenbach, H.; Wansen, G. Laser Raman spectroscopy of amino acids, oligopeptides, polypeptides and enzymes. *Commentationes Physico-Mathematicae* **1972,** *42* (125), 125-207.
33. Olsztynska, S.; Dupuy, N.; Vrielynck, L.; Komorowska, M. Water evaporation analysis of L-phenylalanine from initial aqueous solutions to powder state by vibrational spectroscopy. *Appl. Spectrosc.* **2006,** *60* (9), 1040-1053.

34. Guicheteau, J.; Argue, L.; Hyre, A.; Jacobson, M.; Christesen, S. D. Raman and surface-enhanced Raman spectroscopy of amino acids and nucleotide bases for target bacterial vibrational mode identification. *Society of Photo-Optical Instrumentation Engineers (SPIE) Conference Series* **2006,** *6218*, 621800.
35. Navarrete, J. T. L.; Hernández, V.; Ramírez, F. J. Vibrational study of aspartic acid and glutamic acid dipeptides. *J. Mol. Struct.* **1995,** *348*, 249-252.
36. Asher, S. A.; Ludwig, M.; Johnson, C. R. UV resonance Raman excitation profiles of the aromatic amino acids. *J. Am. Chem. Soc.* **1986,** *108*, 3186-3197.
37. Govani, J. R.; Durrer, W. G.; Manciu, M.; Botez, C.; Manciu, F. S. Spectroscopic study of l-arginine interactions with potassium dihydrogen phosphate crystals. *J. Mater. Res.* **2009,** *24* (7), 2316-2320.
38. Facanha Filho, P. F.; Freire, P. T. C.; Lima, K. C. V.; Mendes Filho, J.; Melo, F. E. A. High temperature Raman spectra of l-leucine crystals. *Braz. J. Phys.* **2008,** *38* (1).
39. Gelder, J. D.; Gussem, K. D.; Vandenabeele, P.; Moens, L. Reference database of Raman spectra of biological molecules. *J. Raman Spectrosc.* **2007,** *38* (9), 1133-1147.
40. Ferraro, J. R.; Nakamoto, K.; Brown, C. W. *Introductory Raman spectroscopy,* second ed.; Academic Press: San Diego, CA, 1994.
41. Xu, Q.; Ye, Q.; Cai, H.; Qu, R. Determination of methanol ratio in methanol-doped biogasoline by a fiber Raman sensing system. *Sens. Actuators, B* **2010,** *146* (1), 75-78.
42. Liu, Y.; Chao, K.; Nou, X.; Chen, Y.-R. Feasibility of colloidal silver SERS for rapid bacterial screening. *Sens. Instrum. Food Qual. Saf.* **2009,** *3* (2), 100-107.
43. Bicknell-Brown, E.; Lim, B. T.; Kimura, T. Laser Raman spectroscopy of adrenal iron-sulfur apoprotein: The anomalous tyrosine residue at position 82. *Biochem. Biophys. Res. Commun.* **1981,** *101* (1), 298-305.
44. Tu, A. T. *Raman spectroscopy in biology: Principles and applications,* John Wiley & Sons, Inc.: New York, 1982.
45. Jenkins, A. L.; Larsen, R. A.; Williams, T. B. Characterization of amino acids using Raman spectroscopy. *Spectrochim. Acta, Part A* **2005,** *61* (7), 1585-1594.
46. Nielsen, C. H.; Abdali, S.; Lundbæk, J. A.; Cornelius, F. Raman spectroscopy of conformational changes in membrane-bound sodium potassium atpase. (cover story). *Spectroscopy* **2007,** *22* (2), 52-63.
47. Graham, J. L.; Loftin, K. A.; Meyer, M. T.; Ziegler, A. C. Cyanotoxin mixtures and taste-and-odor compounds in cyanobacterial blooms from the midwestern United States. *Environ. Sci. Technol.* **2010,** *44* (19), 7361-7368.
48. U.S. Department of Health and Human Services; Center for Disease Control and Prevention; National Institutes of Health. Biosafety in microbiological and biomedical laboratories. 5th ed.; U.S. Government Printing Office: Washington, D.C., 2007.
49. Borders, C. L.; Broadwater, J. A.; Bekeny, P. A.; Salmon, J. E.; Lee, A. S.; Eldridge, A. M.; Pett, V. B. A structural role for arginine in proteins: Multiple hydrogen bonds to backbone carbonyl oxygens. *Protein Sci.* **1994,** *3* (4), 541-548.
50. Dhamelincourt, P.; Ramirez, F. J. Polarized micro-Raman and FT-IR spectra of l-glutamine. *Appl. Spectrosc.* **1993,** *47* (4), 446-451.

51. Aliaga, A. E.; Garrido, C.; Leyton, P.; Diaz F, G.; Gomez-Jeria, J. S.; Aguayo, T.; Clavijo, E.; Campos-Vallette, M. M.; Sanchez-Cortes, S. SERS and theoretical studies of arginine. *Spectrochim. Acta, Part A* **2010,** *76* (5), 458-463.
52. Guicheteau, J.; Christesen, S.; Emge, D.; Tripathi, A. Bacterial mixture identification using Raman and surface-enhanced Raman chemical imaging. *J. Raman Spectrosc.* **2010,** *41* (12), 1632-1637.
53. Pearman, W. F.; Fountain, A. W. Classification of chemical and biological warfare agent simulants by surface-enhanced Raman spectroscopy and multivariate statistical techniques. *Appl. Spectrosc.* **2006,** *60*, 356-365.
54. Jarvis, R. M.; Brooker, A.; Goodacre, R. Surface-enhanced Raman scattering for the rapid discrimination of bacteria. *Faraday Discuss.* **2006,** *132*, 281-292.
55. Halvorson, R. A. Raman spectroscopy for monitoring of microcystins in water. Virginia Tech, Blacksburg, VA, 2010.
56. Meriluoto, J. A.; Spoof, L. E. Chapter 21: Cyanotoxins: Sampling, sample processing and toxin uptake. In *Cyanobacterial harmful algal blooms: State of the science and research needs,* Hudnell, K., Ed. Springer: New York 2008; pp 483-499.
57. Feng, X. G.; Ding, Z.; Wei, T.; Yuan, C. W.; Fu, D. G. Identification and determination of microcystins in source water and waterbloom sample from Meiliang Bay, Taihu Lake, China. *Biomed. Environ. Sci.* **2006,** *19* (3), 225-231.
58. Aranda-Rodriguez, R.; Kubwabo, C.; Benoit, F. M. Extraction of 15 microcystins and nodularin using immunoaffinity columns. *Toxicon* **2003,** *42* (6), 587-599.
59. Zhang, M.-m.; Pan, G.; Yan, H.; Chen, H. A method to extract algae toxin of microcystin-LR. *Journal of Environmental Science* **2004,** *16* (4), 694-696.
60. Pegram, R. A.; Humpage, A. R.; Neilan, B. A.; Runnegar, M. T.; Nichols, T.; Thacker, R. W.; Pflugmacher, S.; Etheridge, S. M.; Love, A. H. Proceedings of the Interagency, International Symposium on Cyanobacterial Harmful Algal Blooms; chapter 15: Cyanotoxins workgroup report. *Adv. Exp. Med. Biol.* **2007**, 303-368.
61. Spoof, L.; Vesterkvist, P.; Lindholm, T.; Meriluoto, J. Screening for cyanobacterial hepatotoxins, microcystins and nodularin in environmental water samples by reversed-phase liquid chromatography-electrospray ionisation mass spectrometry. *J. Chromatogr. A* **2003,** *1020* (1), 105-119.
62. Rule, K.; Vikesland, P. Surface-enhanced resonance Raman spectroscopy for the rapid detection of *Cryptosporidium parvum* and *giardia lamblia*. *Environ. Sci. Technol.* **2009,** *43*, 1147-1152.
63. Golightly, R. S.; Doering, W. E.; Natan, M. J. Surface-enhanced Raman spectroscopy and homeland security: A perfect match? *ACS Nano* **2009,** *3* (10), 2859-2869.
64. Reich, S.; Thomsen, C. Raman spectroscopy of graphite. *Philosophical Transactions of the Royal Society A* **2004,** *362*, 2271-2288.
65. Xie, Y.; Zhang, D.; Ben-Amotz, D. Protein-ligand binding detected using ultrafiltration Raman difference spectroscopy. *Anal. Biochem.* **2008,** *373* (1), 154-160.
66. Li, X.; Ballerini, D. R.; Shen, W. A perspective on paper-based microfluidics: Current status and future trends. *Biomicrofluidics* **2012,** *6* (1), 011301-13.
67. Ngo, Y. H.; Li, D.; Simon, G. P.; Garnier, G. Paper surfaces functionalized by nanoparticles. *Adv. Colloid Interface Sci.* **2011,** *163* (1), 23-38.

68. Govindarajan, A. V.; Ramachandran, S.; Vigil, G. D.; Yager, P.; Bohringer, K. F. A low cost point-of-care viscous sample preparation device for molecular diagnosis in the developing world; an example of microfluidic origami. *LChip* **2012,** *12* (1).
69. Yu, W. W.; White, I. M. A simple filter-based approach to surface enhanced Raman spectroscopy for trace chemical detection. *Analyst* **2012**.
70. Wong, T.-S.; Chen, T.-H.; Shen, X.; Ho, C.-M. Nanochromatography driven by the coffee ring effect. *Anal. Chem.* **2011,** *83* (6), 1871-1873.
71. Gesenhues, U. The mechanism of polyelectrolyte-assisted retention of tio$_2$ filler particles during paper formation. *Adv. Colloid Interface Sci.* **2011,** *162* (1–2), 1-21.
72. Moskovits, M. Surface-enhanced spectroscopy. *RvMP* **1985,** *57* (3), 783-826.
73. Homola, J. Surface plasmon resonance sensors for detection of chemical and biological species. *Chem. Rev.* **2008,** *108* (2), 462-493.
74. Daniel, M.-C.; Astruc, D. Gold nanoparticles: Assembly, supramolecular chemistry, quantum-size-related properties, and applications toward biology, catalysis, and nanotechnology. *Chem. Rev.* **2003,** *104* (1), 293-346.
75. Matthaus, C.; T. Chernenko; M. Miljkovic; Diem., M. In *Biomedical applications of confocal Raman micro-spectroscopy: Label-free monitoring of subcellular organelles and drug uptake*, WiTec Workshop: Introduction to Confocal Raman Microscopy, Ulm, Germany, Ulm, Germany, 2008.
76. Toomre, D.; Pawley, J. B. Chapter 10: Disk-scanning confocal microscopy. In *Handbook of biological confocal microscopy,* Third ed.; Pawley, J. B., Ed. Springer: New York, NY 2006.
77. Carrilho, E.; Phillips, S. T.; Vella, S. J.; Martinez, A. W.; Whitesides, G. M. Paper microzone plates. *Anal. Chem.* **2009,** *81* (15), 5990-5998.
78. Carrilho, E.; Martinez, A. W.; Whitesides, G. M. Understanding wax printing: A simple micropatterning process for paper-based microfluidics. *Anal. Chem.* **2009,** *81* (16), 7091-7095.
79. Frens, G. Controlled nucletion for the regulation of the particle size in monodiperse gold suspensions. *Nature, Phys. Sci.* **1973,** *241*, 20-22.
80. Hull, M. S.; Pati, P.; MacCuspie, R. I.; Vikesland, P. J. A persistence metric for noble metallic nanoparticles in aqueous matrices. *in progress* **2013**.
81. Hull, M. S.; Chaurand, P.; Rose, J.; Auffan, M.; Bottero, J.-Y.; Jones, J. C.; Schultz, I. R.; Vikesland, P. J. Filter-feeding bivalves store and biodeposit colloidally stable gold nanoparticles. *Environ. Sci. Technol.* **2011,** *45* (15), 6592-6599.
82. Brown, K. R.; Walter, D. G.; Natan, M. J. Seeding of colloidal Au nanoparticle solutions. 2. Improved control of particle size and shape. *Chem. Mater.* **1999,** *12* (2), 306-313.
83. Ao, L.-M.; Gao, F.; Pan, B.-F.; Cui, D.-X.; Gu, H.-C. Interaction between gold nanoparticles and bovine serum albumin or sheep antirabbit immunoglobulin g. *Chin. J. Chem* . **2006,** *24* (2), 253-256.
84. Qian, X.; Peng, X.-H.; Ansari, D. O.; Yin-Goen, Q.; Chen, G. Z.; Shin, D. M.; Yang, L.; Young, A. N.; Wang, M. D.; Nie, S. In vivo tumor targeting and spectroscopic detection with surface-enhanced Raman nanoparticle tags. *Nat Biotech* **2008,** *26* (1), 83-90.
85. Smith, D. K.; Korgel, B. A. The importance of the ctab surfactant on the colloidal seed-mediated synthesis of gold nanorods. *Langmuir* **2008,** *24* (3), 644-649.

86. Ma, R.; Levard, C.; Marinakos, S. M.; Cheng, Y.; Liu, J.; Michel, F. M.; Brown, G. E.; Lowry, G. V. Size-controlled dissolution of organic-coated silver nanoparticles. *Environ. Sci. Technol.* **2011,** *46* (2), 752-759.
87. Song, J. E.; Phenrat, T.; Marinakos, S.; Xiao, Y.; Liu, J.; Wiesner, M. R.; Tilton, R. D.; Lowry, G. V. Hydrophobic interactions increase attachment of gum arabic- and pvp-coated Ag nanoparticles to hydrophobic surfaces. *Environ. Sci. Technol.* **2011,** *45* (14), 5988-5995.
88. Silvert, P.-Y.; Herrera-Urbina, R.; Duvauchelle, N.; Vijayakrishnan, V.; Elhsissen, K. T. Preparation of colloidal silver dispersions by the polyol process. Part 1-synthesis and characterization. *J. Mater. Chem.* **1996,** *6* (4), 573-577.
89. Kennedy, A. J.; Hull, M. S.; Bednar, A. J.; Goss, J. D.; Gunter, J. C.; Bouldin, J. L.; Vikesland, P. J.; Steevens, J. A. Fractionating nanosilver: Importance for determining toxicity to aquatic test organisms. *Environ. Sci. Technol.* **2010,** *44* (24), 9571-9577.
90. Qing, S. Surface properties of cellulose and cellulose derivatives: A review. In *Model cellulosic surfaces*, Roman, M., Ed. American Chemical Society: 2009; Vol. 1019, pp 259-289.
91. Kreze, T.; Stana-Kleinschek, K.; Ribitsch, V. The sorption behaviour of cellulose fibres. *Lenzinger Berichte* **2001,** *80*, 28-33.
92. Herrington, T. M.; Petzold, J. C. An investigation into the nature of charge on the surface of papermaking woodpulps 2. Analysis of potentiometric titration data. *ColSu* **1992,** *64* (2), 109-118.
93. Stiernstedt, J. Interactions of cellulose and model surfaces. Royal Institute of Technology, Stockholm, 2006.
94. Pelton. A model of the external surface of wood pulp fibers. *Nordic Pulp & Paper Research Journal* **1993,** *08* (01), 113-119.
95. Dagaonkar, M.; Majumdar, U. Effect of fluid flow, solution chemistry and surface morphology of fibrous material on colloid filtration. *Journal of Engineered Fibers and Fabrics* **2012,** *7* (3), 62-74.
96. Leung, V. Development of paper-based devices for diagnostics and biosensing. McMaster University, Hamilton, Ontario, 2011.
97. Lu, Y.; Shi, W.; Jiang, L.; Qin, J.; Lin, B. Rapid prototyping of paper-based microfluidics with wax for low-cost, portable bioassay. *Electrophoresis* **2009,** *30* (9), 1497-1500.
98. Martinez, A. W.; Phillips, S. T.; Whitesides, G. M.; Carrilho, E. Diagnostics for the developing world: Microfluidic paper-based analytical devices. *Anal. Chem.* **2010,** *82* (1), 3-10.
99. Breton, M. P.; Malhotra, S. L.; Kovacs, G. J. Ink compositions. US Patent 6,593,398, July 15, 2003.
100. Malhotra, S. L.; Wong, R. W.; Breton, M. P. Ink compositions. US Patent 6,461,417, October 8, 2002.
101. Malhotra, S. L.; Wong, R. W.; Breton, M. P. Phase change inks. US Patent 6,306,203, October 23, 2001.
102. Noh, H.; Phillips, S. T. Metering the capillary-driven flow of fluids in paper-based microfluidic devices. *Anal. Chem.* **2010,** *82* (10), 4181-4187.

103. Fu, E. L.; Ramsey, S.; Kauffman, P.; Lutz, B.; Yager, P. Transport in two-dimensional paper networks. *Microfluid. Nanofluid.* **2011,** *10* (1), 29-35.
104. Crowe, C. T.; Elger, D. R.; Roberson, J. A.; Williams, B. C. *Engineering fluid mechanics,* Wiley: New York, 2000.
105. Mays, L. W. *Water resources engineering,* John Wiley & Sons, Inc.: Hoboken, NJ, 2005.
106. Washburn, E. W. The dynamics of capillary flow. *PhRv* **1921,** *17* (3), 273-283.
107. Osborn, J. L.; Lutz, B.; Fu, E.; Kauffman, P.; Stevens, D. Y.; Yager, P. Microfluidics without pumps: Reinventing the t-sensor and h-filter in paper networks. *LChip* **2010,** *10* (20), 2659-2665.
108. Ahuja, S. *Chromatography and separation science,* Academic Press: 2003.
109. Gao, P.; Weaver, M. J. Surface-enhanced Raman spectroscopy as a probe of adsorbate-surface bonding: Benzene and monosubstituted benzenes adsorbed at gold electrodes. *J. Phys. Chem.* **1985,** *89* (23), 5040-5046.
110. Gao, P.; Weaver, M. J. Metal-adsorbate vibrational frequencies as a probe of surface bonding: Halides and pseudohalides at gold electrodes. *J. Phys. Chem.* **1986,** *90* (17), 4057-4063.
111. Bozzini, B.; Romanello, V.; Mele, C. A SERS investigation of the electrodeposition of Au in a phosphate solution. *Surf. Coat. Technol.* **2007,** *201* (14), 6267-6272.
112. Wiley, J. H.; Atalla, R. H. Band assignments in the raman spectra of celluloses. *Carbohydr. Res.* **1987,** *160* (0), 113-129.
113. Sadler, P. J.; Tucker, A. pH-induced structural transitions of bovine serum albumin. *Eur. J. Biochem.* **1993,** *212* (3), 811-817.
114. Levy, Y.; Onuchic, J. N. Water and proteins: A love–hate relationship. *Proc. Natl. Acad. Sci. U. S. A.* **2004,** *101* (10), 3325-3326.
115. Dalgaard, P. *Introductory statistics with r,* Second ed.; Springer: New York, 2008.
116. Stana, K. K.; Pohar, C.; Ribitsch, V. Adsorption of whitening agents on cellulose fibers — monitored by streaming potential measurements, calorimetry and fluorescence. *Colloid. Polym. Sci.* **1995,** *273* (12), 1174-1178.
117. Jiang, J.; Oberdörster, G.; Biswas, P. Characterization of size, surface charge, and agglomeration state of nanoparticle dispersions for toxicological studies. *J. Nanopart. Res.* **2009,** *11* (1), 77-89.
118. van Oss, C. J. *Interfacial forces in aqueous media, second edition,* Taylor & Francis: 2006.
119. Israelachvili, J. N. *Intermolecular and surface forces,* Third ed.; Elsevier: 2011.
120. Derjaguin, B. V.; Landau, L. Theory of the stability of strongly charged lyophobic sols and of the adhesion of strongly charged particles in solutions of electrolytes. *Acta Phys. Chim. URSS* **1941,** *14*, 633-662.
121. Lifshitz, E. M. The theory of molecular attractive forces between solids. *Soviet Physics* **1956,** *2* (1), 73-83.
122. Phenrat, T.; Song, J. E.; Cisneros, C. M.; Schoenfelder, D. P.; Tilton, R. D.; Lowry, G. V. Estimating attachment of nano- and submicrometer-particles coated with organic macromolecules in porous media: Development of an empirical model. *Environ. Sci. Technol.* **2010,** *44* (12), 4531-4538.

123. El Badawy, A. M.; Scheckel, K. G.; Suidan, M.; Tolaymat, T. The impact of stabilization mechanism on the aggregation kinetics of silver nanoparticles. *Sci. Total Environ.* **2012,** *429* (0), 325-331.
124. Lefévre, G.; Jolivet, A. In *Calculation of hamaker constants applied to the deposition of metallic oxide particles at high temperature*, International Conference on Heat Exchanger Fouling and Cleaning VIII, Schladming, Austria, HMuller-Steinhagen, H.; Malayeri, M. R.; Watkinson, A. P., Eds. Heat Exchanger-Fouling: Schladming, Austria, 2009; pp 120-124.
125. Verwey, E. J. W.; Overbeek, J. T. G. *Theory of the stability of lyophobic colloids,* Elsevier: Amsterdam, 1948.
126. Adamczyk, Z.; Weroński, P. Application of the dlvo theory for particle deposition problems. *Adv. Colloid Interface Sci.* **1999,** *83* (1–3), 137-226.
127. Jaycock, M. J.; Pearson, J. L. A study of the retention of pigment during paper formation. *J. Colloid Interface Sci.* **1976,** *55* (1), 181-190.
128. Eijkel, J. T.; Berg, A. Nanofluidics: What is it and what can we expect from it? *Microfluid. Nanofluid.* **2005,** *1* (3), 249-267.
129. Michen, B.; Meder, F.; Rust, A.; Fritsch, J.; Aneziris, C.; Graule, T. Virus removal in ceramic depth filters based on diatomaceous earth. *Environ. Sci. Technol.* **2011,** *46* (2), 1170-1177.
130. Rood, D. *The troubleshooting and maintenance guide for gas chromatographers,* Wiley: 2007.
131. Panwar, V.; Kang, B.-S.; Park, J.-O.; Park, S.-H. New ionic polymer–metal composite actuators based on pvdf/pssa/pvp polymer blend membrane. *Polymer Engineering & Science* **2011,** *51* (9), 1730-1741.
132. Wu, M.; Yuan, Y. Molecular composites of polyimide/poly-n-vinylpyrrolidone by in-situ polycondensation. *Macromolecular Symposia* **1997,** *122* (1), 383-386.
133. Webb, G. A.; Kamienska-Trela, K.; Aliev, A. E. *Nuclear magnetic resonance,* Royal Society of Chemistry: 2010.
134. Masson, J.-F. Cellulose/synthetic-polymer blends. McGill University, Montréal, QC, Canada, 1990.
135. Jeon, S. I.; Lee, J. H.; Andrade, J. D.; De Gennes, P. G. Protein—surface interactions in the presence of polyethylene oxide: I. Simplified theory. *J. Colloid Interface Sci.* **1991,** *142* (1), 149-158.
136. Prime, K. L.; Whitesides, G. M. Adsorption of proteins onto surfaces containing end-attached oligo(ethylene oxide): A model system using self-assembled monolayers. *J. Am. Chem. Soc.* **1993,** *115* (23), 10714-10721.
137. Huynh, K. A.; Chen, K. L. Aggregation kinetics of citrate and polyvinylpyrrolidone coated silver nanoparticles in monovalent and divalent electrolyte solutions. *Environ. Sci. Technol.* **2011,** *45* (13), 5564-5571.
138. Sperling, R. A.; Parak, W. J. Surface modification, functionalization and bioconjugation of colloidal inorganic nanoparticles. *Philosophical Transactions of the Royal Society A: Mathematical, Physical and Engineering Sciences* **2010,** *368* (1915), 1333-1383.

139. Ohshima, H. Electrophoresis of soft particles. *Adv. Colloid Interface Sci.* **1995,** *62* (2–3), 189-235.

140. Sperling, R. A.; Liedl, T.; Duhr, S.; Kudera, S.; Zanella, M.; Lin, C. A. J.; Chang, W. H.; Braun, D.; Parak, W. J. Size determination of (bio)conjugated water-soluble colloidal nanoparticles: A comparison of different techniques. *The Journal of Physical Chemistry C* **2007,** *111* (31), 11552-11559.

141. Bharkatiya, M.; Nema, R. K.; Bhatnagar, M. Designing and characterization of drug free patches for transdermal application *International Journal of Pharmaceutical Sciences and Drug research* **2010,** *2* (1), 35-39.

142. Tobin, M. C. *Laser Raman spectroscopy,* John Wiley & Sons, Inc.: Toronto, Canada, 1971.

143. Edwards, H. G. M.; Falk, M. J. P. Fourier-transform Raman spectroscopic study of unsaturated and saturated waxes. *Spectrochim. Acta, Part A* **1997,** *53* (14), 2685-2694.

144. Mernagh, T. P.; Cooney, R. P.; Johnson, R. A. Raman spectra of graphon carbon black. *Carbon* **1984,** *22* (1), 39-42.

145. Kunjappu, J. T. Ink chemistry. In *Chemistry World*, Royal Society of Chemistry 2003.

146. Zheng, M.; Du, W. Phase behavior, conformations, thermodynamic properties, and molecular motion of multicomponent paraffin waxes: A Raman spectroscopy study. *Vib. Spectrosc* **2006,** *40* (2), 219-224.

147. Brant, J.; Labille, J.; Bottero, J.-Y.; Wiesner, M. R. Nanoparticle transport, aggregation, and deposition. In *Environmental nanotechnology applications and impacts of nanomaterials,* Wiesner, M. R.; Bottero, J.-Y., Eds.; McGraw-Hill: New York 2007; pp 231-294.

148. Zeng, Y.; Grandner, S.; Oliveira, C. L. P.; Thunemann, A. F.; Paris, O.; Pedersen, J. S.; Klapp, S. H. L.; von Klitzing, R. Effect of particle size and debye length on order parameters of colloidal silica suspensions under confinement. *Soft Matter* **2011,** *7* (22), 10899-10909.

149. Holmberg, M.; Berg, J.; Stemme, S.; Ödberg, L.; Rasmusson, J.; Claesson, P. Surface force studies of langmuir–blodgett cellulose films. *J. Colloid Interface Sci.* **1997,** *186* (2), 369-381.

150. Bergström, L.; Stemme, S.; Dahlfors, T.; Arwin, H.; Ödberg, L. Spectroscopic ellipsometry characterisation and estimation of the hamaker constant of cellulose. *Cellu* **1999,** *6* (1), 1-13.

151. Bargeman, D.; van Voorst Vader, F. Van der waals forces between immersed particles. *Journal of Electroanalytical Chemistry and Interfacial Electrochemistry* **1972,** *37* (1), 45-52.

152. Parsegian, V. A.; Weiss, G. H. Spectroscopic parameters for computation of van der waals forces. *J. Colloid Interface Sci.* **1981,** *81* (1), 285-289.

153. Biggs, S.; Mulvaney, P. Measurement of the forces between gold surfaces in water by atomic force microscopy. *The Journal of Chemical Physics* **1994,** *100* (11), 8501-8505.

154. Pinchuk, A. O. Size-dependent hamaker constant for silver nanoparticles. *The Journal of Physical Chemistry C* **2012,** *116* (37), 20099-20102.

155. Vial, J.; Carré, A. Calculation of hamaker constant and surface energy of polymers by a simple group contribution method. *Int. J. Adhes. Adhes.* **1991,** *11* (3), 140-143.

156. Bhattacharya, S. N.; Kamal, M. R.; Gupta, R. K. *Polymeric nanocomposites: Theory and practice,* Hanser Gardner Publications: 2008.

157. Prasanna, P. R. M.; Chemical, T. U.; Engineering, B. *Application of secondary nucleation models to polymorphic systems*, Tufts University: 2008.
158. Srivastava, S. N. Estimate of the hamaker constant for bovine serum albumin and a test of vold's theory of the effect of adsorption on the van der waals interaction. *Z. Phys. Chem* **1966,** *233*, 237-254.
159. Visser, J. The concept of negative hamaker coefficients. 1. History and present status. *Adv. Colloid Interface Sci.* **1981,** *15* (2), 157-169.
160. Paillusson, F.; Dahirel, V.; Jardat, M.; Victor, J. M.; Barbi, M. Effective interaction between charged nanoparticles and DNA. *Physical chemistry chemical physics : PCCP* **2011,** *13* (27), 12603-13.
161. Nelson, E. M.; Rochester, U. o. *The adsorption of DNA onto unmodified gold nanoparticles*, University of Rochester: 2008.
162. Hiemenz, P. C.; Rajagopalan, R. *Principles of colloid and surface chemistry*, Third ed.; CRC Press: Boca Raton, VL, 1997.
163. Fleischmann, M.; Hendra, P. J.; McQuillan, A. J. Raman spectra of pyridine adsorbed at a silver electrode. *Chem. Phys. Lett.* **1974,** *26*, 163-166.
164. Ravindranath, S. P.; Henne, K. L.; Thompson, D. K.; Irudayaraj, J. Raman chemical imaging of chromate reduction sites in a single bacterium using intracellularly grown gold nanoislands. *ACS Nano* **2011,** *5* (6), 4729-4736.
165. Focsan, M.; Ardelean, I. I.; Craciun, C.; Astilean, S. Interplay between gold nanoparticle biosynthesis and metabolic activity of cyanobacterium *Synechocystis* sp. PCC 6803. *Nanotechnology* **2011,** *22* (48), 485101.
166. McAughtrie, S.; Lau, K.; Faulds, K.; Graham, D. 3d optical imaging of multiple SERS nanotags in cells. *Chem. Sci.* **2013,** *4* (9), 3566-3572.
167. Kneipp, J.; Kneipp, H.; Wittig, B.; Kneipp, K. Novel optical nanosensors for probing and imaging live cells. *Nanomed. Nanotechnol. Biol. Med.* **2010,** *6* (2), 214-226.
168. Abbas, A.; Josefson, M.; Nylund, G. M.; Pavia, H.; Abrahamsson, K. Chemical images of marine bio-active compounds by surface enhanced Raman spectroscopy and transposed orthogonal partial least squares (t-opls). *Anal. Chim. Acta* **2012,** *737* (0), 37-44.
169. Jarvis, R. M.; Law, N.; Shadi, I. T.; O'Brien, P.; Lloyd, J. R.; Goodacre, R. Surface-enhanced Raman scattering from intracellular and extracellular bacterial locations. *Anal. Chem.* **2008,** *80* (17), 6741-6746.
170. Shamsaie, A.; Jonczyk, M.; Sturgis, J.; Robinson, J. P.; Irudayaraj, J. Intracellularly grown gold nanoparticles as potential surface-enhanced Raman scattering probes. *J. Biomed. Opt.* **2007,** *12* (2), 020502.
171. Huang, H.; Chen, W.; Pan, J.; Chen, Q.; Feng, S.; Yu, Y.; Chen, Y.; Su, Y.; Chen, R. SERS spectra of a single nasopharyngeal carcinoma cell based on intracellularly grown and passive uptake Au nanoparticles. *Spectroscopy* **2011,** *26* (3), 187-194.
172. Liu, Z.; Hu, C.; Li, S.; Zhang, W.; Guo, Z. Rapid intracellular growth of gold nanostructures assisted by functionalized graphene oxide and its application for surface-enhanced Raman spectroscopy. *Anal. Chem.* **2012,** *84* (23), 10338-10344.
173. Lengke, M. F.; Ravel, B.; Fleet, M. E.; Wanger, G.; Gordon, R. A.; Southam, G. Mechanisms of gold bioaccumulation by filamentous cyanobacteria from gold(III)−chloride complex. *Environ. Sci. Technol.* **2006,** *40* (20), 6304-6309.

174. Parial, D.; Patra, H.; Roychoudhury, P.; Dasgupta, A.; Pal, R. Gold nanorod production by cyanobacteria—a green chemistry approach. *J. Appl. Phycol.* **2012,** *24* (1), 55-60.
175. Lengke, M. F.; Fleet, M. E.; Southam, G. Morphology of gold nanoparticles synthesized by filamentous cyanobacteria from gold(I)−thiosulfate and gold(III)−chloride complexes. *Langmuir* **2006,** *22* (6), 2780-2787.
176. Klaus, T.; Joerger, R.; Olsson, E.; Granqvist, C.-G. Silver-based crystalline nanoparticles, microbially fabricated. *Proc. Natl. Acad. Sci. U. S. A.* **1999,** *96* (24), 13611-13614.
177. Das, N. Recovery of precious metals through biosorption — a review. *Hydrometallurgy* **2010,** *103* (1–4), 180-189.
178. Mata, Y. N.; Torres, E.; Blázquez, M. L.; Ballester, A.; González, F.; Muñoz, J. A. Gold(III) biosorption and bioreduction with the brown alga *fucus vesiculosus*. *J. Hazard. Mater.* **2009,** *166* (2–3), 612-618.
179. Brayner, R.; Barberousse, H.; Hemadi, M.; Djedjat, C.; Yéprémian, C.; Coradin, T.; Livage, J.; Fiévet, F.; Couté, A. Cyanobacteria as bioreactors for the synthesis of Au, Ag, Pd, and Pt nanoparticles via an enzyme-mediated route. *J. Nanosci. Nanotechnol.* **2007,** *7* (8), 2696-2708.
180. Konishi, Y.; Tsukiyama, T.; Tachimi, T.; Saitoh, N.; Nomura, T.; Nagamine, S. Microbial deposition of gold nanoparticles by the metal-reducing bacterium *shewanella algae*. *Electrochim. Acta* **2007,** *53* (1), 186-192.
181. Durán, N.; Marcato, P. D.; Durán, M.; Yadav, A.; Gade, A.; Rai, M. Mechanistic aspects in the biogenic synthesis of extracellular metal nanoparticles by peptides, bacteria, fungi, and plants. *Appl. Microbiol. Biotechnol.* **2011,** *90*, 1609-1624.
182. Rai, M. *Metal nanoparticles in microbiology*, Springer Berlin Heidelberg: 2011.
183. Das, S. K.; Liang, J.; Schmidt, M.; Laffir, F.; Marsili, E. Biomineralization mechanism of gold by zygomycete fungi *rhizopous oryzae*. *ACS Nano* **2012,** *6* (7), 6165-6173.
184. Ting, Y. P.; Teo, W. K.; Soh, C. Y. Gold uptake by *chlorella vulgaris*. *J. Appl. Phycol.* **1995,** *7*, 97-100.
185. Ahmad, A.; Senapati, S.; Khan, M. I.; Kumar, R.; Ramani, R.; Srinivas, V.; Sastry, M. Intracellular synthesis of gold nanoparticles by a novel alkalotolerant actinomycete, *rhodococcus* species. *Nanotechnology* **2003,** *14* (7), 824.
186. Belazi, D.; Solé-Domènech, S.; Johansson, B.; Schalling, M.; Sjövall, P. Chemical analysis of osmium tetroxide staining in adipose tissue using imaging tof-sims. *Histochem. Cell Biol.* **2009,** *132* (1), 105-115.
187. Grow, A. E. Label-free fingerprinting of pathogens by Raman spectroscopy techniques. In *Principles of bacterial detection: Biosensors, recognition receptors and microsystems: Biosensors, recognition receptors, and microsystems*, Zourob, M.; Elwary, S.; Turner, A., Eds.; Springer: New York, NY 2008; pp 525-566.
188. Rospendowski, B. N.; Kelly, K.; Wolf, C. R.; Smith, W. E. Surface-enhanced resonance Raman scattering from cytochromes p-450 adsorbed on citrate-reduced silver sols. *J. Am. Chem. Soc.* **1991,** *113* (4), 1217-1225.
189. Muntean, C. M.; Leopold, N.; Halmagyi, A.; Valimareanu, S. Surface-enhanced Raman scattering assessment of DNA from leaf tissues adsorbed on silver colloidal nanoparticles. *J. Raman Spectrosc.* **2013,** *44* (6), 817-822.

190. Chan, J. W.; Taylor, D. S.; Zwerdling, T.; Lane, S. M.; Ihara, K.; Huser, T. Micro-Raman spectroscopy detects individual neoplastic and normal hematopoietic cells. *Biophys. J.* **2006,** *90* (2), 648-656.
191. Kuznetsova, S.; Knaff, D. B.; Hirasawa, M.; Sétif, P.; Mattioli, T. A. Reactions of spinach nitrite reductase with its substrate, nitrite, and a putative intermediate, hydroxylamine. *Biochemistry (Mosc).* **2004,** *43* (33), 10765-10774.
192. Ondrias, M. R.; Carson, S. D.; Hirasawa, M.; Knaff, D. B. Characterization of the siroheme active site in spinach nitrite reductase by resonance Raman spectroscopy. *Biochimica et Biophysica Acta (BBA) - Protein Structure and Molecular Enzymology* **1985,** *830* (2), 159-163.
193. Dooley, D. M.; Moog, R. S.; Liu, M. Y.; Payne, W. J.; LeGall, J. Resonance Raman spectra of the copper-sulfur chromophores in *achromobacter cycloclastes* nitrite reductase. *J. Biol. Chem.* **1988,** *263* (29), 14625-14628.
194. Chowdhury, J.; Ghosh, M.; Mukherjee, K. M.; Misra, T. N. pH dependent surface enhanced Raman scattering of molecules adsorbed on silver hydrosol. *Internet J. Vib. Spectro.* **2000,** *4* (2), 7.
195. Deckert-Gaudig, T.; Bailo, E.; Deckert, V. Tip-enhanced Raman scattering (ters) of oxidised glutathione on an ultraflat gold nanoplate. *Phys. Chem. Chem. Phys.* **2009,** *11* (34), 7360-7362.
196. Huong, P. V. Metallo-organic complexes and carcinogenesis. In *Molecules in physics, chemistry and biology: Molecular phenomena in biological sciences*, Maruani, J., Ed. Kluwer Academic Publishers: Dordrecht, The Netherlands 1989; pp 87-109.
197. Xiao, Y.-J.; Chen, Y.-F.; Gao, X.-X. Comparative study of the surface enhanced near infrared Raman spectra of adenine and nad+ on a gold electrode. *Spectrochim. Acta, Part A* **1999,** *55* (6), 1209-1218.
198. Xiao, Y.-J.; Wang, T.; Wang, X.-Q.; Gao, X.-X. Surface-enhanced near-infrared Raman spectroscopy of nicotinamide adenine dinucleotides on a gold electrode. *J. Electroanal. Chem.* **1997,** *433* (1–2), 49-56.
199. Zheng, J.; Chen, Y. Q.; Callender, R. A study of the binding of nadp coenzymes to dihydrofolate reductase by Raman difference spectroscopy. *Eur. J. Biochem.* **1993,** *215* (1), 9-16.
200. Chen, D.; Yue, K. T.; Martin, C.; Rhee, K. W.; Sloan, D.; Callender, R. Classical Raman spectroscopic studies of nadh and nad+ bound to liver alcohol dehydrogenase by difference techniques. *Biochemistry (Mosc).* **1987,** *26* (15), 4776-4784.
201. Austin, J. C.; Hester, R. E. Surface-enhanced Raman spectroscopy of nad+ and related compounds. *Journal of the Chemical Society, Faraday Transactions 1: Physical Chemistry in Condensed Phases* **1989,** *85* (5), 1159-1168.
202. Huang, Y. Y.; Beal, C. M.; Cai, W. W.; Ruoff, R. S.; Terentjev, E. M. Micro-Raman spectroscopy of algae: Composition analysis and fluorescence background behavior. *Biotechnol. Bioeng.* **2010,** *105* (5), 889-898.
203. Wood, B. R.; Heraud, P.; Stojkovic, S.; Morrison, D.; Beardall, J.; McNaughton, D. A portable Raman acoustic levitation spectroscopic system for the identification and environmental monitoring of algal cells. *Anal. Chem.* **2005,** *77* (15), 4955-4961.

204. Sengupta, A.; Mujacic, M.; Davis, E. Detection of bacteria by surface-enhanced Raman spectroscopy. *Anal. Bioanal. Chem.* **2006,** *386* (5), 1379-1386.
205. Zeiri, L.; Bronk, B. V.; Shabtai, Y.; Eichler, J.; Efrima, S. Surface-enhanced Raman spectroscopy as a tool for probing specific biochemical components in bacteria. *Appl. Spectrosc.* **2004,** *58* (1), 33-40.
206. Bossuyt, B. T. A.; Janssen, C. R. Long-term acclimation of *pseudokirchneriella subcapitata* (korshikov) hindak to different copper concentrations: Changes in tolerance and physiology. *Aquat. Toxicol.* **2004,** *68* (1), 61-74.
207. Vijayaraghavan, K.; Mahadevan, A.; Sathishkumar, M.; Pavagadhi, S.; Balasubramanian, R. Biosynthesis of Au(0) from Au(III) via biosorption and bioreduction using brown marine alga *turbinaria conoides*. *Chem. Eng. J.* **2011,** *167* (1), 223-227.
208. Kumar, S. A.; Abyaneh, M. K.; Gosavi, S. W.; Kulkarni, S. K.; Ahmad, A.; Khan, M. I. Sulfite reductase-mediated synthesis of gold nanoparticles capped with phytochelatin. *Biotechnol. Appl. Biochem.* **2007,** *047* (4), 191-195.
209. Prasad, M. N. V. *Metals in the environment: Analysis by biodiversity,* Marcel Dekker: 2001.
210. Nelson, E. M.; Rothberg, L. J. Kinetics and mechanism of single-stranded DNA adsorption onto citrate-stabilized gold nanoparticles in colloidal solution. *Langmuir* **2011,** *27* (5), 1770-1777.
211. Zhang, Y. X.; Zheng, J.; Gao, G.; Kong, Y. F.; Zhi, X.; Wang, K.; Zhang, X. Q.; Cui, D. X. Biosynthesis of gold nanoparticles using chloroplasts. *Int. J. Nanomed.* **2011,** *6*, 2899-2906.
212. Barazzouk, S.; Bekale, L.; Hotchandani, S. Enhanced photostability of chlorophyll-*a* using gold nanoparticles as an efficient photoprotector. *J. Mater. Chem.* **2012,** *22* (48), 25316-25324.
213. Ma, X.; Geiser-Lee, J.; Deng, Y.; Kolmakov, A. Interactions between engineered nanoparticles (enps) and plants: Phytotoxicity, uptake and accumulation. *Sci. Total Environ.* **2010,** *408* (16), 3053-3061.
214. Kumar, S. A.; Abyaneh, M. K.; Gosavi, S. W.; Kulkarni, S. K.; Pasricha, R.; Ahmad, A.; Khan, M. I. Nitrate reductase-mediated synthesis of silver nanoparticles from $agno_3$. *Biotechnol. Lett* **2007,** *29* (3), 439-445.
215. Duran, N.; Marcato, P.; Alves, O.; De Souza, G.; Esposito, E. Mechanistic aspects of biosynthesis of silver nanoparticles by several *fusarium oxysporum* strains. *J. Nanobiotechnol.* **2005,** *3* (1), 8.
216. Bantz, K. C.; Meyer, A. F.; Wittenberg, N. J.; Im, H.; Kurtuluş, Ö.; Lee, S. H.; Lindquist, N. C.; Oh, S.-H.; Haynes, C. L. Recent progress in SERS biosensing. *Phys. Chem. Chem. Phys.* **2011,** *13* (24), 11551-11567.
217. OECD. *Test no. 201: Freshwater alga and cyanobacteria, growth inhibition test,* OECD Publishing: 2011.
218. Lowe, K. Tem training and sample processing at the virginia-maryland regional college of veterinary medicine morphology service laboratory. Blacksburg, VA, 2012.
219. Polysciences, I. Spurr low-viscosity embedding media: Technical data sheet 127. 2010.
220. Spurr, A. R. A low-viscosity epoxy resin embedding medium for electron microscopy. *J. Ultrastruct. Res.* **1969,** *26* (1–2), 31-43.

221. Woodrow Wilson International Center for Scholars. The project on emerging nanotechnologies: Consumer products inventory. http://www.nanotechproject.org/inventories/consumer/.
222. Felcher, E. M. The consumer product safety commission and nanotechnology. *PEN 14* **2008,** (August).
223. Quadros, M. E.; Pierson, R.; Tulve, N. S.; Willis, R.; Rogers, K.; Thomas, T. A.; Marr, L. C. Release of silver from nanotechnology-based consumer products for children. *Environ. Sci. Technol.* **2013,** *47* (15), 8894-8901.
224. Quadros, M. E.; Marr, L. C. Silver nanoparticles and total aerosols emitted by nanotechnology-related consumer spray products. *Environ. Sci. Technol.* **2011,** *45* (24), 10713-10719.
225. EPA. Drinking water contaminant candidate list 3 (ccl3). *Fed. Regist.* **2009,** *74* (194), 51850-51862.
226. Marles, R. J.; Barrett, M. L.; Barnes, J.; Chavez, M. L.; Gardiner, P.; Ko, R.; Mahady, G. B.; Dog, T. L.; Sarma, N. D.; Giancaspro, G. I.; Sharaf, M.; Griffiths, J. United States pharmacopeia safety evaluation of *Spirulina*. *Crit. Rev. Food Sci. Nutr.* **2011,** *51* (7), 593-604.
227. Cipriani, P.; Ben-Amotz, D. Characterization of select members of the taxane family using Raman spectroscopy. *J. Raman Spectrosc.* **2005,** *36* (11), 1052-1058.
228. Hajjou, M.; Qin, Y.; Bradby, S.; Bempong, D.; Lukulay, P. Assessment of the performance of a handheld Raman device for potential use as a screening tool in evaluating medicines quality. *J. Pharm. Biomed. Anal.* **2013,** *74* (0), 47-55.
229. Filik, J.; Stone, N. Analysis of human tear fluid by Raman spectroscopy. *Anal. Chim. Acta* **2008,** *616* (2), 177-184.
230. Falconer, I. R. *Cyanobacterial toxins of drinking water supplies,* CRC Press: Boca Raton, Florida, 2005.
231. Chorus, I. *Cyanotoxins: Occurrence, causes, consequences,* Springer-Verlag: Berlin, 2001.
232. Codd, G.; Morrison, L.; Metcalf, J. Cyanobacterial toxins: Risk management for health protection. *Toxicol. Appl. Pharmacol.* **2005,** *203*, 264-272.
233. Djaoued, Y.; Balaji, S.; Priya, S. Non-resonance micro-Raman spectroscopic studies on crystalline domoic acid and its aqueous solutions. *Spectrochim. Acta, Part A* **2007,** *67* (5), 1362-1369.
234. Reichman, W.; et al. Confocal fluorescence and Raman microscopy of femtosecond laser-modified fused silica. *J. Phys.: Condens. Matter* **2003,** *15* (31), S2447.
235. Behrens, H.; Roux, J.; Neuville, D. R.; Siemann, M. Quantification of dissolved h2o in silicate glasses using confocal microraman spectroscopy. *Chem. Geol.* **2006,** *229*, 96-112.
236. Mahapatra, M. K.; Lu, K. Effects of nickel on network structure and thermal properties of a new solid oxide cell seal glass. *J. Power Sources* **2008,** *185*, 993-1000.
237. Walrafen, G. E.; Stone, J. Raman spectral characterization of pure and doped fused silica optical fibers. *Appl. Spectrosc.* **1975,** *29*, 337-344.
238. Eliasson, C.; Macleod, N. A.; Jayes, L. C.; Clarke, F. C.; Hammond, S. V.; Smith, M. R.; Matousek, P. Non-invasive quantitative assessment of the content of pharmaceutical capsules using transmission Raman spectroscopy. *J. Pharm. Biomed. Anal.* **2008,** *47* (2), 221-229.

239. Esmonde-White, K. A.; Le Clair, S. V.; Roessler, B. J.; Morris, M. D. Effect of conformation and drop properties on surface-enhanced Raman spectroscopy of dried biopolymer drops. *Appl. Spectrosc.* **2008,** *62* (5), 503-511.
240. Ortiz, C.; Zhang, D.; Ribbe, A. E.; Xie, Y.; Ben-Amotz, D. Analysis of insulin amyloid fibrils by Raman spectroscopy. *Biophys. Chem.* **2007,** *128* (2-3), 150-155.
241. Shi, H.-X.; Qu, J.-H.; Wang, A.-M.; Ge, J.-T. Degradation of microcystins in aqueous solution with in situ electrogenerated active chlorine. *Chemosphere* **2005,** *60* (3), 326-333.
242. Jones, G. J.; Orr, P. T. Release and degradation of microcystin following algicide treatment of a microcystis aeruginosa bloom in a recreational lake, as determined by hplc and protein phosphatase inhibition assay. *Water Res.* **1994,** *28* (4), 871-876.
243. Ashton, L.; Dusting, J.; Imomoh, E.; Balabani, S.; Blanch, E. W. Shear-induced unfolding of lysozyme monitored in situ. *Biophys. J.* **2009,** *96*, 4231-4236.
244. WiTec. Witec alpha 500 user manual. 2008.
245. Lastek. Horiba jobin-yvon labram hr high resolution Raman spectrometer; http://www.Lastek.Com.Au/content/view/233/748/. Accessed 1/15/2011.
246. Hendra, P.; Jones, C.; Warnes, G. *Fourier transform Raman spectroscopy : Instrumentation and chemical applications,* Ellis Horwood: New York, 1991.

Appendix A: Microcystin-LR Detection in Environmental Waters at Environmentally Relevant Concentrations

*Rebecca A. Halvorson and Peter J. Vikesland**

Department of Civil and Environmental Engineering and Institute of Critical Technology and
Applied Science (ICTAS), Virginia Tech, 418 Durham Hall, Blacksburg, VA 24060-0246
* pvikes@vt.edu, tel. 540-231-3568

Reproduced with permission from
Environmental Science and Technology **2011**, 45 (13): 5644-5651.

Chapter three includes the environmentally relevant analyses from the 2011 *Environmental Science and Technology* article “Drop coating deposition Raman (DCDR) for microcystin-LR identification and quantitation” by Halvorson and Vikesland that were not included in the M.S. thesis of R.H. Lahr.[2,55] The full article is included herein for reference.

ABSTRACT

A drop coating deposition Raman (DCDR) method was developed for the analysis of 2-200 ng samples of microcystin-LR (MC-LR), a ubiquitous and deadly hepatotoxin secreted by cyanobacteria. Solid phase extraction (SPE) of the toxin from a water sample enabled identification of MC-LR at 5 μg/L to 100 mg/L concentrations and the collected results suggest lower detection limits can be readily attained following DCDR substrate modification. The DCDR process was applied to aqueous sample volumes of 0.5-20 μL that generated sample deposits from which MC-LR Raman spectra could be obtained within seconds. Larger volume samples were not required to improve spectral resolution. Volumes of 2 μL were ideal, producing “coffee-ring” MC-LR deposits that displayed distinct MC-LR Raman signals with high signal to noise within 1 s for a 200 ng sample and 300 s for a 2 ng sample. A linear correlation between Raman signal intensity and concentration was observed for 2-100 ng MC-LR samples after signal normalization. Reproducible MC-LR Raman spectra were collected from both fresh and aged samples. The presence of dissolved organic matter (DOM) did not preclude

MC-LR identification in DCDR deposits of 3 µg DOM mixed with 0.7 µg MC-LR. Application of DCDR to environmental samples will require sample purification such as SPE before analysis, including critical cartridge wash and toxin rinsing steps. Raman based methods may one day facilitate simpler and faster sample throughput than traditional MC-LR detection methods.

INTRODUCTION

Contamination of drinking water by cyanobacteria (blue-green algae) and their neurotoxic, hepatotoxic, cytotoxic, and gastrointestinal toxins is a significant health risk in freshwaters (e.g., reservoirs, lakes, rivers) used for drinking water supply throughout the world.[16,230-232] The World Health Organization (WHO) has recommended an action level of 1 µg/L for microcystin-LR (MC-LR), one of the most commonly observed cyanotoxins. Unfortunately, MC-LR and the other cyanotoxins are not always completely removed by conventional drinking water treatment processes.[10,231] Monitoring programs that have been implemented for cyanotoxin detection are hindered by the prevalence of >80 structurally similar forms of microcystin that cannot easily be differentiated by most conventional methods, the overlapping UV-Vis profiles of the microcystin variants, the common occurrence of false positives and negatives in microcystin immunoassays, the lack of variant discrimination in enzyme inhibition assays, and the cost and expertise required to run LC-MS/MS instruments for large numbers of samples.[12,16] A dire need exists for a microcystin detection method that can provide rapid, reliable, cost effective, and accurate results. Such a method would allow monitoring programs to identify problematic water bodies before the public is exposed to the toxins.

Raman spectroscopy provides unique fingerprint spectra that reflect the molecular bond vibrations of polarizable molecules. Raman measurements can be made in aqueous matrices, with portable spectrometers, through glass or plastic, and can be non-destructive under many circumstances.[4] As a vibrational spectroscopic technique, Raman spectroscopy can identify subtle molecular differences such as chirality or local molecular environment, and can easily distinguish between the variant amino acids in different microcystins (e.g., leucine, arginine, alanine, phenylalanine, tryptophan).[4,19,39]

Historically, Raman spectroscopy has not been applied for routine monitoring in the environmental field because of characteristically low intensity Raman signals and background fluorescence that can overshadow the analyte Raman signal. Recently, however, a drop coating deposition Raman (DCDR) method has facilitated successful analysis of human, bovine, and porcine insulin, lysozyme, glucose, glycan, taxane, domoic acid, human tear fluid, and the synovial fluid of osteoarthritis patients, among other biomolecules at low concentrations, even in the presence of fluorescing matrices and mixtures.[8,20,22,24,227,233] DCDR involves application of a few microliters of a sample solution to a substrate with a low solvent affinity and the absence of interfering Raman signals, absorbance, or adverse reflections. PTFE coated stainless steel, quartz, coated or uncoated glass, calcium fluoride slides, and gold foil are all effective DCDR substrates.[20,23-24] As a drop of sample dries on a substrate, it leaves a “coffee-ring” of residue outlined by the pinned drop perimeter. This residue contains a majority of the sample conveniently concentrated at the drop edge.[20,25] Raman analysis has shown that the DCDR sample drying process can segregate mixtures of analytes, fluorescing impurities, or buffer components from analytes such that the inner portion of the residue contains more soluble or less dense components such as sugars or buffer components, while the outer edge of the sample deposit is composed of denser proteins.[21,23-24] Partial least squares (PLS) regression and principal component analysis (PCA) can be used to distinguish DCDR spectra of human, bovine, and porcine insulin as well as lysozyme, lactoferrin, and albumin proteins in human tear fluid.[22,24] Concentrations of lysozyme, lactoferrin, and albumin in mixtures analyzed by DCDR were also predicted by PCA with root-mean-square errors of ≈10%.[24]

Despite the capabilities of DCDR, a sample purification and pre-concentration step will be required for DCDR to be successful for the analysis of MC-LR at environmentally relevant concentrations. Solid phase extraction (SPE) using octadecyl silanised (C18) cartridges is routinely employed as a pre-concentration and purification step for analysis of plant, animal, or complex water samples containing MC-LR.[17] An ISO standard (ISO 20179:2005) exists for reverse-phase SPE and HPLC of microcystins-LR, -RR, and –YR.[56] The current study provides evidence that the DCDR method can be applied for rapid analysis and quantitation of samples containing MC-LR at quantities as low as 2 ng, even if this mass of material must be obtained after a solid phase extraction (SPE) step.

EXPERIMENTAL

MC-LR was purchased from Enzo Life Sciences (ALX-350-012) and was used without further purification. Volumes of 0.5-20 µL containing 1-100 mg/L MC-LR were applied to quartz substrates and allowed to air dry in a fume hood. Raman spectra of a dried 100 mg/L sample were collected on two instruments to optimize the instrument parameters for MC-LR Raman analysis: 1) A WiTec Alpha500R AFM Raman spectrometer with a UHTS300 spectrometer, DU 401 BR-DD CCD camera, 10× and 100× microscope objectives, 300 and 1200 gr/mm gratings, a TOPTICA XTRA diode 785 nm laser, and a 633 nm He-Ne laser; and 2) A JY Horiba LabRAM HR 800 spectrometer with an Olympus BX-41 petrographic microscope, an Andor electronically cooled CCD detector, 10× and 100× microscope objectives, 600 gr/mm grating, a 514 nm laser, and a 633 nm He-Ne laser. The UV-Vis spectrum of MC-LR was collected on a Varian Cary 5000 spectrophotometer between 200 and 900 nm. All subsequent Raman spectra were collected with the WiTec instrument, 785 nm laser, and 300 gr/mm grating (**Figure SI.A. 1** & **Figure SI.A. 2**).

Optical images and Raman spectra of sample deposits of interest were collected using 10× and 100× microscope objectives. Raman spectral maps 6 µm wide by 50-100 µm long were collected perpendicularly to the sample residue ridge with 1 s acquisitions per spectrum, 2 spectra per µm perpendicular to the drop edge, and 1 spectra per 2 µm parallel to the drop edge. The Raman laser probed approximately 0.5 µm laterally during each acquisition using the 785 nm laser and a microscope objective with a numerical aperture of 0.9 (see the SI for details). The shorter maps were collected for samples with narrower sample ridges formed by drop coating deposition.

Low concentration (1-10 mg/L) samples were also probed with 30 s and 300 s acquisitions per spectrum across Raman spectral maps in the same region. The point of most intense Raman signal in each Raman spectral map was probed to obtain a single Raman spectrum based upon the average of 10 spectra collected with 5 s acquisitions per spectrum. Additional Raman spectral maps of varying sizes were collected at points of interest. WiTec Project 2.0 software was used to extract the average spectrum across the sample drop edge and subsequently for the quartz background for each spectral map. Spectra were compared before and after the quartz background was subtracted from the sample Raman signal. Samples were stored at room temperature in the dark after analysis and re-analyzed following storage to assess sample stability. Image J software was used to estimate drop sizes from optical images and sample ridge thicknesses from Raman spectral maps. PLS regressions were computed using MATLAB 7.10 (R2010a) and the Statistics Toolbox 7.3 (R2010a).

Dissolved organic matter (DOM) was extracted from the Great Dismal Swamp in North Carolina by freeze drying swamp water after pretreatment thru a cascade of filters down to a pore size of 0.45 µm. DOM was rehydrated and mixed thoroughly with MC-LR before application onto quartz substrates.

Samples of 2-500 mL containing 5 mg/L, 10 µg/L, and 5 µg/L MC-LR were extracted with 6 mL Empore™ C18 and 3 mL Oasis® Waters SPE cartridges. The cartridge washing protocol included sequential 6 mL washes of methanol, nanopure water, methanol, and water again before application of the toxin to the cartridge; however, additional washing protocols were considered. Two to five hundred milliliters of aqueous MC-LR solutions were applied to cartridges at slow drip rates (<5 mL/min) before the toxin was eluted by 11 mL of methanol. The methanol was evaporated from the SPE elutant by heating to 45° C under nitrogen. Sample vials were rinsed with 1.5 mL of methanol and the samples transferred to smaller amber vials, from which the methanol was completely evaporated again as above. The toxin residue was finally dissolved in 100 µL of nanopure water, thoroughly vortexed and shaken, and briefly centrifuged for a few seconds to produce the solution analyzed by DCDR.

Water from the New River at McCoy Falls, Virginia was collected on 3/4/2011 and filtered through a series of filters to a final pore size of 0.45 µm. New River water samples were spiked to 10 µg/L MC-LR prior to SPE and DCDR.

RESULTS & DISCUSSION

MC-LR drop volumes of 0.5-20 µL at 100 mg/L concentrations (without SPE) dried in characteristic “coffee-ring” shapes expected for the DCDR method (**Figure A. 1**).[23,25] The rings were systematically analyzed by collecting Raman spectral maps of the sample surface. The Raman spectrum of MC-LR alone was isolated by subtracting the Raman spectrum of the quartz substrate from the spectrum of the sample (**Figure A. 1**).

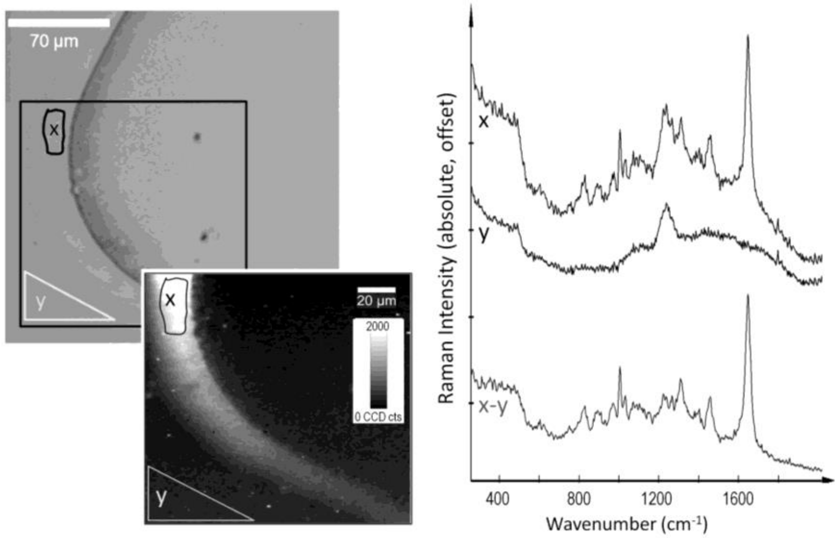

Figure A. 1. Optical images of DCDR samples display a “coffee-ring” residue deposit (left panel). MC-LR Raman signals are strong along the DCDR sample ridge (x). The region inside the ring and outside the ring exhibit quartz Raman signals only (y; center panel). The Raman spectral map of the region outlined in the optical image was created by tracking the intensity of the 1006 cm^{-1} Raman peak (produced by aromatic ring vibrations in the Adda portion of MC-LR; right panel). Thirty thousand spectra of 1 s acquisition/spectra were collected to create the spectral map.

Raman peaks were assigned to their corresponding molecular vibrational origins (**Table A. 1**). The most intense MC-LR Raman peaks include carboxylate vibrations observed at 1645 cm^{-1}, symmetric aromatic ring breathing modes at 1006 cm^{-1}, and CH_3/CH_2 modes at 1307 cm^{-1}.[29-31] A quartz substrate was chosen because quartz exhibits minimal overlap with the MC-LR Raman spectrum while simultaneously producing a Raman spectrum that could be used for signal normalization (**Table A. 2**). In addition, quartz substrates are generally readily available in analytical laboratories. Experimental results suggest that the Raman intensities of quartz peaks below 1140 cm^{-1} are largely dependent upon the instrument focal depth in relation to the sample (**Figure SI.A. 3**). Such changes have also been observed for quartz that was etched by laser irradiation; more intense signals were associated with the etched silica positions on the sample than the unmodified silica regions.[234] Behrens and co-workers observed a dependence of Raman signal intensity on instrument focal depth for alkalialuminosilicate glass; T-O-T bending vibrations observed at 500 cm^{-1} were stable and could be used to normalize Raman spectra, while other silicate peaks varied with focal depth.[235]

Table A. 1. MC-LR Raman peaks were assigned by comparison to literature spectra.[29-31]

Peak (cm^{-1})	Intensity	Molecular vibration
751	weak	CH_2 out of plane bending
828	moderate	C-H out of plane bending in phenyl ring
887	moderate	C-COOH stretch, methylene rocking
970	moderate	v(C-C) wagging, $p(CH_3)$, δ(CCH)
1004	strong	Phenyl C-C vibrations, symmetric ring breathing, methyl aspartic acid
1031	moderate	Phenyl C-H in plane bending, C-N stretching in peptide bonds, C-C skeletal
1086	weak	v(C-C) gauche
1204-1214	weak	Phenyl ring vibrations
1200-1300	moderate	Amide III
1307	strong	CH_3/CH_2 modes (twist, wag, bend)
1384	weak	CH vibrations
1453	moderate	C-H bending modes of proteins
1645	strong	COO vibrations, water in L-lysine aqueous sample

Table A. 2. Quartz Raman peaks were assigned by comparison to literature spectra.[234-237]

Peak (cm^{-1})	**Molecular vibration**
400-500	Si-O-Si stretching and bending
~600	Three-membered ring structures of silica or –Si+ and –O-Si- defects
~800	Si-O-Si bending
1000-1140	Si-O stretching or stretching between disilicate and three bridging O atoms
970-1860	Silica, H_2O contained in the glass

The signal to noise ratio was consistently high and the peak positioning constant for the average of ten Raman spectra collected using 5 s acquisitions for 0.5, 1, 2, 10, and 20 µL samples. This finding is consistent with literature reports for DCDR of lysozyme and insulin.[20,23] For MC-LR samples of 2 µL containing 2-200 ng of toxin (1-100 mg/L without SPE), the Raman signal strength declines as the analyte concentration decreases (**Figure A. 2**). Although the Raman signal of the quartz becomes more intense than the MC-LR signal for the low concentration samples, spectral subtraction of the quartz spectrum from the sample spectrum produces a clear MC-LR Raman spectrum even for the 2 ng sample (**Figure SI.A. 4**).

Normalized MC-LR Raman peak heights were monitored to create calibration curves for 2-100 ng of MC-LR using the intense Raman bands at 1006, 1307, 1457, and 1648 cm^{-1} under two different acquisition conditions (**Figure A. 3 & Figure SI.A. 5**). Non-zero y-intercepts in each of these figures are not surprising for any of the trend lines due to the contribution of the quartz substrate to the measured spectra. To assess the general utility of these calibration curves the mass of a 100 ng control sample (without SPE) was estimated based upon its observed Raman spectral intensity and the four calibration curves in **Figure A. 3.** Using all four calibration curves, an average sample mass of 110 ng (range: 84-157 ng) was computed, an overestimate of the expected concentration by only 10%. This result, coupled with the ability to obtain calibration curves using alternate acquisition parameters (**Figure SI.A. 5**), illustrates the potential quantitative capacity of the DCDR method. Raman peak height analyses are preferred because of their simplicity, especially for pure samples, but PLS regressions could be advantageous and possibly even required to produce calibration curves for complex samples and mixtures.[24,238] By considering the entire Raman spectrum rather than four peak maximum intensities, PLS regressions can differentiate between Raman peaks that remain constant and peaks that correlate with the sample concentration, thus producing potentially more robust calibration curves (Figure SI.A. 6).

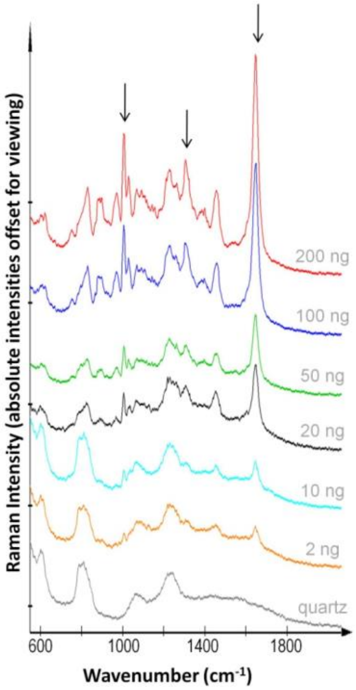

Figure A. 2. MC-LR DCDR spectra for 2 µL samples of 2-200 ng (1-100 mg/L concentrations). Highlighted peaks correspond to the 1006 cm^{-1} aromatic MC-LR ring breathing peak, 1307 cm^{-1} CH$_2$ and CH$_3$ vibrations, and 1650 cm^{-1} COO$^-$ vibrations. Each spectrum is the average of 10 acquisitions collected over 5 s each.

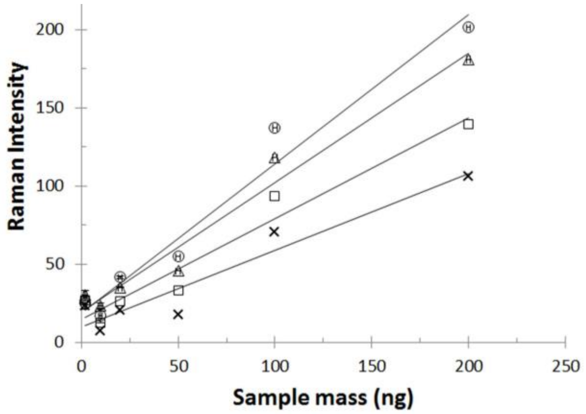

symbol	Raman peak (cm^{-1})	slope with 95% confidence	y-intercept with 95% confidence	R²
o	1006	0.825 ± 0.204	19.631 ± 19.193	0.967
Δ	1648	0.956 ± 0.245	18.551 ± 23.013	0.969
□	1307	0.644 ± 0.203	14.314 ± 19.08	0.951
x	1457	0.49 ± 0.207	9.871 ± 19.437	0.915

Figure A. 3. MC-LR DCDR calibration. Raman intensity was computed by subtracting the quartz background spectrum, multiplying the spectrum by a laser power correction factor, and normalizing the Raman intensities to an acquisition time of five seconds. Each point represents the average of many 1 s, 30 s, or 300 s acquisitions collected across the DCDR drop edge of a 2 µL sample.

Raman signal normalization was necessitated by inconsistencies in the quartz background signal, laser power, sample acquisition time, and variations in the focal plane of the Raman instrument during DCDR sample analysis. Raman spectra were collected after setting the focal plane to the depth that produced the most intense MC-LR Raman spectrum. This position was identified specifically for each sample by tweaking the focal plane of the Raman instrument and scanning across the sample rim in a direction perpendicular to the rim. Raman spectra for 2-200 ng MC-LR were baseline corrected by subtracting a specific background quartz spectrum from each toxin spectrum, collected at the same focal depth as the sample spectrum. The collected Raman spectra were also multiplied by a correction factor to normalize for day to day fluctuations in Raman laser power, determined based upon the 520 cm^{-1} and 942 cm^{-1} peak heights from the Raman spectrum of a silicon standard collected using maximum laser power on each analysis day. The peak height on analysis day A was divided by the peak height on analysis day B, and the ratios computed using the two different peaks were averaged to come up with a single correction factor describing the relative change in laser power. The final spectral correction normalized all spectra to an acquisition time of five seconds by multiplying the spectrum by 5 s and dividing it by the acquisition time for that spectrum. After such a correction, the intensity of peaks acquired in 1 s was similar to that acquired in 300 s for a comparable sample.

A logical hypothesis for the strong correlation between MC-LR Raman signals and sample concentration is that the thickness of the deposited sample ring on the DCDR substrate correlates with sample concentration. The toxicity of MC-LR makes AFM measurements of MC-LR DCDR sample deposit thickness hazardous, so instead the approximate sample thickness was calculated using estimates of drop perimeters from optical images of the DCDR sample drops, sample ridge widths estimated from Raman spectral maps, and assumptions of MC-LR size and volume estimated from molecular models of MC-LR (downloaded from the Protein Data Bank, PDB file lfjm.pdb). The MC-LR DCDR sample ridge thicknesses were computed to be between 2.43 and 0.16 µm (**Table A. 3**). However, drops were not of uniform shape, so these estimates contain a significant margin of error. Nonetheless the drop area did not correlate with concentration. In contrast, Raman spectral maps suggest the width of the sample ridge declined with decreasing concentration (though the sample ridge width was also not uniform), and this trend was reflected in the ridge thickness calculations. AFM measurements of 3 µL DCDR samples of 14.3 to 1430 mg/L lysozyme suggest sample thickness decreases with a decrease in concentration, but a linear correlation was also not observed when a PTFE coated stainless steel substrate was employed.[23] The hydrophobicity of this substrate produces more condensed sample droplets than those deposited for the MC-LR experiments. A 0.77 µm thick sample ridge was observed for the 14.3 mg/L sample. The sample thickness of hyaluronic acid samples on Klarite SERS substrates (D3 Technologies Ltd) were estimated using thin film destructive interference principles for 0.2 µL volume samples at 5, 1, and 0.25 g/L. Relative sample thickness was estimated to be ≈1.4 µm, ≈150 nm, and ≈150 nm respectively;[239] however, the sample volume was much lower than those used in the MC-LR studies. Zhang et al. estimated insulin DCDR samples from 10 µL of 100 µM insulin (~57 mg/L) to be on the order of 10 µm thick on gold foil substrates.[20] These observations suggest that sample ridge thicknesses of 0.2 to 2.4 µm for MC-LR DCDR samples and the lack of a linear correlation between thickness and sample mass are reasonable.

Table A. 3. Computed sample ridge thickness for optimal Raman signal.

MC-LR Sample ID	**Mass (ng)**	**Measured drop edge width (µm)**	**Measured drop area (µm^2)**	**Measured drop perimeter (µm)**	**Calculated thickness at ridge (µm)**
100 mg/L, no SPE	200	16	3.0×10^6	6300	2.43
50 mg/L, no SPE	100	12	5.1×10^6	8100	1.30
25 mg/L, no SPE	50	10	2.8×10^6	6000	1.02
10 mg/L, no SPE	20	5	2.7×10^6	6000	0.79
5 mg/L, no SPE	10	7	4.9×10^6	8200	0.22
1 mg/L, no SPE	2	2	3.0×10^6	6500	0.16
SPE of 2 mL, 5 mg/L	200	36.0	1.3×10^7	13000	0.5
SPE of 500 mL, 5 µg/L	50	33.6	8.7×10^6	10600	0.2
SPE of 500 mL, River Water with 10 µg/L MCLR spike	100	79.9	1.6×10^7	14400	0.11

* Assumes MC-LR volume of 2 nm^3, a uniform drop edge, and 100% recovery of MC-LR thru the SPE process. High recoveries of MC-LR during SPE are reasonable.[57]

MC-LR DCDR sample aging. Sample stability was examined by collecting Raman spectra of DCDR samples that had been stored at room temperature in the dark after drop coating deposition on quartz (**Figure A. 4**). Spectra are largely similar; however, an increase in the wavenumber of the ≈1006 cm^{-1} symmetric ring breathing peak and a decrease in the intensity of the 1648 cm^{-1} peak occur as samples age. These peaks correspond to symmetric aromatic ring breathing in the Adda group and C=O vibrations in MC-LR, although water O-H bending modes are also observed around 1650 cm^{-1}.[240] Considering the stability and persistence of MC-LR in aquatic environments,[241-242] significant degradation at room temperature in the dark is not expected. Instead, desiccation of the sample is a likely cause of the changes observed in the Raman spectrum with aging. Most protein DCDR spectra resemble solution phase spectra,[20,23] potentially due to the formation of a "glassy skin" at the surface of the deposited DCDR sample ring that keeps the sample under the surface hydrated over short timescales.[26] Zhang et al. also observed stable Raman spectra of lysozyme DCDR samples stored at 0 °C for three weeks, and the lysozyme spectrum continued to resemble the aqueous phase spectrum following the storage period.[20] Sample drying could cause a decrease in H_2O vibrations as observed at 1650 cm^{-1} as well as a shift in the position of the 1006 cm^{-1} peak.[30,243] The Adda side chain of MC-LR resembles phenylalanine, for which symmetric ring breathing vibrations are observed in the region of 1000-1008 cm^{-1}, with the peak position shifting for different proteins; it is not unreasonable to assume the position of this peak is affected by the hydration state of the molecule.

Effects of DOM on MC-LR DCDR. An experiment was conducted to determine if the presence of DOM would overshadow the MC-LR Raman signal during DCDR analysis. Mixtures of 1:1 and 1:5 MC-LR and DOM by mass were prepared and DCDR spectra collected. MC-LR was clearly identified in the deposited sample residue in every case (**Figure A. 5**), although regions of fluorescence were more common in the sample with the greatest amount of DOM. DCDR has been well established as a more effective method of fluorescence reduction than extended photobleaching.[21] The drying process also can facilitate segregation of impurities or mixture components.[21,23] Separation of mixture components during DCDR sample drying occurs due to differences in mass or the size of the solution components, solubilities, crystallization kinetics, or free energies of pure solids in comparison to solid solutions.[21]

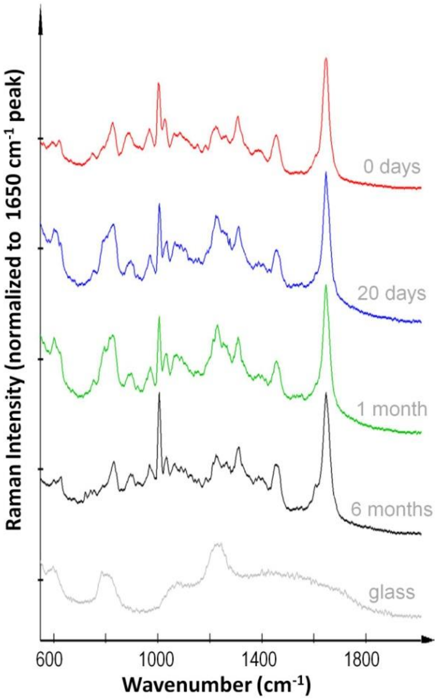

Figure A. 4. MC-LR DCDR sample aging. Raman spectra collected on fresh samples are compared with samples collected after aging periods of 20 days, 1 month, and 6 months. Spectral subtractions suggest small amounts of variation occur in the 1006 and 1648 cm^{-1} peaks.

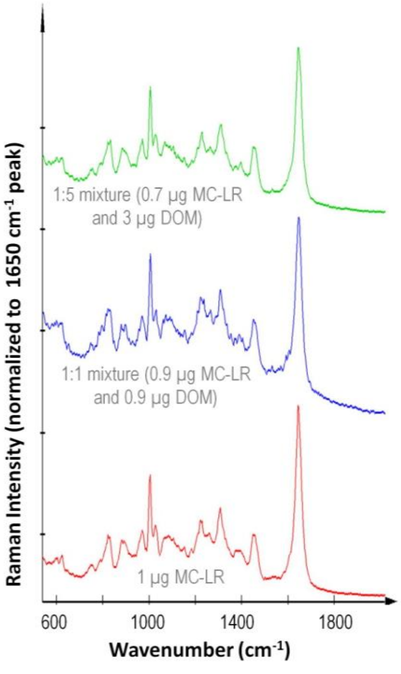

Figure A. 5. Raman spectra of MC-LR mixed with DOM at ratios of 1:5, 1:1, and 1:0 MC-LR: DOM by mass. Samples contain 0.7 µg MC-LR and 3 µg DOM, 0.9 µg MC-LR and 0.9 µg DOM, and 1 µg MC-LR with no DOM. Regions with intense MC-LR Raman signal were located by conducting Raman scans across the surface of the largely fluorescing samples.

Environmentally Relevant Concentrations. Before DCDR will be applicable to environmental samples containing MC-LR at concentrations of concern (i.e., 1 μg/L WHO drinking water limit or 6-20 μg/L U.S. recreational water guidelines),[10,16] it must be combined with purification and concentration steps, an example of which is provided in the schematic in **Figure SI.A. 7** (SPE followed by DCDR). DCDR spectra of an array of samples with differing concentrations and volumes extracted by SPE resembled the pre-SPE MC-LR spectrum, but a decrease in the intensity and sharpness of the 1648 cm^{-1} peak, an increase in the intensity of the 1457 cm^{-1} peak, and additional differences in the overall intensity of the toxin signal were consistently observed (**Figure 3.2 & Figure SI.A. 8**). SPE was determined to be the step in the sample concentration procedure that caused the greatest changes to the MC-LR spectrum. This conclusion was reached after comparison of DCDR spectra collected from each step of the SPE process, including the MC-LR stock solutions, organic solvent spiked samples, heated and rehydrated samples, various SPE "blanks" after limited and extensive cartridge rinsing, and SPE elutants from MC-LR extractions (**Figure SI.A. 9**). Only after the SPE process were peak shifts and intensity changes in the MC-LR Raman spectrum observed. Thorough rinsing of the cartridge greatly decreased the amount of background material detected by DCDR.

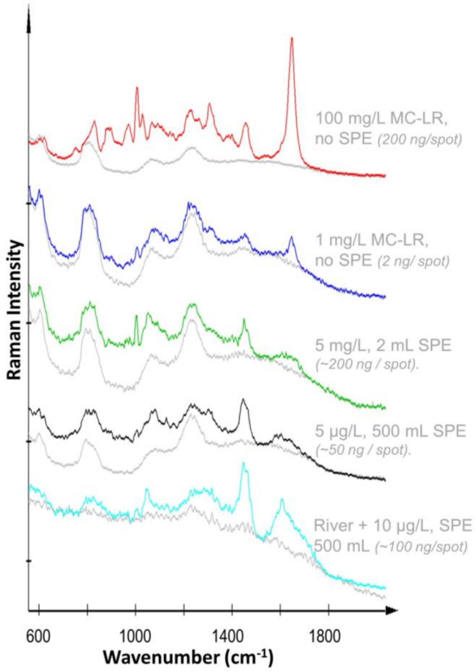

Figure A. 6. MC-LR DCDR spectra are affected by the SPE process, but features including the 1006 cm^{-1}, 1307 cm^{-1}, 1457 cm^{-1}, and 1648 cm^{-1} peaks remain. The quartz background for each sample is indicated in grey.

Following SPE, the intensity of the toxin spectra decreased more than ten-fold compared to that expected if SPE recoveries were high. The intensity drop was correlated to an increase in both drop area and drop edge width as measured from optical images of post-SPE samples (**Table 3.1** & **Figure SI.A. 10**). Contamination of the DCDR sample drop by organic solvent, SPE media components, or other impurities likely decrease the surface tension of the sample droplet, creating a larger drop area despite application of a constant sample volume. Modified substrates such as AnchorChip targets designed for matrix-assisted laser desorption/ionization (MALDI) applications use a polymeric, hydrophobic outer ring of specified dimensions on a hydrophilic substrate to contain sample drops within a designated area, and such a substrate may produce the drop size containment necessary to lower the detection limits of the DCDR method for cyanotoxin detection.

Environmental Waters. SPE was applied to a 500 mL sample of New River water spiked with 10 μg/L of MC-LR, and the resulting DCDR drop exhibited a great deal of impurities compared to a sample prepared in nanopure water (**Figure SI.A. 11**). The calculated drop edge thickness is expected to contain significant error considering impurities that co-deposit with the toxin in the drop edge. Despite the error, the increases in drop area and drop edge width still account for the weak intensity of the toxin Raman signal (**Figure 3.2** and **Table 3.1**). Techniques have been developed to deal with impurities that are soluble in methanol during SPE, including sample rinse steps that increase the methanol percentage in water several times before the final toxin elution.[58-59] Such rinse steps were not incorporated in the current study. Additionally, photobleaching a DCDR sample with the Raman laser prior to Raman acquisition can eliminate some of the background fluorescence produced by impurities in the sample; extensive MC-LR degradation by the 785 nm laser in this case is not expected considering the stability of DCDR spectra collected for a 10 μL sample containing 100 mg/L MC-LR over time under the 785 nm Raman laser. At least 11 minutes of photobleaching were required to produce the spectrum shown for the New River sample (**Figure 3.2** & **Figure SI.A. 12**). Furthermore, Zhang et al. documented success in coupling HPLC and DCDR for human insulin; this coupling applied to MC-LR may provide ample purification, while also producing more descriptive information of the eluted compounds than UV-Vis, PDA, or MS detectors in relation to the microcystins.[20,60-61]

The development of surface-enhanced Raman (SERS) tags that specifically bind to MC-LR may also enable enhancement of the toxin spectrum despite the presence of impurities.[1,62-63]

FUTURE OUTLOOK

The strength of the correlation between concentration and Raman intensity in the pre-SPE samples, the previous success of DCDR for predictions of sample concentration for a number of different biomolecules in sample mixtures, and the concentration levels that DCDR was capable of identifying despite dramatic increases in the DCDR drop area following SPE suggest the DCDR method could be applied for identification and quantitation of MC-LR at environmentally relevant concentrations.[24,65] The ability of Raman to identify MC-LR through a DOM matrix is promising; however, further DCDR experiments should be conducted on microcystin mixtures and impure solutions to identify constituents that will hinder analysis. Development of a substrate to contain DCDR droplets, determination of specific washing protocols for SPE cartridges, and identification of a proper purification protocol utilizing SPE rinses, HPLC purification, or SERS tags that preferentially bind MC-LR will be necessary before DCDR will be practical for analysis of environmental samples at sub μg/L concentrations. The success of DCDR in classifying similar types of insulin despite only one amino acid difference between the tested varieties suggests DCDR may be capable of identifying the composition of a mixture of microcystin variants.[22] Furthermore, similar proteins observed in human tear fluid have not only been distinguished from one another, but concentrations were also successfully predicted.[24]

Although Raman instruments may not yet be established in all environmental laboratories, their initial cost is more economical than LC-MS-MS systems, Raman methods require fewer laboratory consumables than ELISA and PPIA, and Raman methods can utilize portable field instrumentation. The potential utility of a Raman method for microcystin analyses may one day enable cyanotoxin monitoring at more frequent intervals, thus resulting in a more robust detection program that would allow utilities to quickly respond to elevated toxin levels and to adjust their treatment practices accordingly. DCDR should not be overlooked for its potential in cyanotoxin monitoring.

ACKNOWLEDGEMENTS

This work was supported by an EPA STAR graduate research fellowship to R.A.H. (F08B20329) and research grants from the Water Research Foundation (#4212) and the Virginia Tech Institute for Critical Technology and Applied Science (ICTAS). We thank Dr. Weinan Leng for his insights and assistance with the WITec Alpha 500R.

SUPPORTING INFORMATION

Raman instrument parameters. Raman spectra of MC-LR obtained using 514, 633, and 785 nm laser excitation contained similar features with different resolutions, which can be explained by the detector sensitivity and instrument focal length (**Figure SI.A. 1**). The quantum efficiency of the CCD camera on the WITec instrument reaches a maximum near 785 nm and is lower (< 85%) at 633 nm.[244] Therefore, the instrument collects more intense signals with the 785 nm laser and requires shorter acquisition times. The 514 nm spectrum displays clearer, sharper peaks because the JY Horiba instrument is a High Resolution Raman spectrometer; it has a focal length of 800 mm while most spectrometers have a focal length of 300 mm. The longer focal length increases the resolution by a factor of approximately three, allowing more accurate description of peak shapes and band position.[245-246] The UV-Vis absorbance spectrum of MC-LR is free of any absorbance between 300 to 900 nm, suggesting that resonance does not contribute to Raman spectra collected using 514, 633, and 785 nm lasers (**Figure SI.A. 2**). Such will be the case for most microcystins; most variants absorb only between 200 and 300 nm due to the Adda group that contains a conjugated diene that absorbs at 238 nm.[17] Tryptophan containing microcystins also absorb at 222 nm, but this absorbance will not affect Raman spectra collected with laser wavelengths 514, 633, or 785 nm. All subsequent spectra were collected on the WITec system because of its ability to rapidly collect high quality spectral maps. The 785 nm laser is less likely to burn samples than more powerful lower wavelength lasers, the CCD camera on the WITec instrument is most sensitive to Raman signals in the vicinity of 785 nm, and the lowest acquisition times were required with the 785 nm laser.

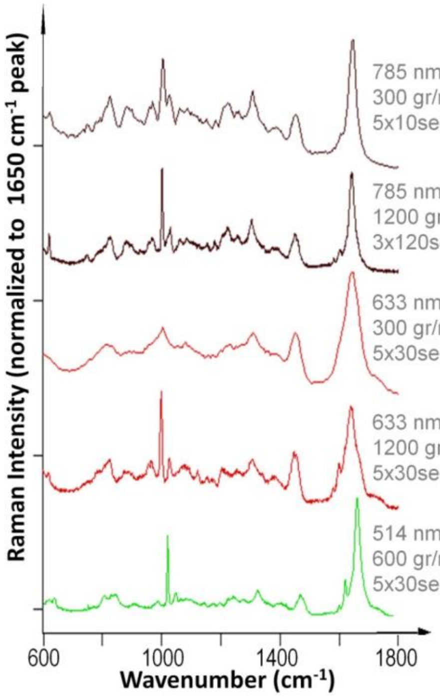

Figure SI.A. 1. MC-LR Raman spectra collected under a series of instrument parameters. WITec Alpha 500 and JY Horiba LabRAM HR 800 spectrometers were used to collect spectra using a 100× microscope objective and the indicated parameters. The Raman spectrum of MC-LR is affected by the Raman laser wavelength and grating choice; the 785 nm laser and 300 gr/mm grating produced the fastest spectra with sufficient resolution for peak identification.

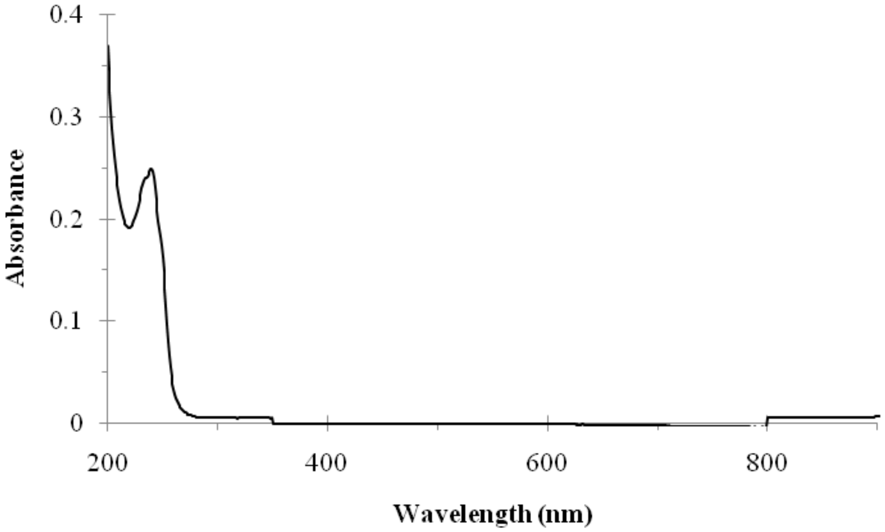

Figure SI.A. 2. UV-Vis spectrum of 4 mg/L MC-LR in a quartz cuvette. The maximum absorbance occurs at 240 nm, and no absorbance was observed above 300 nm. Molecules that absorb the Raman laser wavelength will resonate upon laser contact and display more intense Raman signals than molecules that do not resonate; the lack of absorbance in the UV-Vis spectrum of MC-LR over the 300 – 900 nm region suggests resonance will not affect the Raman spectrum of MC-LR at any of the tested wavelengths.

Raman probed region. The dimensions of the sampling region for a Raman spectrum can be estimated using the following equation.[76]

$$\delta_{lateral} = \frac{0.61\,\lambda}{NA}$$

A laser spot size of approximately 0.5 µm in the lateral direction is computed for a 785 nm laser wavelength and a microscope objective with a numerical aperture of 0.9.

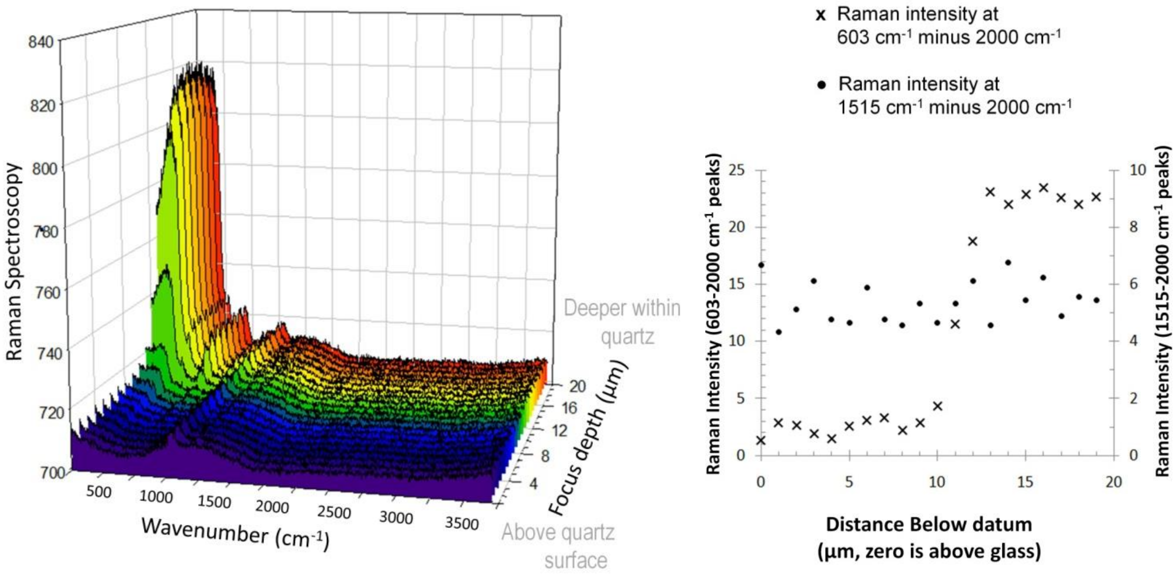

Figure SI.A. 3. Depth profile of quartz Raman spectra. Spectra were collected at 1 µm intervals and plotted on a true y scale. Quartz is an ideal substrate because it produces little Raman signal in the region of interest at its surface (600-1800 cm^{-1}), but still provides some signal that can be used to normalize spectra.

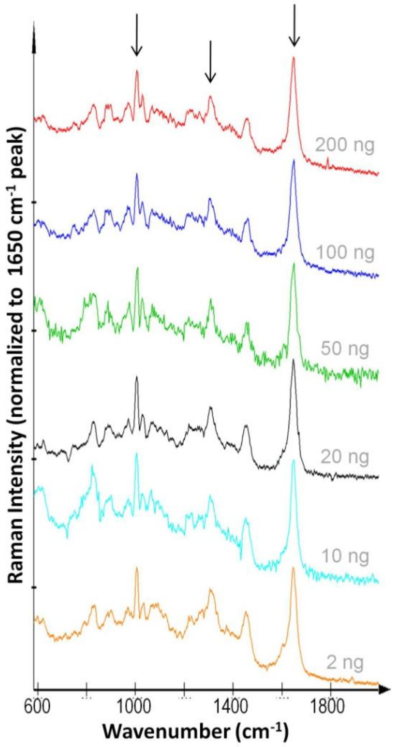

Figure SI.A. 4. DCDR spectra for 2 µL samples containing 200 – 2 ng of MC-LR. Highlighted peaks belong to 1006 cm^{-1} aromatic MC-LR vibrations, 1307 cm^{-1} CH_2 and CH_3 vibrations, and 1645 cm^{-1} COO^- vibrations. Each spectrum is the average of multiple acquisitions of 1 – 300 s each (200, 100, and 50 ng required 1 s acquisitions; the 20 and 10 ng samples required 30 s, and the 2 ng sample required 300 s acquisitions) from which the quartz background signals have been subtracted. Spectra are normalized to the 1650 cm^{-1} peak.

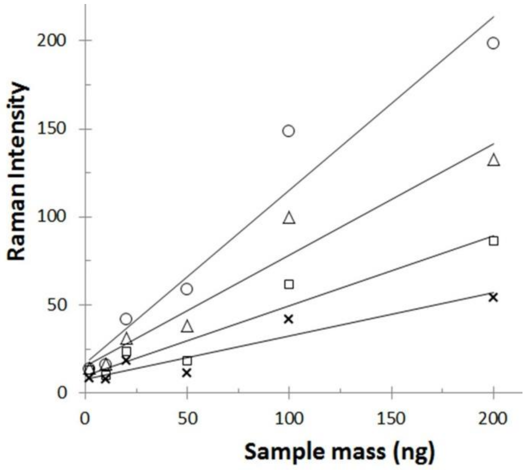

symbol	Raman peak (cm^{-1})	slope with 95% confidence	y-intercept with 95% confidence	R^2
o	1006	0.629 ± 0.211	15.497 ± 19.861	0.9670
Δ	1648	0.983 ± 0.323	16.851 ± 30.405	0.9690
□	1307	0.397 ± 0.151	10.07 ± 14.214	0.93
x	1457	0.245 ± 0.117	8.057 ± 11.006	0.894

Figure SI.A. 5. MC-LR calibration by the DCDR method. Raman intensity was computed by subtracting the quartz background spectrum, multiplying the spectrum by a laser power correction factor, and normalizing the Raman intensities to an acquisition time of five seconds. Each point represents the average of ten acquisitions of five seconds each collected across the DCDR drop edge of a 2 µL sample.

Partial Least Squares (PLS) Regressions. DCDR spectra were collected from 1-100 mg/L MC-LR samples and incorporated into a PLS regression after considering the variance explained by each principal component and a 10-fold cross validation (Figure SI.A. 6**a & b**). When considering two principal components only, such as would be described by the quartz background and MC-LR, a correlation with an R^2 value of 0.9231 is generated. Loading plots for the principal components suggest the first two components clearly describe the toxin at two different background levels, and components three through six appear to resemble remnants from the quartz background that was subtracted (Figure SI.A. 6**c**). It is therefore logical that samples of lower concentrations in which the background signals are more prominent would be more accurately predicted when principal components three through five are included in the model (Figure SI.A. 6**d & e**).

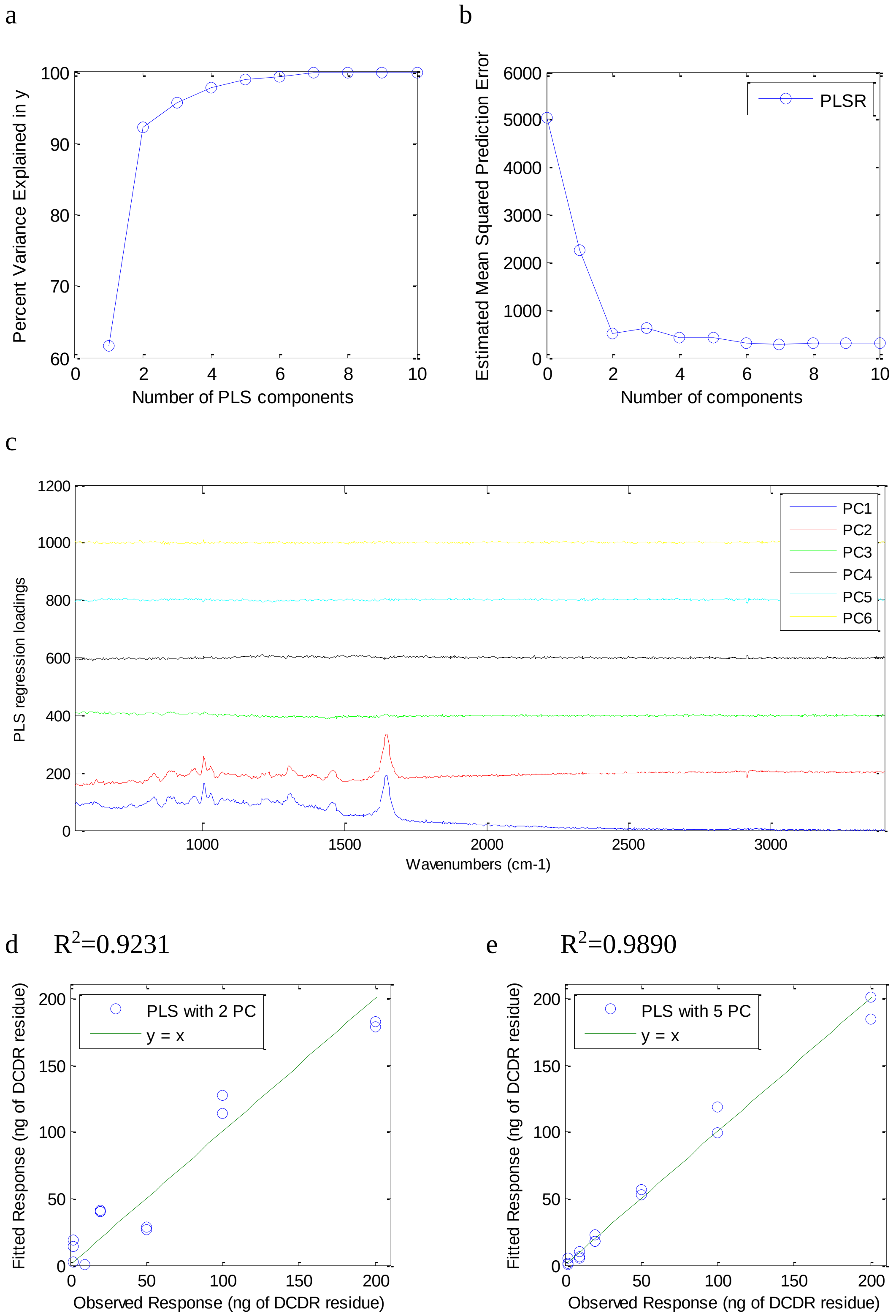

Figure SI.A. 6. PLS regressions of DCDR samples containing 1-100 mg/L MC-LR. The number of principal components used to create the model was determined by (a) the percent variance explained in Y, (b) the estimated mean squared prediction error computed by 10-fold cross validation of the PLS model, and (c) loadings for each principal component. PLS regressions computed using two and five principal components are shown (d & e).

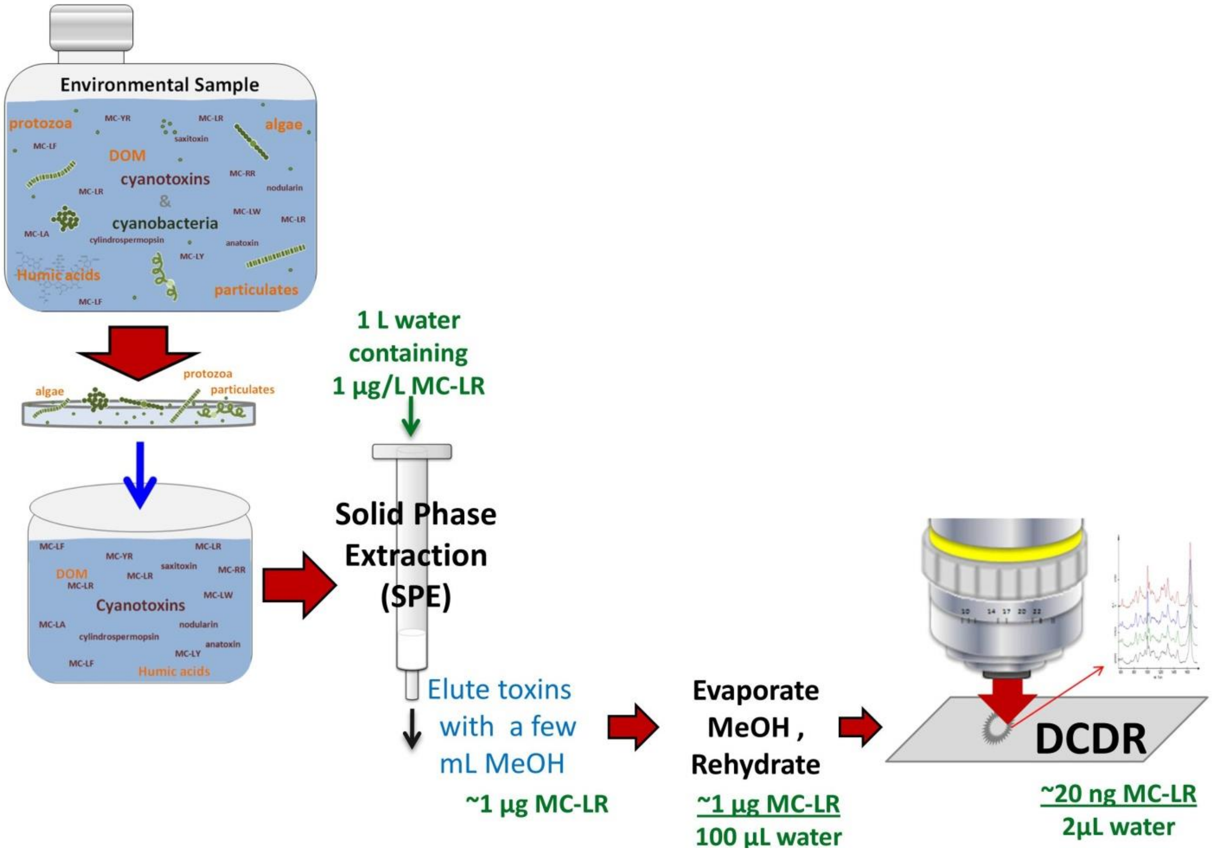

Figure SI.A. 7. SPE may be applied for sample purification and concentration before DCDR. Estimated toxin outputs assume high recoveries of toxin following SPE, which are not impossible to achieve as documented in the literature.[57]

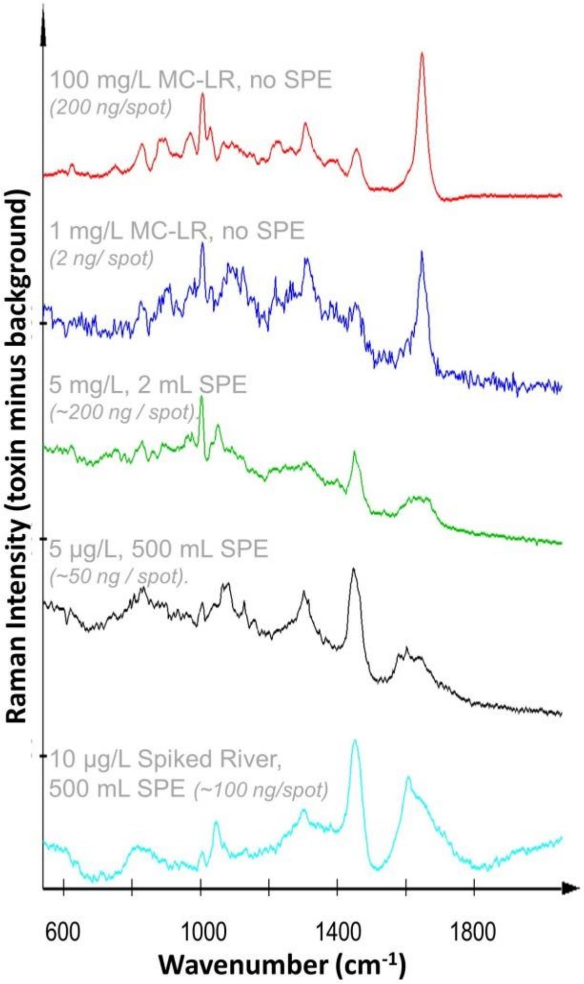

Figure SI.A. 8. Background subtracted MC-LR DCDR spectra. Although the quartz background signal is useful for documenting perspective of the overall intensity of the toxin signals relative to the background, background subtracted spectra were used for more thorough analysis of peak differences.

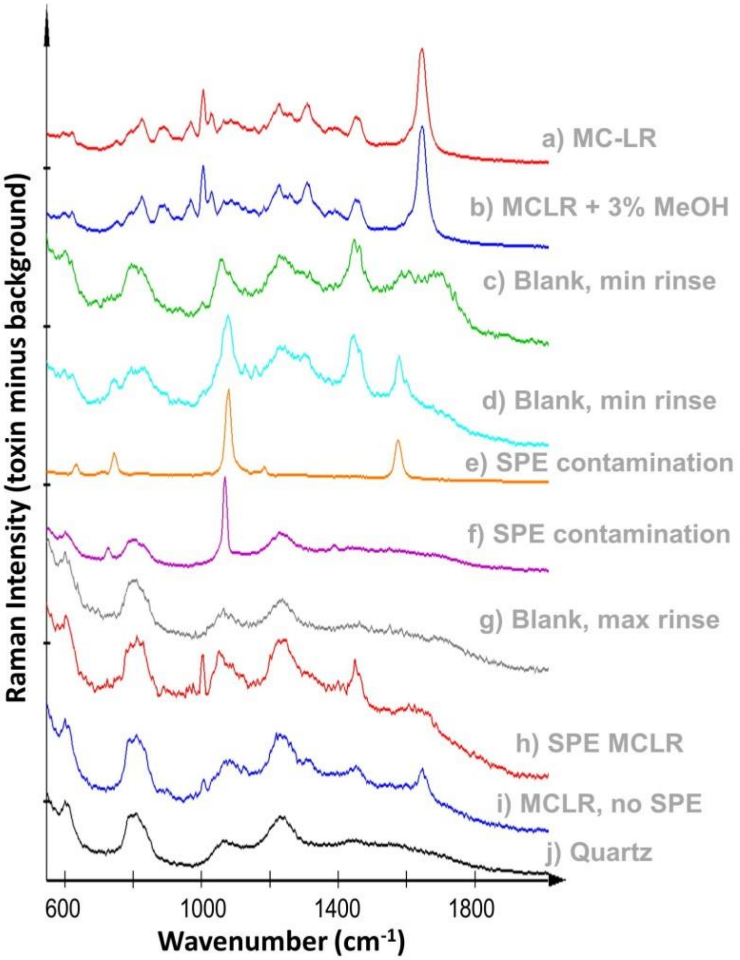

Figure SI.A. 9. DCDR spectra tracking both toxin and impurity signals throughout the SPE process. Thorough rinsing of the SPE cartridge before extraction is necessary to obtain the clearest toxin spectra. Two microliters of each of the following samples were applied for DCDR analysis: (a) a freshly prepared 50 mg/L MC-LR aqueous solution; (b) a 50 mg/L MCLR aqueous solution with 3% v/v methanol; (c) a “blank” sample of anything that eluted from the SPE cartridge in methanol after limited cartridge rinsing (6 mL each of methanol, water, methanol, and more water); (d) a “blank” sample with limited cartridge rinsing; (e & f) any sample after SPE commonly contained crystals in the inner portions of the drop with the spectra indicated here; (g) a “blank” sample of the elutant from a SPE cartridge in methanol after extensive cartridge rinsing (the same steps as c, with additional methanol, water, acetone, water, methanol, and water rinses, (h) the SPE elutant resulting from extraction of 2 mL of a 5 mg/L MC-LR solution, made from the same stocks as samples a and b above and rehydrated in 100 μL water; (i) a 1 mg/L MC-LR solution that did not undergo SPE; and (j) the quartz background observed beneath all samples. The spectrum of MC-LR after heating with methanol to evaporate solvent followed by rehydration in water, without SPE is identical to a & b.

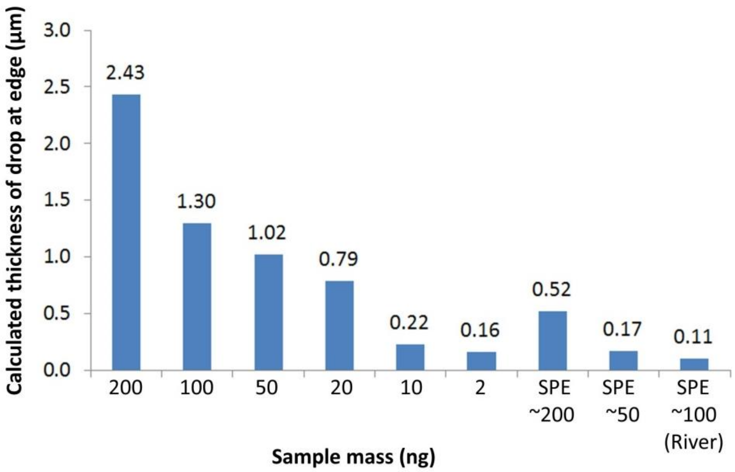

Figure SI.A. 10. Comparisons between the calculated DCDR drop edge thickness for samples of different masses pre- and post- SPE.

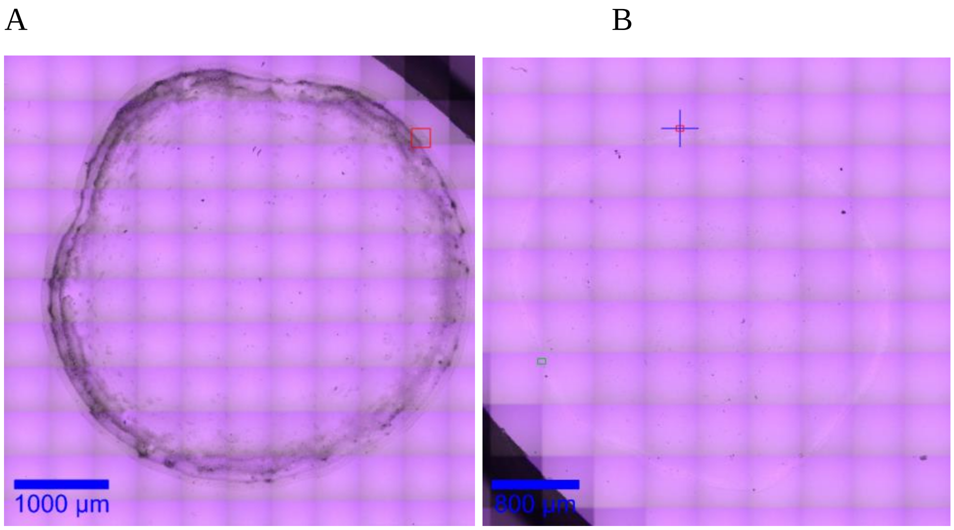

Figure SI.A. 11. Optical images of a DCDR drop after SPE of 500 mL of samples containing (A) New River water spiked with 10 µg/L MC-LR and (B) nanopure water containing 5 µg/L MC-LR.

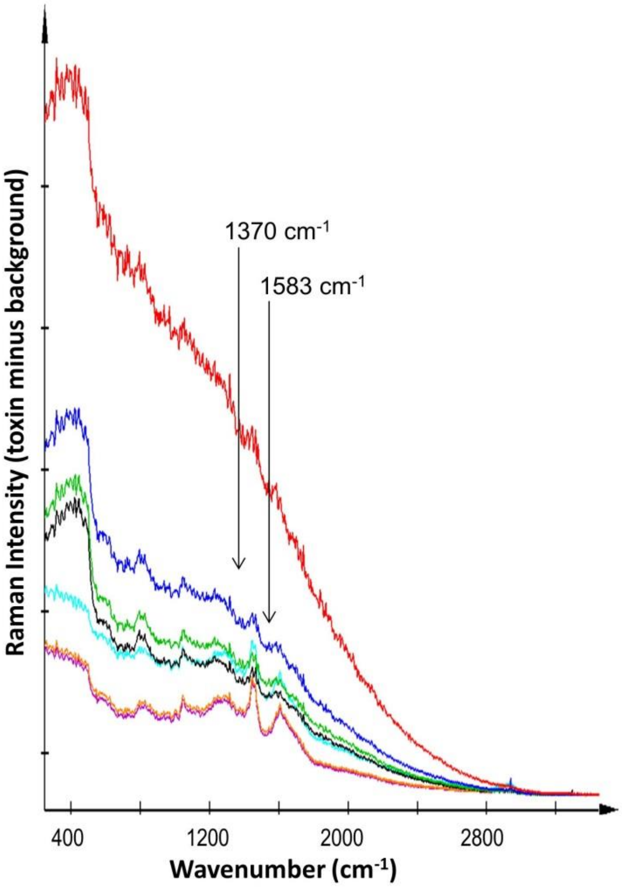

Figure SI.A. 12. Photobleaching decreased background fluorescence, and allowed signals from the sample to shine thru the background. Spectra were collected in a single location at the following time intervals (top down): 0 min, 1.3 min, 2.5 min, 3.5 min, 6.6 min, 11.2 min, 12.6 min, and 14.6 min. Graphite peaks due to the decomposition of organic matter upon laser contact observed by peaks at 1370 and 1583 cm^{-1} do not grow in these spectra as the samples are exposed to the laser.[64]

Appendix B: Copyright

Halvorson, R. A.; Leng, W.; Vikesland, P. J. Differentiation of microcystin, nodularin, and their component amino acids by drop-coating deposition Raman spectroscopy. *Anal. Chem*. 2011, 83 (24), 9273-9280.

Halvorson, R. A.; Vikesland, P. J. Drop coating deposition Raman (DCDR) for microcystin-LR identification and quantitation. *Environ. Sci. Technol*. 2011, 45 (13), 5644-5651.

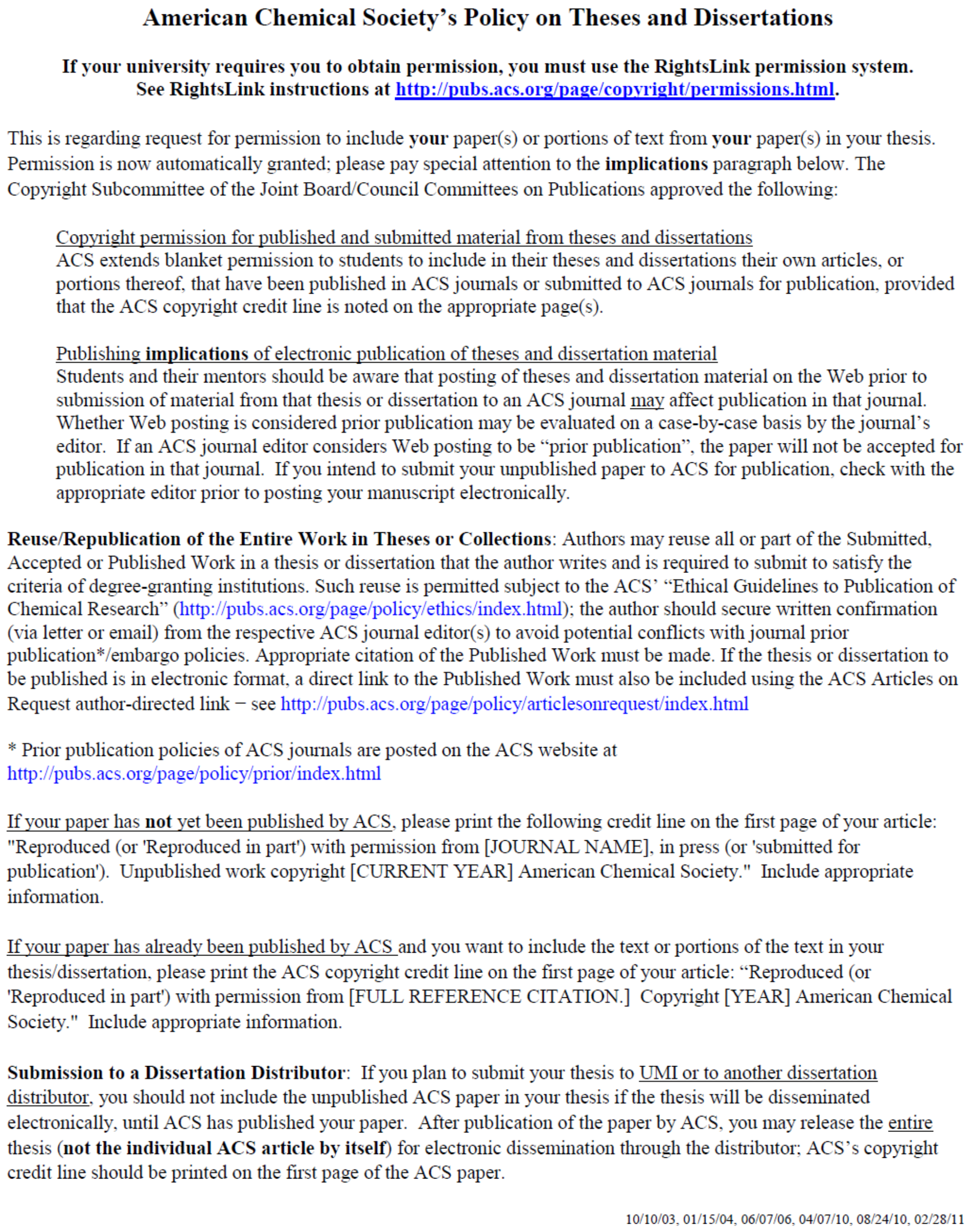

American Chemical Society's Policy on Theses and Dissertations

If your university requires you to obtain permission, you must use the RightsLink permission system. See RightsLink instructions at http://pubs.acs.org/page/copyright/permissions.html.

This is regarding request for permission to include **your** paper(s) or portions of text from **your** paper(s) in your thesis. Permission is now automatically granted; please pay special attention to the **implications** paragraph below. The Copyright Subcommittee of the Joint Board/Council Committees on Publications approved the following:

> Copyright permission for published and submitted material from theses and dissertations
> ACS extends blanket permission to students to include in their theses and dissertations their own articles, or portions thereof, that have been published in ACS journals or submitted to ACS journals for publication, provided that the ACS copyright credit line is noted on the appropriate page(s).
>
> Publishing **implications** of electronic publication of theses and dissertation material
> Students and their mentors should be aware that posting of theses and dissertation material on the Web prior to submission of material from that thesis or dissertation to an ACS journal may affect publication in that journal. Whether Web posting is considered prior publication may be evaluated on a case-by-case basis by the journal's editor. If an ACS journal editor considers Web posting to be "prior publication", the paper will not be accepted for publication in that journal. If you intend to submit your unpublished paper to ACS for publication, check with the appropriate editor prior to posting your manuscript electronically.

Reuse/Republication of the Entire Work in Theses or Collections: Authors may reuse all or part of the Submitted, Accepted or Published Work in a thesis or dissertation that the author writes and is required to submit to satisfy the criteria of degree-granting institutions. Such reuse is permitted subject to the ACS' "Ethical Guidelines to Publication of Chemical Research" (http://pubs.acs.org/page/policy/ethics/index.html); the author should secure written confirmation (via letter or email) from the respective ACS journal editor(s) to avoid potential conflicts with journal prior publication*/embargo policies. Appropriate citation of the Published Work must be made. If the thesis or dissertation to be published is in electronic format, a direct link to the Published Work must also be included using the ACS Articles on Request author-directed link – see http://pubs.acs.org/page/policy/articlesonrequest/index.html

* Prior publication policies of ACS journals are posted on the ACS website at http://pubs.acs.org/page/policy/prior/index.html

If your paper has **not** yet been published by ACS, please print the following credit line on the first page of your article: "Reproduced (or 'Reproduced in part') with permission from [JOURNAL NAME], in press (or 'submitted for publication'). Unpublished work copyright [CURRENT YEAR] American Chemical Society." Include appropriate information.

If your paper has already been published by ACS and you want to include the text or portions of the text in your thesis/dissertation, please print the ACS copyright credit line on the first page of your article: "Reproduced (or 'Reproduced in part') with permission from [FULL REFERENCE CITATION.] Copyright [YEAR] American Chemical Society." Include appropriate information.

Submission to a Dissertation Distributor: If you plan to submit your thesis to UMI or to another dissertation distributor, you should not include the unpublished ACS paper in your thesis if the thesis will be disseminated electronically, until ACS has published your paper. After publication of the paper by ACS, you may release the entire thesis (**not the individual ACS article by itself**) for electronic dissemination through the distributor; ACS's copyright credit line should be printed on the first page of the ACS paper.

10/10/03, 01/15/04, 06/07/06, 04/07/10, 08/24/10, 02/28/11